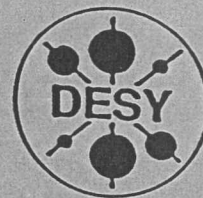E/C

liegt aus

DEUTSCHES ELEKTRONEN-SYNCHROTRON

DESY

X1998-00952

Charmonium Production in Deep Inelastic Scattering at HERA

by

A. Meyer

To be sure that your reports and preprints are promptly included in the
HEP literature database
send them to (if possible by air mail):

DESY	DESY
Zentralbibliothek	Bibliothek
Notkestraße 85	Platanenallee 6
22603 Hamburg	15738 Zeuthen
Germany	Germany

Charmonium Production
in Deep Inelastic Scattering
at HERA

DISSERTATION

zur Erlangung des Doktorgrades
des Fachbereichs Physik
der Universität Hamburg

vorgelegt von

Arnd Meyer

aus Bremen

Hamburg
1998

Gutachter der Dissertation: Prof. Dr. B. Naroska
                                Prof. Dr. R. Klanner

Gutachter der Disputation: Prof. Dr. B. Naroska
                                Prof. Dr. A. Wagner

Datum der Disputation: 8.6.1998

Dekan des Fachbereichs Physik und
Vorsitzender des Promotionsausschusses: Prof. Dr. B. Kramer

Im ersten Zustand stellt sich der Gedanke ein,
im zweiten wünscht man zu sehen,
im dritten folgen tiefe Seufzer,
im vierten wird man von Fieber befallen,
im fünften brennen die Glieder,
im sechsten schmeckt einem das Essen nicht mehr,
im siebenten stellt sich Zittern ein,
im achten wird man verrückt,
im neunten schwinden die Lebensgeister
und im zehnten haucht man sein Leben aus.

VETALAPANCAVIMSCHATIKA, ~ 10. JH.

Im ersten Zustand stellt sich der Gedanke ein,
im zweiten wünscht man zu sehen,
im dritten folgen tiefe Seufzer,
im vierten wird man von Fieber befallen,
im fünften brennen die Glieder,
im sechsten schmeckt einem das Essen nicht mehr,
im siebenten stellt sich Zittern ein,
im achten wird man verrückt,
im neunten schwinden die Lebensgeister
und im zehnten haucht man sein Leben aus.

VETALAPANCAVIMSCHATIKA, ~ 10. JH.

Contents

Chapter 1

Introduction

The goal of high energy physics is the understanding of the fundamental interactions between the elementary constituents of matter. Upon this quest, the *Standard Model* provided over the last twenty years a satisfactory description of the strong, weak and electromagnetic interactions of all known elementary particles. In the numerous comparisons between experiment and theory only few discrepancies have been found, and these are at the level of a few standard deviations or less.

Given these successes, one should expect that the description of a bound state of two reasonably heavy quarks, namely *Charmonium*, can be incorporated rather easily into the model — but on the contrary, the measurement of Charmonium production rates at large transverse momentum at the Tevatron collider came as a surprise. The cross sections for the direct production have been observed to be about one order of magnitude larger than expected in the *Colour Singlet Model*, which previously had been thought to correctly describe Charmonium production.

Following these results in 1992, the calculations of the production of Charmonium states have been put on a solid formal basis by the work of Bodwin, Braaten and Lepage; the inclusion of *colour octet* mechanisms, using a new factorization formalism based on an effective field theory called non-relativistic Quantum Chromodynamics (NRQCD), provides a natural explanation of the measured cross sections. This formalism can be applied to Charmonium production in many different processes, among others also the photo- and electroproduction of J/ψ mesons at the electron-proton collider HERA. The only free parameters are non-perturbative matrix elements fot the transition to the observable J/ψ; measuring these cross sections is therefore a crucial test of the theory's universality.

Another field of interest is the production of Charmonium states in *diffractive* scattering at HERA. Attempts exist to apply perturbative QCD to so-called *elastic J/ψ* production, modeling the interaction with the proton with a gluon ladder, which corresponds to the *Pomeron* known from soft hadronic interactions. In the case that elastic J/ψ production can be described within such a model, it would offer a direct and highly sensitive way to measure the gluon density in the proton. However, before this becomes feasible, other predictions of these models concerning for example the fraction of longitudinally polarized J/ψ, the diffractive slope parameter, or the ratio of $\psi(2S)$ to J/ψ production have to be studied. The particular relevance of HERA in these topics compared to previous experiments is due to the large values of Q^2, the square of the four-momentum transferred at the electron vertex, and especially W^2, the squared centre of mass energy of the hadronic system, which can be accessed.

It is a unique possibility of HERA that the transition between the soft, non-perturbative and the hard, perturbative regime in exclusive vector meson production can be accessed on a variety of scales:

- m_V^2, the *mass* of the vector meson;

- Q^2, the *virtuality* of the process;

- t, the four-momentum transferred at the proton vertex.

The subject of this thesis is the analysis of Charmonium electroproduction at the HERA collider, using data taken with the H1 experiment in the years 1995 to 1997. Electroproduction means here that Q^2 is large enough for the scattered electron to be detected in the main detector ($Q^2 \gtrsim 1 \, \text{GeV}^2$), as opposed to photoproduction ($Q^2 \simeq 0$) which has been analyzed previously. This kinematic region is advantageous both experimentally and theoretically: generally perturbative calculations become more reliable as Q^2 increases. Experimentally, the detection of the scattered electron over-constrains the kinematics of the scattering process, leading to small experimental errors. Furthermore, the scattered electron's detection facilitates the triggering of events which often contain only a low energy J/ψ meson and little other hadronic activity.

The structure of this thesis is as follows. An overview of the HERA collider and the H1 detector is given first. This covers, after a short section on HERA kinematics and the HERA accelerator chain, all detector components relevant for this analysis, as well as the trigger and data acquisition scheme of H1.

In chapter 3, different models for Charmonium production are discussed, in particular their predictions for the kinematic range of HERA.

The remaining chapters focus on the analysis of Charmonium production in the H1 experiment, using the leptonic decay channels $J/\psi \to \mu^+\mu^-$, $J/\psi \to e^+e^-$ and $\psi(2S) \to J/\psi\pi^+\pi^-$, where the J/ψ again decays either in two electrons or two muons. In chapter 4 the data sets used in this analysis are introduced. Furthermore a description of the Monte Carlo data sets which have been used for acceptance corrections is given. The next chapter contains the results obtained for diffractive J/ψ production. Inefficiencies of the detector are to a large extent directly determined from the data, and extensive comparisons between the data and the Monte Carlo simulation are performed. Cross sections are given as a function of different kinematical variables and discussed in the light of phenomenological models.

The first measurement of $\psi(2S)$ production in deep inelastic scattering at HERA is presented in chapter 6, including the ratio of cross sections for $\psi(2S)$ over J/ψ production as a function of Q^2.

In chapter 7 a novel approach towards a largely model independent analysis of inclusive J/ψ production is presented. A Monte Carlo description of inclusive J/ψ production is obtained using a combination of existing generators based on Regge theory and the Colour Singlet Model. The calculated differential cross sections are compared to predictions within the NRQCD factorization approach, and possibilities to suppress diffractive contributions are discussed.

In the final chapter, all results are summarized and the prospects for future analyses are discussed.

Chapter 2

HERA and the H1 Detector

The HERA (Hadron–Elektron–Ring–Anlage) collider at DESY in Hamburg offers the unique possibility to store and collide electrons and protons in counter rotating beams at high centre of mass energies, $\sqrt{s} \simeq 300\,\text{GeV}$. Since 1992, the HERA beams have been used by the two multi-purpose detectors H1 and ZEUS, situated at the northern and southern interaction regions. Two further experiments, HERMES and HERA-B, make use of only the electron or proton beam, respectively, and are operated in the western and eastern area of HERA.

In this chapter, the kinematic variables used for the description of deep inelastic scattering at HERA will be introduced. A brief overview of the HERA collider and its pre-accelerators is given, followed by a description of the H1 detector as far as relevant for the present analysis. Figures on the functioning and performance of the detector components, as well as a description of the most important components of the trigger and data acquisition system are included.

2.1 HERA Kinematics

Although the variables specific to Charmonium production won't be discussed until chapter 3, the basic kinematic variables for any deep inelastic scattering (DIS) process at HERA will be introduced here.

In figure 2.1, the basic process for deep inelastic ep scattering is illustrated:

$$\text{a)} \quad e^{\pm} p \rightarrow e^{\pm} X \ \ (\text{NC}) \qquad\qquad \text{b)} \quad e^{\pm} p \rightarrow \overset{(-)}{\nu_e} X \ \ (\text{CC}). \tag{2.1}$$

The incoming lepton with four-momentum k scatters off the proton via the exchange of the electroweak gauge bosons γ, Z^0 (neutral current, NC) or $W^{\pm}$ (charged current, CC) with four-momentum q. The total centre of mass energy $\sqrt{s}$ and the square of the four-momentum transferred are given by

$$s = (p_p + k)^2 \simeq 4 \cdot E \cdot E_p \ \ \text{and} \tag{2.2}$$

$$Q^2 = -q^2, \tag{2.3}$$

where E and E_p are the energies of the incoming electron and proton, respectively, and the electron and proton masses have been neglected.

3
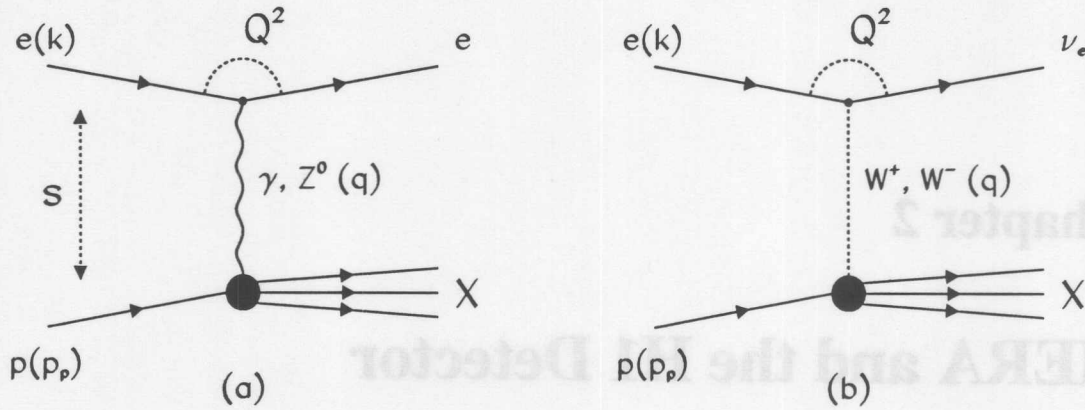
Figure 2.1: *Generic diagrams for a) NC and b) CC deep inelastic ep scattering. Symbols in brackets denote the particle's four-momenta.*

In addition to the centre of mass energy, two further Lorentz scalars are sufficient to describe the DIS process. Conventionally, the Bjorken scaling variable x or the inelasticity y are chosen besides Q^2:

$$x = \frac{-q^2}{2p_p \cdot q};$$ (2.4)

$$y = \frac{q \cdot p_p}{k \cdot p_p}.$$ (2.5)

In the Quark Parton Model, x is the fraction of the proton momentum carried by the struck parton; y describes the relative energy transferred to the proton in its rest frame. Neglecting the masses of the electron and proton, Q^2, x and y are related by the simple equation

$$Q^2 \simeq xys.$$ (2.6)

Finally, the square of the invariant mass W^2 of the hadronic final state X is related to x and Q^2 by momentum conservation at the hadronic vertex:

$$W^2 = (p+q)^2 = Q^2 \cdot \left(\frac{1}{x} - 1\right) + m_p^2$$ (2.7)

$$= y \cdot s - Q^2 + m_p^2,$$ (2.8)

where m_p denotes the mass of the proton.

For the remaining part of this work, only the neutral current process $e^{\pm} p \rightarrow e^{\pm} X$, where the exchange particle is a virtual photon, will be considered; Z^0 exchange is suppressed by a factor

$$\sim \frac{Q^2}{Q^2 + M_Z^2},$$ (2.9)

and therefore negligible as long as Q^2 is much smaller than the square of the Z^0 mass M_Z^2. For the same reason, charged current contributions are negligible.

Three kinematic regions can be distinguished: for $x \rightarrow 1$, *elastic scattering* occurs ($W^2 \rightarrow m_p^2$); for $Q^2 \rightarrow 0$, the exchanged photon is almost real, and the region of *photoproduction* is reached; large Q^2 ($Q^2 \gtrsim 1\,\text{GeV}^2$) and $W^2 \gg m_p^2$ is the domain of deep inelastic scattering, the region of interest for this thesis.
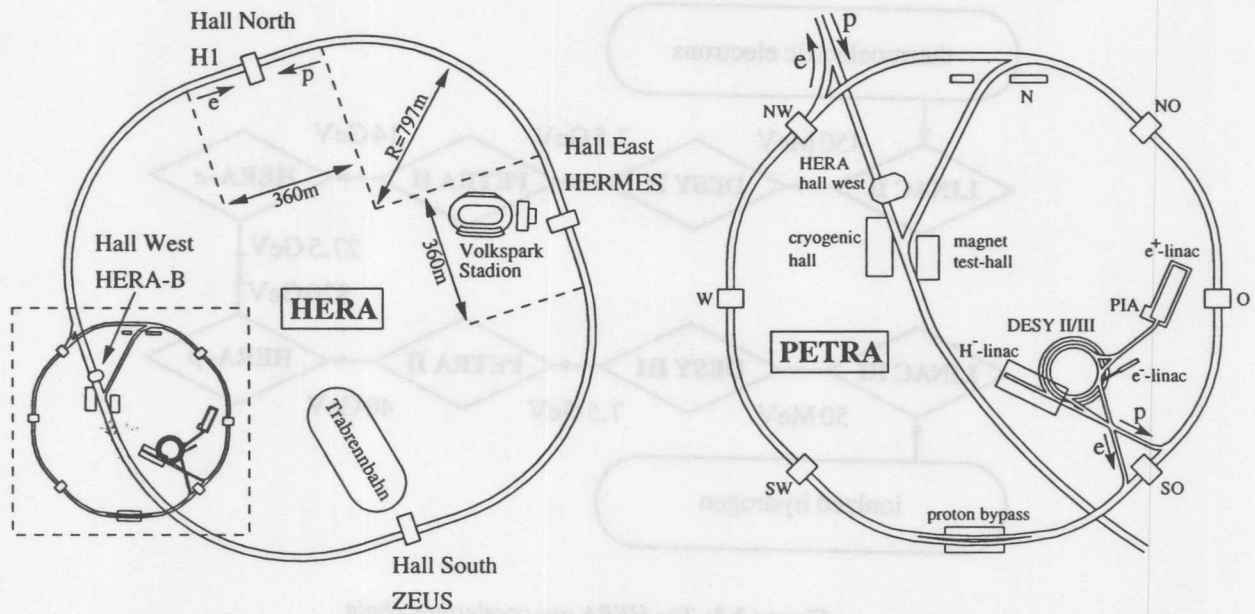
Figure 2.2: *Layout of the HERA accelerator (left) and its pre-accelerators (right).*

2.2 The HERA Collider

In 1990, after six years of construction, the world's first electron-proton collider HERA (figure 2.2) was completed in Hamburg. Two independent storage rings of 6.4 km circumference, HERA-e and HERA-p, are housed in a tunnel between 15 and 25 m underground.

Protons and electrons or positrons[1] are passed through a complex system of pre-accelerators as sketched in figure 2.3. Afterwards, the beams are accelerated using superconducting and warm RF-cavities to energies of 820 GeV and 27.5 GeV respectively.

The beams are collided at almost zero crossing angle at two interaction points in the north and south halls of the accelerator, where the H1 and ZEUS detectors are positioned. The centre of mass energy reached by HERA is $\sqrt{s} \simeq 300$ GeV, equivalent to a fixed target experiment operating with an electron beam of approximately 50 TeV.

In order to achieve high integrated luminosities, HERA is operating with up to 210 bunches of electrons and protons each, resulting in a bunch crossing frequency of 10 MHz. A small number of non-colliding electron and proton bunches, termed *pilot-bunches*, is usually preserved as a means to study beam induced background arising from interactions of the beam with the residual gas in the beam pipe, or with its wall. The luminosity lifetime is typically 10 h; it is dominated by the electron beam lifetime ($\simeq$ 10 h) rather than by the proton beam lifetime which is of order 100 h. Nevertheless, the storage time for protons is usually much smaller than expected from the current lifetime; due to a slow growth of the transverse beam emittance during *ep* collisions, the proton beam is routinely dumped and re-filled for each electron fill.

---

[1] During 1995 to 1997, HERA was operated with positrons instead of electrons. The terms electron and positron are used synonymously in this work whenever related to the incoming or scattered lepton.
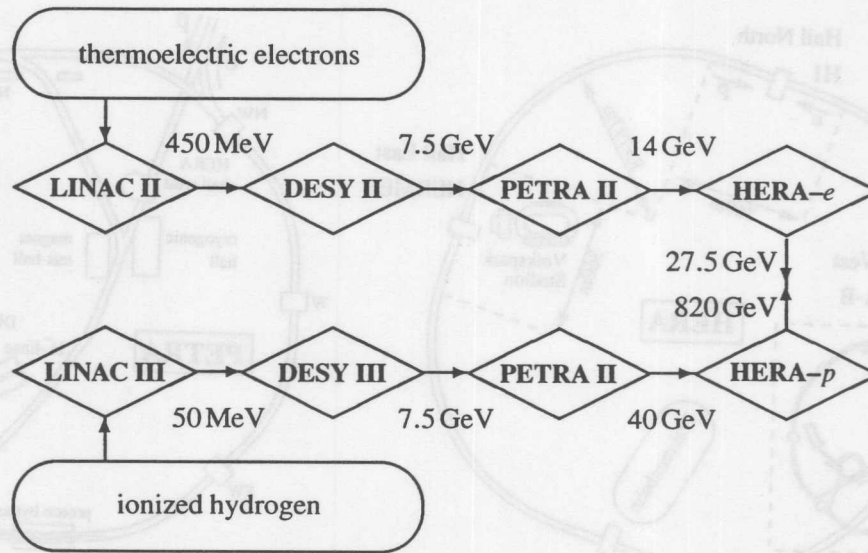
Figure 2.3: *The HERA pre-accelerator chain.*

Some figures for the performance of HERA from the years 1995 to 1997, upon which this analysis is based, are given in table 2.1.

2.3 The H1 Detector

The H1 detector, shown in figure 2.4, is built according to the same principles as most modern collider experiments, differing in the enhanced instrumentation in the proton direction to take into account the asymmetric proton and electron beam energies. The coordinate system used within the H1 collaboration, indicated in figure 2.4, has its origin at the nominal interaction point with the z-axis pointing in the outgoing proton direction (defined as "forward"). In this frame, the x-axis points towards the centre of the HERA ring, the y-axis upwards. The polar angle θ is measured with respect to the proton beam direction, while the azimuthal angle ϕ is measured with respect to the x-axis.

The H1 detector is a multi-purpose detector, designed with the demands of the rich physics programme in mind. In order to study the deep inelastic scattering process, excellent electron identification and measurement is required. A high degree of hermicity is important in order to identify missing transverse momentum and investigate phenomena involving energetic neutrinos. Good energy resolution, both for hadrons and electrons, is also essential for making inclusive energy flow measurements. Heavy flavour physics demands precise momentum measurement and good muon identification, which is also important to allow searches for new particles. All these facilities must be complemented by a sophisticated trigger and data acquisition system in order to overcome the high background conditions which result from the high bunch crossing rates.

A very detailed description of the entire H1 detector can be found in [1]; here only its major components, especially those relevant to this analysis, will be discussed.

The main H1 detector has the approximate dimensions $x \times y \times z = 12 \times 15 \times 10\,\mathrm{m}^3$ with a weight of 2800 t. The first ep collisions were observed in May 1992. The main components from inside out are:
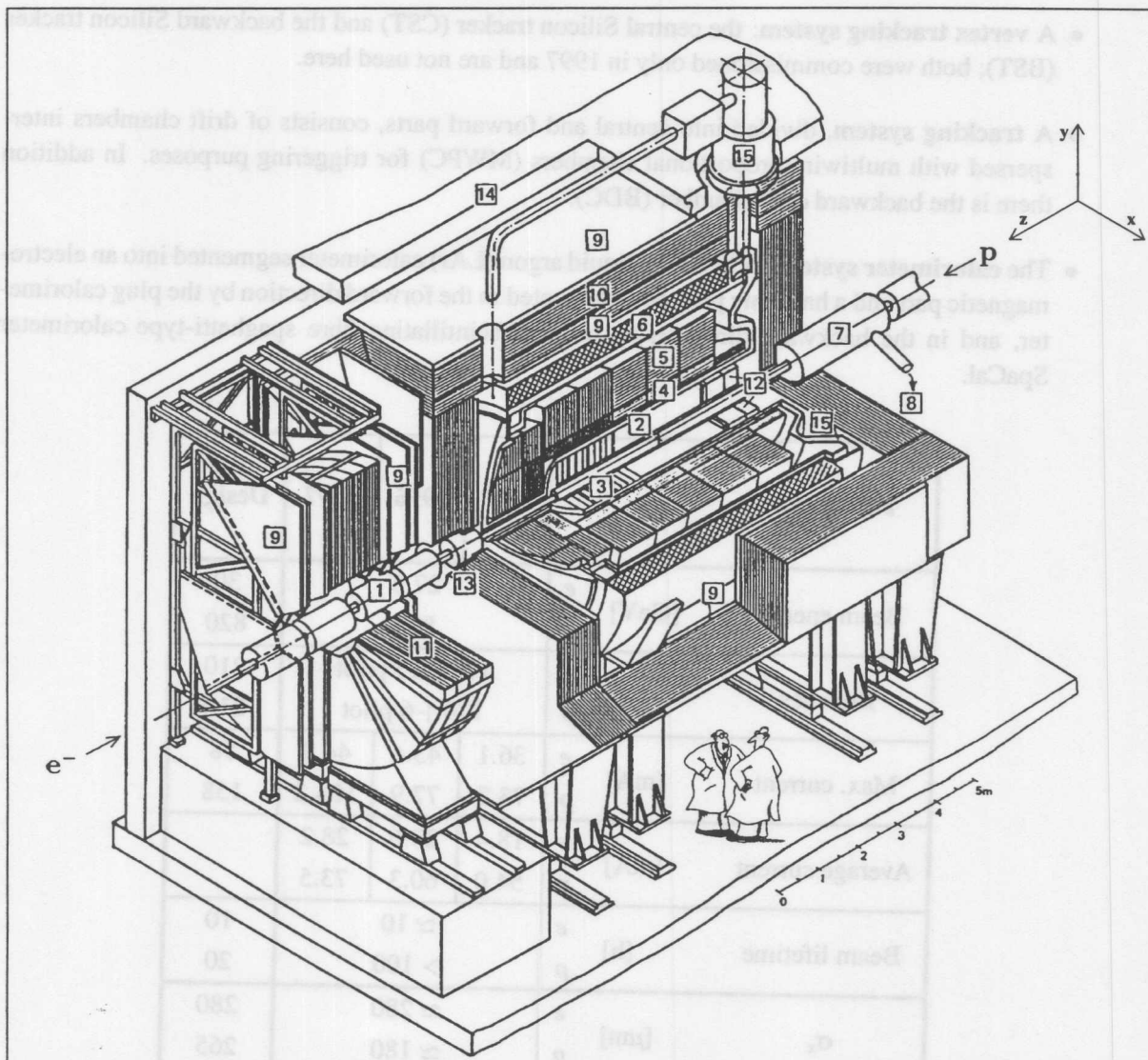
1 | Beam pipe and beam magnets
2 | Central tracking chambers
3 | Forward tracking chambers
4 | Electromagnetic calorimeter (lead/liquid argon)
5 | Hadronic calorimeter (steel/liquid argon)
6 | Superconducting coil ($B = 1.15\,\text{T}$)
7 | Compensating magnet ($B = 4.83\,\text{T}$)
8 | Helium cryogenics
9 | Muon chambers
10 | Instrumented iron (iron stabs and streamer tube detectors)
11 | Muon toroid magnet ($B = 1.6\,\text{T}$)
12 | Backward drift chamber and calorimeter
13 | Plug calorimeter
14 | Concrete shielding
15 | Liquid argon cryostat

Figure 2.4: *The H1 Detector. The H1 coordinate system is defined in the top right corner.*

- The **beam pipe**, consisting of Aluminium with an outer radius of 46.7 mm.

- A **vertex tracking system**: the central Silicon tracker (CST) and the backward Silicon tracker (BST); both were commissioned only in 1997 and are not used here.

- A **tracking system**, divided into central and forward parts, consists of drift chambers interspersed with multiwire proportional chambers (MWPC) for triggering purposes. In addition there is the backward drift chamber (BDC).

- The **calorimeter system** includes the liquid argon (LAr) calorimeter segmented into an electromagnetic part and a hadronic part, complemented in the forward direction by the plug calorimeter, and in the backward direction by the lead/scintillating fibre spaghetti-type calorimeter SpaCal.

Parameter		1995	1996	1997	Design
Beam energy [GeV]	e		27.5		30
	p		820		820
Bunches	e		174 + 15 pilot		210
	p		174 + 6 pilot		210
Max. current [mA]	e	36.1	43.4	44.9	58
	p	73.3	77.9	104.2	158
Average current [mA]	e	18.4	20.6	28.2	
	p	54.0	60.3	73.5	
Beam lifetime [h]	e		$\simeq 10$		10
	p		> 100		20
σ_x [μm]	e		$\simeq 280$		280
	p		$\simeq 180$		265
σ_y [μm]	e		$\simeq 60$		37
	p		$\simeq 60$		84
σ_z [cm]	e		$\simeq 1$		0.8
	p		$\simeq 11$		11
Average specific luminosity $[10^{29}\text{cm}^{-2}\text{s}^{-1}\text{mA}^{-2}]$		4.1	4.1	4.9	4.0
Max. luminosity $[10^{30}\text{cm}^{-2}\text{s}^{-1}]$		5.9	8.4	10.1	16
Integrated luminosity $[\text{pb}^{-1}\text{a}^{-1}]$		11	14	34	100

Table 2.1: *HERA performance figures.*

- A **superconducting coil** with a diameter of 3 m outside the LAr calorimeter provides a homogeneous magnetic field of 1.15 T, enabling momentum measurement for charged particles in the tracking system.

- The **iron return yoke** of the magnet is instrumented to allow measurement of hadronic energy not contained in the LAr calorimeter, and muon identification. In the forward direction, the forward muon detector, consisting of layers of drift chambers on either side of a toroidal magnet, provides identification and measurement of muons in the forward region.

- The **luminosity system**, outside of the main detector, consists of electron and photon detectors ("taggers") placed well downstream in the electron direction.

The remainder of this chapter contains a brief overview of each detector component used in this work.

2.3.1 Tracking system

The tracking system (figure 2.5) has been designed to provide precise measurement of the momentum, angle and energy loss of isolated charged particles, and to reconstruct jets with high track densities. Major design criteria were a momentum resolution of $\sigma_p/p^2 \approx 0.3 \% \text{GeV}^{-1}$ and an angular resolution of $\sigma_\theta \approx 1$ mrad. In order to facilitate good triggering and reconstruction over the whole solid angle, the tracking system is divided into two mechanically distinct tracking detectors: the central and forward trackers.

Central Tracking Detector

The central tracking detector (CTD, figure 2.6) consists of six chambers in total, housed in a cylindric tank built of Aluminium, and covers polar angles $15° \lesssim \theta \lesssim 165°$. From inside out, these are the
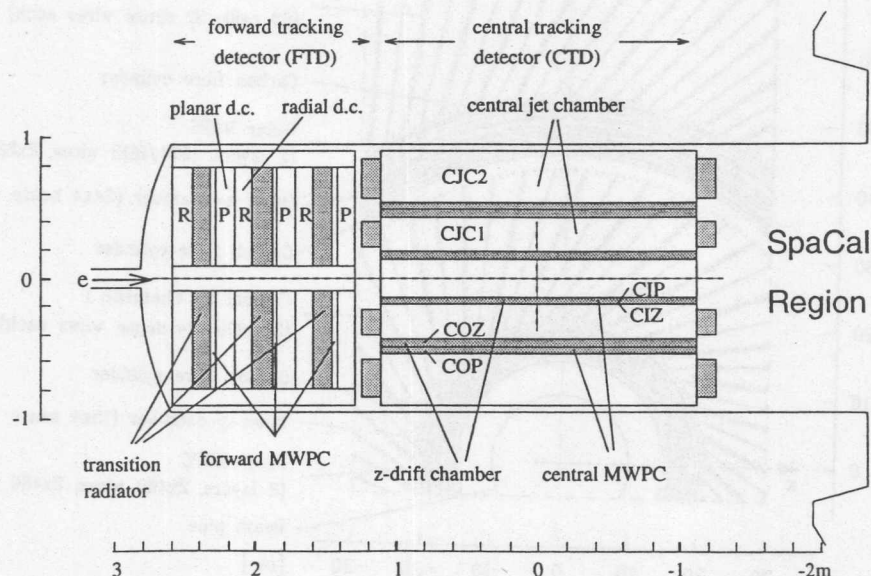
Figure 2.5: *Schematic side view of the tracking system.*

Central Inner Proportional Chamber (CIP), the Central Inner z-Chamber (CIZ), the Inner Jet Chamber (CJC 1), the Central Outer z-Chamber (COZ), the Central Outer Proportional Chamber (COP), and finally the Outer Jet Chamber (CJC 2). Four of them are used for track reconstruction (CJC 1 and 2, CIZ and COZ), while the remaining two (CIP and COP) serve triggering purposes.

Of major importance for track reconstruction are the Central Jet Chambers (CJC), the design following the one used by the JADE collaboration at PETRA. The CJCs cover the polar angular range $15° \lesssim \theta \lesssim 165°$. Their 2640 sense wires are strung parallel to the beam axis to give accurate reconstruction in the $r\phi$ plane. CJC 1 consists of 30 drift cells, each containing 24 sense wires, whilst CJC 2 consists of 60 drift cells, each with 32 sense wires. The drift cells are tilted at 30° to the radial direction such that ionization electrons drift approximately perpendicular to high momentum tracks in order to reach optimum track resolution and also to solve drift ambiguities by matching track segments from neighbouring cells. The CJC has a spatial resolution of approximately $170\,\mu m$ in the $r\phi$ plane, and a momentum resolution σ_p/p^2 of better than $0.01\,\mathrm{GeV^{-1}}$. The z-coordinate is determined from charge division with a precision of 2 to 3 cm. The energy loss of particles in the chamber gas ($\mathrm{Ar\text{--}CO_2CH_4}$-mixture) can be used for particle identification and is measured to an accuracy $\sigma_{dE/dx} \simeq 7\,\%$ for long tracks.

In order to improve the z-resolution, two thin cylindrical "z-chambers" (CIZ and COZ) sandwich the inner jet chamber CJC 1, each with four layers of sense wires strung perpendicular to the beam axis. They provide a z-measurement with a typical resolution of $300\,\mu m$, and cover the polar angular range $16° \lesssim \theta \lesssim 169°$ (CIZ) and $25° \lesssim \theta \lesssim 156°$ (COZ), respectively.
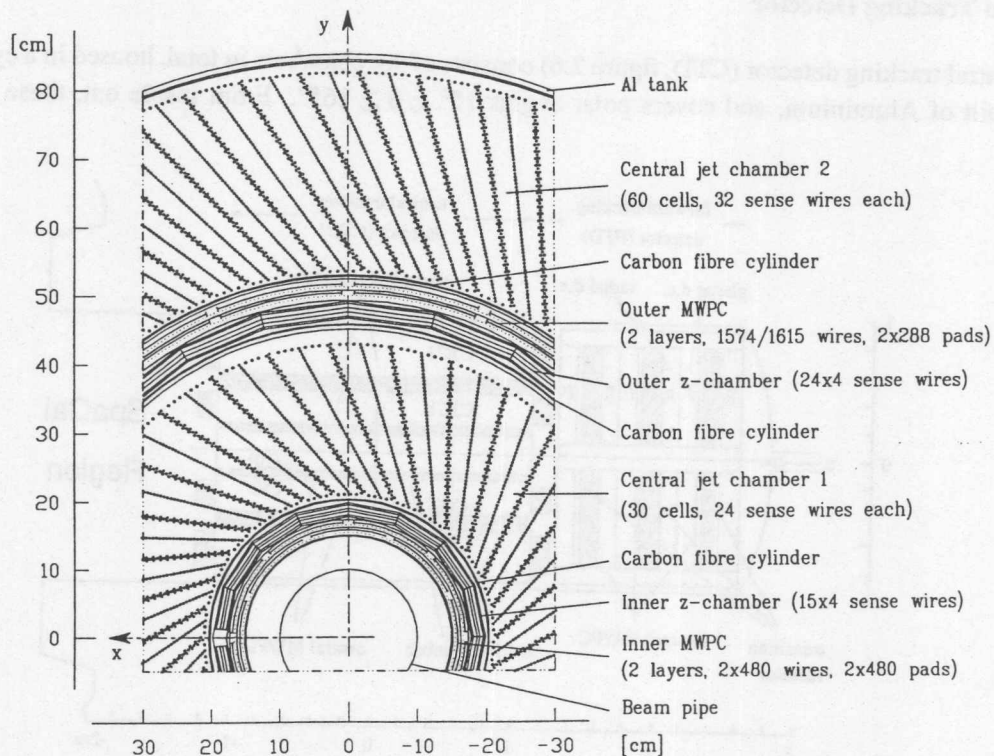
Figure 2.6: *Radial view of the central tracking chambers. The Silicon tracking detectors are indicated in a detailed view of the backward region in figure 2.8.*

The inner and outer proportional chambers CIP and COP, located inside of the CIZ and outside of CJC 2 respectively, provide fast space-point information for the level one and level two trigger systems (section 2.3.6). Each consists of two layers of chambers with wires strung parallel to the beam axis, read out via 480 (CIP) and 288 (COP) cathode pads.

Forward Tracking Detector

Charged particle tracks leaving the interaction region at small polar angles $\theta \lesssim 30°$ are only bent weakly in the axial magnetic field compared to tracks in the central region of the detector. In order to obtain a momentum measurement with sufficient accuracy, a dedicated Forward Tracking Detector (FTD) with a higher density of sense wires in the bending plane of the magnetic field has been installed (figure 2.5).

The FTD consists of three identical *supermodules* along the z-direction. Each supermodule consists of three layers of planar drift chambers, followed by multiwire proportional chambers, a transition radiator and finally a radial drift chamber. The FTD has an angular coverage of $5° \lesssim \theta \lesssim 30°$.

Each of the three layers of planar drift chambers in each supermodule consists of 32 cells with four sense wires strung in parallel, and uniformly separated in z. The layers are rotated by 60° in azimuth with respect to the previous layer in order to facilitate the resolution of drift ambiguities and improve spatial resolution, which is of the order of 150 to 170 μm in x, y. The forward proportional chambers with two planes of wires serve triggering purposes. The transition radiators are designed for the separation of electrons and pions by means of soft transition radiation that is detected in the radial drift chambers. Finally, the radial drift chambers complement the planar drift chambers giving a precise momentum measurement; their wires are strung radially, giving a resolution of 180 to 200 μm in $r\phi$.

Backward Drift Chamber

The main purpose of the Backward Drift Chamber (BDC) is to provide an accurate determination of the scattering angle of electrons in deep inelastic processes with $Q^2 \lesssim 100\,\text{GeV}^2$. It is mounted in front of the SpaCal calorimeter (figure 2.8, section 2.3.2) and has a similar angular acceptance of $151° \lesssim \theta \lesssim 177.5°$.

The BDC is constructed out of double-layer drift chambers. In total four planes are mounted along the z-direction, each consisting of chambers of octagonal shape. The sense wires are strung along this octagonal shape, which results in an approximately radial drift direction and thus optimized resolution in the polar angle. The four planes are rotated in ϕ by 11.5° with respect to one another in order to achieve a homogeneous efficiency. The resolution of the BDC for the measurement of the scattering angle θ of the DIS electron is better than 1 mrad, with a systematic shift estimated to be below 0.5 mrad [2].

2.3.2 Calorimetry

In order to measure accurately the hadronic energy flow and the position and energy of the scattered electron at high Q^2, calorimeters capable of identification and precision measurement of electrons, muons and hadrons, as well as measurement of jets with high particle densities are required. In the

case of H1 these calorimeters are placed *within* the coil which provides the magnetic field for the tracking detectors in order to minimize the amount of dead material in front of them and their overall size.

The main calorimeter of H1, which will subsequently be referred to as the LAr calorimeter, is a sampling calorimeter using liquid argon as active material with steel and lead as passive absorption material. It is complemented by three additional calorimeters: the SpaCal in the backward region ($153° \lesssim \theta \lesssim 178°$), a lead/scintillating fibre calorimeter of *spaghetti* type, and a Plug calorimeter in the very forward region ($0.7° \lesssim \theta \lesssim 3.3°$), consisting of copper absorber plates interleaved with sensitive layers of large area Silicon detectors. To measure hadronic energy leaking out of the LAr and SpaCal calorimeters, a "Tail Catcher" is integrated into the Central Muon Detector (see section 2.3.3).

Further calorimeters for specific purposes exist, e.g. the luminosity detectors (see section 2.3.4), or the Forward Neutron Calorimeter for the detection of high energy neutrons in the extreme forward direction.

The LAr Calorimeter

By far the largest range in the polar angle θ, $4° \lesssim \theta \lesssim 154°$, is covered by the non compensating LAr calorimeter (figure 2.7). It is segmented along the beam axis into eight self supporting "wheels", each of these wheels being segmented in ϕ into eight identical stacks. The electromagnetic part uses lead plates of 2.4 mm thickness as absorbing material with gaps of 2.35 mm filled with liquid argon as the active material. Except for the very backward part (BBE), the electromagnetic section is surrounded by a hadronic calorimeter, consisting of 19 mm stainless steel absorber plates, with double gaps of two times 2.4 mm of liquid argon. In total 65000 electronic channels are read out.

The LAr calorimeter covers the regime $Q^2 \gtrsim 100 \, \text{GeV}^2$ for the detection of the scattered electron in DIS processes.

The depth of the LAr calorimeter varies with the polar angle between 20 and 30 radiation lengths, X_0, for the electromagnetic section, whilst the total depth is 4.5 to 8 nuclear interaction lengths, λ; the larger values are for the forward direction, where in addition the granularity is highest.

Before starting the operation of the LAr calorimeter within H1 several testbeam measurements were performed [3]–[6], yielding the following results. The energy resolution of the LAr calorimeter for electrons is $\sigma_E/E \simeq 12\,\%/\sqrt{E[\text{GeV}]} \oplus 1\,\%$, and for pions $\sigma_E/E \simeq 50\,\%/\sqrt{E[\text{GeV}]} \oplus 2\,\%$. The linearity was proven to be better than 1 % up to 166 GeV. Since the LAr calorimeter is a non compensating calorimeter — the energy response of hadrons is typically 30 % less than that for electrons —, it is calibrated at two different energy scales. Using deep inelastic *ep* data, the absolute hadronic energy scale is currently known to a precision of 3 % to 4 %, while the precision of the electromagnetic energy scale was verified to be 3 % [7].

The Backward Calorimeter SpaCal

In order to allow access to the tracking system, the LAr calorimeter does not extend to large polar angles $\theta \gtrsim 155°$. Instead a dedicated lead/scintillating fibre calorimeter of spaghetti type, the SpaCal [7, 8, 9] has been installed. It extends the polar angular acceptance up to almost $\theta = 178°$, and covers the kinematic range $1 \lesssim Q^2 \lesssim 100 \, \text{GeV}^2$ for the detection of the DIS electron. The geometric position

of the SpaCal within the H1 environment can be seen in figure 2.8. It consists of an electromagnetic and a hadronic section of 25 cm active depth each. Specific features of the SpaCal are small cell sizes of $4 \times 4 \, cm^2$ in the electromagnetic section, with high spatial resolution, and extremely low noise at the level of 3 MeV. Furthermore its time resolution is better than 1 ns, allowing for efficient background rejection.

The electromagnetic part of the SpaCal comprises in total 1192 cells, of which 18 are shaped differently from the rest and housed in the so-called insert to access the region closest to the beam pipe (figure 2.9). The hadronic section consists of 136 cells ($12 \times 12 \, cm$ each). The electromagnetic energy resolution achieved is $\sigma_E/E = 7.5\% / \sqrt{E[\text{GeV}]} \oplus 1\%$, with an energy scale uncertainty of 0.7 % at 27.5 GeV determined from deep inelastic ep scattering events. For hadrons, the energy resolution is $\sigma_E/E \simeq 30\% / \sqrt{E[\text{GeV}]}$.

2.3.3 Muon System

The muon system is divided into the Central Muon Detector (in the following just called "Muon Detector") which consists of the iron return yoke instrumented with limited streamer tubes, and the Forward Muon Detector (FMD). In this thesis, the FMD is not used for muon detection but for the separation of J/ψ production mechanisms, namely elastic and proton dissociative J/ψ production.

It should be noted that both muon systems can only determine the direction and momentum of a muon within the limits of multiple scattering which the muon suffers, and therefore the primary purpose of the muon detectors is to *identify* tracks left by muons in the tracking detectors.

Central Muon Detector

Muons with an energy greater than about 1.2 GeV can be detected in the Muon Detector ("instrumented iron") and their direction and approximate momentum can be determined. It consists of ten iron layers, each 7.5 cm thick, interleaved with ten layers of limited streamer tubes (figure 2.10). Both at the inside and outside of the iron, three streamer tube layers are attached in addition. The gas filled streamer tubes have a square cross-section of 1 cm $\times$ 1 cm and a single sense wire in the middle running along the length of the tube. Five layers are equipped with strip electrodes running perpendicular to the wires. In total 103700 wires and 28700 strips are read out digitally. The single layer efficiency reaches around 80 %.

The instrumented iron covers a polar angular region of about $4° \lesssim \theta \lesssim 175°$ and is divided into four subdetectors (forward endcap, forward and backward barrel and backward endcap). Forward and backward endcap correspond to polar angular regions of $\theta \lesssim 34°$ and $\theta \gtrsim 127°$, respectively. In the endcaps the tubes are oriented such that the wires run in the x-direction, whereas in the barrel they are strung parallel to the z-axis. The resolution of the position measurement is determined by the chamber geometry and reaches about 3 to 4 mm perpendicular to the wires and 10 to 15 mm in the other coordinate using the strips. Using pad electrodes, which are glued on the tubes in eleven layers, a space-point can be determined with an accuracy of about 10 cm. The hit information from the wires and strips is combined to reconstruct tracks, while the pad information is used to resolve track ambiguities. Because of limited geometrical acceptance, e.g. due to support structures and cryogenic supplies, the muon reconstruction efficiency is limited to about 90 %.

The instrumented iron in addition serves as a "Tail Catcher" calorimeter to detect and measure hadronic energy leaking from the LAr and SpaCal calorimeters. For this purpose the pads are
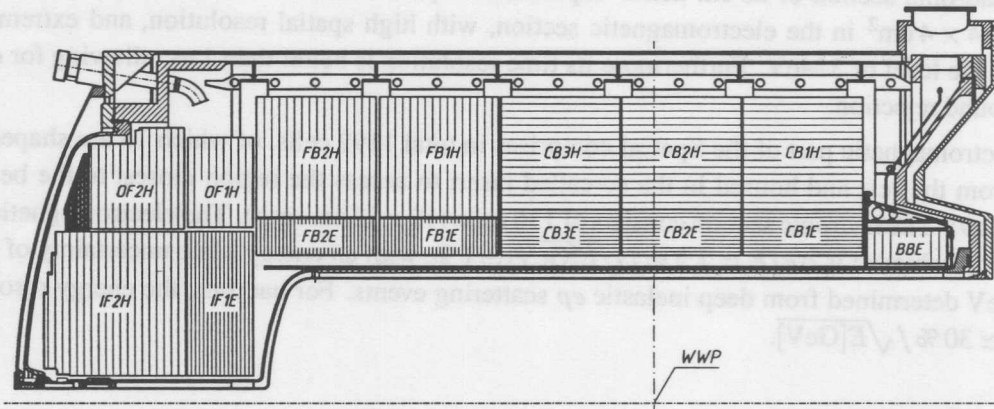
Figure 2.7: *Side view of the LAr calorimeter. "WWP" is the nominal interaction point.*
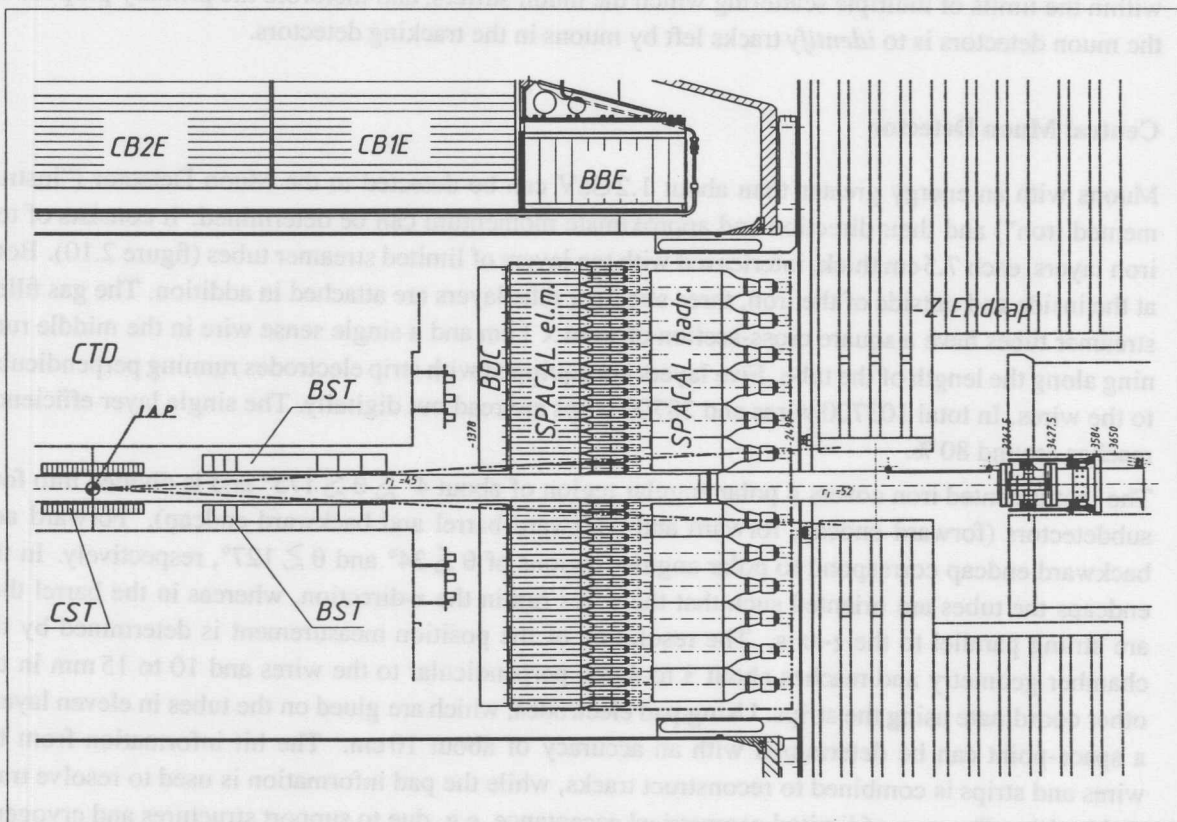
Figure 2.8: *Schematic view of the SpaCal calorimeter and the Backward Drift Chamber BDC. IAP denotes the nominal interaction point.*

16.2 cm

Tantalum Shielding

Veto Layer

5.7 cm

6.5 cm

4.05 cm
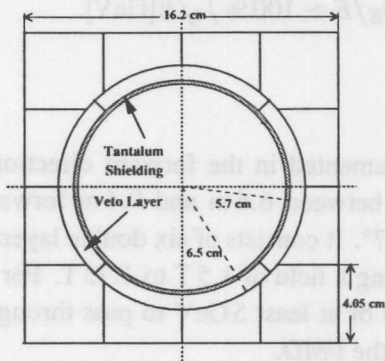
Figure 2.9: *Radial view of the cell geometry of the insert module in the centre of the electromagnetic SpaCal.*

Layers with strips

Layers with pads

Layers with strips

50 mm

25 mm

75 mm

Layers with pads

Layers with strips

Figure 2.10: *Cross section of the Central Muon Detector.*

equipped with analogue readout, and the iron is used as passive absorption material. The energy resolution of the Tail Catcher is $\sigma_E/E \simeq 100\,\% / \sqrt{E[\text{GeV}]}$.

Forward Muon Detector

The H1 Muon System is complemented in the forward direction by the Forward Muon Detector (FMD), a spectrometer situated between 6.4 m and 9.4 m forward of the nominal H1 vertex and covering polar angles $3° \lesssim \theta \lesssim 17°$. It consists of six double layers of drift chambers, three on either side of a toroidal magnet providing a field of 1.5 T to 1.75 T. For a muon to be reconstructed in the FMD, it must have a momentum of at least 5 GeV to pass through the calorimeters, the iron return yoke and the solid iron toroid of the FMD.

Besides providing identification and momentum measurement for high energy muons, the FMD is used for tagging the dissociated proton in diffractive interactions; the diffracted proton scatters either in the beam wall or in collimators, and the scattering products are detected as hits in the pre-toroid layers of the FMD. In the analyses discussed here only this tagging ability is used, not the reconstruction of muons.

2.3.4   Luminosity System

The H1 luminosity system [10] has four tasks:

- Online during data taking, it has to provide a fast relative luminosity measurement and electron beam monitoring for the HERA machine, as well as an absolute luminosity measurement with an accuracy of $\simeq 5\,\%$, without introducing dead time for the experiment.

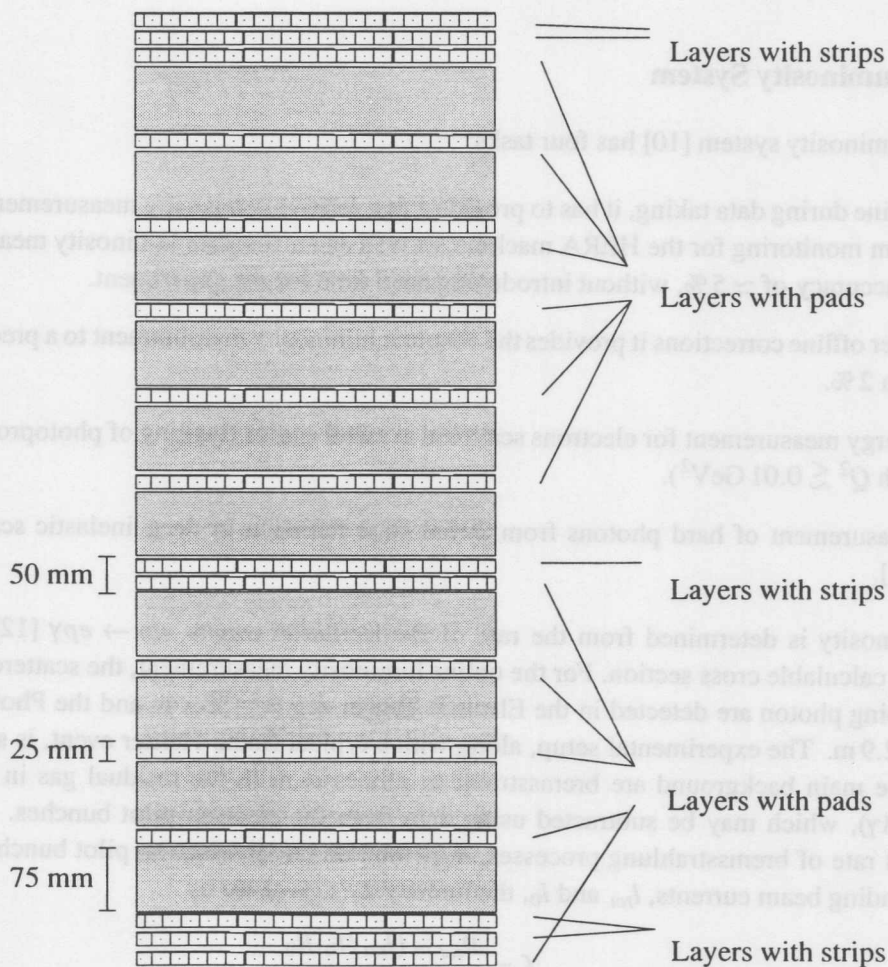- After offline corrections it provides the absolute luminosity measurement to a precision of better than $2\,\%$.

- Energy measurement for electrons scattered at small angles (tagging of photoproduction events with $Q^2 \lesssim 0.01\,\text{GeV}^2$).

- Measurement of hard photons from initial state radiation in deep inelastic scattering events [11].

The luminosity is determined from the rate of Bethe-Heitler events, $ep \rightarrow ep\gamma$ [12], which has a large and calculable cross section. For the online luminosity measurement, the scattered electron and the outgoing photon are detected in the Electron Tagger at $z = -33.4\,\text{m}$ and the Photon Detector at $z = -102.9\,\text{m}$. The experimental setup, along with a typical Bethe-Heitler event, is shown in figure 2.11. The main background are bremsstrahlung processes with the residual gas in the beam pipe ($eA \rightarrow eA\gamma$), which may be subtracted using data from the electron pilot bunches. With the total measured rate of bremsstrahlung processes, R_{tot}, the rate due to electron pilot bunches, R_0, and the corresponding beam currents, I_{tot} and I_0, the luminosity $\mathcal{L}$ is given by

$$\mathcal{L} = \frac{R_{tot} - (I_{tot}/I_0)R_0}{\sigma_{vis}}, \tag{2.10}$$

where σ_{vis} is the visible part of the $ep \rightarrow ep\gamma$ cross section including acceptance and trigger efficiencies.

For the offline determination of the final total integrated luminosity, only the detected photon is used in order to keep the systematic error to a minimum.

The Electron Tagger and Photon Detector consist of crystal Cherenkov counters segmented in 7×7 and 5×5 cells respectively of about $2\,\text{cm} \times 2\,\text{cm}$ size. The Photon Detector is protected against synchrotron radiation by a lead absorber ($2.2 X_0$) followed by a water Cherenkov veto counter ($0.8 X_0$).

The acceptance of the Electron Tagger for photoproduction events is limited to $0.2 \lesssim y \lesssim 0.8$. Additional smaller devices similar to the Electron Tagger have been installed to access the high and low y regime.

2.3.5   Further Detector Components

Quite a few further components have been installed for specific purposes; those that are of relevance for this work are:

Time-of-Flight Detectors In addition to the SpaCal, which due to its excellent time resolution of better than 1 ns can serve as a Time-of-Flight device, several components have been installed [13] to efficiently reduce background already on the first level of the trigger (see next section). Firstly, the FToF ("Forward" ToF) is located in the Forward Muon Detector at $z = 7.0\,\text{m}$ and
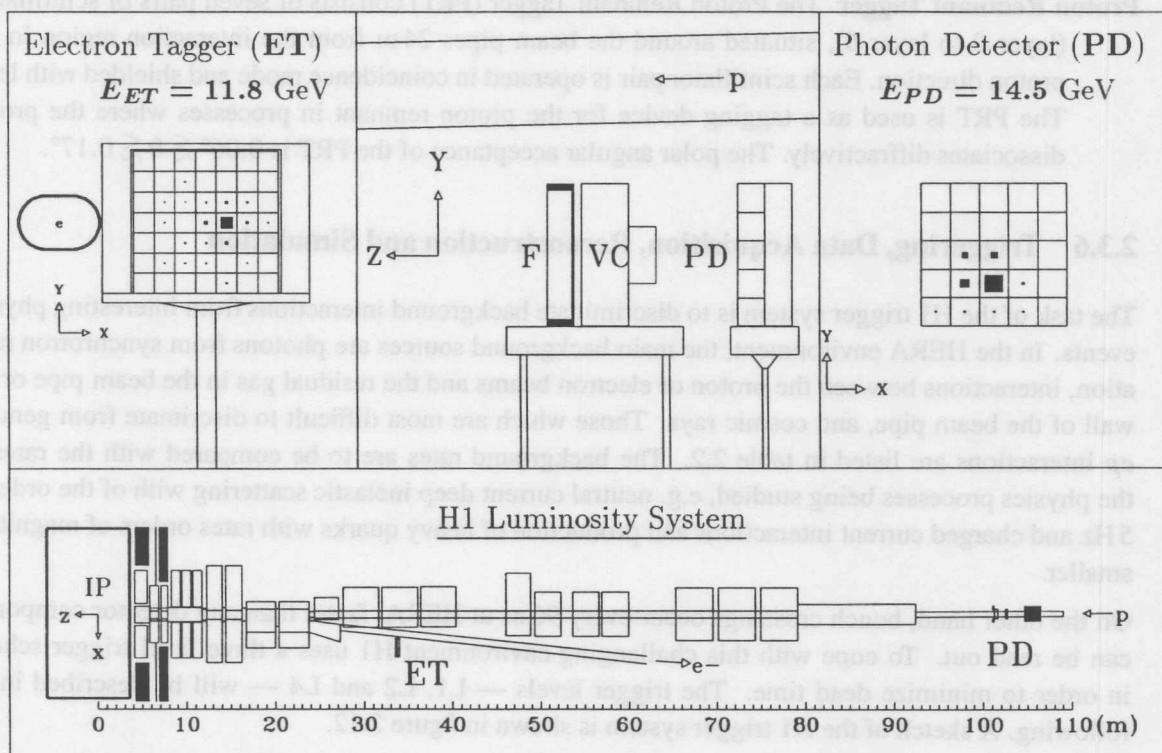
Figure 2.11: *Bethe-Heitler bremsstrahlung event measured by the luminosity system. The electron deposits $E_e = 11.8\,\text{GeV}$ in the Electron Tagger ET (upper left), while the photon energy of $14.5\,\text{GeV}$ is measured in the photon detector PD (top right). In the lower part, a side view of the complete luminosity system is drawn, the upper central picture shows details of the photon detection system. F is the lead absorber, VC the water Cherenkov veto counter.*

Background	Expected rate in interaction region
Proton-gas interactions	1 kHz
Proton-beam pipe interactions	50 kHz
Cosmic ray muons	2 kHz

Table 2.2: *Major sources of background in the H1 detector for HERA design currents [14, 15, 16].*

consists of two layers of scintillator with dimensions 200 mm × 600 mm × 10 mm. The PToF ("Plug" ToF) at $z = 5.3$ m has eight 150 mm × 150 mm scintillators mounted inside the absorber structure of the Plug calorimeter. The four semi-circular BToF ("Backward" ToF) scintillators are placed at $z = -3.2$ m near the compensator magnet, with inner and outer radii of 67 mm and 250 mm respectively. BToF and PToF have a time resolution of 0.7 ns and $1 - 1.5$ ns. Finally, two large veto walls are installed at $z = -6.5$ m and $z = -8.1$ m. The smaller inner veto wall with size 100 cm × 90 cm covers the area close to the beam, while the outer one (5 m × 4 m) overlaps the inner veto wall and nearly all of the LAr calorimeter. The time resolution is 3 ns for the inner and 8 ns for the outer veto wall.

Proton Remnant Tagger The Proton Remnant Tagger (PRT) consists of seven pairs of scintillators (layer 0 to layer 6), situated around the beam pipes 24 m from the interaction region in the proton direction. Each scintillator pair is operated in coincidence mode and shielded with lead. The PRT is used as a tagging device for the proton remnant in processes where the proton dissociates diffractively. The polar angular acceptance of the PRT is $0.06° \lesssim \theta \lesssim 0.17°$.

2.3.6   Triggering, Data Acquisition, Reconstruction and Simulation

The task of the H1 trigger system is to discriminate background interactions from interesting physics events. In the HERA environment, the main background sources are photons from synchrotron radiation, interactions between the proton or electron beams and the residual gas in the beam pipe or the wall of the beam pipe, and cosmic rays. Those which are most difficult to discrimate from genuine ep interactions are listed in table 2.2. The background rates are to be compared with the rates of the physics processes being studied, e.g. neutral current deep inelastic scattering with of the order of 5 Hz and charged current interactions and production of heavy quarks with rates orders of magnitude smaller.

On the other hand, bunch crossings occur every 96 ns at HERA, faster than any detector component can be read out. To cope with this challenging environment H1 uses a three level trigger scheme in order to minimize dead time. The trigger levels — L1, L2 and L4 — will be described in the following. A sketch of the H1 trigger system is shown in figure 2.12.

L1 Because of the high input rates, cable delays of the order of a few hundred ns and the maximum drift time in the tracking detectors of the order of 1 μs, the L1 trigger is pipelined; the output from all subsystems is stored in memory for 24 bunch crossings (2.3 μs). When an event is triggered by one of the 128 "subtriggers", an "L1 keep" signal is sent to all the different subsystems, and the pipeline is frozen. The resulting dead time, i.e. the time between the L1 keep
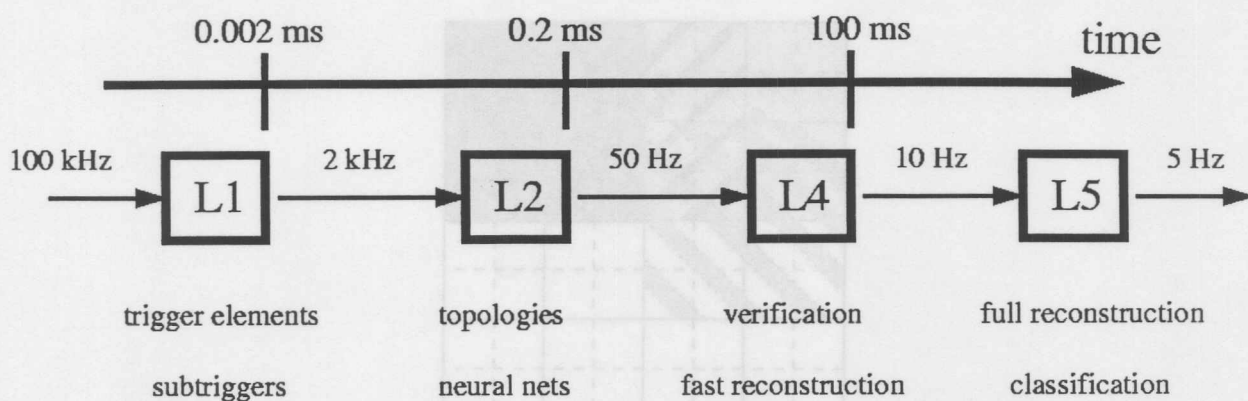
Figure 2.12: *Trigger levels used during 1995 to 1997 data taking.*

signal and the completion of the read out, lasts typically 1 to 2 ms per event.

The subtriggers of L1 are logical compositions of 192 trigger elements that are delivered by the different subdetector trigger systems; the relevant trigger elements for the present analysis will be described later.

The L1 trigger reduces the rate by roughly a factor 100: from the rate of non-empty H1 events (100 kHz) to about 1 kHz.

L2 On L2, neural networks and topological correlations are used to reduce the input rate of 1 kHz by another factor of 20 to about 50 Hz. L2 uses a fixed dead time of 30 μs, therefore an L2 input rate of 1 kHz induces an additional 3 % dead time for the experiment. Each of the maximum number of 32 L2 trigger elements (16 neural nets and 16 topological conditions) is logically connected to one or more L1 subtriggers, therefore L2 is in practice used to reduce the rate of specific L1 subtriggers with high rates.

Upon an "L2 keep" signal the front-end data readout is started.

L4 The L4 trigger is a multi processor farm consisting of around 30 Power PC boards that reduces the input rate of up to 50 Hz to 10 Hz. With the complete detector information available, a preliminary event reconstruction is performed, and the decision of the lower trigger levels is verified. Background filters against cosmic ray muons and proton beam induced background are applied. Finally, since 1997 a physics selection is performed which rejects a fraction of physics processes with high rates, e.g. inclusive photoproduction events.

Events which have passed L4 are written to tape and fully reconstructed off-line by the H1 reconstruction software on a dedicated computing farm (L5).

Level 1 Trigger Elements

In this section all trigger elements which are used in the present analysis will be briefly presented. The discussion is in no way complete, therefore references for a more thorough description will be given.
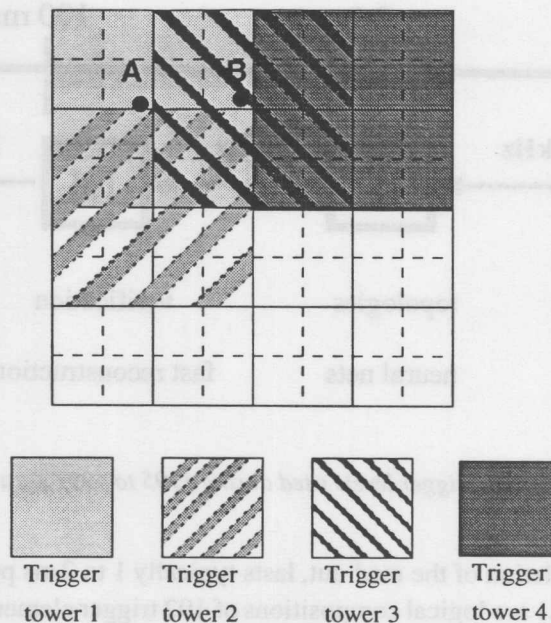
Trigger   Trigger   Trigger   Trigger
tower 1   tower 2   tower 3   tower 4

Figure 2.13: *Illustration of the "sliding window" technique used in the inclusive electron trigger. For an impact point of the electron at "A", all deposited energy is contained in trigger tower 1. Electrons at "B" deposit half of their energy in trigger towers 1 and 4 respectively, but the full energy is recovered in trigger tower 3 [18].*

SpaCal Trigger The SpaCal trigger [17] is divided into two separate branches, the ToF and AToF ("Anti"-ToF) branch, corresponding to signals in-time and out-of-time with respect to the nominal beam timing. The trigger produces analog energy sums that are compared to adjustable thresholds separately for the electromagnetic and the hadronic SpaCal. While in the AToF branch only coarse energy sums are formed, the ToF branch is highly segmented to provide the "inclusive electron trigger" IET. The ToF branch is defined by a time window of typically $\simeq 20\,\mathrm{ns}$, and is relatively insensitive to proton beam related background.

For the inclusive electron trigger, the analog sum of the in-time energy (ToF branch) of only 16 cells (one trigger tower) is summed in overlapping "sliding windows" that allow to localize the position of the scattered electron already at the first trigger level (figure 2.13). Three different energy thresholds are available (`Spcle_IET>0`, `Spcle_IET>1` and `Spcle_IET>2`), adjustable between $\simeq 100\,\mathrm{MeV}$ and $\simeq 20\,\mathrm{GeV}$. Typical IET thresholds are 0.5, 2 and 6 GeV. Furthermore a coarse discrimination in the radial distance R from the beam pipe is possible, the corresponding trigger elements will be identified by an additonal "(inner)" ($R \lesssim 16\,\mathrm{cm}$) and "(outer)" ($R \gtrsim 16\,\mathrm{cm}$) appended to the trigger element name.

Further trigger elements are formed from the total energy sums in the electromagnetic and hadronic SpaCal both in the ToF and AToF branch. Used here are:

`Spcle_ToF_E2` Total in-time energy deposit in the electromagnetic SpaCal above $\simeq 12\,\mathrm{GeV}$.

`Spclh_AToF_Cl1` Total out-of-time energy deposit in one of the hadronic SpaCal "Big Towers" above $\simeq 0.6\,\mathrm{GeV}$. The AToF Big Towers correspond to the inner and outer region of the SpaCal.
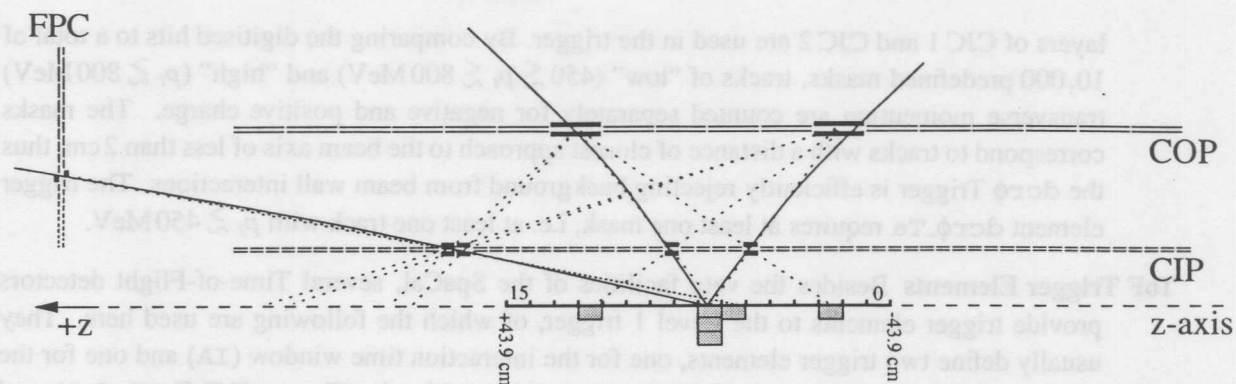
Figure 2.14: *Principle of operation of the z Vertex Trigger [19]. The building of the z vertex histogram in the rz view for one ϕ sector is shown. Rays originating from genuine particles are indicated by full lines, while the dotted lines include the "wrong" combinations.*

Spclh_AToF_E1 Total out-of-time energy deposit in the hadronic SpaCal above $\simeq 0.6\,\text{GeV}$. The AToF trigger elements are used to veto out-of-time background.

z **Vertex Trigger** The aim of the *z* Vertex Trigger [14, 19] is to provide a rough determination of the *z* position of the event vertex already on the first trigger level. For this purpose, the pad signals of the multiwire proportional chambers CIP, COP and the first forward proportional chamber FPC are combined into *rays*; a ray is defined as the coincidence of four pads that can be connected by a straight line in the *rz* plane. For inefficient pads, the coincidence condition is relaxed to three out of four. The number of these rays in a given bunch crossing and ϕ sector is entered into a 16 bin wide histogram, where each bin is related to the origin of its respective rays along the *z*-axis; the resulting 16 histograms, one for each ϕ sector, are combined to give the *z vertex histogram*; it covers an area $-44\,\text{cm} \lesssim z \lesssim 44\,\text{cm}$ in *z*, where the bin with the most entries is expected to contain the interaction vertex of the *ep* collision. The principle of operation of the *z* Vertex Trigger is illustrated in figure 2.14.

A large variety of significance and multiplicity conditions exists. The most important one is the zvtx_t0 trigger element which demands the existence of at least one ray. The single track efficiency of the *z* Vertex Trigger as a function of the transverse momentum p_t is about 50 % at 450 MeV and reaches 80 % for tracks with $p_t \gtrsim 1\,\text{GeV}$. The trigger element zvtx_mul<7 is applied in order to veto very large background events; it requires less than 200 entries in the *z* vertex histogram.

One step further, the rays are grouped into so-called *Big Rays* with a coarser granularity identical to the granularity of the LAr calorimeter trigger. A special branch of the *z* Vertex Trigger looks for a back-to-back topology in the $R\phi$ projection of these big rays; the corresponding trigger element Topo_BR allows to efficiently trigger on the decay leptons from exclusively produced J/ψ mesons.

Rays are also formed from the signals in the forward proportional chambers and CIP; if at least one ray pointing to the nominal interaction region is found, the trigger element fwd_ray_t0 is set. Finally, the logical "OR" of zvtx_t0 and fwd_ray_t0 is called ray_t0.

Central Drift Chamber Trigger Complementary to the *z* Vertex Trigger, the Drift Chamber Trigger (dcrϕ Trigger) is able to find charged tracks in the $R\phi$ projection. 10 out of the 56 wire

layers of CJC 1 and CJC 2 are used in the trigger. By comparing the digitised hits to a total of 10,000 predefined masks, tracks of "low" ($450 \lesssim p_t \lesssim 800\,\text{MeV}$) and "high" ($p_t \gtrsim 800\,\text{MeV}$) transverse momentum are counted separately for negative and positive charge. The masks correspond to tracks with a distance of closest approach to the beam axis of less than 2 cm, thus the dcrϕ Trigger is efficiently rejecting background from beam wall interactions. The trigger element dcrϕ_Ta requires at least one mask, i.e. at least one track with $p_t \gtrsim 450\,\text{MeV}$.

ToF Trigger Elements Besides the veto facilities of the SpaCal, several Time-of-Flight detectors provide trigger elements to the Level 1 trigger, of which the following are used here. They usually define two trigger elements, one for the interaction time window (IA) and one for the background (BG). FToF_IA and FToF_BG are delivered by the "Forward" ToF, PToF_IA and PToF_BG by the "Plug" ToF, and BToF_BG by the "Backward" ToF; finally, VETO_inner_BG and VETO_Outer_BG are the trigger elements of the inner and outer veto wall, respectively.

Outline of the Event Reconstruction Software

The main steps in the event reconstruction (so-called L5) are:

- Track reconstruction in the tracking devices. In the case of central tracks, the reconstruction starts from hit triples, which are clustered together to track elements in CJC 1 and CJC 2. Track elements from CJC 1 and CJC 2 are merged, and a link to CIZ and COZ tracks is performed. Finally, the tracks are constrained to primary or secondary vertices whenever possible. These vertex fitted tracks are the starting point of the track information used in most physics analyses.

- Reconstruction of cell energies and cluster finding in the calorimeters. Electronic noise is subtracted, a charge-to-energy calibration performed, and cells are grouped into clusters. Cell energies are finally available on three "scales": "0 scale", which corresponds to the energy deposited by electrons or photons in a homogeneous structure; "1 scale", which includes additionally the correction for dead material in front of the calorimeter; "final scale", containing the energy deposited by hadrons, taking into account the non compensating nature of the calorimeter, after application of topological noise cuts.

- Track finding in the muon system and linking of these with inner tracks.

The output of the reconstruction is stored in a proprietary format that can be accessed via special I/O routines [20, 21]. The final data sets either contain the full detector information — Production Output Tapes (POT), usually stored on tape — or a reduced set of information that is sufficient for physics analysis — DSTs (Data Summary Tapes), stored on disk. Only events that fulfill the criteria of at least one physics selection are kept in reconstructed form (event classification). A typical H1 event has a size of 100 kByte on raw data tapes and 10 kByte on DST. In 1997, H1 logged a total of 90 million events corresponding to more than 6 TByte of raw data tapes; the resulting DSTs with about 50 million events occupy 500 GByte of disk space.

Simulation

For the correction of measured quantities in the detector, Monte Carlo simulations are used. The Monte Carlo generator delivers four-vectors of all particles with lifetimes longer than typically 8 ns.

The first (and most time consuming) step of the simulation is the tracking of particles through the detector. This is done using a GEANT [22] based application, and includes the tracking in the magnetic field, secondary particle generation and shower development. The output of the GEANT module are so-called "hit banks", which contain the xyz-coordinates of entry and exit points of the particle trajectories for the sensitive detector parts in the tracking part and deposited energy for calorimeter type detectors. In the next step, the response of the sensitive detector parts, e.g. sense wires, is simulated and an output very similar to that for "real" events is produced. Finally, the trigger response is simulated.

To take into account noise in the LAr calorimeter, SpaCal calorimeter and the Central Proportional Chambers, randomly triggered events from special runs are used.

The events produced in this way are fed through the same reconstruction software as the data.

Chapter 3

Phenomenology of Charmonium Production

In this chapter, an overview of Charmonium phenomenology will be given, focussing on the production of the S-wave states J/ψ (1^3S_1) and its radial excitation $\psi(2S)$ $(2^3S_1)^1$ at HERA. In the first section, kinematical variables and cross sections are introduced; this includes a discussion of kinematical properties of the decay leptons in the decays $J/\psi \to \mu^+\mu^-$ and $J/\psi \to e^+e^-$, since these decay channels will be used in the analyses presented in forthcoming chapters. Models for the diffractive production of J/ψ and $\psi(2S)$ mesons in deep inelastic scattering will be presented next. A description of the most important models for inelastic Charmonium production follows, namely the Colour Evaporation Model, the Colour Singlet Model and the non-relativistic QCD factorization approach, often and somewhat misleading called the Colour Octet Model.

Since no unique nomenclature for different production mechanisms is being used for J/ψ production at HERA, a somewhat pragmatic way is chosen with respect to terminology. In this analysis, *exclusive* and *inclusive* J/ψ production will be distinguished. Exclusive production denotes event topologies where the reconstructed hadronic final state consists exclusively of the J/ψ, while the term inclusive comprises all possible production mechanisms. Phrased differently, the exclusive part can be thought of as comprising diffractive J/ψ production, i.e. elastic and proton diffractive dissociation, while the inclusive cross section has additional *inelastic* contributions.

The important scale in Charmonium physics is set by the mass m_c of the charm quark. Its value $m_c \simeq 1.5\,\text{GeV}$ is considerably larger than the QCD scale Λ_{QCD}, thus permitting perturbative expansions in $\alpha_s(m_c)$. Another important fact is that the Charmonium states are well described by potential models, because the resulting wave functions are needed for calculations of Charmonium production and decay. A significant amount of theoretical work has been carried out in the last twenty years to understand Charmonium in the framework of QCD.

---

[1]The notation $n^{2S+1}L_J$ is used here, where n is the radial quantum number, and S, L and J denote spin, orbital and total angular momentum.

3.1 Kinematics of Charmonium Production in Deep Inelastic Scattering

The basic variables used to describe deep inelastic lepton nucleon scattering, $\sqrt{s}$, x, y, W and Q^2, have already been introduced in the last chapter. Here deep inelastic cross sections will be defined and additional variables relevant for the production of Charmonium introduced.

3.1.1 Cross Sections for Deep Inelastic Scattering

For purely electromagnetic interactions, the double differential cross section for $ep \to eX$ can be written in terms of two structure functions F_1 and F_2:

$$\frac{d^2\sigma_{ep}(x,Q^2)}{dx\,dQ^2} = \frac{4\pi\alpha^2}{xQ^4}\left(y^2 x F_1(x,Q^2) + (1-y)F_2(x,Q^2)\right), \tag{3.1}$$

where α is the electromagnetic coupling. Equation 3.1 defines the so-called *Born* cross section. In the quark parton model, F_1 and F_2 are only functions of x (Bjorken scaling [23]) and can be written as a sum of spin $= 1/2$ parton densities q_i for partons with charge e_i:

$$F_1(x) = \frac{1}{2}\sum_i e_i^2(q_i(x) + \overline{q_i}(x)); \tag{3.2}$$

$$F_2(x) = \sum_i e_i^2 x(q_i(x) + \overline{q_i}(x)). \tag{3.3}$$

In Quantum Chromodynamics, these equations are generalized, using a factorization theorem, into short and long distance phenomena and including gluon densities. The inclusion of gluons leads to a violation of the scale invariance — the structure functions depend logarithmically on Q^2 — and to the violation of the Callan-Gross-Relation $F_2 = 2xF_1$ [24] which is a direct consequence of equations 3.2–3.3.

For single photon exchange, the process $ep \to eX$ can be viewed as the scattering of a virtual photon off a proton $\gamma^* p \to X$; the electron emits a flux of virtual photons. The total cross section $\sigma_{\gamma^* p}$ is via the optical theorem related to the imaginary part of the forward scattering amplitude. Introducing a flux factor K for virtual photons, $\sigma_{\gamma^* p}$ can be written as

$$\sigma_{\gamma^* p}(\lambda) = \frac{4\pi^2\alpha}{K} \cdot \varepsilon_\lambda^{*\mu} H_{\mu\nu} \varepsilon_\lambda^\nu. \tag{3.4}$$

Here ε_λ is the polarization vector for virtual photons in helicity states $\lambda = 0, \pm 1$, for the longitudinal and transverse polarization of massive photons ($Q^2 > 0$) respectively, and $H_{\mu\nu}$ denotes the hadronic tensor.

In the case of real photons K is simply the photon energy ν; for virtual photons the definition of K is arbitrary: following the convention of Hand [25], K is taken to be equal to the energy of the equivalent real photon that could produce the final state involved[2]:

$$K = \frac{W^2 - m_p^2}{2m_p} \xrightarrow{Q^2 \to 0} \nu. \tag{3.5}$$

---

[2]Another popular definition is that of Gilman [26]: $K = \sqrt{\nu^2 + Q^2}$.

The cross sections for transverse and longitudinally polarized photons can be written as

$$\sigma_{\gamma^* p}^T = \frac{1}{2}\left(\sigma_{\gamma^* p}^{\lambda=1} + \sigma_{\gamma^* p}^{\lambda=-1}\right) = \frac{4\pi^2\alpha}{Q^2} \cdot 2xF_1;$$ (3.6)

$$\sigma_{\gamma^* p}^L = \sigma_{\gamma^* p}^{\lambda=0} = \frac{4\pi^2\alpha}{Q^2} \cdot (F_2 - 2xF_1);$$ (3.7)

$$\sigma_{\gamma^* p} = \sigma_{\gamma^* p}^T + \sigma_{\gamma^* p}^L = \frac{4\pi^2\alpha}{Q^2} \cdot F_2.$$ (3.8)

The longitudinal structure function $F_L = F_2 - 2xF_1$ is thus directly related to the cross section for longitudinally polarized photons, $\sigma_{\gamma^* p}^L$, while the total cross section is connected to F_2. Finally, the quantity R is defined as the ratio of the cross sections for longitudinal and transverse polarized photons:

$$R = \frac{\sigma_{\gamma^* p}^L}{\sigma_{\gamma^* p}^T} = \frac{F_L}{F_2 - F_L}.$$ (3.9)

Defining the flux of transverse polarized photons $\Gamma_T \sim K$ as

$$\Gamma_T := \frac{\alpha}{2\pi y Q^2} \cdot \left(1 + (1-y)^2 - 2m_e^2 \frac{y^2}{Q^2}\right),$$ (3.10)

the polarization parameter ε:

$$\varepsilon := \frac{\Gamma_L}{\Gamma_T} = \frac{1-y}{1-y+y^2/2},$$ (3.11)

and the flux of longitudinally polarized photons $\Gamma_L = \varepsilon\Gamma_T$, the double differential ep cross section is related to the total photoproduction cross section by

$$\frac{d^2\sigma_{ep}(y, Q^2)}{dy\,dQ^2} = \Gamma_L \cdot \sigma_{\gamma^* p}^L + \Gamma_T \cdot \sigma_{\gamma^* p}^T$$ (3.12)

$$= \Gamma_T \cdot \sigma_{\gamma^* p}^T \cdot (1 + \varepsilon R)$$ (3.13)

$$= \Gamma_T \cdot \sigma_{\gamma^* p} \cdot \frac{1 + \varepsilon R}{1 + R}$$ (3.14)

$$\simeq \Gamma_T \cdot \sigma_{\gamma^* p}.$$ (3.15)

The value of ε in the kinematic range analyzed here varies between 0.95 and 1 with an average of 0.99, therefore the approximation in equation 3.15 is fulfilled to a very good accuracy. Equation 3.15 will be used later on to translate ep into virtual photoproduction cross sections; it should thus be kept in mind that, whenever values for $\sigma_{\gamma^* p} = \sigma_{\gamma^* p}^T + \sigma_{\gamma^* p}^L$ are quoted, the measured quantity is rather $\sigma_{\gamma^* p}^T + \varepsilon\sigma_{\gamma^* p}^L$. Equation 3.14 is not used since precision measurements of R are not available for the processes studied here.

3.1.2 Charmonium

In what was later to become the November Revolution of particle physics, two groups discovered in 1974 simultaneously the particle today known as the J/ψ meson. Aubert et al. [27] observed at Brookhaven an enhancement in the e^+e^- mass spectrum in the reaction

$$\text{p Be} \longrightarrow e^+e^- + X,$$ (3.16)

naming it "J", while the second group, Augustin et al. [28], measured the e^+e^- annihilation cross section

$$e^+e^- \longrightarrow \text{hadrons} \tag{3.17}$$

at the SPEAR machine at SLAC and named the new particle "ψ" (see figure 3.1). The discovery was awarded with the 1976 nobel prize in physics for Samuel C. C. Ting and Burton Richter.

The mass of the J/ψ is most precisely determined using a depolarization method [29] that gives results one order of magnitude better than the direct mass determination in e^+e^- storage rings which is limited by the uncertainty of the absolute beam energy scale. The current world average is [30]

$$m_\psi = 3.09688 \pm 0.00004 \, \text{GeV}. \tag{3.18}$$

Since the J/ψ is produced in large numbers in e^+e^- annihilation, it is very plausible that it has the same quantum numbers as the photon, $J^{PC} = 1^{--}$. It turns out that the J/ψ is the lightest vector meson in the *Charmonium* family (figure 3.2) that is interpreted as consisting of bound states of a *charm* and *anti-charm* quark. The only lighter $c\bar{c}$ meson is the pseudoscalar ($J^{PC} = 0^{-+}$) η_c with mass $m_{\eta_c} \simeq 2.98 \, \text{GeV}$. The first radial excitation of the J/ψ, the $\psi(2S)$, has a mass of [30]

$$m_{\psi(2S)} = 3.68600 \pm 0.00009 \, \text{GeV}. \tag{3.19}$$

The most peculiar property of the J/ψ and the $\psi(2S)$ mesons is probably their extremely small width [30]:

$$\Gamma_\psi = 87 \pm 5 \, \text{keV}; \tag{3.20}$$

$$\Gamma_{\psi(2S)} = 277 \pm 31 \, \text{keV}. \tag{3.21}$$

This is about three orders of magnitude below that of typical hadronic decays, e.g. of the ρ meson. The reason for this is that the J/ψ has very few options for decaying via the strong force. The most obvious decay mode would be the decay into two charmed mesons (D mesons) — but both the J/ψ and the $\psi(2S)$ have masses below the threshold of $\bar{D}D$ production[3], since the mass of the lightest D meson, the D^0, is $m_{D^0} \simeq 1.86 \, \text{GeV}$. Other hadronic decays can only proceed via diagrams which are forbidden by the OZI rule [32], and thus strongly suppressed[4]. In addition, the decays via a single gluon and via two gluons are not possible due to colour and C-parity conservation, such that at least three gluons are needed for the hadronic decay of the J/ψ (figure 3.3a)).

Of experimental importance is the electromagnetic decay of the J/ψ meson (figure 3.3b)), with rather large branching fractions due to the above reasons. Lepton universality implies almost identical branching ratios for the decay into $\mu^+\mu^-$ and e^+e^-; the measured values are [30]:

$$BR(J/\psi \rightarrow \mu^+\mu^-) = (6.01 \pm 0.19) \, \%; \tag{3.22}$$

$$BR(J/\psi \rightarrow e^+e^-) = (6.02 \pm 0.19) \, \%. \tag{3.23}$$

The $\psi(2S)$ has also a significant branching fraction into electrons and muons:

$$BR(\psi(2S) \rightarrow \mu^+\mu^-) = (0.77 \pm 0.17) \, \%; \tag{3.24}$$

$$BR(\psi(2S) \rightarrow e^+e^-) = (0.88 \pm 0.13) \, \%, \tag{3.25}$$

---

[3]All Charmonium states above the $\psi(2S)$ can decay in charmed mesons, resulting in a much larger width.
[4]The OZI rule states that diagrams containing disconnected quark lines are suppressed relative to those with connected ones.
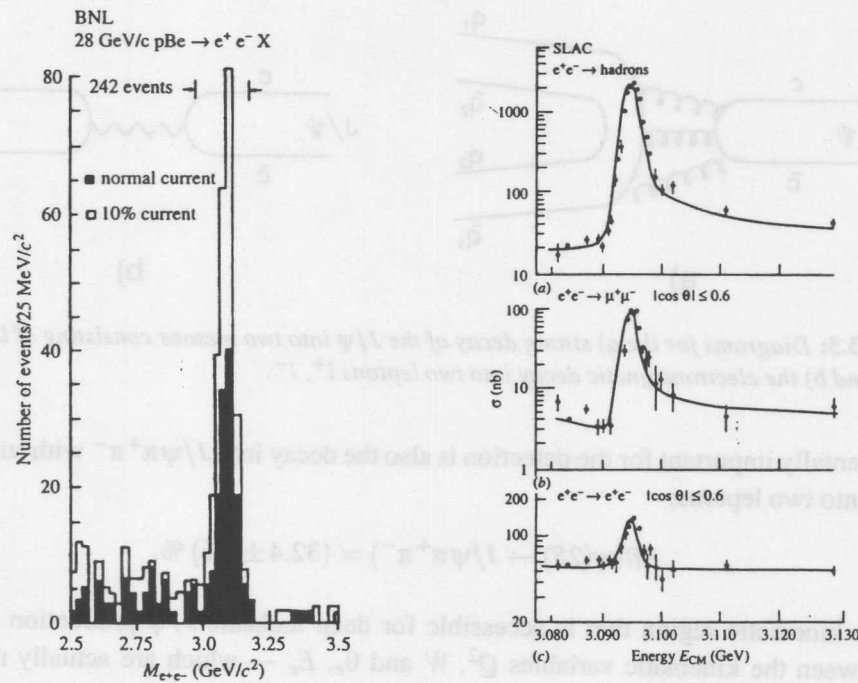
Figure 3.1: *Discovery of the J/ψ at BNL and SLAC. On the left the invariant e^+e^- mass spectrum in the reaction $p\,Be \rightarrow e^+e^- + X$ [27], on the right the energy dependence of the e^+e^- cross section [28].*
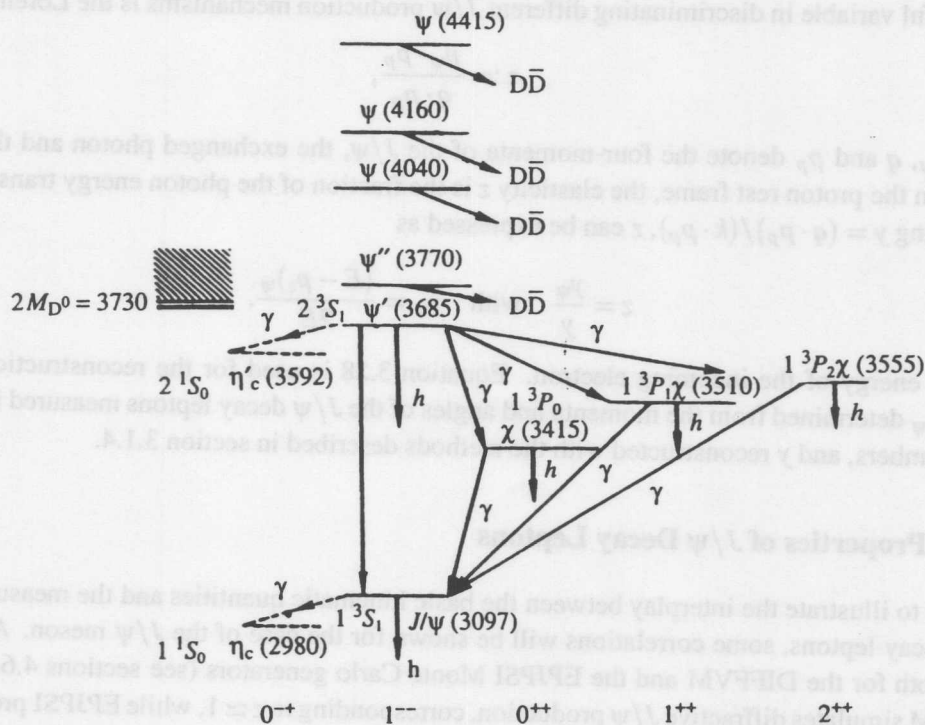

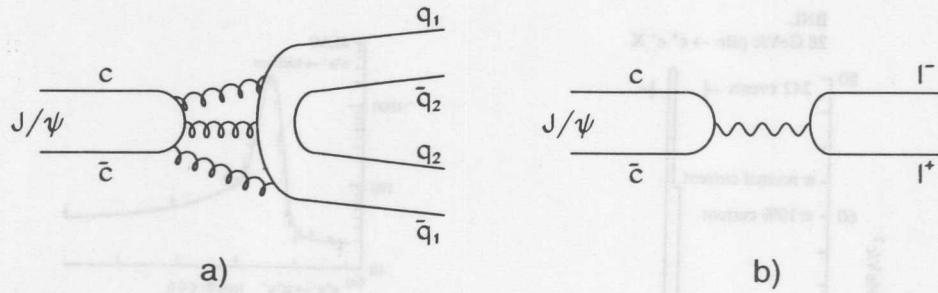**Figure 3.2:** *Level diagram of the Charmonium family (from [31]).*

Figure 3.3: *Diagrams for the a) strong decay of the J/ψ into two mesons consisting of light quarks q_1, q_2 and b) the electromagnetic decay into two leptons l^+, l^-.*

but experimentally important for the detection is also the decay into $J/\psi \pi^+ \pi^-$ with subsequent decay of the J/ψ into two leptons:

$$BR(\psi(2S) \to J/\psi \pi^+ \pi^-) = (32.4 \pm 2.6)\,\%. \tag{3.26}$$

What is the kinematic region that is accessible for deep inelastic J/ψ production at HERA? The relation between the kinematic variables Q^2, W and θ_e, E_e — which are actually measured in the detector — is illustrated in the kinematic plane in figure 3.4. The angular acceptance of the SpaCal limits the Q^2 acceptance to $2 \lesssim Q^2 \lesssim 80\,\text{GeV}^2$, while the angular acceptance of the central tracking detector is the limiting factor for the accessible range in W, $40 \lesssim W \lesssim 170\,\text{GeV}$. For these values of W, the energy of the scattered electron is always above $18\,\text{GeV}$.

A powerful variable in discriminating different J/ψ production mechanisms is the Lorentz invariant

$$z := \frac{p_\psi \cdot p_p}{q \cdot p_p}, \tag{3.27}$$

where p_ψ, q and p_p denote the four-momenta of the J/ψ, the exchanged photon and the incoming proton. In the proton rest frame, the elasticity z is the fraction of the photon energy transferred to the J/ψ. Using $y = (q \cdot p_p)/(k \cdot p_p)$, z can be expressed as

$$z = \frac{y_\psi}{y} \quad \text{with} \quad y_\psi = \frac{(E - p_z)_\psi}{2E}. \tag{3.28}$$

E is the energy of the incoming electron. Equation 3.28 is used for the reconstruction of z, with $(E - p_z)_\psi$ determined from the momenta and angles of the J/ψ decay leptons measured in the central drift chambers, and y reconstructed with the methods described in section 3.1.4.

3.1.3 Properties of J/ψ Decay Leptons

In order to illustrate the interplay between the basic kinematic quantities and the measured Charmonium decay leptons, some correlations will be shown for the case of the J/ψ meson. All results are given both for the DIFFVM and the EPJPSI Monte Carlo generators (see sections 4.6.1 and 4.6.3). DIFFVM simulates diffractive J/ψ production, corresponding to $z \simeq 1$, while EPJPSI produces events covering $0.2 \lesssim z \lesssim 1$ and is based on the Colour Singlet Model.

The hadronic mass W and the polar angle of the J/ψ are strongly correlated, and this correlation is to a large extent transferred to the decay leptons (figure 3.5). This limits the accessible range in W when

the central tracking detector is used for the reconstruction of the decay leptons. The W acceptance of the central tracker is slightly extended towards higher W in the case of EPJPSI as compared to DIFFVM.

Only a weak correlation is observed between Q^2 and the momentum of the decay leptons (figure 3.6). This is advantageous since possible errors of the central tracker simulation will be largely independent of Q^2.

For large and small W, the J/ψ meson is boosted along the z-axis, leading to larger momenta of the decay leptons in the backward and forward direction; this is shown in figure 3.7. As in the previous figures there is very little difference visible between DIFFVM and EPJPSI.

Finally, the polar and azimuthal correlation of the two decay leptons is displayed in figure 3.8. Shown are the differences $\Delta\theta = |\theta_{l1} - \theta_{l2}|$ and $\Delta\phi = |\phi_{l1} - \phi_{l2}|$. Both leptons have predominantly the same direction of flight in θ. In ϕ, only in a very small fraction of events the leptons are close to each other. Note also that due to the Q^2 values being significantly larger than 0, the DIFFVM $\Delta\phi$ distribution is vastly different from that observed in photoproduction, where the leptons are mostly opposite in ϕ.
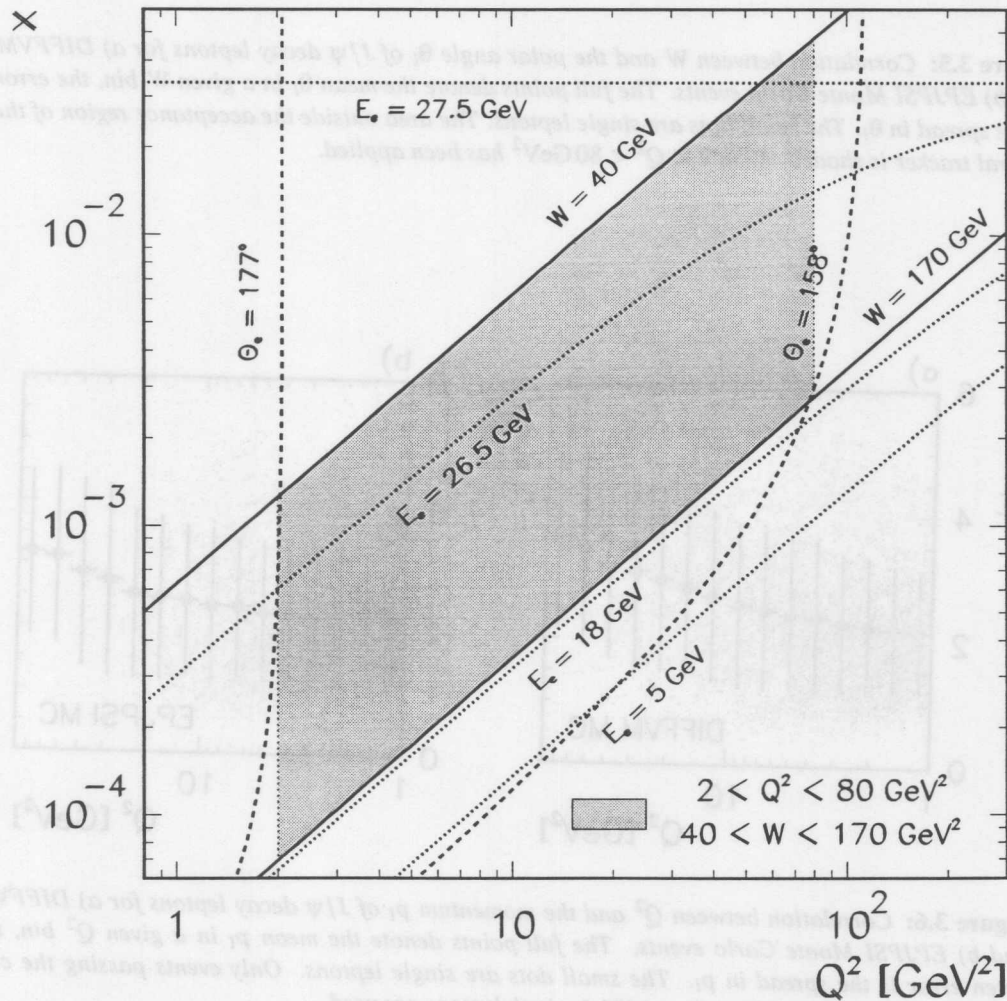

Figure 3.4: *Kinematic plane of x and Q^2. The area typically accessed by the analyses is hatched.*
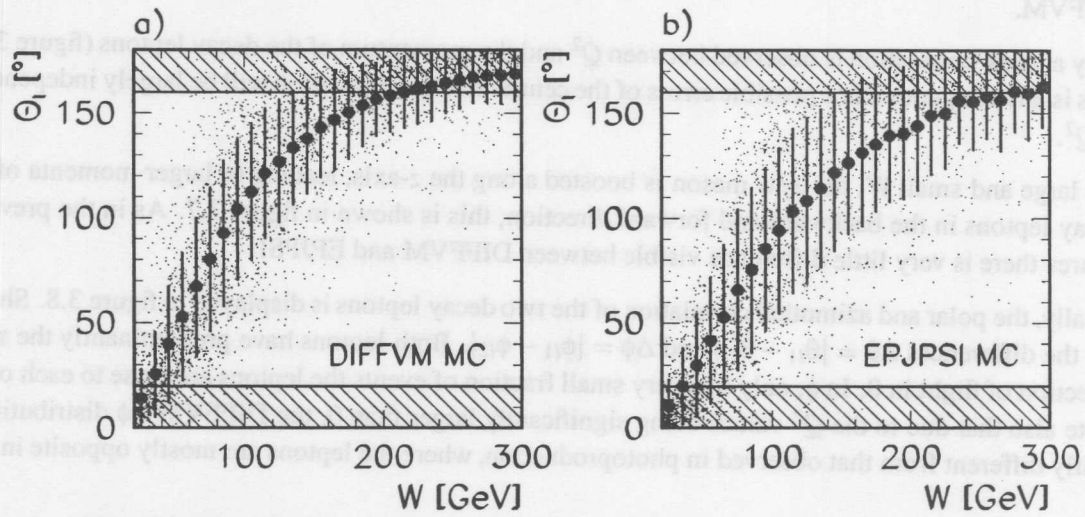
Figure 3.5: *Correlation between W and the polar angle θ_l of J/ψ decay leptons for a) DIFFVM and b) EPJPSI Monte Carlo events. The full points denote the mean θ_l in a given W bin, the error is the spread in θ_l. The small dots are single leptons. The area outside the acceptance region of the central tracker is shaded. A cut $2 < Q^2 < 80\,\mathrm{GeV}^2$ has been applied.*

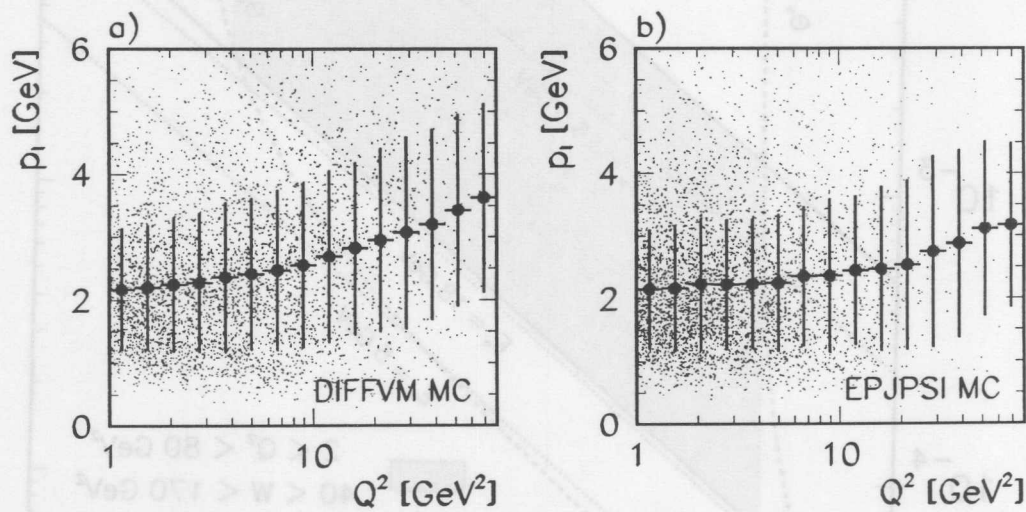**Figure 3.6:** *Correlation between Q^2 and the momentum p_l of J/ψ decay leptons for a) DIFFVM and b) EPJPSI Monte Carlo events. The full points denote the mean p_l in a given Q^2 bin, the given error is the spread in p_l. The small dots are single leptons. Only events passing the cuts $40 < W < 160\,\mathrm{GeV}$ and $20 < \theta_l < 160°$ for both leptons are used.*
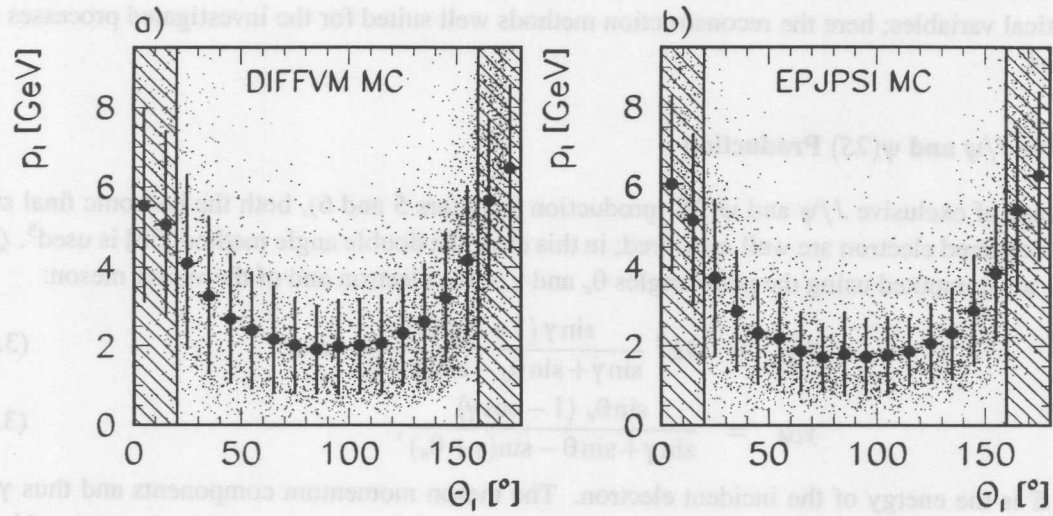
Figure 3.7: *Correlation between the momentum p_l and the polar angle θ_l of J/ψ decay leptons for a) DIFFVM and b) EPJPSI Monte Carlo events. The full points denote the mean p_l in a given θ_l bin, the given error is the spread in p_l. The small dots are single leptons. The area outside the acceptance region of the central tracker is hatched. Only events in $2 < Q^2 < 80\,\text{GeV}^2$ are used.*
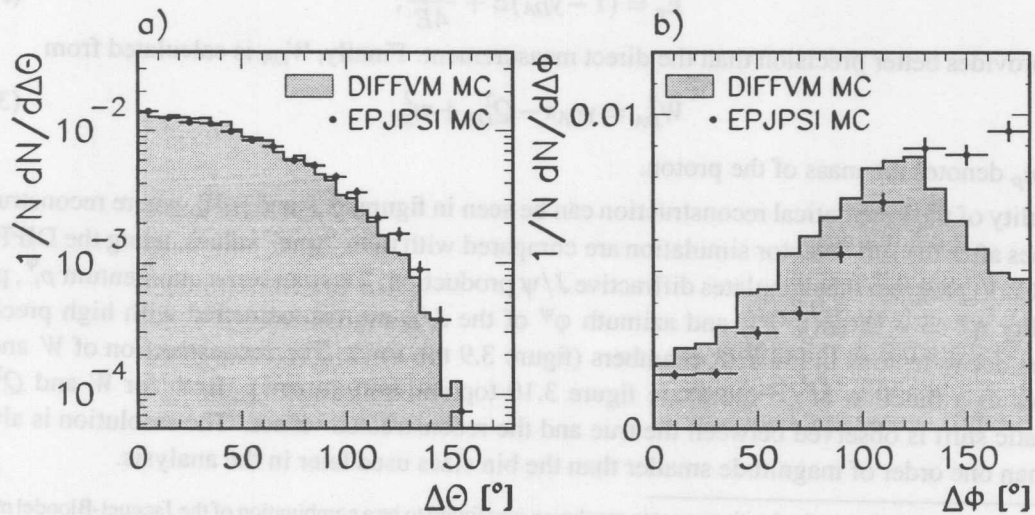

Figure 3.8: *Difference in a) polar and b) azimuthal angle of J/ψ decay leptons in DIFFVM and EPJPSI Monte Carlo events. The cuts $2 < Q^2 < 80\,\text{GeV}^2$ and $40 < W < 160\,\text{GeV}$ have been applied.*

3.1.4   Reconstruction of kinematical variables

Due to the over-constrained final state a variety of methods is available for the reconstruction of kinematical variables; here the reconstruction methods well suited for the investigated processes are described.

Exclusive J/ψ and $\psi(2S)$ Production

In the case of exclusive J/ψ and $\psi(2S)$ production (chapters 5 and 6), both the hadronic final state and the scattered electron are well measured; in this case, the double angle method [33] is used[5]. Q_{DA}^2 and y_{DA} are computed using the polar angles θ_e and γ of the electron and of the vector meson:

$$Q_{DA}^2 = 4E^2 \frac{\sin\gamma\,(1+\cos\theta_e)}{\sin\gamma + \sin\theta_e - \sin(\gamma+\theta)} \quad \text{and} \tag{3.29}$$

$$y_{DA} = \frac{\sin\theta_e\,(1-\cos\gamma)}{\sin\gamma + \sin\theta - \sin(\gamma+\theta_e)}, \tag{3.30}$$

where E is the energy of the incident electron. The meson momentum components and thus γ are obtained from the measured decay products. The double angle method has the advantage of being almost independent of the energy calibration of the calorimeters.

An important observable in exclusive Charmonium production is t, the four-momentum transferred at the proton vertex; the energy transfer to the proton being negligible, the value of $|t|$ is given by:

$$|t| \simeq (\vec{p}_{t,p})^2 = (\vec{p}_{t,e} + \vec{p}_{t,V})^2, \tag{3.31}$$

where $\vec{p}_{t,p}$, $\vec{p}_{t,e}$ and $\vec{p}_{t,V}$ are, respectively, the momentum components transverse to the beam direction of the final state proton, positron and vector meson[6]. Here the momentum of the scattered positron is computed from Q_{DA}^2 and y_{DA}:

$$E_e = (1 - y_{DA})E + \frac{Q_{DA}^2}{4E}, \tag{3.33}$$

which provides better precision than the direct measurement. Finally, W_{DA} is calculated from

$$W_{DA}^2 = y_{DA}s - Q_{DA}^2 + m_p^2, \tag{3.34}$$

where m_p denotes the mass of the proton.

The quality of the kinematical reconstruction can be seen in figures 3.9 and 3.10, where reconstructed quantities after the full detector simulation are compared with their "true" values, using the DIFFVM Monte Carlo program that simulates diffractive J/ψ production. The transverse momentum p_t^ψ, pseudorapidity $\eta^\psi := -\ln\tan(\theta^\psi/2)$ and azimuth φ^ψ of the J/ψ are reconstructed with high precision from the decay leptons in the drift chambers (figure 3.9 top row). The reconstruction of W and Q^2 improves as a function of Q^2 (compare figure 3.10 top and bottom row). Both for W and Q^2, no systematic shift is observed between the true and the reconstructed values. The resolution is always more than one order of magnitude smaller than the bin sizes used later in the analysis.

---

[5]The best reconstruction method with respect to resolution was found to be a combination of the Jacquet-Blondel method [34] for y and the double angle method for Q^2. The improvement compared to the use of double angle variables alone is however small.

[6] The lowest $|t|$ value kinematically possible to allow for the transition $\gamma^* \to J/\psi$,

$$|t_{min}| \simeq (Q^2 + m_V^2)^2\, m_p^2 / (ys)^2, \tag{3.32}$$

is negligible here; it is of the order of $10^{-7}\,\mathrm{GeV}^2$ at $W = 100\,\mathrm{GeV}$.
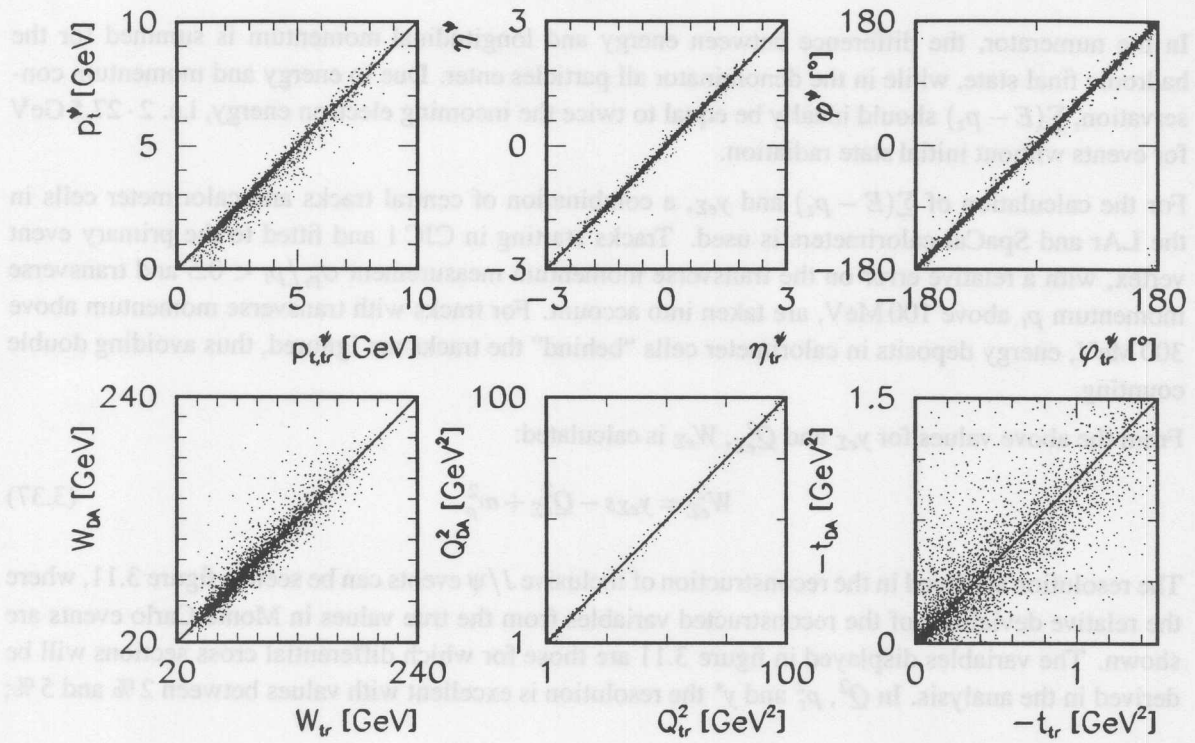
Figure 3.9: *Reconstruction of kinematical variables for* **exclusive** *J/ψ production determined from simulated events using the DIFFVM program. The correlation between the true (tr) and the reconstructed p_t, η and φ of the J/ψ (top row) and W, Q^2 and t (bottom row) is shown, where W, Q^2 and t are reconstructed with the double angle (DA) method.*

In figure 3.9 and 3.10, the quality of the t reconstruction is also illustrated. The relative precision of the reconstruction improves with $|t|$, from about 45 % for $|t| < 0.2\,\text{GeV}^2$ to 18 % for $|t| > 0.6\,\text{GeV}^2$. The bin size used in the analysis will be between 1.5 (small $|t|$) and 2 times (large $|t|$) the resolution. It has been checked with the simulation that the limited resolution has little impact on the measured slope of the t distribution.

Inclusive J/ψ Production

For the analysis of inclusive J/ψ production (chapter 7) a reconstruction method has been chosen that is more independent of the hadronic final state in order to be as far as possible independent of the details of the production mechanism. The $e\Sigma$ method [35] uses Q^2 measured with the scattered electron:

$$Q^2_{e\Sigma} = 4 \cdot E \cdot E_e \cdot \cos^2 \frac{\theta_e}{2}, \tag{3.35}$$

whereas y is measured with the Σ method, which exploits the redundancy of the measured variables to achieve a better resolution and, more importantly, is less sensitive to QED inital state radiation. In this method, the incoming electron energy is replaced with the beam energy "measured" by the reconstruction of the final state, $\sum (E - p_z)/2$:

$$y_{e\Sigma} = \frac{\sum_{had}(E - p_z)}{\sum (E - p_z)}. \tag{3.36}$$

In the numerator, the difference between energy and longitudinal momentum is summed for the hadronic final state, while in the denominator all particles enter. Due to energy and momentum conservation, $\sum(E - p_z)$ should ideally be equal to twice the incoming electron energy, i.e. $2 \cdot 27.5\,\text{GeV}$ for events without initial state radiation.

For the calculation of $\sum(E - p_z)$ and $y_{e\Sigma}$, a combination of central tracks and calorimeter cells in the LAr and SpaCal calorimeters is used. Tracks starting in CJC 1 and fitted to the primary event vertex, with a relative error on the transverse momentum measurement $\sigma_{p_t}/p_t < 0.5$ and transverse momentum p_t above 100 MeV, are taken into account. For tracks with transverse momentum above 300 MeV, energy deposits in calorimeter cells "behind" the tracks are ignored, thus avoiding double counting.

From the above values for $y_{e\Sigma}$ and $Q_{e\Sigma}^2$, $W_{e\Sigma}$ is calculated:

$$W_{e\Sigma}^2 = y_{e\Sigma} s - Q_{e\Sigma}^2 + m_p^2. \tag{3.37}$$

The resolution achieved in the reconstruction of inclusive J/ψ events can be seen in figure 3.11, where the relative deviations of the reconstructed variables from the true values in Monte Carlo events are shown. The variables displayed in figure 3.11 are those for which differential cross sections will be derived in the analysis. In Q^2, p_t^2 and y^* the resolution is excellent with values between 2 % and 5 %;
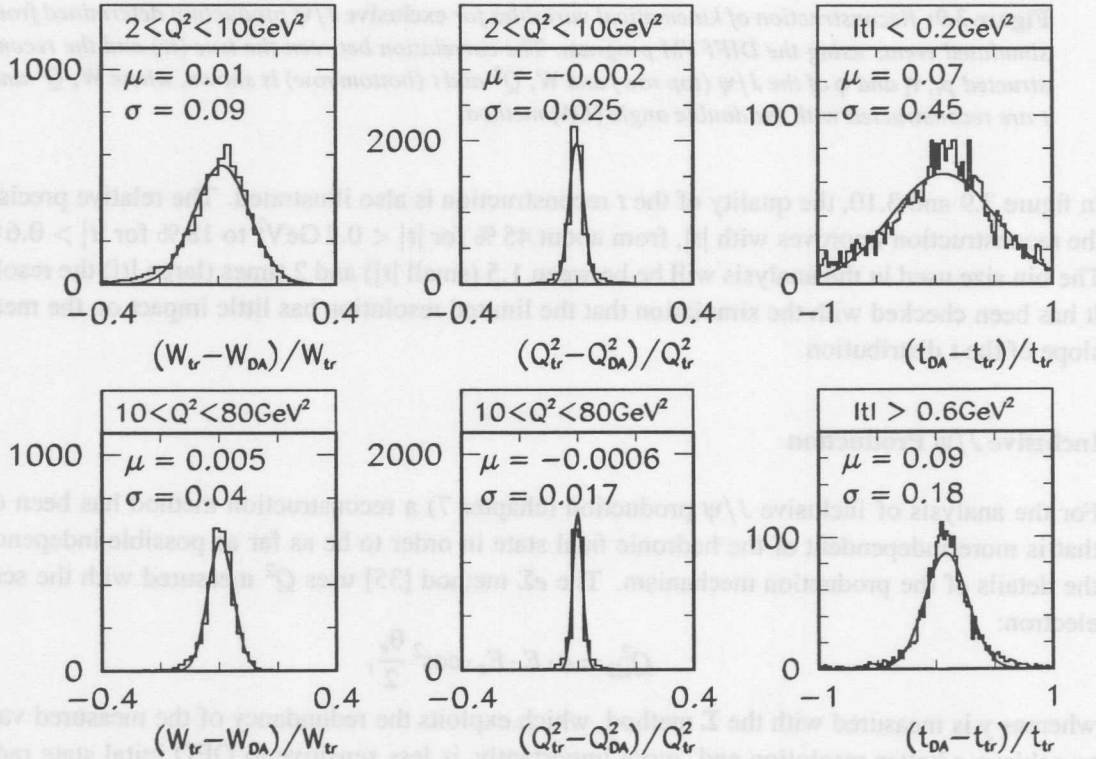

Figure 3.10: *Resolution in the reconstruction of W (left), Q^2 (middle) and t (right) with the double angle method for* **exclusive** *J/ψ production determined from simulated events using the DIFFVM event generator. Only events that pass the exclusive J/ψ selection (section 4.5.1 later applied in the analysis are used, and W is restricted to $40 < W < 160\,\text{GeV}$. The mean μ and width σ of a Gaussian fit to the distributions are given for each plot.*

p_t^2 is the transverse momentum of the J/ψ in the laboratory frame, and y^* denotes the rapidity of the J/ψ in the photon proton centre of mass frame,

$$y^* = \frac{1}{2}\ln\frac{E_\psi + p_{z,\psi}}{E_\psi - p_{z,\psi}}, \tag{3.38}$$

where E_ψ, $p_{z,\psi}$ are the energy and longitudinal momentum component of the J/ψ in this frame, and the z-axis is defined by the photon direction of flight. The resolution in the elasticity z degrades towards lower z, as can be seen in the upper row of figure 3.11c), but it is sufficient for the coarse binning used later in the analysis.

In figure 3.12, the quality of the W reconstruction is shown. It is best for large z and degrades towards lower z.

In the following chapters, the index to the variables denoting the resonstruction method — DA or $e\Sigma$ — will usually be omitted whenever the method of reconstruction is obvious.

3.1.5 Helicity Structure of J/ψ Production

The helicity of the virtual photon in the reaction $ep \rightarrow eJ/\psi\, p$ cannot be directly measured. An important question is whether the helicity of the photon is conserved in the s-channel process $\gamma^* p \rightarrow$
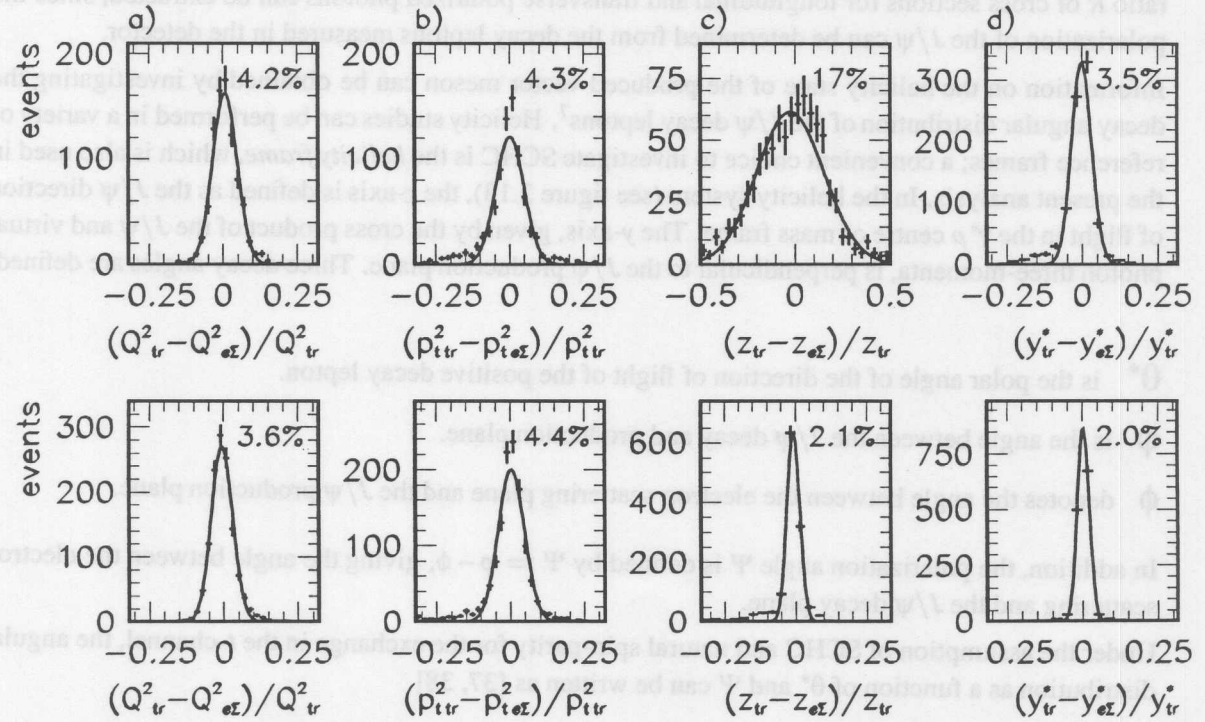

Figure 3.11: *Reconstruction of kinematical variables for* **inclusive** J/ψ *production determined from simulated events using the EPJPSI and DIFFVM event generators; a) Q^2, b) transverse momentum squared of the J/ψ in the laboratory frame, c) elasticity z and d) rapidity y^* in the photon proton centre of mass frame. The* **upper row** *of histograms is for $z < 0.9$, the* **lower row** *for $z > 0.9$. The number in the top right corner of each plot is the width (σ) of a Gaussian fitted to the histogram.*
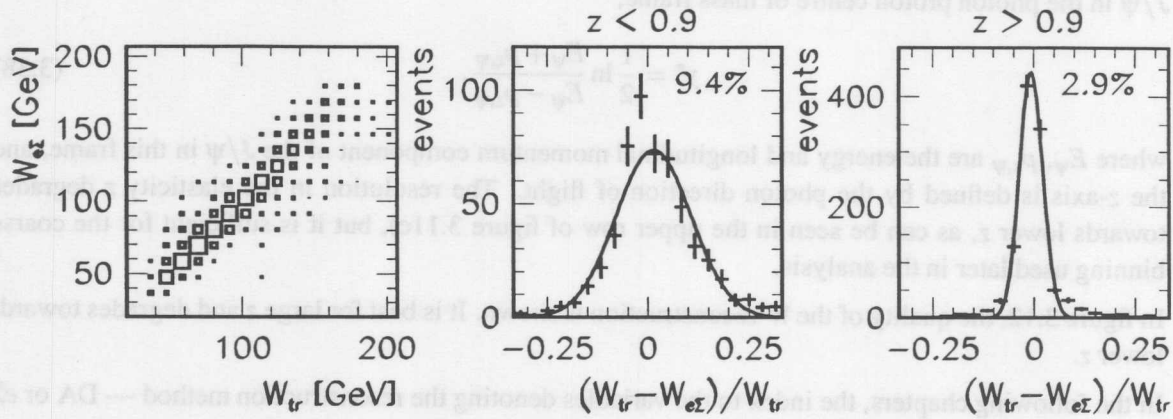
Figure 3.12: *Reconstruction of W for* **inclusive** *J/ψ production determined from simulated events using the EPJPSI and DIFFVM event generators. The number in the top right corner is the width (σ) of a Gaussian fitted to the histogram.*

$J/\psi\,p$, referred to as the hypothesis of *s*-channel helicity conservation (SCHC); if this is the case, the ratio R of cross sections for longitudinal and transverse polarized photons can be extracted, since the polarization of the J/ψ can be determined from the decay leptons measured in the detector.

Information on the helicity state of the produced vector meson can be obtained by investigating the decay angular distribution of the J/ψ decay leptons[7]. Helicity studies can be performed in a variety of reference frames; a convenient choice to investigate SCHC is the *helicity frame*, which is also used in the present analysis. In the helicity system (see figure 3.13), the *z*-axis is defined as the J/ψ direction of flight in the $\gamma^* p$ centre of mass frame. The *y*-axis, given by the cross product of the J/ψ and virtual photon three-momenta, is perpendicular to the J/ψ production plane. Three decay angles are defined:

θ^* is the polar angle of the direction of flight of the positive decay lepton.

φ is the angle between the J/ψ decay and production plane.

ϕ denotes the angle between the electron scattering plane and the J/ψ production plane.

In addition, the polarization angle Ψ is defined by $\Psi := \varphi - \phi$, giving the angle between the electron scattering and the J/ψ decay plane.

Under the assumption of SCHC and natural spin-parity for the exchange in the *t*-channel, the angular distribution as a function of θ^* and Ψ can be written as [37, 38]

$$W(\theta^*, \Psi) \sim 1 + \cos^2\theta^* + 2\varepsilon R\sin^2\theta^* - \varepsilon\sin^2\theta^*\cos 2\Psi + \sqrt{2\varepsilon R(1+\varepsilon)}\cos\delta\cos\Psi\sin 2\theta^*, \tag{3.39}$$

where δ is the phase difference between the amplitudes for J/ψ production by photons with longitudinal and transverse polarization. Integrating over one of the angles, the one-dimensional distributions

---

[7]For a full discussion of the helicity structure in vector meson leptoproduction, see [36].

are obtained. The $\cos\theta^*$ distribution can be expressed using the spin density matrix element r_{00}^{04} that denotes the probability of the J/ψ to be longitudinally polarized; it is related to R by

$$R = \frac{1}{\varepsilon} \frac{r_{00}^{04}}{1 - r_{00}^{04}}. \tag{3.40}$$

The expression for $W(\cos\theta^*)$ in terms of r_{00}^{04} is thus

$$W(\cos\theta^*) \sim 1 + r_{00}^{04} + (1 - 3r_{00}^{04})\cos^2\theta^*. \tag{3.41}$$

3.1.6 Radiative Corrections

Measured cross sections in deep inelastic scattering do not only include the lowest order diagram depicted in figure 2.1, but all orders of electroweak interaction diagrams. In order to derive Born level cross sections, corrections have to be applied. The most important corrections arise due to QED processes of order α, where a bremsstrahlung photon is radiated off the electron either before or after the *ep* interaction, commonly called ISR (initial state radiation) and FSR (final state radiation). The photon is radiated predominantly collinear with the electron, therefore ISR photons escape mostly through the backward beampipe, while FSR photons are usually measured together with the scattered electron in one calorimeter cluster; in less than 2 % of inclusive DIS events with FSR the electron and photon can be resolved in two clusters [9].
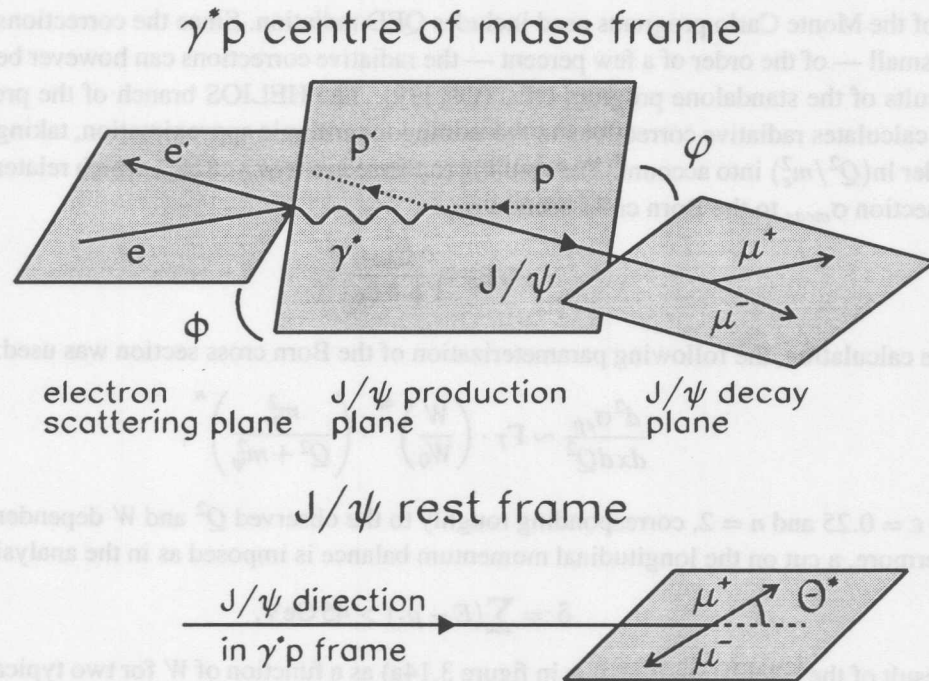

Figure 3.13: *Illustration of the angles used for the description of the J/ψ helicity structure in the decays $J/\psi \to \mu^+\mu^-$ and $J/\psi \to e^+e^-$. θ^* is the decay lepton angle in the helicity frame, φ the angle between the production and decay planes of the J/ψ meson, and ϕ the angle between the electron scattering and J/ψ production plane.*

Method	y		Q^2	
	ISR	FSR	ISR	FSR
double angle	y	y	$z^2 Q^2$	Q^2
$e\Sigma$	y	$\dfrac{yz}{1-y(1-z)}$	zQ^2	Q^2/z

Table 3.1: *Effect on kinematical variables due to initial and final state radiation. Given are the expressions for the measured values of y and Q^2 in the presence of ISR and FSR as a function of the electron's fractional energy loss z.*

QED radiation leads to a change in kinematics and thus to a bias in the cross section measurement. As an example, collinear emission of an ISR photon with energy E_γ leads to a reduction of the electron beam energy E by the photon energy E_γ in the interaction:

$$E \longmapsto z \cdot E \quad \text{with} \quad z := 1 - \frac{E_\gamma}{E} \tag{3.42}$$

with consequently reduced centre of mass energy $s \longmapsto z \cdot s$.

Obviously, the effects of ISR and FSR depend on the chosen reconstruction method for the event kinematics. Expressed in terms of the fractional energy loss of the electron, they are summarized in table 3.1 for the methods used here, the double angle and the $e\Sigma$ method.

None of the Monte Carlo programs used includes QED radiation. Since the corrections turn out to be rather small — of the order of a few percent — the radiative corrections can however be applied using the results of the standalone program HECTOR [39]. The HELIOS branch of the program is used, which calculates radiative corrections in the leading logarithmic approximation, taking only terms of the order $\ln(Q^2/m_e^2)$ into account. The result is expressed in terms of δ_{RC}, which relates the measured cross section σ_{meas} to the Born cross section σ_{ep}:

$$\sigma_{ep} = \frac{\sigma_{meas}}{1 + \delta_{RC}}. \tag{3.43}$$

For the calculation, the following parameterization of the Born cross section was used:

$$\frac{d^2\sigma_{ep}}{dx\,dQ^2} \sim \Gamma_T \cdot \left(\frac{W}{W_0}\right)^{4\varepsilon} \cdot \left(\frac{m_\psi^2}{Q^2 + m_\psi^2}\right)^n, \tag{3.44}$$

where $\varepsilon = 0.25$ and $n = 2$, corresponding roughly to the observed Q^2 and W dependence in the data. Furthermore, a cut on the longitudinal momentum balance is imposed as in the analysis:

$$\delta := \sum (E - p_z) > 45\,\text{GeV}, \tag{3.45}$$

The result of the calculation is shown in figure 3.14a) as a function of W for two typical values of Q^2. The corrections depend only little on W and Q^2, and are of the order of 2% for the double angle and 7% for the $e\Sigma$ method.

In order to prove the stability of the corrections against different parameterizations of the cross section and to show the influence of the $\sum (E - p_z)$ cut, further calculations have been performed; some typical results are shown in figure 3.14b)–d), and can be summarized as follows:

- Changing the $\sum(E - p_z)$ cut from 45 GeV to 35 GeV leads to an increased dependence of δ_{RC} on Q^2 in the double angle method.

- Assuming a steeper Q^2 dependence of the cross section ($n = 2 \mapsto n = 3$) changes the double angle correction by at most 0.02 in δ_{RC}, and has almost no impact for the $e\Sigma$ reconstruction.

- A flat W dependence of the cross section ($\varepsilon = 0.25 \mapsto \varepsilon = 0$) has almost no impact in the case of the double angle method, and changes the $e\Sigma$ result by about 0.02.

In summary, the radiative corrections are small and relatively stable against variations of the input parameterization of the cross section. The systematic error on the measured cross sections due to uncertainties in the radiative corrections — missing higher orders and uncertainties in the cross section parameterization — is estimated to 3 %. Similar values are quoted in recent H1 structure function measurements (2 %, [40, 41]).
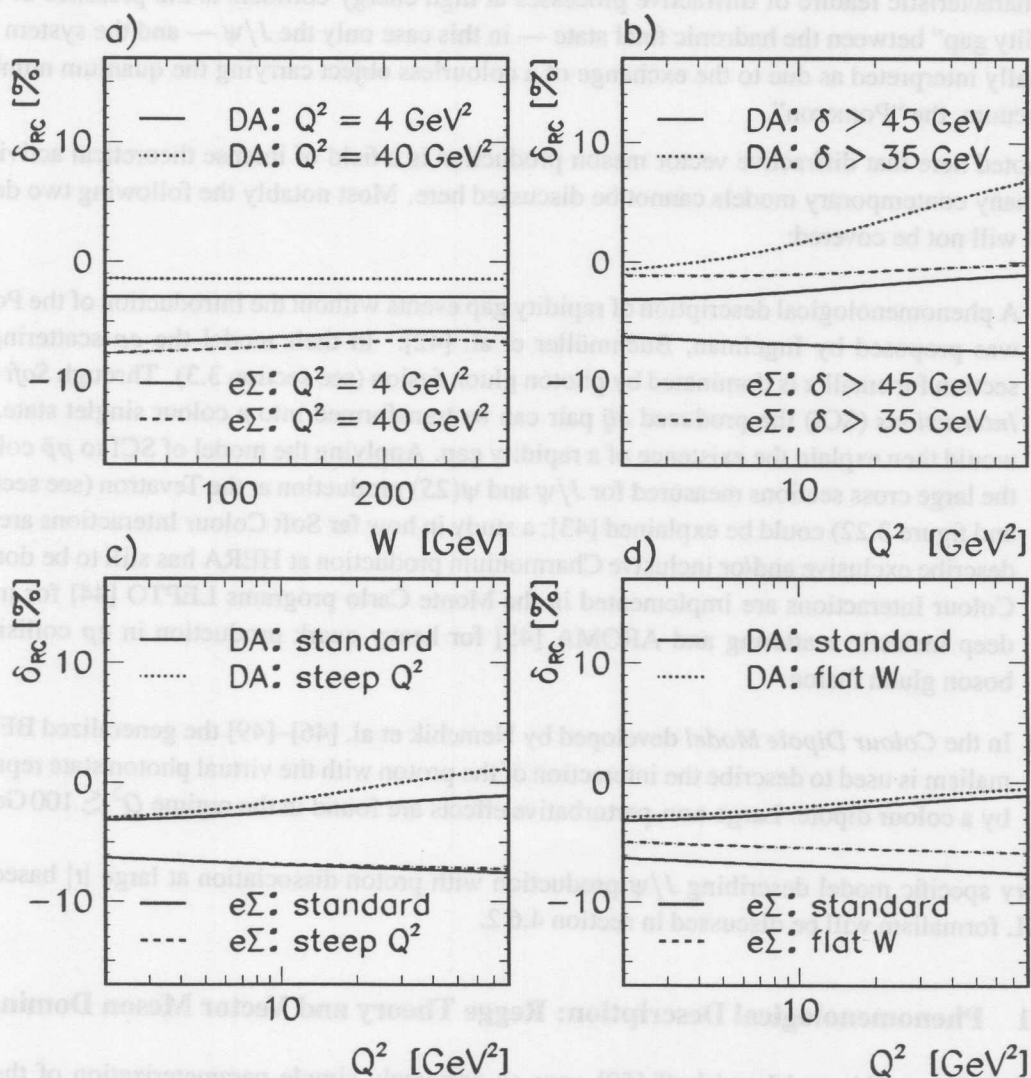

Figure 3.14: *Radiative Corrections as a function of a) W and b)–d) Q^2 for the double angle and the $e\Sigma$ reconstruction methods. b)–d) are calculated for $W = 90$ GeV. See text for further explanations.*

3.2 Diffraction

High energy hadron hadron scattering shows many features characteristic of optical diffraction. About 40 years ago, a phenomenological description of high energy diffraction had been developed, which experienced a revival when the importance of diffractive processes at HERA was discovered.

In this section, a brief summary of the models used to describe the diffractive production of J/ψ mesons at HERA will be given. After a presentation of the traditional phenomenological description using Vector Meson Dominance and Regge theory, two recent attempts to describe J/ψ production in the framework of perturbative QCD are discussed.

In general, two generic processes are distinguished in diffractive J/ψ production: the "elastic" process ($z \simeq 1$) depicted in figure 3.15a), where the proton stays intact, and the "proton dissociation" process ($z \gtrsim 0.95$) in figure 3.15b), where the proton breaks up, giving rise to a system Y with mass $M_Y > m_p$. The characteristic feature of diffractive processes at high energy colliders is the presence of a large "rapidity gap" between the hadronic final state — in this case only the J/ψ — and the system Y; this is usually interpreted as due to the exchange of a colourless object carrying the quantum numbers of the vacuum, the "Pomeron".

It is noted here that diffractive vector meson production is a field of intense theoretical activity, and thus many contemporary models cannot be discussed here. Most notably the following two developments will not be covered:

- A phenomenological description of rapidity gap events without the introduction of the Pomeron was proposed by Ingelman, Buchmüller et al. [42]. In their model the ep scattering cross section for small x is dominated by photon gluon fusion (see section 3.3). Through *Soft Colour Interactions* (SCI) the produced $q\bar{q}$ pair can be transformed into a colour singlet state, which would then explain the existence of a rapidity gap. Applying the model of SCI to $p\bar{p}$ collisions, the large cross sections measured for J/ψ and $\psi(2S)$ production at the Tevatron (see section 3.3 and figure 3.22) could be explained [43]; a study in how far Soft Colour Interactions are able to describe exclusive and/or inclusive Charmonium production at HERA has still to be done. Soft Colour Interactions are implemented in the Monte Carlo programs LEPTO [44] for inclusive deep inelastic scattering and AROMA [45] for heavy quark production in ep collisions via boson gluon fusion.

- In the *Colour Dipole Model* developed by Nemchik et al. [46]–[49] the generalized BFKL formalism is used to describe the interaction of the proton with the virtual photon state represented by a colour dipole. Large non-perturbative effects are found in the regime $Q^2 \lesssim 100 \, \text{GeV}^2$.

A very specific model describing J/ψ production with proton dissociation at large $|t|$ based on the BFKL formalism will be discussed in section 4.6.2.

3.2.1 Phenomenological Description: Regge Theory and Vector Meson Dominance

In 1992, Donnachie and Landshoff [50] gave an extremely simple parameterization of the energy dependence of all hadronic total cross sections and the total photoproduction cross section:

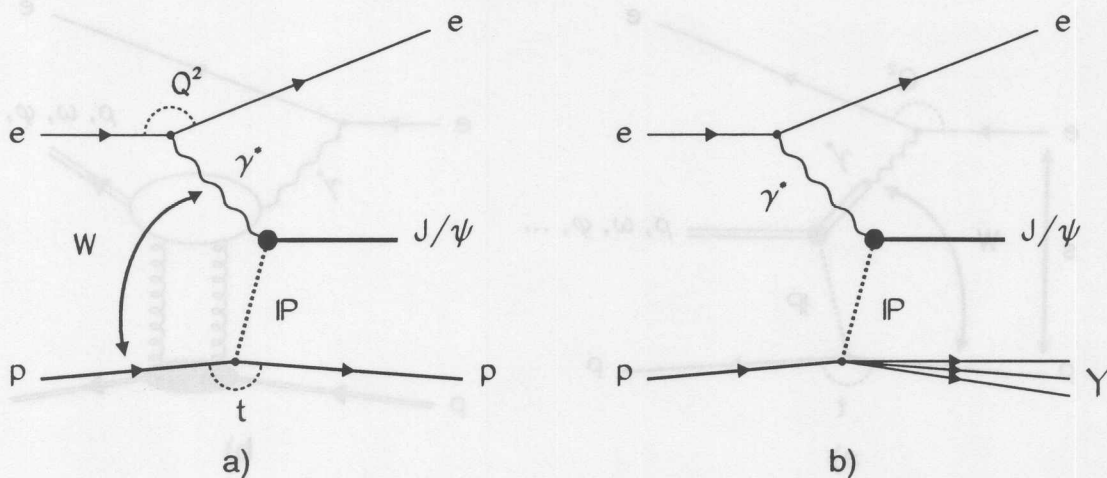$$\sigma_{tot} = X s^{\varepsilon} + Y s^{-\eta} \tag{3.46}$$

Figure 3.15: *Generic graphs for a) elastic and b) proton dissociative J/ψ production in ep collisions.*

with the universal exponents

$$\varepsilon = 0.0808 \quad \text{and} \quad \eta = 0.4525. \tag{3.47}$$

This parameterization is based on Regge theory [51, 52, 53], where the first term corresponds to "Pomeron" exchange, and the second to "Reggeon" exchange. At HERA energies, the Pomeron term dominates, leading to a slow increase of the total photoproduction cross section. The values for ε and η have been determined from fits to total cross section measurements (pp, $p\bar{p}$, pn, πp, Kp and γp); other authors obtained slightly different values.

In Regge theory, hadron-hadron cross sections are described by the t-channel exchange of so-called Regge trajectories, which show up as lines if one plots the spin of possible exchange particles against their mass squared (Chew-Frautschi-plot). Summing the contributions of all Regge trajectories, total cross sections can be written as

$$\sigma_{tot} = \sum_i A_i s^{a_i(0)-1}, \tag{3.48}$$

where $a_i(0)$ denotes the intercept of the trajectory i. For large energies only two trajectories contribute, and equation 3.46 emerges. While the second term in equation 3.46 can be related to observed particles (ρ, ω, f_2, a_2), no particle is known to lie on the Pomeron trajectory.

Applying the ideas of the Vector Meson Dominance Model (VDM), Regge theory can be used to describe real and virtual photoproduction processes. In VDM [54, 55], the photon is described as a quantum mechanical superposition of the bare QED photon state $|\gamma_{qed}\rangle$ and a hadronic state $|h\rangle$:

$$|\gamma\rangle = |\gamma_{qed}\rangle + |h\rangle. \tag{3.49}$$

Naturally, the state $|h\rangle$ should have the same additive quantum numbers as the photon: $J^{PC} = 1^{--}$, $Q = B = S = 0$. Applied to the production of vector mesons by real and virtual photons, the photon is thought to fluctuate into a vector meson (ρ, ω, ϕ, etc.) which then elastically scatters off the proton (figure 3.16a)). The virtual photon proton cross section $\sigma_{\gamma^* p}$ for $\gamma^* p \to J/\psi p$ is related to the cross section for $J/\psi p \to J/\psi p$, $\sigma_{J/\psi p}$:

$$\sigma^T_{\gamma^* p} = \frac{4\pi\alpha}{f_\psi^2} \left(\frac{m_\psi^2}{m_\psi^2 + Q^2} \right)^2 \sigma^T_{J/\psi p} \tag{3.50}$$
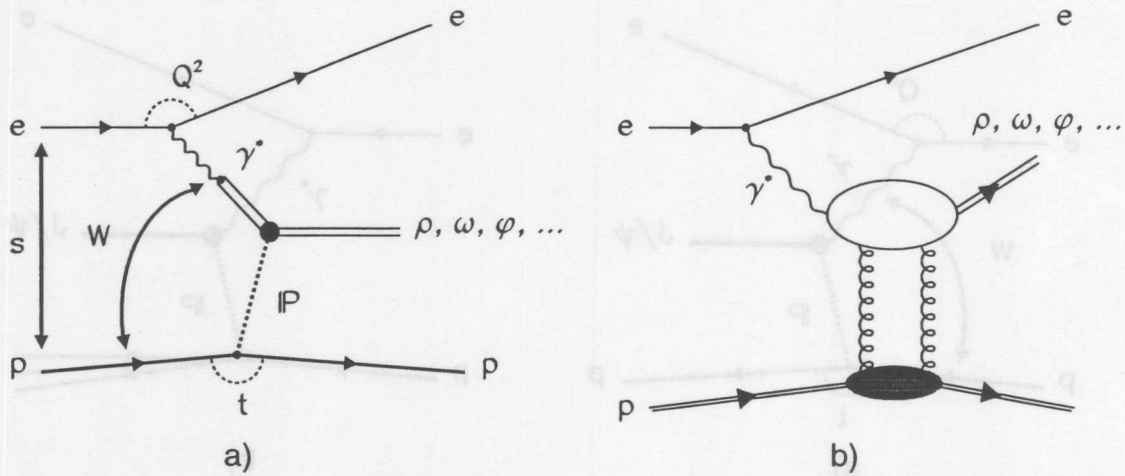
Figure 3.16: *Graphs for elastic vector meson production in ep collisions in a) Regge theory / Vector Meson Dominance and b) in pQCD based models.*

for photons with transverse polarization. f_ψ is the VDM coupling, which is assumed to be Q^2 independent and gives the probability for the transition of the photon to the vector meson, in this case the J/ψ; it is determined by the electronic width Γ_{ee} of the J/ψ decay via [55]

$$\frac{f_\psi}{4\pi} = \frac{\alpha^2 m_\psi}{3\Gamma_{ee}}. \tag{3.51}$$

The somewhat irritating terminology to call the reaction $\gamma^* p \to J/\psi\, p$ "elastic" originates from its interpretation as elastic J/ψ-proton scattering. Note also the shortcoming of the VDM in the above form, that it does not include "off-diagonal" contributions, e.g. $\gamma \to \psi(2S)$, $\psi(2S)p \to J/\psi\, p$. It has been argued [56] that this is the reason for the failure of VDM to produce results for $\sigma_{J/\psi p}$ that are consistent with those extracted from the A dependence of J/ψ production in proton nucleus (pA) collisions [57, 56].

The cross section for longitudinally polarized photons is obtained from

$$\sigma^L_{\gamma^* p} = R \cdot \sigma^T_{\gamma^* p} = \xi \frac{Q^2}{m_\psi^2} \cdot \sigma^T_{\gamma^* p}, \tag{3.52}$$

where ξ is a purely phenomenological parameter of order 1.

The W and t dependence of the J/ψ production cross section is determined by the intercept $\alpha_P(0) = 1 + \varepsilon$ and the slope α' of the Pomeron trajectory:

$$\frac{d\sigma_{\gamma^* p}}{dt} = \left.\frac{d\sigma_{\gamma^* p}}{dt}\right|_{t=0, W=W_0} \cdot e^{b|t|} \cdot \left(\frac{W}{W_0}\right)^{4\varepsilon} \quad \text{with} \tag{3.53}$$

$$|b(W)| = |b(W_0)| + 2\alpha' \ln\left(\frac{W^2}{W_0^2}\right). \tag{3.54}$$

Donnachie and Landshoff determined the slope of the Pomeron trajectory from measurements of elastic pp and $p\bar{p}$ scattering to be $\alpha' = 0.25\,\text{GeV}^{-2}$ [58].

Equations 3.53 and 3.54 contain three essential features of high energy diffractive processes:

- An exponentially falling $|t|$ distribution $\sim e^{b|t|}$, $b < 0$. In analogy to optical diffraction, the slope parameter b can be interpreted as a measure for the interaction radius R, $|b| = R^2/4$ [59]. Typical $|b|$ values for elastic vector meson production are in the range of $4 - 10\,\mathrm{GeV}^2$, while the slope parameter in the case of proton diffractive dissociation is smaller.

- A logarithmic increase of the slope parameter $|b|$ with energy (*shrinkage* of the elastic peak).

- A slow increase of the cross section $\sim W^{0.22-0.32}$; the lower value 0.22 takes the effect of shrinkage into account.

For vector meson production with proton dissociation, the same W dependence of the cross section is expected as in the elastic case. Furthermore, the cross section is expected to fall like $1/M_Y^{2(1+\varepsilon)} \simeq 1/M_Y^2$, where M_Y is the mass of the dissociated proton system [59, 60].

For the case of J/ψ photoproduction, the experimentally measured W dependence of the elastic cross section at HERA ($\sim W^{0.9}$, see section 3.2.3) excludes the "soft Pomeron" picture outlined above. The small values measured for the slope parameter $|b|$ of the order of $4 - 5\,\mathrm{GeV}^{-2}$ indicate that the J/ψ behaves almost pointlike. In the following section, two attempts to describe elastic J/ψ production as a *hard process* calculable in perturbative QCD will be described.

3.2.2 Calculations Based on Perturbative QCD

The description of elastic J/ψ production with perturbative QCD relies on the factorization of the process into three parts:

- The fluctuation of the virtual photon into a $c\bar{c}$ pair "long" before the interaction.

- The interaction between the $c\bar{c}$ pair and the target proton, on a "short" time scale.

- The formation of the bound Charmonium state, a "long" time after the interaction.

The region of applicability of this assumption can be estimated from the requirement that the interaction time should be much shorter than the formation time of the vector meson; Frankfurt et al. give the estimate [61] $x \ll 0.06$, which is fulfilled at HERA but not necessarily in previous fixed target experiments.

The idea that the Pomeron is basically a two gluon system dates back to the seventies [62]. Recent measurements performed by H1 indicate that indeed the majority of the momentum of the Pomeron is carried by gluons [63]. In the following models, these gluons are treated perturbatively, and the basic idea of the process is depicted in figure 3.16b).

The Approach of Ryskin et al.

Ryskin proposed in 1992 the measurement of elastic J/ψ production at HERA as a new way of extracting the gluon density in the proton [57]. His calculation is in leading order based on the exchange of a pair of gluons. Perturbative QCD can be applied since the relevant scale for the process

$$Q_{eff}^2 = \frac{Q^2 + m_\psi^2}{4} \tag{3.55}$$

is much larger than Λ_{QCD} even in photoproduction. For the J/ψ meson, a non-relativistic wave function is assumed with the c and the $\bar{c}$ each carrying half of the photon momentum.

Taking only terms of the order $\alpha_s \ln(Q^2_{eff}/\Lambda^2_{QCD})$ (leading logarithmic approximation, neglecting terms of order α_s), the virtual photon proton cross section at $t = 0$ is, in leading order

$$\frac{d\sigma_{\gamma p}}{dt}\bigg|_{t=0} = \frac{\Gamma_{ee}m_\psi^3\pi^3}{48\alpha} \cdot \frac{\alpha_s^2(Q^2_{eff})}{Q^8_{eff}} \cdot [xg(x,Q^2_{eff})]^2 \cdot \left(1 + \frac{Q^2}{m_\psi^2}\right) \tag{3.56}$$

with

$$x = \frac{4Q^2_{eff}}{W^2}. \tag{3.57}$$

The total cross section is obtained from equation 3.56 by integrating equation 3.53 over t:

$$\sigma_{\gamma p} = \frac{1}{b} \cdot \frac{d\sigma_{\gamma p}}{dt}\bigg|_{t=0}. \tag{3.58}$$

Using parton density functions that describe recent HERA structure function measurements [40, 41, 64], the Ryskin model predicts a much stronger rise of the cross section with W than in the soft Pomeron picture. The quadratic dependence on the gluon density $xg(x, Q^2_{eff})$, which is strongly increasing towards small x, leads to a strong rise of the cross section with W. Measurements of J/ψ photoproduction are in qualitative agreement with this prediction [65, 66]. The Q^2 dependence of the cross section is from equation 3.56 expected to be roughly $\sim 1/(Q^2 + m_\psi^2)^3$, but slightly weaker due to the Q^2 dependence of the gluon density. The ratio of the longitudinal to transverse cross sections is assumed to be

$$R = \frac{Q^2}{m_\psi^2}. \tag{3.59}$$

Corrections beyond the leading $\ln Q^2$ approximation have been estimated by the authors of [67] and predominantly change the absolute normalization of the result, with little impact on the shape as a function of W; the effect on the Q^2 dependence is not quantified. The following corrections have been investigated:

- The effect of transverse momentum k_t of the gluons; in the leading log approximation it is assumed that $k_t^2 \ll Q^2_{eff}$.

- Relativistic effects in the J/ψ wave function due to Fermi motion of the quarks within the J/ψ.

- $c\bar{c}$ rescattering or absorption through the exchange of additional gluon pairs.

- Higher order effects in the form of QCD radiative corrections.

It should however be noted that these estimates are controversial and still not settled (see e.g. [68]).

Helicity conservation in the s-channel is fulfilled for the exchange of a perturbative two gluon system. In ref. [57] it was stated that certain helicity flip amplitudes are non-zero, thus leading to a violation of SCHC; this was later shown to be wrong [69].

The leading order result of Ryskin is implemented in the Monte Carlo program DIPSI [69], which is however not interfaced to the H1 software environment and thus cannot be used in the present analysis.

The Approach of Frankfurt et al.

Brodsky et al. [70] calculated the production of longitudinally polarized vector mesons V with mass m_V in the region $Q^2 \gg m_V^2$ and $Q^2 \gg \Lambda_{QCD}^2$ in the double leading logarithmic approximation, that is $\alpha_s \ln \frac{Q^2}{\Lambda_{QCD}^2} \ln \frac{1}{x} \approx 1$, and confirmed the predicted dependence of the production cross section on the square of the gluon density[8].

In subsequent publications by Frankfurt et al. [61, 68], this model was generalized to the leading $\alpha_s \ln \frac{Q^2}{\Lambda_{QCD}^2}$ approximation and extended to the production of transversely polarized vector mesons and heavy vector mesons (J/ψ, $\psi(2S)$ and Υ) in photoproduction, taking into account non-perturbative contributions more thoroughly.

The final expression for the forward differential cross section for heavy vector mesons in virtual and real photoproduction is [68]

$$\frac{d\sigma_{\gamma^* p}}{dt}\bigg|_{t=0} = \frac{12\pi^3 \Gamma_{ee} m_V^3}{\alpha (Q^2 + 4m^2)^4} \cdot \left| \alpha_s(Q_{eff}^2)(1 + i\beta) xg(x, Q_{eff}^2) \right|^2 \cdot \left(1 + \varepsilon \frac{Q^2}{m_V^2} \right) \cdot C(Q^2), \quad (3.60)$$

where m is the pole mass of the quarks in the vector meson, set to $m_c = 1.5\,\text{GeV}$ for J/ψ, and Γ_{ee} is the measured electronic decay width of the vector meson. The polarization parameter $\varepsilon = \Gamma_L / \Gamma_T$ was introduced in section 3.1.1. x is given by

$$x = \frac{Q^2 + m_V^2}{W^2}, \quad (3.61)$$

and β denotes the (small) relative contribution of the amplitude's real part:

$$\beta = \frac{\text{Re}\mathcal{A}}{\text{Im}\mathcal{A}} \simeq \frac{\pi}{2} \frac{\partial \ln(xg(x, Q_{eff}^2))}{\partial \ln x}. \quad (3.62)$$

Equation 3.60 is separated in an asymptotic part for $Q^2 \to \infty$ and a finite Q^2 correction $C(Q^2)$ given by

$$C(Q^2) = \left(\frac{\eta_V}{3} \right)^2 \left(\frac{Q^2 + 4m^2}{Q^2 + 4m_{run}^2} \right)^4 \mathcal{T}(Q^2) \frac{\mathcal{R}(Q^2) + \varepsilon \frac{Q^2}{m_V^2}}{1 + \varepsilon \frac{Q^2}{m_V^2}}. \quad (3.63)$$

Neglecting the factor $C(Q^2)$, the result of Frankfurt et al. predicts the same Q^2 behaviour of the cross section as the model of Ryskin et al., that is essentially $\sim 1/(Q^2 + m_V^2)^3$ times the Q^2 dependence of the gluon density. The finite Q^2 correction leads to an effectively harder Q^2 spectrum; $C(Q^2)$ is significantly smaller than 1 in the whole Q^2 range currently accessible for elastic J/ψ production at HERA: $C(Q^2) \simeq 0.1$ in photoproduction and $C(Q^2) \simeq 0.5$ at $Q^2 = 100\,\text{GeV}^2$. The following corrections are included in $C(Q^2)$:

- The pole mass m of the quarks is replaced by the running mass m_{run} given by

$$m_{run}^2(Q_{eff}^2) = m^2 \left(1 - \frac{8\alpha_s(Q_{eff}^2)}{3\pi} \right). \quad (3.64)$$

---

[8]A discrepancy between the predictions of Brodsky et al. [70] and Ryskin [57] by a factor of four in the absolute normalization, as quoted in [70], turned out to be an error [61].

- Fermi motion of the quarks in the produced vector meson is taken into account by a factor $\mathcal{T}(Q^2)$:

$$\mathcal{T}(Q^2) = \left(\frac{(Q^2 + 4m^2)^2}{4} \frac{\int \frac{dz}{z(1-z)} \int d^2 k_t \phi_V(z, k_t) \Delta_t \phi_\gamma(z, k_t)}{\int \frac{dz}{z(1-z)} \int d^2 k_t \phi_V(z, k_t)} \right)^2. \tag{3.65}$$

Here, z denotes the fraction of the $q\bar{q}$ momentum carried by one of the quarks, $\pm k_t$ are their transverse momenta, and Δ_t is the transverse Laplace operator. $\phi_V(z, k_t)$ and $\phi_\gamma(z, k_t)$ are the vector meson's and photon's $q\bar{q}$ light-cone wave functions.

The Fermi motion correction was found to be negligible by Ryskin et al. [67], while it is a significant correction in the model of Frankfurt et al. — it is the main contribution to the finite Q^2 factor $C(Q^2)$. This is explained by the fact that in [67] a Gaussian approximation for the Charmonium wave function is used, thus neglecting high momentum tails present in the wave functions based on reasonable potential models [68].

- The deviation of $R = \sigma^L/\sigma^T$ from the assumption made in the Ryskin model, $R = Q^2/m_V^2$, is parameterized with the correction factor $\mathcal{R}(Q^2)$:

$$\mathcal{R}(Q^2) := \frac{Q^2}{m_V^2} \frac{\sigma^T}{\sigma^L} = \left(\frac{m^2}{4m_V^2} \frac{\int \frac{dz}{z^3(1-z)^3} \int d^2 k_t \phi_V(z, k_t) \Delta_t \phi_\gamma(z, k_t)}{\int \frac{dz}{z(1-z)} \int d^2 k_t \phi_V(z, k_t) \Delta_t \phi_\gamma(z, k_t)} \right)^2. \tag{3.66}$$

$\mathcal{R}(Q^2)$ increases with Q^2, thus leading to less suppression of tranversely polarized vector meson production at large Q^2 than expected with $R = Q^2/m_V^2$. Note that $\mathcal{R} = 1$ for $m_V = 2m$ and $\phi_V(z, k_t) = \delta(z - \frac{1}{2})\phi_V(k_t)$ as in the Ryskin model.

- The factor $\eta_V \simeq 3$ takes into account the difference between the vector meson *decay* into an $e^+ e^-$ pair and elastic vector meson *production*.

- The quarkonium wave functions, which are based on non-relativistic potential models, are modified for small transverse $q\bar{q}$ distances and large transverse momenta; the authors call this "hard physics correction".

The effective scale Q^2_{eff} of heavy vector meson production to be used in equation 3.60 is related to the dominant $q\bar{q}$ transverse distances in the respective quark loops; the value Frankfurt et al. quote is significantly larger than in the Ryskin model, where $Q^2_{eff} = (Q^2 + m_V^2)/4$ is used. For J/ψ photoproduction, $Q^2_{eff} \simeq 2.4\,\text{GeV}^2$ in the Ryskin model and $Q^2_{eff} \simeq 5.1\,\text{GeV}^2$ here. Even at higher Q^2 the two estimates differ significantly: at $Q^2 = 40\,\text{GeV}^2$, the effective scales are $Q^2_{eff} \simeq 12\,\text{GeV}^2$ and $Q^2_{eff} \simeq 20\,\text{GeV}^2$, respectively.

The influence of the corrections applied in the model of Frankfurt et al. is illustrated in figure 3.17 for J/ψ production as a function of W and Q^2. For this and the following figure, input values of $\Gamma_{ee} = 5.26\,\text{keV}$ [30] and an elastic slope parameter $|b| = 4.5\,\text{GeV}^{-2}$ have been used.

As a function of W, the main effect of all corrections together is a change of the normalization of the cross section (figure 3.17a)) by more than a factor of five in photoproduction and more than a factor of two at $Q^2 = 40\,\text{GeV}^2$. the largest single contribution is the Fermi motion suppression factor. The Q^2 spectrum (figure 3.17b)) becomes significantly harder due to the Fermi motion correction.
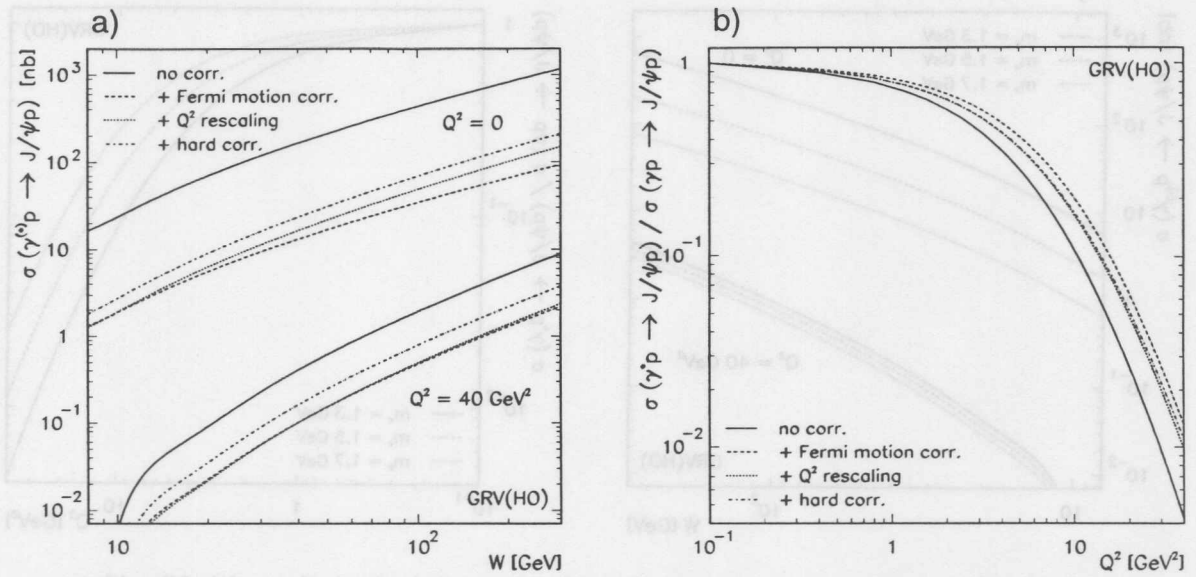
Figure 3.17: *a) Predicted J/ψ cross section by real and virtual photons in the model of Frankfurt et al. [68] as a function of W for $Q^2 = 0$ and $Q^2 = 40\,\text{GeV}^2$; b) the ratio $\sigma_{\gamma^* p}/\sigma_{\gamma p}$ as a function of Q^2 for $W = 90\,\text{GeV}$. The curves illustrate the effect of the different corrections in the cross section formula.*
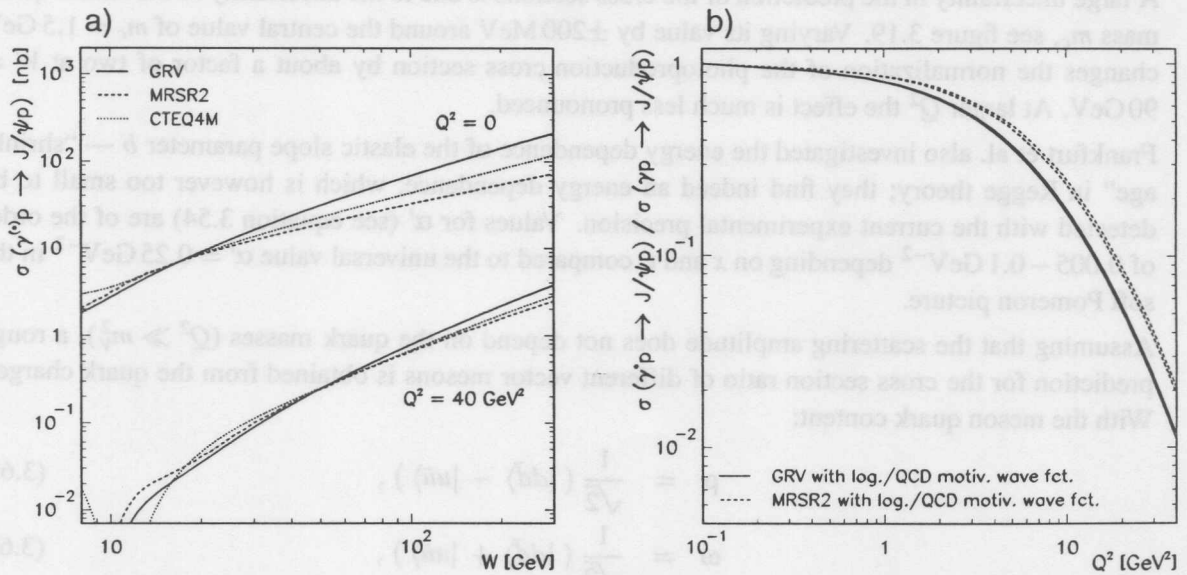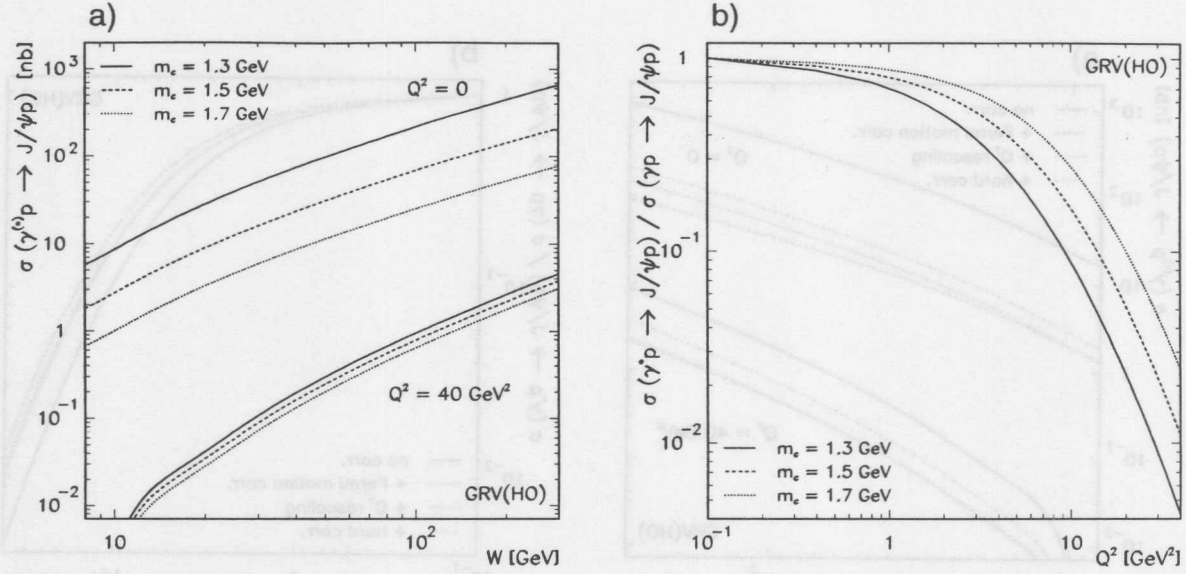

Figure 3.18: *a) Predicted J/ψ cross section by real and virtual photons in the model of Frankfurt et al. [68] as a function of W for $Q^2 = 0$ and $Q^2 = 40\,\text{GeV}^2$; b) the ratio $\sigma_{\gamma^* p}/\sigma_{\gamma p}$ as a function of Q^2 for $W = 90\,\text{GeV}$. The curves show the effect of the choice of different parton density functions (GRV(HO) vs. MRSR2) and potential models (logarithmic vs. QCD motivated).*

Figure 3.19: *a) Predicted J/ψ cross section by real and virtual photons in the model of Frankfurt et al. [68] as a function of W for $Q^2 = 0$ and $Q^2 = 40\,\mathrm{GeV}^2$; b) the ratio $\sigma_{\gamma^* p}/\sigma_{\gamma p}$ as a function of Q^2 for $W = 90\,\mathrm{GeV}$. The curves show the effect of the choice of the charm quark pole mass m_c.*

The influence of different gluon density functions and potential models for the J/ψ is shown in figure 3.18. While different gluon densities lead to changes in the shape and normalization of the predicted cross section, the influence of the chosen potential model turns out to be very small.

A large uncertainty in the prediction of the cross sections is due to the uncertainty of the charm quark mass m_c, see figure 3.19. Varying its value by $\pm 200\,\mathrm{MeV}$ around the central value of $m_c = 1.5\,\mathrm{GeV}$ changes the normalization of the photoproduction cross section by about a factor of two at $W = 90\,\mathrm{GeV}$. At larger Q^2 the effect is much less pronounced.

Frankfurt et al. also investigated the energy dependence of the elastic slope parameter b — "shrinkage" in Regge theory; they find indeed an energy dependence, which is however too small to be detected with the current experimental precision. Values for α' (see equation 3.54) are of the order of $0.005 - 0.1\,\mathrm{GeV}^{-2}$ depending on x and t, compared to the universal value $\alpha' = 0.25\,\mathrm{GeV}^{-2}$ in the soft Pomeron picture.

Assuming that the scattering amplitude does not depend on the quark masses ($Q^2 \gg m_V^2$), a rough prediction for the cross section ratio of different vector mesons is obtained from the quark charges. With the meson quark content:

$$\rho = \frac{1}{\sqrt{2}} \left(|d\bar{d}\rangle - |u\bar{u}\rangle \right), \tag{3.67}$$

$$\omega = \frac{1}{\sqrt{2}} \left(|d\bar{d}\rangle + |u\bar{u}\rangle \right), \tag{3.68}$$

$$\phi = |s\bar{s}\rangle \quad \text{and} \tag{3.69}$$

$$J/\psi = |c\bar{c}\rangle, \tag{3.70}$$

the ratio of the production rates is given by the squares of the quark charges:

$$\rho : \omega : \phi : J/\psi = 9 : 1 : 2 : 8. \tag{3.71}$$

This $SU(4)$ prediction is strongly violated for J/ψ photoproduction compared to ρ photoproduction, thus a strong increase of the ratio $\rho : J/\psi$ as a function of Q^2 is expected and indeed observed (see next section). Frankfurt et al. predict even an excess over the $SU(4)$ prediction for heavy vector mesons due to the larger probability for small distances of the quarks in a heavy meson [61].

The production rates for excited vector meson states are predicted to be of comparable size to the ground states in the limit $Q^2 \gg m_V^2$. For the ratio $\psi(2S)/\psi$ the asymptotic value is estimated to be[9] $\sigma_{\psi(2S)}/\sigma_\psi \simeq 0.5$.

For the photoproduction of Υ mesons at HERA, a ratio

$$\frac{\sigma_\Upsilon}{\sigma_\psi} \simeq \frac{1}{200} \tag{3.72}$$

is predicted, which is consistent with preliminary ZEUS results [71] and an ongoing H1 analysis [72].

3.2.3 Overview of Experimental Results

Up to now, elastic photoproduction of vector mesons at HERA has been investigated for the ρ, ω, ϕ and J/ψ meson. Virtual photoproduction, for $Q^2 \gtrsim 8\,\text{GeV}^2$, has been studied for the ρ, ϕ and J/ψ meson, and a ρ' signal was presented by H1. Results for the transition region between $Q^2 \approx 0$ and $Q^2 \approx 8\,\text{GeV}^2$ are available for the ρ and, with very limited statistics, for the ϕ and the J/ψ meson; the transition region between the "soft" and "hard" regime is thus best studied with the ρ meson. A compilation of cross sections as a function of W is shown in figure 3.20, where also the references are given.

Data of vector meson production with proton dissociation have been presented by the H1 collaboration for J/ψ photoproduction [65] and ρ production in deep inelastic scattering [82], and by the ZEUS collaboration for ρ photoproduction. Further results exist for J/ψ and ρ production at large $|t|$, and exclusive $\psi(2S)$ photoproduction.

The experimental results obtained at HERA can be summarized as follows:

- Photoproduction of light vector mesons (ρ, ω, ϕ) is well described by the soft Pomeron picture and Vector Meson Dominance: the cross section rises slowly $\sim W^{0.22-0.32}$, and the elastic slope parameter is of the order of $b \simeq -10\,\text{GeV}^{-2}$.

- Whenever a hard scale is present in the process, the cross section rises strongly with W, $\sim W^{0.5-1.2}$, and the slope parameter is of the order of $|b| \simeq 4 - 6\,\text{GeV}^{-2}$. The scale can be either Q^2, t, or the mass of the vector meson m_V^2.

- HERA data alone do not yet allow to confirm or exclude shrinkage of the elastic peak for any vector meson. For elastic J/ψ photoproduction, Levy [87] investigated the available fixed target *and* HERA data and extracted a slope of the Pomeron trajectory $\alpha' = -0.001 \pm 0.072\,\text{GeV}^{-2}$, concluding that the "soft" Pomeron picture ($\alpha' \simeq 0.25\,\text{GeV}^{-2}$) is excluded in this case, and that the process is fully calculable in perturbative QCD.

---

[9]An increase of $\sigma_{\psi(2S)}/\sigma_\psi$ is also predicted in the Colour Dipole Model of Nemchik et al. [46]–[49]; the asymptotic regime is in this model already reached for $Q^2 \approx 3 \cdot m_V^2$ [48].

- The ratio of cross sections for elastic ρ and J/ψ production rises dramatically with Q^2; while in photoproduction the J/ψ is suppressed by two orders of magnitude, the cross sections are of the same order at $Q^2 \simeq 20\,\mathrm{GeV}^2$, close to the expectation from $SU(4)$ quark flavour symmetry.

- The slope parameter $|b|$ for proton diffractive dissociation is significantly smaller than for the elastic process.

- No sign for a possible violation of the SCHC hypothesis has been found.

Note that in all figures in the forthcoming chapters where results from previous experiments are displayed, the data have been rescaled to the currently best value for the branching fraction $J/\psi \rightarrow \mu^+\mu^-$ [30]

$$BR(J/\psi \rightarrow \mu^+\mu^-) = (6.01 \pm 0.19)\,\%. \tag{3.73}$$
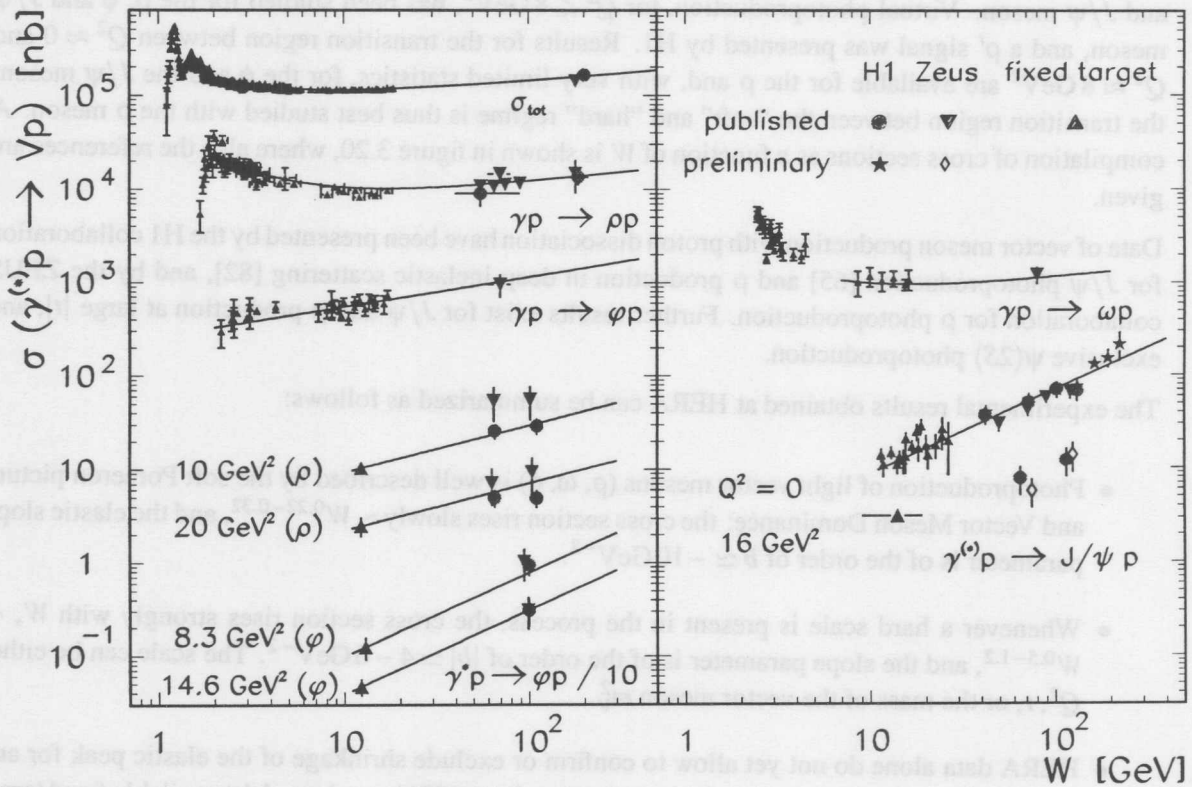
Figure 3.20: *Compilation of (virtual) photon proton cross sections for elastic vector meson production as a function of W. The curves for the total cross section and ρ and ω photoproduction are based on Regge parameterizations from [50, 73], the other lines are $\sim W^\delta$ with $\delta = 0.32$ (φ, $Q^2 = 0$), $\delta = 0.5$ (ρ, $Q^2 > 0$) and $\delta = 0.9$ (φ, $Q^2 > 0$; J/ψ). Results at intermediate Q^2 have been left out to maintain readability. Experimental results are from [74, 75] ($\sigma^{\gamma p}_{tot}$); [74],[76]-[80] (ρ); [81] (ω); [82, 83, 84] (φ); [78, 65, 66, 85, 86] (J/ψ), and references therein for the fixed target experiments.*

3.3 Inelastic Charmonium Production

In the present section, the three main models for inelastic Charmonium production will be presented in their historical order. In all models, the production of the $c\bar{c}$ pair is treated separately from its evolution into a bound state (factorization); factorization is considered to be legitimate because the production of the $c\bar{c}$ pair proceeds on a short time scale of order $1/m_c$, while the formation of the bound state is a non-perturbative long distance process on a time scale longer than $1/\Lambda_{QCD}$. The dominant process by which heavy quark pairs are produced at HERA is the photon gluon fusion graph depicted in figure 3.21a), but all models are equally well applicable to other processes, e.g. hadroproduction of Charmonium via gluon gluon fusion.

To get a thorough overview of the current theoretical status, two reviews [88, 89] are recommended.

3.3.1 The Colour Evaporation Model

The Colour Evaporation Model — also referred to as the "local duality approach" — has been developed in the late seventies by Fritzsch et al. [90, 91, 92]. In this approach, the sum of the cross sections of all $c\bar{c}$ bound states is given by the integral of the cross section for $c\bar{c}$ production, $\sigma_{c\bar{c}}$, from the lower threshold $2m_c$ up to the threshold for the production of a pair of heavy-light mesons, $2m_D$:

$$\sigma_{onium} = \frac{1}{9} \int_{2m_c}^{2m_D} dm \frac{d\sigma_{c\bar{c}}}{dm}, \tag{3.74}$$

where $\sigma_{c\bar{c}}$ is calculated in perturbation theory. The factor $1/9$ represents the statistical probability for the quark pair to be asymptotically in the colour singlet state. This transition is thought to proceed via multiple soft-gluon interactions, implying a statistical treatment of colour. Due to the multiple soft-gluon exchanges, Charmonium produced via the colour evaporation mechanism is predicted to be unpolarized [93], which is a very distinct feature compared to other models for inelastic Charmonium production.

To obtain the cross section for a specific Charmonium state such as J/ψ, the factor ρ_ψ is introduced:

$$\sigma_\psi = \rho_\psi \cdot \sigma_{onium}. \tag{3.75}$$

The factor ρ_ψ is of the order of $1/N_{onium}$, where N_{onium} is the number of Charmonium states with mass between $2m_c$ and $2m_D$. Since ρ_ψ can depend on the specific state, the production process, the centre of mass energy, the transverse momentum of the Charmonium, m_c and the gluon density in the target(s), absolute predictions in the Colour Evaporation Model are difficult.

A comparison to recent experimental data is given in [93]. Although qualitative agreement with the data is observed, the Colour Evaporation Model receives rather little interest in the literature due to its weak predictive power. One should however note that the underlying ideas, especially the treatment of colour as a non-perturbative phenomenon, are remarkably similar to those found in the Buchmüller model for diffractive processes ("Soft Colour Interactions", see section 3.2) and also in the factorization approach of Braaten et al. (section 3.3.3).

3.3.2 The Colour Singlet Model

The Colour Singlet Model [94, 95, 96], developed since 1980, was the first to provide quantitative predictions for Charmonium production in a wide variety of environments: in hadron collisions,
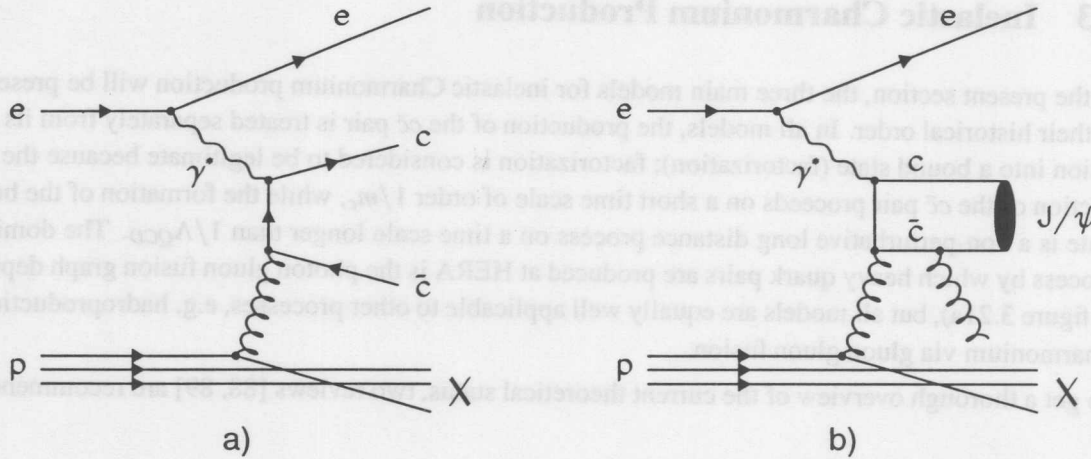
Figure 3.21: *a) $c\bar{c}$ production via photon gluon fusion and b) a leading order graph for J/ψ production in the Colour Singlet Model.*

photoproduction and e^+e^- collisions. The J/ψ production is thought to proceed in two steps: in the first step, a $c\bar{c}$ pair with the same quantum numbers — spin, angular momentum and C-parity — as the Charmonium state is produced in a colour singlet state; the second step contains the binding of the $c\bar{c}$ into the Charmonium state. The cross section can then be factorized into a short distance matrix element describing the $c\bar{c}$ production in a region of size $1/m_c$, and a long distance factor that describes the non-perturbative dynamics of the bound state formation. The differential cross section for e.g. $\gamma p \rightarrow J/\psi X$ can thus be written as

$$d\sigma(J/\psi + X) = d\hat{\sigma}(c\bar{c}(\underline{1},^3S_1) + X)|R_\psi(0)|^2, \qquad (3.76)$$

where $R_\psi(0)$ is the J/ψ wave function at the origin, and the notation "$\underline{1}$" is used to denote that the $c\bar{c}$ pair is in a colour singlet state.

The short distance part $d\hat{\sigma}$ can be calculated using a perturbative expansion in $\alpha_s(m_c)$, while the long distance part is related to the electronic width Γ_{ee} of the Charmonium:

$$\Gamma(J/\psi \rightarrow e^+e^-) := \Gamma_{ee} \simeq \frac{4\alpha^2}{9m_c^2}|R_\psi(0)|^2 \text{ (leading order) }. \qquad (3.77)$$

Applied to J/ψ production at HERA, the leading contribution in the photon gluon fusion process is of order (α, α_s^2), since at least one additional gluon is needed to produce a $c\bar{c}$ pair with the quantum numbers of the J/ψ (see figure 3.21b)). In order to ensure the applicability of the perturbative expansion, the additional gluon has to be hard; therefore the Colour Singlet Model prediction can only be reliable in the region $z \lesssim 0.9$. The next-to-leading order diagrams ($O(\alpha, \alpha_s^3)$) have been calculated [97] and were found to give large corrections to the leading order prediction for $z \gtrsim 0.8$ and $p_{t,\psi} \lesssim 1 \, \text{GeV}^2$, thus further restricting the regime of applicability.

The Colour Singlet Model has enormous predictive power, with only one non-perturbative parameter for each angular momentum multiplet — e.g. $R_\psi(0)$ for the J/ψ and η_c — in any high energy process. On the other hand, severe experimental and theoretical problems persist. Theoretically, the most serious limitation of the Colour Singlet Model is the absence of a general theorem ensuring the validity of the above factorization also in the higher orders of perturbation theory. It can also be considered
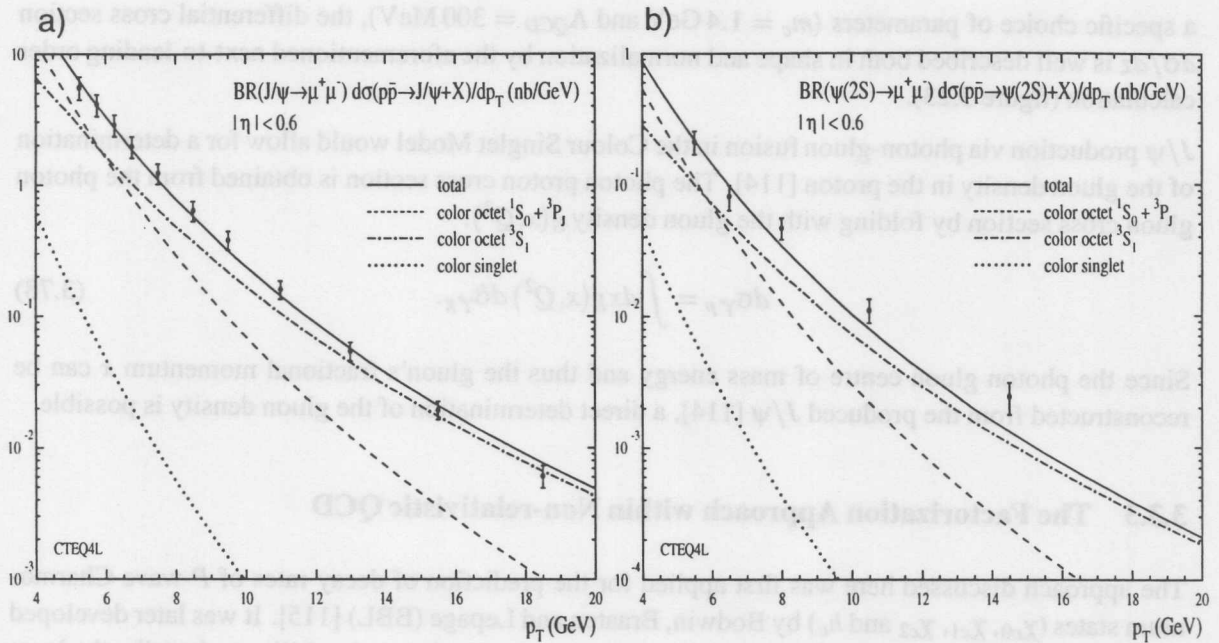
Figure 3.22: *Differential cross section $d\sigma/dp_t$ times the branching ratio $BR(J/\psi \to \mu^+\mu^-)$ for a) direct J/ψ and b) prompt $\psi(2S)$ production in $p\bar{p}$ collisions measured by CDF [99, 100] at $\sqrt{s} = 1.8\,TeV$. Contributions from b hadron decays and χ decays have been removed. The lines are the theoretical expectations based on the Colour Singlet Model, and the result of a fit of colour octet contributions to J/ψ and, in the case of $\psi(2S)$, of a simultaneous fit to J/ψ and $\psi(2S)$. For J/ψ, the data include feeddown from $\psi(2S)$ decays which is accounted for in the theoretical curves. For the theoretical predictions, CTEQ4L [108] parton distribution functions have been used. Figures are from [109].*

incomplete, since it does not cover the production of $c\bar{c}$ pairs in colour octet states which evolve into colour singlet Charmonium states through the emission of soft gluons.

Experimentally, the Colour Singlet Model is more or less ruled out by several observations. The most prominent failure of the model are the cross sections for prompt J/ψ and $\psi(2S)$ production[10] measured by the CDF and D0 collaborations at the Tevatron $p\bar{p}$ collider [98]–[102]. For large transverse momenta p_t of the J/ψ meson, the Colour Singlet Model predictions are more than one order of magnitude below the data, see figure 3.22. Prior to these measurements, the dominant contribution to Charmonium production at the Tevatron was expected to proceed via gluon gluon fusion in the Colour Singlet Model, with the leading order being $\sim \alpha_s^3$.

A mismatch between theoretical expectation and measured cross sections was also found by the UA1 collaboration [103] at CERN in $p\bar{p}$ collisions at $\sqrt{s} = 630\,\text{GeV}$. In fixed target experiments the Colour Singlet Model predictions were found to be up to two orders of magnitude too small [104, 105, 106, 107].

Nevertheless, the Colour Singlet Model has been quite successful in describing inelastic ($z < 0.9$) J/ψ photoproduction at HERA and at fixed target muoproduction experiments (EMC, NMC). With

---

[10]"Prompt" means here that J/ψ and $\psi(2S)$ from b hadron decays have been removed; "direct" J/ψ production includes in addition feeddown from $\psi(2S)$ decays. Indirect contributions from χ decays are removed.

a specific choice of parameters ($m_c = 1.4$ GeV and $\Lambda_{QCD} = 300$ MeV), the differential cross section $d\sigma/dz$ is well described both in shape and normalization by the aforementioned next-to-leading order calculation (figure 3.23).

J/ψ production via photon-gluon fusion in the Colour Singlet Model would allow for a determination of the gluon density in the proton [114]. The photon proton cross section is obtained from the photon gluon cross section by folding with the gluon density $g(x, Q^2)$:

$$d\sigma_{\gamma p} = \int dx \, g(x, Q^2) \, d\hat{\sigma}_{\gamma g}. \tag{3.78}$$

Since the photon gluon centre of mass energy and thus the gluon's fractional momentum x can be reconstructed from the produced J/ψ [114], a direct determination of the gluon density is possible.

3.3.3 The Factorization Approach within Non-relativistic QCD

The approach discussed here was first applied for the prediction of decay rates of P-wave Charmonium states ($\chi_{c0}, \chi_{c1}, \chi_{c2}$ and h_c) by Bodwin, Braaten and Lepage (BBL) [115]. It was later developed into a complete theory [116, 117], and received much attention due to the ability to describe the large
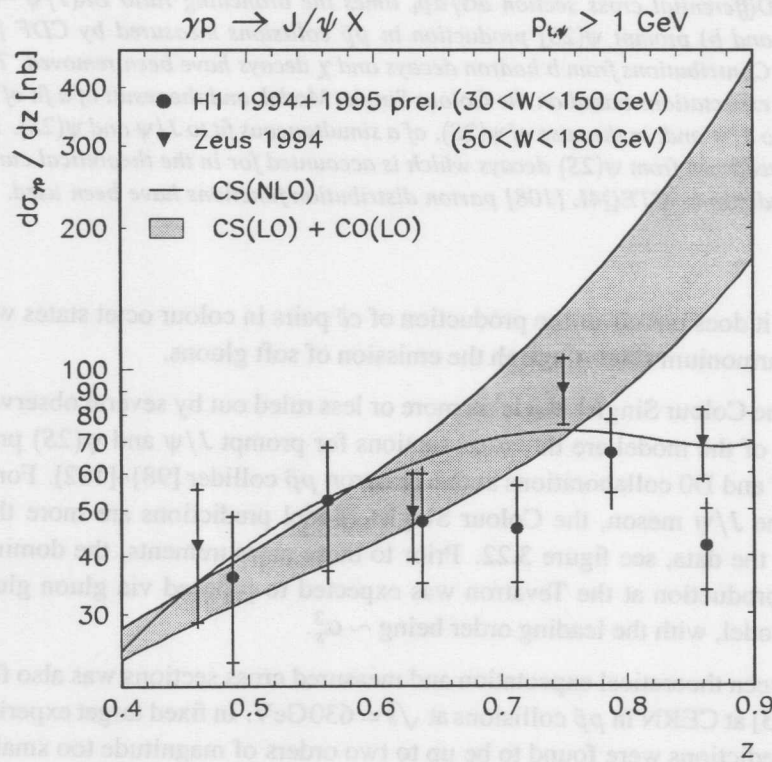
Figure 3.23: *Differential cross section $d\sigma_{\gamma p}/dz$ for inelastic J/ψ production measured at HERA [110, 111]. The line is the result of the next-to-leading order calculation [97] in the Colour Singlet Model with the GRV(HO) [112] parton densities, $m_c = 1.4$ GeV and $\Lambda_{QCD} = 300$ MeV, while the upper boundary of the filled area is the sum of the leading order colour singlet and colour octet contributions [113]; the filled area itself indicates an estimate of the uncertainty in the colour octet prediction due to effective primordial transverse momentum of the interacting gluon.*

production rates for high p_t hadroproduction of J/ψ and $\psi(2S)$ at the Tevatron [118], first reported by the CDF experiment (figure 3.22).

In the BBL formalism, the production cross section for a Charmonium state, e.g. $A + B \rightarrow J/\psi + X$, can be expressed as

$$\sigma(A + B \rightarrow J/\psi + X) = \sum_n c_n(A + B \rightarrow c\bar{c}[n] + X)\langle 0|O_n^{J/\psi}|0\rangle, \qquad (3.79)$$

where n denotes an on-shell $c\bar{c}$ pair in a definite colour, spin and angular momentum state. For each n, the cross section factorizes into a short distance part c_n calculable in a perturbative QCD expansion in $\alpha_s(2m_c)$ and a long distance matrix element $\langle O_n^{J/\psi}\rangle$ giving the probability for the $c\bar{c}$ pair to form a J/ψ meson; the $\langle O_n^{J/\psi}\rangle$ describe the evolution of the $c\bar{c}$ pair into a J/ψ plus additional soft gluons. While in the Colour Singlet Model all c_n not corresponding to a colour singlet $c\bar{c}$ are set to zero, the BBL formalism includes states where the $c\bar{c}$ system is a colour octet. In the following the notation $\langle O_{(1,8)}^{J/\psi}(^{2S+1}L_J)\rangle$ will be used, where the subscripts 1 or 8 refer to the colour configuration of the $c\bar{c}$ system, 1 for a colour singlet and 8 for a colour octet.

The major second ingredient in the theory besides factorization is the introduction of non-relativistic QCD (NRQCD, [119]) velocity scaling rules that make the application of equation 3.79 possible; NRQCD is an effective field theory in which the heavy quark and antiquark are treated non-relativistically. At first sight, equation 3.79 is not particularly useful since it involves an infinite number of non-perturbative factors $\langle O_n^{J/\psi}\rangle$. However, it can be deduced from NRQCD that the matrix elements $\langle O_n^{J/\psi}\rangle$ scale with powers of the square of the typical velocity v of the heavy quark in the Charmonium state. If v^2 is a small quantity — and this is indeed the case, with $v^2 \simeq 0.3$ for the J/ψ — the Charmonium production cross section can be calculated to arbitrary precision with a double expansion in powers of $\alpha_s(2m_c)$ and v^2.

Note that in the limit $v \rightarrow 0$ the Colour Singlet Model is restored; colour octet contributions are suppressed by powers of v^2, and can only become important when the corresponding short distance coefficients c_n for colour octet states are large. A rather drastic example is high p_t hadroproduction of Charmonium at the Tevatron: in the Colour Singlet Model, the leading order process — gluon gluon fusion (figure 3.24a)) — is of order α_s^3 and falls like $1/p_t^8$ [88], while the colour octet contributions (α_s^3) are only $\sim 1/p_t^4$ and dominate at large p_t. In the BBL approach, high p_t Charmonium production is dominated by gluon fragmentation (figure 3.24b)), which is due to the emission of additional hard gluons suppressed (α_s^5) in the Colour Singlet Model.

Colour Octet Matrix Element Phenomenology

The non-perturbative matrix elements $\langle O_n^{J/\psi}\rangle$ can be determined experimentally or in lattice QCD [120]. If factorization holds, they are universal. The measurement of colour octet matrix elements provides thus a crucial test of the theory.

Besides quarkonium production at $p\bar{p}$ colliders that has already been mentioned, the formalism has been applied to a wide variety of processes, among them J/ψ production in fixed target experiments [121], in e^+e^- collisions via annihilation and in hadronic decays of the Z^0 [122], and in $\gamma\gamma$ collisions [123]. Colour octet states have even been proposed [124] as an explanation for the tiny branching fraction of $\psi(2S) \rightarrow \rho\pi$ relative to that for $J/\psi \rightarrow \rho\pi$.
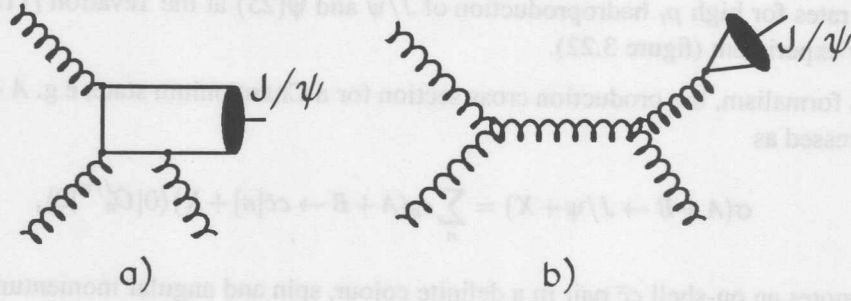
Figure 3.24: *Diagrams contributing to J/ψ production in $p\bar{p}$ collisions at the Tevatron via a) gluon gluon fusion and b) gluon fragmentation.*

For HERA, colour octet contributions have been calculated for real [125]-[128] and virtual [127, 129] photoproduction of J/ψ, for J/ψ production via fragmentation (relevant at large p_t and small z) [130], for the associated production of $J/\psi + \gamma$ [131, 132], and for h_c photoproduction [133].

A very clean signature for colour octet processes is the measurement of J/ψ mesons from hadronic Z^0 decays at LEP. Such measurements have been performed [134, 135], but the small branching fractions lead to small event samples with subsequently large experimental errors.

On the other hand, the extraction of colour octet matrix elements from the Tevatron turned out to have other difficulties. Cho and Leibovich [136] extracted from the CDF data the matrix elements

$$\langle O_{(8)}^{J/\psi}(^3S_1)\rangle = (6.6 \pm 2.1) \cdot 10^{-3}\,\text{GeV}^3 \quad \text{and} \tag{3.80}$$

$$\frac{\langle O_{(8)}^{J/\psi}(^3P_0)\rangle}{m_c^2} + \frac{\langle O_{(8)}^{J/\psi}(^1S_0)\rangle}{3} = (2.2 \pm 0.5) \cdot 10^{-2}\,\text{GeV}^3. \tag{3.81}$$

It was later shown [137] that the effective primordial k_t of the interacting gluons (or quarks) due to Fermi motion and initial state radiation leads to dramatic changes in the extracted matrix elements; simulating this effect with the PYTHIA Monte Carlo program [138], the authors obtain the values

$$\langle O_{(8)}^{J/\psi}(^3S_1)\rangle = (2.1 \pm 0.5) \cdot 10^{-3}\,\text{GeV}^3 \quad \text{and} \tag{3.82}$$

$$\frac{\langle O_{(8)}^{J/\psi}(^3P_0)\rangle}{m_c^2} + \frac{\langle O_{(8)}^{J/\psi}(^1S_0)\rangle}{3} = (4.4 \pm 0.7) \cdot 10^{-3}\,\text{GeV}^3 \tag{3.83}$$

when MRSD0 [139] parton density functions are used as in [136]. Neglecting gluon k_t leads to a significant overestimation of colour octet matrix elements, by about one order of magnitude in the case of the linear combination in equation 3.83. Furthermore, the choice of the parton density function has significant influence on the result and can change for example the numbers given in equation 3.83 by another factor of two.

This observation has important consequences for the predictions [113] of colour octet contributions to J/ψ photoproduction at HERA. For the colour octet curve shown in figure 3.23 rather "large" values of $\langle O_{(8)}^{J/\psi}(^1S_0)\rangle = 10^{-2}\,\text{GeV}^3$ and $\langle O_{(8)}^{J/\psi}(^3P_0)\rangle/m_c^2 = 10^{-2}\,\text{GeV}^3$ have been used, and the band indicates a rough estimate of the uncertainty due to the aforementioned k_t-effect. Thus from figure 3.23 the non-universality of colour octet matrix elements cannot be concluded. The same conclusion was recently drawn by Kniehl and Kramer [140]. It is an unlucky coincidence that J/ψ photoproduction

Matrix element	Cho (MRSD0) [136]	Beneke (CTEQ4L) [109]	Cano-Col. (MRSD0) [137]	Cano-Col. (GRVHO) [137]
$\langle O_{(8)}^{J/\psi}(^3S_1)\rangle$	0.66 ± 0.21	$1.06^{+1.06}_{-0.61}$	0.21 ± 0.05	0.34 ± 0.04
$\langle O_{(8)}^{J/\psi}(^3P_0)\rangle/m_c^2 + \langle O_{(8)}^{J/\psi}(^1S_0)\rangle/3$	2.2 ± 0.5		0.44 ± 0.07	0.20 ± 0.04
$3.5\langle O_{(8)}^{J/\psi}(^3P_0)\rangle/m_c^2 + \langle O_{(8)}^{J/\psi}(^1S_0)\rangle$		$4.38^{+1.91}_{-1.37}$		

Matrix element	Krämer [128]	Fleming [129]
$\langle O_{(1)}^{J/\psi}(^3S_1)\rangle$	116	110 ± 10
$\langle O_{(8)}^{J/\psi}(^1S_0)\rangle$	0.8	1
$\langle O_{(8)}^{J/\psi}(^3P_0)\rangle/m_c^2$	0.8	0.5

Table 3.2: *Summary of NRQCD matrix elements for J/ψ production extracted from CDF data (upper table). Units are always $10^{-2}\,\text{GeV}^3$. In the lower table matrix elements used by different authors for the prediction of J/ψ production cross sections at HERA are given.*

at HERA is sensitive to those matrix elements that are most affected by higher order corrections at the Tevatron.

Summarizing the current status of the NRQCD factorization approach, there is so far no evidence for the non-universality of colour octet matrix elements, but also no other experimental result is known where colour octet contributions have as dramatic effects as observed in large p_t hadroproduction of J/ψ. On the theoretical side, development continues and next-to-leading order calculations have already become available for some processes. A very powerful observable could be the polarization of the Charmonium states, both in hadroproduction and real and virtual photoproduction [109, 128, 129], but up to now no experimental results are available.

Values extracted for the long distance matrix elements for J/ψ production based on the CDF data are summarized in table 3.2, showing that currently these can only be considered as order-of-magnitude estimates.

One of the processes where no experimental results are currently available, but theoretical predictions — albeit only in leading order — exist, is the production of J/ψ mesons at HERA at reasonably large Q^2, i.e. more than a few GeV^2, which is the topic of this thesis.

Production of J/ψ Mesons in Deep Inelastic Scattering

Fleming and Mehen [129] calculated the production cross sections within the NRQCD factorization approach. This process could provide a sensitive probe of the colour octet matrix elements $\langle O_{(8)}^{J/\psi}(^3P_0)\rangle/m_c^2$ and $\langle O_{(8)}^{J/\psi}(^1S_0)\rangle$, which are only poorly determined from the Tevatron data. Their calculation includes the types of diagrams of order α_s shown in figure 3.25a) and b) and α_s^2 (figure 3.25c), d) and e)); colour octet terms of order α_s are found to dominate the cross section.

The predicted cross sections for the production of J/ψ mesons in deep inelastic ep scattering at HERA, $d\sigma/dQ^2$, including the contributions from the colour octet states $^3P_0$, $^1S_0$ ($O(\alpha_s)$) and the colour singlet state $^3S_1$ ($O(\alpha_s^2)$) are shown in figure 3.26 for the kinematical region $40 < W < 180\,\text{GeV}$, using GRV(LO) [112] parton densities. The sum of the colour octet contributions dominates the cross section for all Q^2; since the $^3P_0$ and $^1S_0$ contributions have a similar shape, the cross section is only sensitive to a linear combination of the two corresponding matrix elements. Fleming and Mehen estimate the prediction to be reliable for $Q^2 > 4\,\text{GeV}^2$. The following values for the matrix elements have been used in figure 3.26:

$$\langle O_{(1)}^{J/\psi}(^3S_1)\rangle = 1.1\,\text{GeV}^3; \tag{3.84}$$

$$\langle O_{(8)}^{J/\psi}(^1S_0)\rangle = 0.01\,\text{GeV}^3; \tag{3.85}$$

$$\langle O_{(8)}^{J/\psi}(^3P_0)\rangle/m_c^2 = 0.005\,\text{GeV}^3. \tag{3.86}$$

The singlet matrix element is determined — analogous to the Colour Singlet Model — from the measured electronic decay width of the J/ψ with the relation [141]

$$\Gamma_{ee} = \frac{8\pi\alpha^2 e_c^2}{9m_\psi^2} \cdot \langle O_{(1)}^{J/\psi}(^3S_1)\rangle \cdot \left(1 - \frac{16}{3}\frac{\alpha_s(m_\psi)}{\pi}\right). \tag{3.87}$$

As can be seen in figure 3.23, colour octet contributions to J/ψ photoproduction are in leading order in α_s predominantly expected at large z. This is for the same reason also true for J/ψ production
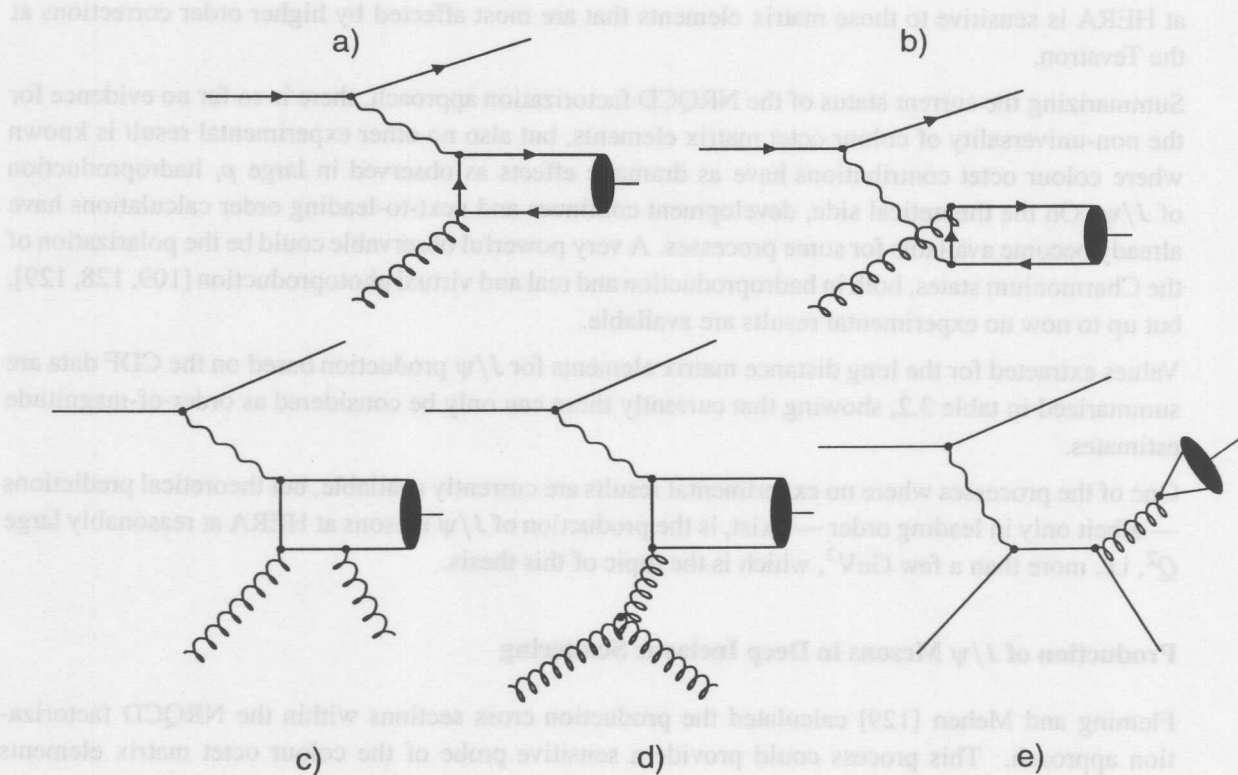
Figure 3.25: *Diagrams contributing to the virtual photoproduction of J/ψ up to order α_s^2. Only diagrams of type c) contribute to the production of a $c\bar{c}$ pair in a colour singlet $^3S_1$ state.*
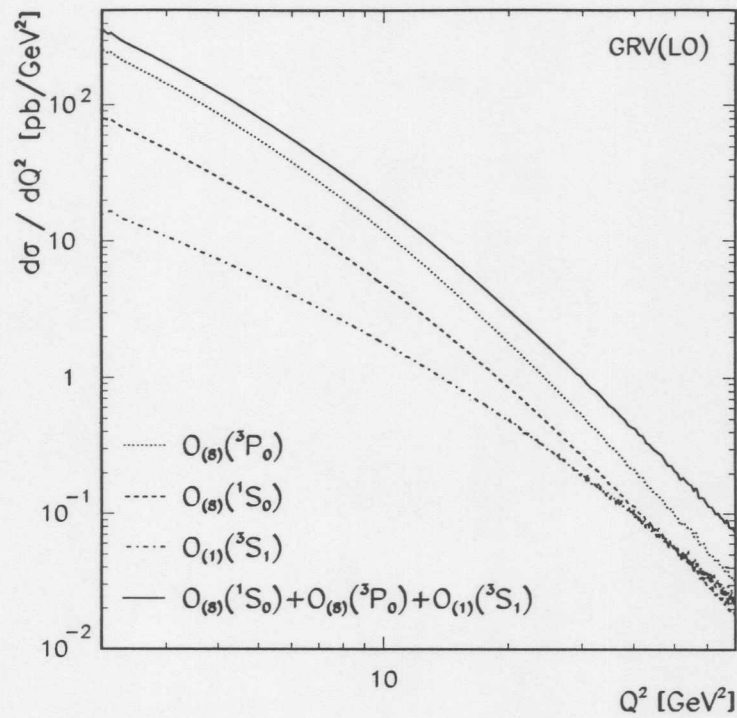
Figure 3.26: *Prediction by Fleming and Mehen [129] for the J/ψ virtual photoproduction cross section $d\sigma/dQ^2$ in the region $40 < W < 180\,\text{GeV}$. The colour octet contributions are $O(\alpha_s)$ and the colour singlet prediction is $O(\alpha_s^2)$.*

by virtual photons: for colour octet states, the $c\bar{c}$ pair can be produced with no other particles in the final state, i.e. $z = 1$. The non-perturbative evolution into the J/ψ meson reduces the value of z only slightly to typically $z \approx 1 - v^2$. Experimentally, J/ψ mesons produced via colour octet states are thus expected to be kinematically very similar to diffractively produced J/ψ mesons, which are also produced at large z.

Figure 3.26: Prediction by Fleming and Maltoni [129] for the J/ψ virtual photoproduction cross section $d\sigma/dQ^2$ in the region $40 < W < 180 \, \text{GeV}$. The colour octet contributions are $O(\alpha_s)$ and the colour singlet prediction is $O(\alpha_s^2)$.

by virtual photons: for colour octet states, the $c\bar{c}$ pair can be produced with no other particles in the final state, i.e. $z = 1$. The non-perturbative evolution into the J/ψ meson reduces the value of z only slightly to typically $z \approx 1 - v^2$. Experimentally, J/ψ mesons produced via colour octet states are thus expected to be kinematically very similar to diffractively produced J/ψ mesons, which are also produced at large z.

Chapter 4

Event Selection and Monte Carlo Simulation

The criteria used to select events for the analyses presented in this thesis are designed to meet two opposing demands: loose cuts are needed in order to increase the statistical significance for processes with small cross sections of the order of pb, while tighter cuts generally lead to smaller experimental systematic uncertainties. The selection developed in order to reach these goals is presented in this chapter.

The data taking periods and the criteria in order to ensure a reliable detector performance, as well as the determination of the available luminosity are discussed in the first section. Since both J/ψ and $\psi(2S)$ are identified via either a $\mu^+\mu^-$ or a e^+e^- pair in the final state, the identification of relatively low momentum leptons of the order of $2\,\mathrm{GeV}$ is a crucial point in any Charmonium analysis at HERA. The method adopted in this work is presented in the next section. In the following two sections, the cuts to select deep inelastic scattering events, based on the scattered electron identified in the backward calorimeter SpaCal, and the cuts applied online, i.e. trigger and event classification, are given.

The final step of the event selection is then to define data sets which are later used for cross section determination: one for the analysis of the exclusive production of a J/ψ in the final state — exclusive in the sense that no particles are detected in addition to the J/ψ, the scattered electron, and possibly the dissociated proton — , one for the inclusive analysis of J/ψ production, and one consisting of $\psi(2S)$ candidate events.

In the final section of this chapter, the Monte Carlo generators used for acceptance calculations, the underlying models, and the available data sets are presented.

4.1 Selection of Data Taking Periods

In order to achieve precise measurements, special care must be taken that all relevant detector components are fully operational. The necessary selection of units of data taking (so-called *runs*) and the resulting luminosity are now presented.

4.1.1 Run Selection

During data taking, the slow control status (high voltage and readout) of all relevant detector components is logged approximately every 10 seconds in the H1 database. For all three years of data taking considered in this analysis, 1995 to 1997, only data have been used where the following detector components have been operational: the inner central drift chamber CJC 1, the central proportional chambers CIP/COP, the LAr calorimeter, the SpaCal calorimeter, all Time-of-flight devices, the luminosity system, and finally the central muon detector.

In addition, all runs have to be classified by the H1 data quality responsibles as "good" or "medium" quality, thus ensuring that the data acquisition and central trigger logic worked properly. Runs with a trigger setup deviating from the standard one are also excluded from the analysis, as well as runs taken very early during a luminosity fill (so-called trigger-phase 1).

Since the SpaCal calorimeter was only commissioned during the winter shutdown 1994/95, a dedicated run selection [142] was applied for data taken during 1995. For this run selection, the number of events collected by different triggers (one based on the inclusive electron trigger, one based on the total energy deposit in the electromagnetic SpaCal) is required to be, for each run, in the range expected for inclusive deep inelastic scattering. Furthermore, the average energy of scattered electrons in the SpaCal had to be compatible with the expectation. As a result of this run selection, only runs with a working SpaCal trigger and a reliable energy calibration enter the analysis. As an example of the stability achieved in 1995, the average energy of scattered electrons taken with the total energy trigger is shown in figure 4.1.

From the 1997 data, only those runs are accepted which have been continuously available at the time of writing; this corresponds to roughly two thirds of the full 1997 data[1].
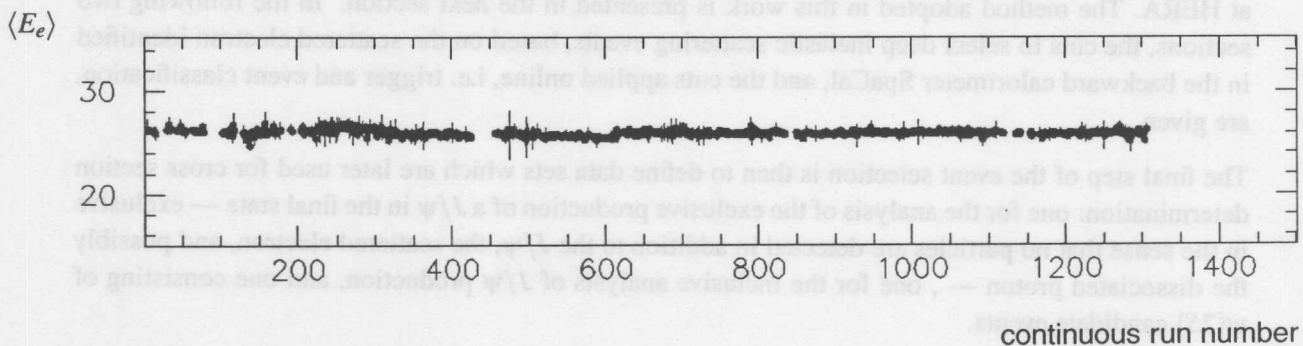
Figure 4.1: *Average energy $\langle E_e \rangle$ of electrons triggered by the total energy trigger in 1995.*

4.1.2 Luminosity Determination

The criteria described in section 4.1.1 have been applied to the three data taking periods, and the luminosity has been corrected accordingly. In addition, a certain fraction of luminosity originates not from the main bunches colliding at the nominal interaction point z_{nom}, but from early and late satellite

---

[1] Technically, data have been used which were reconstructed *online* during data taking.

		1995	1996	1997	Sum
$\int \mathcal{L}dt$ prod. by HERA	[nb^{-1}]	10698	15313	34085	60096
$\int \mathcal{L}dt$ delivered to H1	[nb^{-1}]	9804	14190	32390	56384
$\int \mathcal{L}dt$ H1 on tape	[nb^{-1}]	5999	9703	27300	43002
$\int \mathcal{L}dt$ H1 G+M runs	[nb^{-1}]	5381	9426	23723	38530
$\int \mathcal{L}dt$ after run/HV sel.	[nb^{-1}]	2402	7899	12045	22346
Sat. bunch correction	[%]	3.7 ± 2.0	7.2 ± 1.2	6.5 ± 2.0	
$\int \mathcal{L}dt$ final	[nb^{-1}]	2311 ± 53	7347 ± 132	11262 ± 315	20920 ± 501

Table 4.1: *Integrated luminosities 1995 to 1997.*

bunches, leading to collisions up- and downstream. To a large extent, these events are rejected by a cut on the z position of the event vertex z_{vtx}, and the loss in luminosity has to be corrected for, depending on where exactly this cut is placed. For this analysis, a cut $|z_{vtx} - z_{nom}| < 40$ cm was chosen.

For 1997, no final values for the satellite bunch corrections were available at the time of writing; a preliminary value of 6.5 ± 2.0 % was used [143]. Also the final offline corrections for the luminosity were not yet available, therefore the total error on the 1997 integrated luminosity is 2.8 % compared to 2.3 % and 1.8 % for 1995 and 1996, respectively.

The final integrated luminosity used amounts to 20920 ± 580 nb^{-1}. A breakdown of the contributions from different years is given in table 4.1.

4.2 Decay Lepton Identification

The identification of the J/ψ decay leptons can be divided into two parts: selection of tracks in the tracking devices in order to ensure a good *momentum and angular measurement*, and *identification* by corresponding lepton signatures in the LAr calorimeter and the Muon Detector. As the tracking reconstruction, the lepton identification is part of the H1 reconstruction software and described in detail elsewhere [144, 145, 146]; here only its main features are described.

4.2.1 Tracks

Track selection criteria are restricted to a minimum, since decay leptons from J/ψ mesons have typical momenta of 2 GeV, a regime where the tracker performance is best, and background from non ep interactions is generally negligible in the analyses discussed here. The cuts imposed are summarized in table 4.2 and will be explained briefly.

Only tracks reconstructed in the Central Tracking Detector (*central tracks*) are allowed as lepton candidates, since the performance of the Forward Tracking Devices varies with the data taking period under study and is difficult to describe in the detector simulation.

Furthermore, only tracks constrained to the primary event vertex are considered; it turned out that in addition to the worse resolution for tracks not fitted to the vertex, track multiplicities are badly described for these tracks. On top of that, tracks are required to start in the inner jet chamber CJC 1, and to have a minimal radial length of 12 cm.

Track selection

- at least 5 hits in CJC
- primary vertex fit
- $R_{start} < 40$ cm
- $R_{end} - R_{start} > 12$ cm

Table 4.2: *Track selection criteria for decay leptons.*

4.2.2   Identification of Muons

Muons with energy greater than about 1.2 GeV can reach the Central Muon Detector, and are identified by reconstructing tracks in the Muon Detector and linking them to tracks found in the inner tracking devices. For muon momenta above 0.8 GeV this method is complemented by the identification of muons as particles leaving the signature characteristic for minimum ionizing particles in the LAr calorimeter. Requiring either of these signatures, an identification efficiency of typically 80 % is achieved for muons with energy greater than 0.8 GeV.

Central Muon Detector

The identification of muons in the Central Muon Detector (CMD) is a two step procedure: "iron tracks" are reconstructed first, using only the information from the Muon Detector itself; these tracks are then linked to tracks reconstructed in the inner tracking devices.

The iron track reconstruction [16] uses the method of conformal mapping to find hit associations with a minimum of three wire hits and a minimum length of 15 cm. The track candidates are then described by combining parabolas for each region of approximately constant magnetic field and energy loss. Three dimensional tracks are obtained by adding the strip information. The pad information is used to resolve ambiguities in the case that no strips could be associated to a track.

For the linking between tracks found in the inner trackers and in the Muon Detector, only inner tracks that can geometrically reach the CMD are taken into account by imposing the condition

$$|\kappa| < \frac{0.003 \, \text{cm}^{-1}}{\sin \theta}, \tag{4.1}$$

where κ and θ denote the curvature and polar angle of the track measured in the inner tracking chambers. This translates into a cut on the transverse momentum

$$p_t > 1.16 \, \text{GeV} \cdot \sin \theta. \tag{4.2}$$

Furthermore, inner tracks and iron tracks have to match in polar angle:

$$|\theta - \theta_{CMD}| < 0.25 \, \text{rad} \tag{4.3}$$

and azimuthal angle:

$$-\frac{\pi}{2} < Q \cdot \sin(\phi_{CMD} - \phi) < 0.2, \tag{4.4}$$

where θ_{CMD} and ϕ_{CMD} are the angles defined by a straight line between the first measured point in the Muon Detector and the event vertex, and θ, ϕ and Q denote the angles and charge ($= \pm 1$) measured in the inner trackers. The second cut is asymmetric in order to take into account the curvature of the particle due to the magnetic field.

Inner tracks passing this preselection are extrapolated from the active volume of the tracker to the Muon Detector taking into account energy loss in between and propagating errors. The extrapolated track and the iron track are compared and their compatibility is tested by calculating a χ^2, which is then integrated to obtain a link probability $P(\chi^2)$ with values between 0 and 1. Only links with $P(\chi^2) > 10^{-4}$ are kept.

For the analyses presented here, a track is said to be identified in the Muon Detector if it is linked with a probability $P(\chi^2) > 10^{-3}$ to any iron track.

LAr Calorimeter

The muon identification in the LAr calorimeter starts from tracks found in the inner tracking chambers. These are extrapolated into the calorimeter as a helix. Around the extrapolated track two cylinders with radii $r_a = 15$ cm and $r_b = 30$ cm are defined (see figure 4.2 for illustration). These radii are chosen such that the inner cylinder contains all signals of the minimum ionizing muon, while the outer cylinder contains on average 90 % of the hadronic shower originating from pions. To suppress noise, only cells with an energy deposit above 10 MeV are taken into account.

For each muon candidate, four estimators discriminating muon from pion signatures in the LAr calorimeter are defined:

E_{EMC}: summed energy in the electromagnetic section of the LAr calorimeter in the inner cylinder;
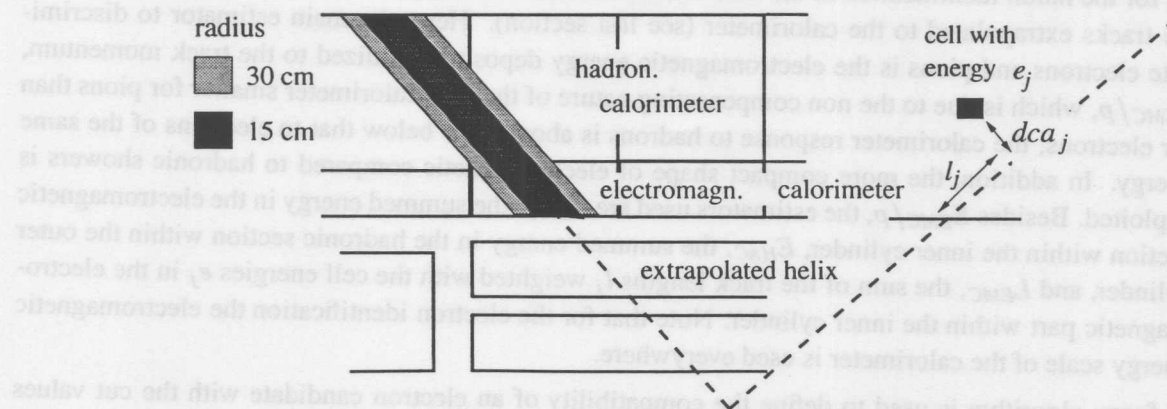
Figure 4.2: *Schematic illustration of the muon identification in the LAr calorimeter.*

Quantity	Lower Cut	Upper Cut
E_{EMC}	$\simeq 0.1\,\text{GeV}$	$\simeq 0.8\,\text{GeV}$
E_{tot}	$\simeq 0.4\,\text{GeV}$	$\simeq 2.4\,\text{GeV}$
L_{max}	$\simeq 80\,\text{cm}$	–
L_{HAC}	$\simeq 150\,\text{cm}$	–

Table 4.3: *Cuts for the identification of muons in the LAr calorimeter. The mean cut values for the central region are given.*

E_{tot}: summed energy in the electromagnetic and hadronic section in the outer cylinder;

L_{max}: maximum value for the "track length" l_j as defined in figure 4.2 in the inner cylinder;

L_{HAC}: sum of the "track length" l_j in the hadronic part of the calorimeter for the inner cylinder.

All energies used here are on the "final" scale, that is after dead material correction, topological noise suppression and reweighting of hadronic energy deposits to compensate for the different calorimeter response of electrons or photons and hadrons.

In order to be insensitive to changes in the calorimeter calibration and errors in the track reconstruction, the cuts applied on the above estimators as well as the radii r_a and r_b are in practice smeared by a technique adapted from fuzzy logic. The relative importance of the different quantities is taken into account. Since the energy deposited by a muon in the calorimeter strongly depends on its momentum p and polar angle θ, the cuts are chosen p and θ dependent. Typical cut values are given in table 4.3.

Depending on the compatibility of a muon candidate with the cut values, four *muon qualities* are defined: *good* ($Q_\mu = 3$), *medium* ($Q_\mu = 2$), *weak* ($Q_\mu = 1$) and *no* ($Q_\mu = 0$) muon. For $Q_\mu = 2$ and $Q_\mu = 3$, the probability to misidentify a pion as a muon is of the order of 5 % and $1 - 2$ %, respectively.

4.2.3   Identification of Electrons

As for the muon identification in the LAr calorimeter, the starting point of the electron identification are tracks extrapolated to the calorimeter (see last section). Here, the main estimator to discriminate electrons and pions is the electromagnetic energy deposit normalized to the track momentum, E_{EMC}/p, which is due to the non compensating nature of the LAr calorimeter smaller for pions than for electrons; the calorimeter response to hadrons is about 30 % below that to electrons of the same energy. In addition, the more compact shape of electromagnetic compared to hadronic showers is exploited. Besides E_{EMC}/p, the estimators used are E_{EMC}, the summed energy in the electromagnetic section within the inner cylinder, E_{HAC}, the summed energy in the hadronic section within the outer cylinder, and L_{EMC}, the sum of the track lengths l_j weighted with the cell energies e_j in the electromagnetic part within the inner cylinder. Note that for the electron identification the electromagnetic energy scale of the calorimeter is used everywhere.

A fuzzy algorithm is used to define the compatibility of an electron candidate with the cut values given in table 4.4; note that the cuts for the electron identification do not depend on the momentum or polar angle of the electron candidate measured in the drift chambers, as was the case for the muon

Quantity	Lower Cut	Upper Cut
E_{EMC}/p	0.7	1.8
E_{EMC}	0.75 GeV	–
E_{HAC}	–	0.3 GeV
L_{EMC}	8 GeV cm	20 GeV cm

Table 4.4: *Cuts for the identification of electrons in the LAr calorimeter.*

identification. Again, four *qualities* are defined: *good* ($Q_e = 3$), *medium* ($Q_e = 2$), *weak* ($Q_e = 1$) and *no* ($Q_e = 0$) electron; the probability to misidentify a pion as an electron is of the order of 5 % for $Q_e = 2$ and $1 - 2$ % for $Q_e = 3$, comparable to the purity of the muon identification in the LAr calorimeter.

4.3 Selection of Deep Inelastic Scattering Events

The considerations for the selection of deep inelastic scattering events — summarized in table 4.5 — are somewhat different for the analysis presented here compared to inclusive measurements like the structure function F_2 [40]. While there the focus is on a minimization of systematic uncertainties, little kinematical bias over a large range in x and Q^2, and efficient background rejection, the cuts imposed here can be much looser: systematic uncertainties of a few percent are well acceptable given total systematic errors of up to 20 %. The kinematics are much better controlled due to the very well measured hadronic final state, and background from e.g. non-*ep* interactions and photoproduction is negligible. The selection *must* even be adopted to the special needs of this analysis, in order to minimize statistical errors for small cross section processes.

Starting point of the selection are clusters in the electromagnetic section of the SpaCal calorimeter, found by a clustering algorithm that assigns each cell to a local energy maximum. The cluster energy E is given by the sum of the single cell energies E_i inside the cluster. The shower position is reconstructed by determining the centre of gravity $\vec{r}_{cog}$ of the cluster from

$$\vec{r}_{cog} = \frac{\sum w(E_i)\vec{r}_i}{\sum w(E_i)}, \tag{4.5}$$

where the sum runs over all cells i in the cluster, and $\vec{r}_i$ denotes the position of the i-th cell. In this analysis, the special shape of the cells in the SpaCal insert is taken into account according to [147]. For the weighting function $w(E_i)$ the form $w(E_i) = \sqrt{E_i}$ (square-root weighting) is chosen.

As seen in section 3.1 and figure 3.4, the energy of the scattered electron E_e is — due to event kinematics — in general well above 15 GeV. Misidentified hadrons become only important at lower electron energies. By imposing a cut $E_e > 12$ GeV, the full kinematic range is preserved while reducing the background from hadrons.

The lateral width of a shower, estimated by the energy-weighted cluster radius R_{cl}, can be used to discriminate between electromagnetic and broader hadronic showers. It is calculated from

$$R_{cl} = \frac{1}{E} \sum E_i |\vec{r}_i - \vec{r}_{cog}|, \tag{4.6}$$

DIS selection

- Most energetic cluster in electromagnetic SpaCal
- $E_e > 12\,\text{GeV}$
- $R_{cl} < 3.5\,\text{cm}$
- $R_{cog} > 8.1\,\text{cm}$
- $E_{VL} < 2\,\text{GeV}$

- $\sum(E - p_z) > 45\,\text{GeV}$

Table 4.5: *DIS selection criteria.*

where the sum extends over all cells i attributed to a cluster. R_{cl} is required to be smaller than 3.5 cm.

To ensure full containment of the electromagnetic shower, fiducial cuts are applied: the distance of the cluster's centre of gravity to the beam in the radial direction, R_{cog}, has to fulfil $R_{cog} > 8.1$ cm, corresponding to the outer radius of the SpaCal insert module. This value is roughly equivalent to a polar angle θ_e of 177.1° for electrons originating from the nominal interaction point. To reject remaining events with energy leakage into the beampipe, the summed energy in the four cells of the veto layer E_{VL} is required to be below 2 GeV.

These four cuts are illustrated in figure 4.3 using candidate events for exclusive J/ψ production (section 4.5.1) and the DIFFVM diffractive J/ψ Monte Carlo for comparison; note that the data contain the full mass spectrum from 2 GeV upwards including non-resonant lepton pair production events, and therefore need not necessarily agree in every detail with the Monte Carlo. Nevertheless, except in the case of the radial cluster position R_{cog}, both in data and Monte Carlo only tails of distributions are cut away. To describe the cluster radius R_{cl} in the simulation, it has been multiplied by a factor 1.1 in the Monte Carlo; this correction is necessary because of the inappropriate description of the shower development in the Monte Carlo simulation [9].

No explicit cut has been applied on the lower limit of the scattering angle of the DIS electron θ_e; since however only electrons in the SpaCal are used, this corresonds to an effective cut $\theta_e \gtrsim 155°$.

Note also that no track associated to the scattered electron in the Backward Drift Chamber is required. The analyses presented here are not affected by non-DIS background, and the spatial resolution of the SpaCal alone (3.4 mm, [9]) is sufficient. However, if an associated BDC track is found within 3 cm distance from the SpaCal cluster centre of gravity extrapolated back to the BDC plane, its information on the electron's impact position and scattering angle is used for the reconstruction of the kinematics. The fraction of events in the final event samples having a BDC reconstructed electron is above 90 % and well reproduced by the Monte Carlo simulations.

Finally, the difference between the energy and the z-component of the momentum summed over all particles, denoted as $\sum(E - p_z)$, is required to be greater than 45 GeV. It is calculated using tracks in the central tracker and energy deposited in cells in the LAr and SpaCal calorimeter as far as they are not located "behind" tracks. For fully contained deep inelastic scattering events, $\sum(E - p_z)$ equals twice the incoming electron energy, i.e. 55 GeV, while losses especially in the backward direction as

well as initial state radiation (ISR) lower its value. To minimize the corrections arising from ISR, a high cut on $\sum(E - p_z)$ is desirable.

4.4 Trigger and Event Classification

The aim of the trigger selection is to define an (almost) stable set of triggers with at the same time high efficiency. Further criteria are the possibility to determine trigger efficiencies from the data — therefore requiring that independent triggers to the chosen set exist —, and a preference for triggers independent of the hadronic final state in order to avoid as far as possible any bias in its measurement. These considerations led to the selection of SpaCal based triggers for the scattered electron including weak track requirements.

For a short description of the trigger elements forming the L1 triggers, see section 2.3.6.

The full definitions of the triggers used are given in table 4.6. For data taken in early 1995 s0 is used[2], a minimum-bias inclusive electron trigger Spcle_IET>1 including varying veto conditions of the

----

[2]up to run 122397
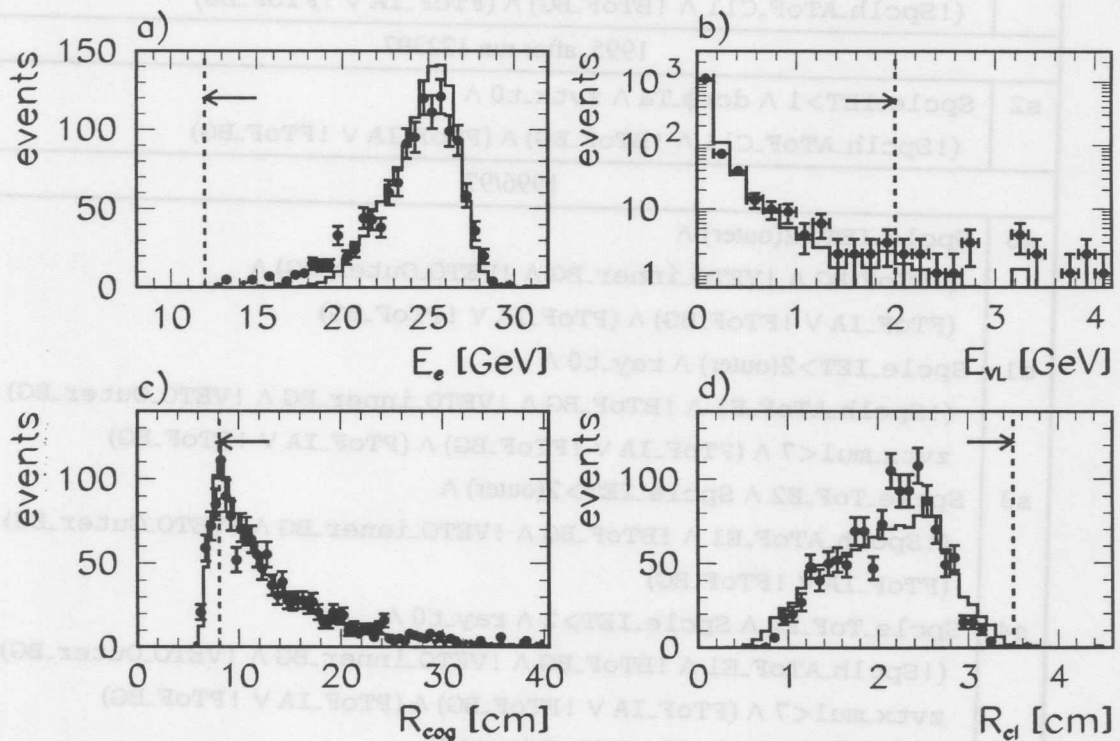
Figure 4.3: *Cuts to select DIS events; a) electron energy E_e, b) energy in the veto layer E_{VL}, c) radial distance from the cluster to the beam axis R_{cog}, and d) energy-weighted cluster radius R_{cl}. The selected area is marked by arrows. The points are candidates for exclusive J/ψ production (section 4.5.1, table 4.7), the histograms are DIFFVM Monte Carlo events normalized to the number of events in the data. For each figure, all cuts except the one shown have been applied.*

Time-of-Flight system. The energy threshold of this trigger is 6 GeV in 1995. For the remainder of 1995 s2 is selected that included additional track requirements: dcrφ_Ta and zvtx_t0 first, later on ray_t0 only.

For data taken in 1996 and 1997, a common set of five triggers is used. It consists of three triggers based on a total energy deposit greater than 12 GeV in the electromagnetic SpaCal (Spcle_ToF_E2): one for the outer SpaCal region, one covering the entire SpaCal, which includes an additional track requirement ray_t0, and one for the inner SpaCal. The other two triggers are based on the inclusive electron trigger Spcle_IET>2 in the outer SpaCal region, with a threshold of 6 GeV in 1996 and 1997; one of these includes again the ray_t0 track trigger element. All triggers mentioned include additional veto conditions against non *ep* background.

With respect to the event classification performed during the L5 reconstruction, all selection criteria imposed in this thesis are customized in such a way that the cuts applied are harder than those performed in the event classification[3]. Using the Monte Carlo simulation it has been verified that the

---

[3]For completeness it is mentioned that the so-called FPACK classes actually used are an 'OR' of classes 17, 18, 24.

1995, up to run 122397	
s0	Spcle_IET>1 ∧ (!Spclh_AToF_Cl1 ∧ !BToF_BG) ∧ (FToF_IA ∨ !FToF_BG)
1995, after run 122397	
s2	Spcle_IET>1 ∧ dcrφ_Ta ∧ zvtx_t0 ∧ (!Spclh_AToF_Cl1 ∧ !BToF_BG) ∧ (FToF_IA ∨ !FToF_BG)
1996/97	
s0	Spcle_IET>2(outer) ∧ (!BToF_BG ∧ !VETO_inner_BG ∧ !VETO_Outer_BG) ∧ (FToF_IA ∨ !FToF_BG) ∧ (PToF_IA ∨ !PToF_BG)
s1	Spcle_IET>2(outer) ∧ ray_t0 ∧ (!Spclh_AToF_E1 ∧ !BToF_BG ∧ !VETO_inner_BG ∧ !VETO_Outer_BG) ∧ zvtx_mul<7 ∧ (FToF_IA ∨ !FToF_BG) ∧ (PToF_IA ∨ !PToF_BG)
s3	Spcle_ToF_E2 ∧ Spcle_IET>2(outer) ∧ (!Spclh_AToF_E1 ∧ !BToF_BG ∧ !VETO_inner_BG ∧ !VETO_Outer_BG) ∧ (FToF_IA ∨ !FToF_BG)
s4	Spcle_ToF_E2 ∧ Spcle_IET>2 ∧ ray_t0 ∧ (!Spclh_AToF_E1 ∧ !BToF_BG ∧ !VETO_inner_BG ∧ !VETO_Outer_BG) ∧ zvtx_mul<7 ∧ (FToF_IA ∨ !FToF_BG) ∧ (PToF_IA ∨ !PToF_BG)
s7	Spcle_ToF_E2 ∧ Spcle_IET>2(inner) ∧ (!Spclh_AToF_E1 ∧ !BToF_BG ∧ !VETO_inner_BG ∧ !VETO_Outer_BG) ∧ zvtx_mul<7 ∧ (FToF_IA ∨ !FToF_BG) ∧ (PToF_IA ∨ !PToF_BG)

Table 4.6: *Full definitions of triggers used. For the (varying) veto conditions, typical settings are given. The symbols ∧, ∨ and ! are used for the logical operators 'AND', 'OR' and 'NOT'.*

event classification is within errors 100 % efficient for events that pass all analysis cuts.

4.5 Definition of Data Sets

In the previous sections, all the ingredients for the selection of Charmonium events in deep inelastic scattering have been presented. In the following, the data sets used for the analysis will be defined.

4.5.1 Exclusive Sample

The exclusive selection — summarized in table 4.7 — comprises events without activity in the H1 detector except the J/ψ decay leptons, the scattered electron, and possibly the dissociated proton. For this purpose, events are required to have exactly two tracks (excluding the scattered electron) with opposite charge fitted to the primary event vertex; these have to fulfil the track selection criteria of section 4.2.1, and to lie in the region of high acceptance of the central tracker, $20° < \theta < 160°$. The invariant mass of the two tracks has to exceed 2 GeV. For the muon channel, at least one of the tracks must be validated either by a high quality muon signature in the LAr calorimeter or by a linked track in the instrumented iron; for the decay into electrons, both tracks are required to be identified as electrons in the LAr calorimeter, with one being classified as "good" (see section 4.2).

In addition, the selection of DIS events based on the scattered electron (section 4.3), the run selection (section 4.1.1) and the trigger criteria (section 4.4) must be fulfilled. The invariant mass spectrum for the two tracks of events thus selected is shown in figure 4.4 separately for the $\mu^+\mu^-$ and the e^+e^- channel. No event is assigned to both channels. The width of the signals is completely determined by the experimental resolution, since the natural width of the J/ψ meson is only a few keV.

Note that there is no physics process that produces a comparable number of like-sign exclusive lepton pairs as in the unlike-sign case. The mass spectrum of like-sign lepton pairs with otherwise the same selection criteria is shown for comparison in figure 4.4.

A typical event is shown in figure 4.5.

In order to be able to disentangle the different diffractive production mechanisms, namely elastic and with proton dissociation, the sample is divided into two non overlapping data sets. Depending on the presence or absence of activity in very forward detector components, elastic or proton dissociation events can be enriched. The detectors used here are the LAr calorimeter below $\theta = 10°$, the pre-toroid layers of the Forward Muon Detector (FMD), and the Proton Remnant Tagger (PRT); they are partly redundant, but mostly tag different regions in the mass M_Y of the diffracted system (see figure 5.9). The cuts on the forward detectors are designed such that accidental tags of elastic events are small. By requiring either no activity in any of the three forward detectors, or activity in at least one of them, the data sets *forward untagged* and *forward tagged* are defined. The thresholds for forward tagging are at least 1 GeV summed energy in the forward LAr calorimeter, at least two hit pairs in the pre-toroid sections of the FMD, or at least one hit in the layers 0, 1, 2 or 3 of the PRT. The remaining PRT layers are either affected by synchroton radiation or badly simulated in the Monte Carlo [149, 148]; in the FMD, one hit pair is compatible with noise.

In order to ensure a consistent description of the forward detectors in the detector simulation, they had partly to be excluded from consideration for specific run ranges. For data taken in early 1997 corresponding to an integrated luminosity of $1.7\,\text{pb}^{-1}$ the Forward Muon Detector could not be used
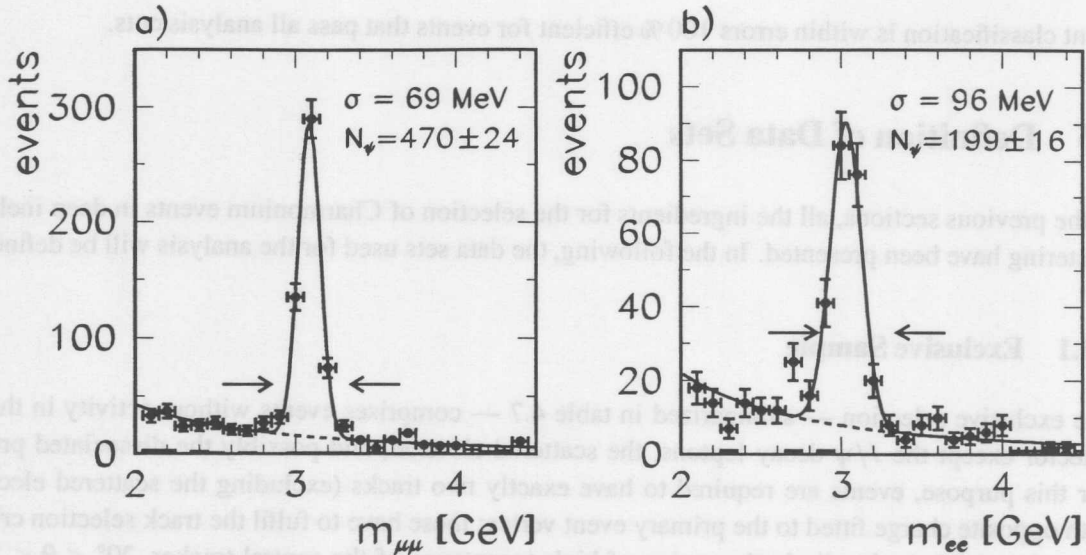
Figure 4.4: *Mass spectra of events in the exclusive J/ψ selection; a) $\mu^+\mu^-$ pairs, b) e^+e^- pairs. The curves are fits of a Gaussian plus a power law m_{ll}^{-n} to describe the non-resonant background. The arrows denote the mass interval defining the signal region. In addition, the mass spectra of a) $\mu^-\mu^-$, $\mu^+\mu^+$ and b) e^-e^-, e^+e^+ pairs are shown as black histograms. N_ψ is the number of J/ψ events according to the fit.*
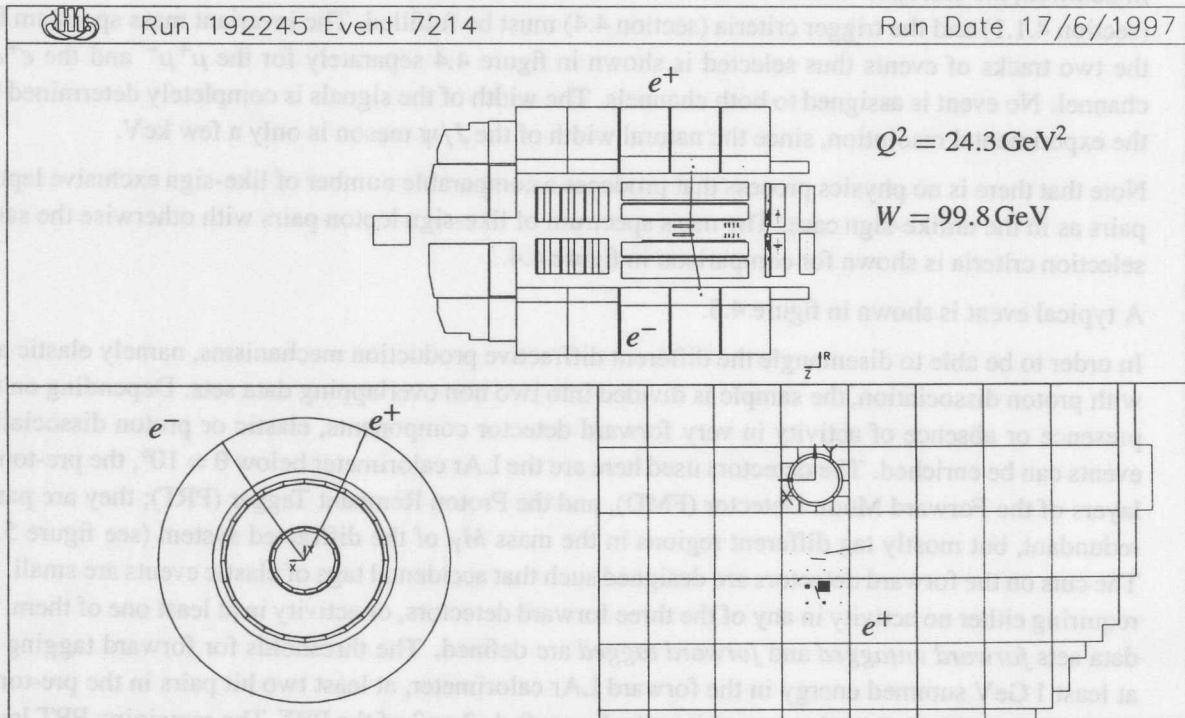
Figure 4.5: *A candidate event for exclusive J/ψ production in the decay channel $J/\psi \rightarrow e^+e^-$, shown in the side view (upper plot), radial view of the central tracker (bottom left), and radial view of the electromagnetic SpaCal (bottom right). The invariant mass of the e^+e^- pair is $3.08\,\text{GeV}$, the e^+ and e^- momenta as measured in the central tracking system are $2.76\,\text{GeV}$ and $2.97\,\text{GeV}$ respectively. The scattered e^+ has the energy $E_e = 24.6\,\text{GeV}$.*

because information from different events was mixed. For several run ranges the Proton Remnant Tagger was unusable due to either reduced high voltage or several channels being switched off; another $1.7\,\mathrm{pb}^{-1}$ of luminosity are affected by this. The number of hits in the PRT and the number of hit pairs in the FMD have been artificially set to 0 for the data in all these runs.

Some characteristics of the selected J/ψ candidate events are shown in figure 4.6. For these plots a mass window of $250\,\mathrm{MeV}$ around the nominal J/ψ mass has been chosen in order to select a rather pure event sample; the non-resonant contribution amounts to approximately 12 %. In total 784 events are selected.

The average energy of the scattered electron is $24.5\,\mathrm{GeV}$ (figure 4.6a)); E_e is always larger than $15\,\mathrm{GeV}$, as expected from the kinematics of the process (see section 3.1). The difference between the energy and the z-component of the momentum summed over all particles ($\sum(E - p_z)$, figure 4.6b)) peaks nicely at the expected value of $55\,\mathrm{GeV}$, proving the good knowledge of the absolute energy

Exlusive J/ψ selection		
• ≥ 1 muon with $Q_\mu = 3$ identified in LAr		or
≥ 1 muon identified in Muon Detector		or
2 electrons (one with $Q_e = 3$, one with $Q_e > 0$)		
• Run selection (section 4.1.1)		
Tracks		
• exactly 2 tracks in CTD according to table 4.2 with invariant mass $M > 2\,\mathrm{GeV}$		
• $20° < \theta < 160°$		
• opposite charge, $p_t > 0.1\,\mathrm{GeV}$		
• $\|z_{vtx} - z_{nom}\| < 40\,\mathrm{cm}$		
• possibly one additional track associated to scattered electron		
DIS selection		
• Electron in SpaCal according to table 4.5		
• Trigger (section 4.4)		
• $\sum(E - p_z) > 45\,\mathrm{GeV}$		
forward untagged		**forward tagged**
$E_{Lar}^{10°} < 1\,\mathrm{GeV}$	and	$E_{Lar}^{10°} > 1\,\mathrm{GeV}$ or
$N_{PRT} = 0$	and	$N_{PRT} > 0$ or
$N_{FMD} < 2$		$N_{FMD} \geq 2$

Table 4.7: *Selection of elastic and proton dissociative J/ψ candidate events.*

scale of the SpaCal. A Gaussian fit to the peak region results in a mean of 54.9 GeV and a width of 1.8 GeV. Towards smaller values of $\Sigma(E - p_z)$, the tail originating from events with initial state radiation is visible. The Q^2 distribution (figure 4.6c)) is steeply falling towards larger Q^2, and exhibits large acceptance losses for $Q^2 \lesssim 2\,\text{GeV}^2$ (first bin) due to the requirements on the scattered electron to be well contained in the H1 main detector. Also the W spectrum (figure 4.6d)) is falling, with acceptance losses in the small and large W regime, caused mainly by the angular cuts on the decay leptons.

The ratio of Q^2 measured with the double angle method Q^2_{DA} to the electron measurement Q^2_e is shown in figure 4.6e); it is sharply peaked at 1.01 with a width of 5 %, another confirmation of the SpaCal energy calibration. Finally, the momenta of the J/ψ decay leptons are displayed in figure 4.6f), with a mean of 2.4 GeV, and in a region where the central tracker has excellent momentum resolution.
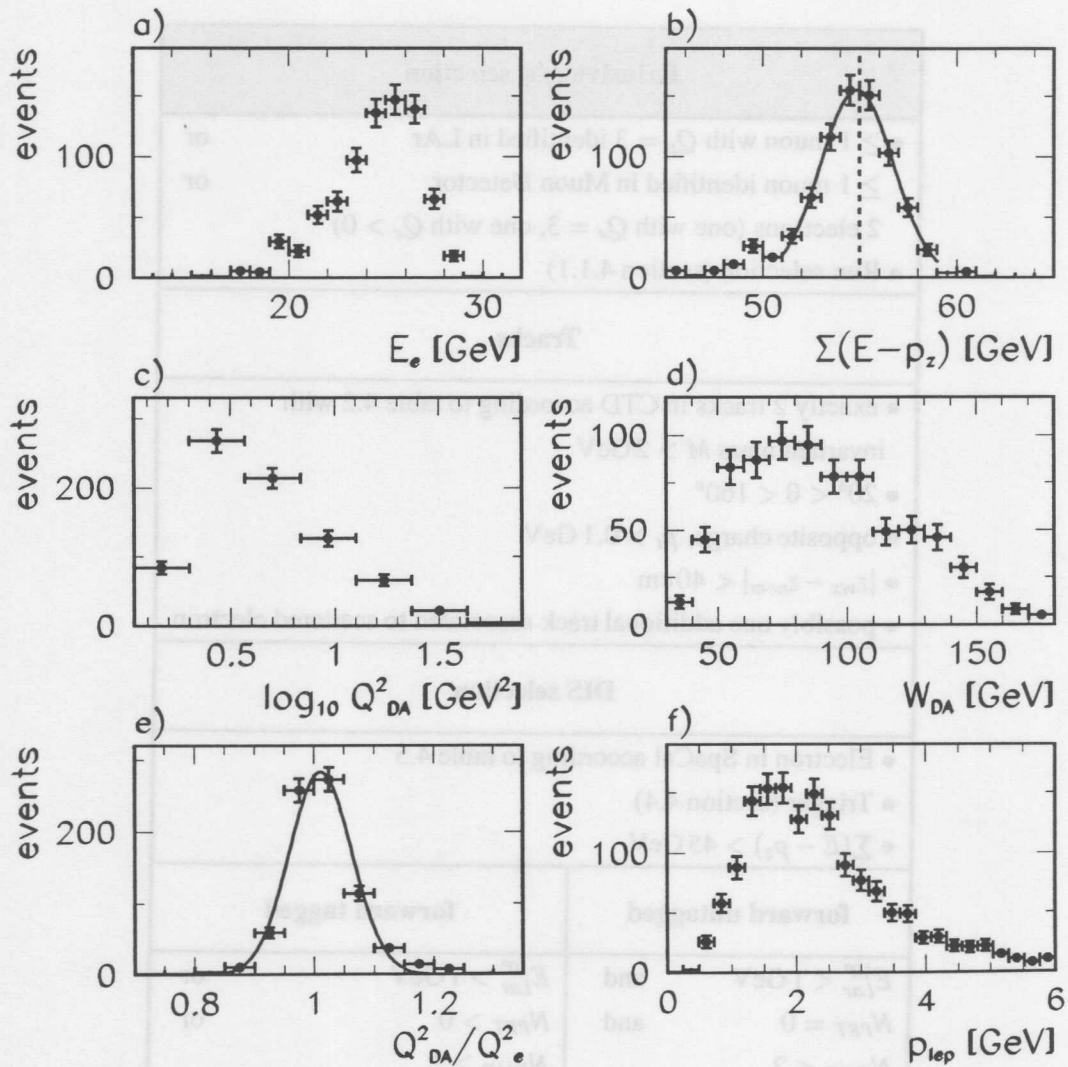
Figure 4.6: *Some properties of exclusive J/ψ candidate events with $|M_{ll} - M_\psi| < 250\,\text{MeV}$.*
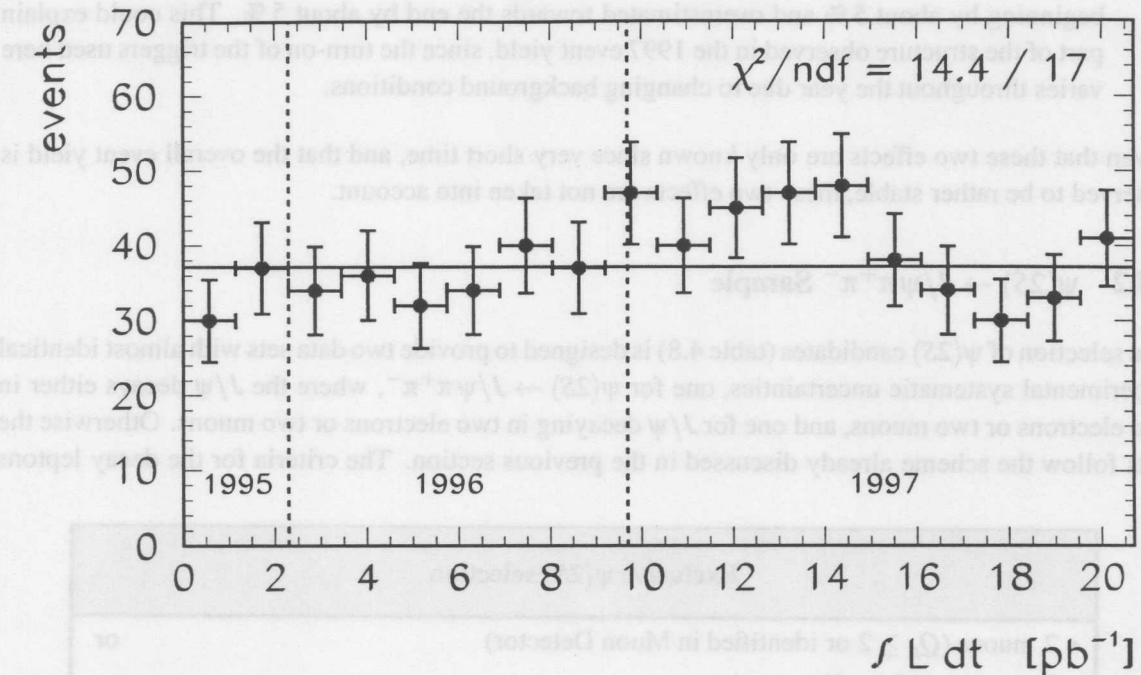
Figure 4.7: *Yield of exclusive J/ψ candidate events as a function of the accumulated luminosity.*

The stability of the yield of events has been checked by plotting the number of events as a function of the accumulated luminosity (figure 4.7). Here the kinematic region in W and Q^2 has been restricted to the one that is finally used for cross section calculation (section 5.1.2):

$$2 < Q^2 < 80\,\text{GeV}^2 \quad \text{and} \tag{4.7}$$
$$40 < W < 160\,\text{GeV}. \tag{4.8}$$

In general, the event yield — in average 37.1 ± 1.4 events per luminosity interval — is stable within statistical fluctuations ($\chi^2/ndf = 14.4/17$). The average number of events per bin for the three data taking periods 1995, 1996 and 1997 is 33.1 ± 4.1, 36.6 ± 2.3 and 38.6 ± 2.1 respectively, with values for χ^2/ndf of 0.73, 0.61 and 1.06. The relatively low event yield in 1995 can be explained by the trigger inefficiency of around 10 % in 1995 due to track trigger requirements (see section 5.1.3). Since for the 1997 data only preliminary values with global (not time dependent) corrections for the luminosity have been available, fluctuations with a consequently worse χ^2 than in previous years are observed; nevertheless the absolute normalization of all three data sets is compatible.

Very recently two systematic effects concerning the H1 luminosity measurement mainly in 1997 have been discovered [151]:

- Due to a difference in the counting of events in the online luminosity measurement and the events accepted by the central trigger logic, the 1997 luminosity used here is estimated to be 2.9 % too low. Taking this into account would lead to a better agreement in the number of events per bin averaged over the whole year.

- A so far unknown time dependence of the luminosity measurement during each HERA luminosity fill was discovered. For a typical luminosity fill, the luminosity is underestimated in the

beginning by about 5 % and overestimated towards the end by about 5 %. This could explain part of the structure observed in the 1997 event yield, since the turn-on of the triggers used here varies throughout the year due to changing background conditions.

Given that these two effects are only known since very short time, and that the overall event yield is observed to be rather stable, these two effects are not taken into account.

4.5.2 $\psi(2S) \to J/\psi\pi^+\pi^-$ Sample

The selection of $\psi(2S)$ candidates (table 4.8) is designed to provide two data sets with almost identical experimental systematic uncertainties, one for $\psi(2S) \to J/\psi\pi^+\pi^-$, where the J/ψ decays either in two electrons or two muons, and one for J/ψ decaying in two electrons or two muons. Otherwise the cuts follow the scheme already discussed in the previous section. The criteria for the decay leptons

Exclusive $\psi(2S)$ selection	
• 2 muons ($Q_\mu \geq 2$ or identified in Muon Detector)	or
2 electrons ($Q_e = 3$)	
• $p_t > 0.8\,\mathrm{GeV}$ for both leptons, oppositely charged	
• Run selection (section 4.1.1)	

Tracks	
• exactly 4 tracks with charges $+ - + -$	
• $|z_{vtx} - z_{nom}| < 40\,\mathrm{cm}$	
• possibly one additional track associated to scattered electron	

DIS selection	
• Electron in SpaCal according to table 4.5	
• Trigger (section 4.4)	
• $\sum(E - p_z) > 45\,\mathrm{GeV}$	

loose selection	tight selection
all 4 tracks within $10° < \theta < 162°$	all 4 tracks within $20° < \theta < 160°$ and track selection (table 4.2) for all 4 tracks and $p_t > 120\,\mathrm{MeV}$ for $\pi^+\pi^-$

J/ψ reference selection	
• all cuts as for $\psi(2S)$ except for the $\pi^+\pi^-$	

Table 4.8: *Selection of $\psi(2S)$ candidate events.*

are slightly tightened with respect to the exclusive selection, especially their transverse momenta are required to exceed 800 MeV. The two data sets will allow to determine the cross section ratio of $\psi(2S)$ to J/ψ with a minimal systematic error.

In the case of $\psi(2S)$, exactly four tracks must be reconstructed in the Central Tracking Detector, of which two have to be identified as electrons or muons, while for the J/ψ exactly two tracks identified as electrons or muons with the same selection criteria as for $\psi(2S)$ are required.

Two cut scenarios are defined: a data sample with loose cuts especially on the $\pi^+\pi^-$ pair which maximises the available statistics, and another one with tighter cuts to be in a region of well understood tracker performance. All cuts are summarized in table 4.8, and a $\psi(2S)$ candidate event is shown in figure 4.8.

4.5.3 Inclusive Sample

The inclusive J/ψ selection — summarized in table 4.9 — is designed to provide a clean sample of J/ψ candidate events irrespective of the production mechanism, i.e. the same criteria are used to select exclusive production and J/ψ procuction where much hadronic activity is present in the event. For this purpose, the conditions required for the decay leptons are tightened with respect to the exlusive selection. In addition to a cut on the transverse momentum of the leptons, $p_t > 0.8$ GeV, both leptons have either to be identified as "good" electrons in the LAr calorimeter, or by a muon signature in the
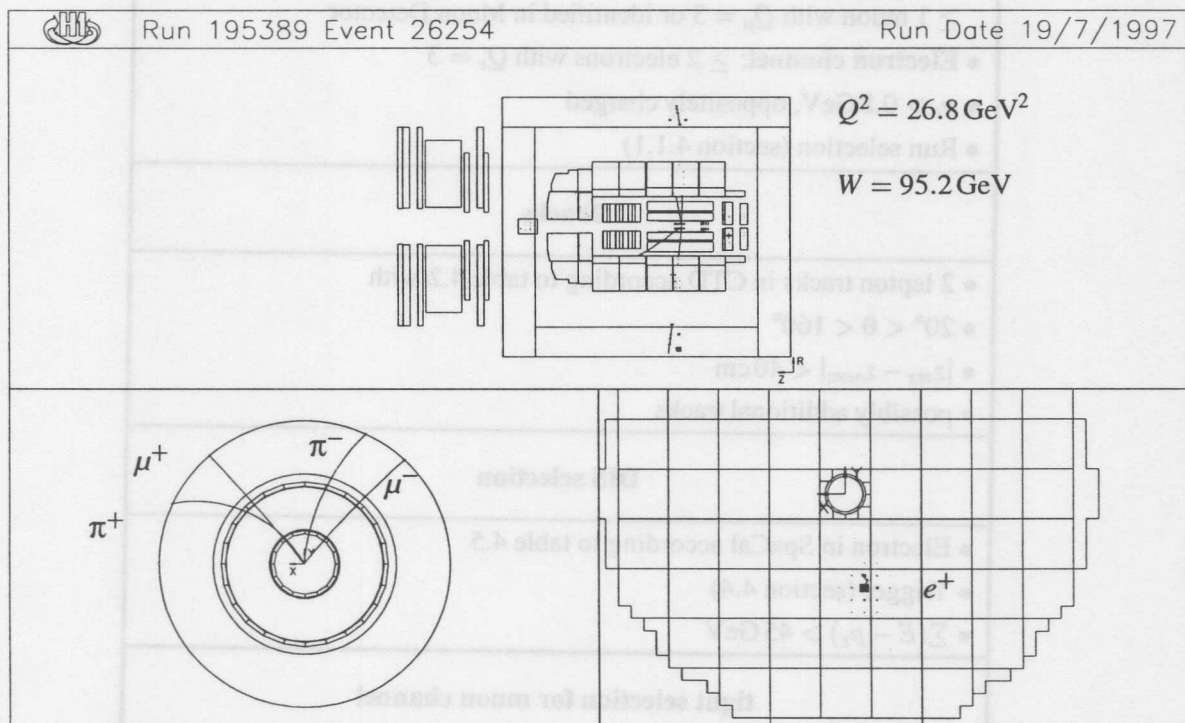
Figure 4.8: *A candidate event for $\psi(2S)$ production in the decay channel $\psi(2S) \to J/\psi\,\pi^+\pi^-$, $J/\psi \to \mu^+\mu^-$. The $\mu^+\mu^-$ invariant mass is 3.21 GeV, the mass difference between the four-prong mass and the $\mu^+\mu^-$ mass is $\Delta m = 0.57$ GeV, and the particle momenta are 3.53 GeV (μ^+), 1.85 GeV (μ^-), 0.41 GeV (π^+) and 0.43 GeV (π^-). The energy of the scattered e^+ is $E_e = 25.4$ GeV.*

LAr calorimeter or a linked track in the Central Muon Detector. The remaining criteria — regarding the selection of DIS events, the run selection and the trigger criteria — are identical to the exclusive J/ψ selection.

To provide the purest possible data sample — for example at small z, where charged particle multiplicities and the background level are high — an additional, even tighter selection for the muon decay channel is defined.

Events in the inclusive selection are forced to have exactly one J/ψ candidate; this is accomplished by selecting — in the case that more than two unlike-signed muons or electrons are found — one J/ψ candidate with the following priorities, and rejecting remaining candidates:

- Muon pairs are preferred to electron pairs.

- Muons/electrons are sorted by p_t, and the muon/electron with the highest p_t is combined with the unlike-signed muon/electron that has the next highest p_t.

A typical inelastic event in the J/ψ mass region that passes the inclusive selection is shown in figure 4.9.

Inclusive J/ψ selection
• **Muon channel**: ≥ 2 muons ($Q_\mu \geq 2$ or identified in Muon Detector), ≥ 1 muon with $Q_\mu = 3$ or identified in Muon Detector   • **Electron channel**: ≥ 2 electrons with $Q_e = 3$ • $p_t > 0.8\,\mathrm{GeV}$, oppositely charged   • Run selection (section 4.1.1)
Tracks
• 2 lepton tracks in CTD according to table 4.2 with   • $20° < \theta < 160°$ • $|z_{vtx} - z_{nom}| < 40\,\mathrm{cm}$ • possibly additional tracks
DIS selection
• Electron in SpaCal according to table 4.5   • Trigger (section 4.4)   • $\sum(E - p_z) > 45\,\mathrm{GeV}$
tight selection for muon channel
• Muons identified in LAr: use only $Q_\mu = 3$ • in Muon Detector: at least 9 of 16 wires hit for $\theta < 30°$ and $\theta > 130°$

Table 4.9: *Selection of inclusive J/ψ candidate events.*
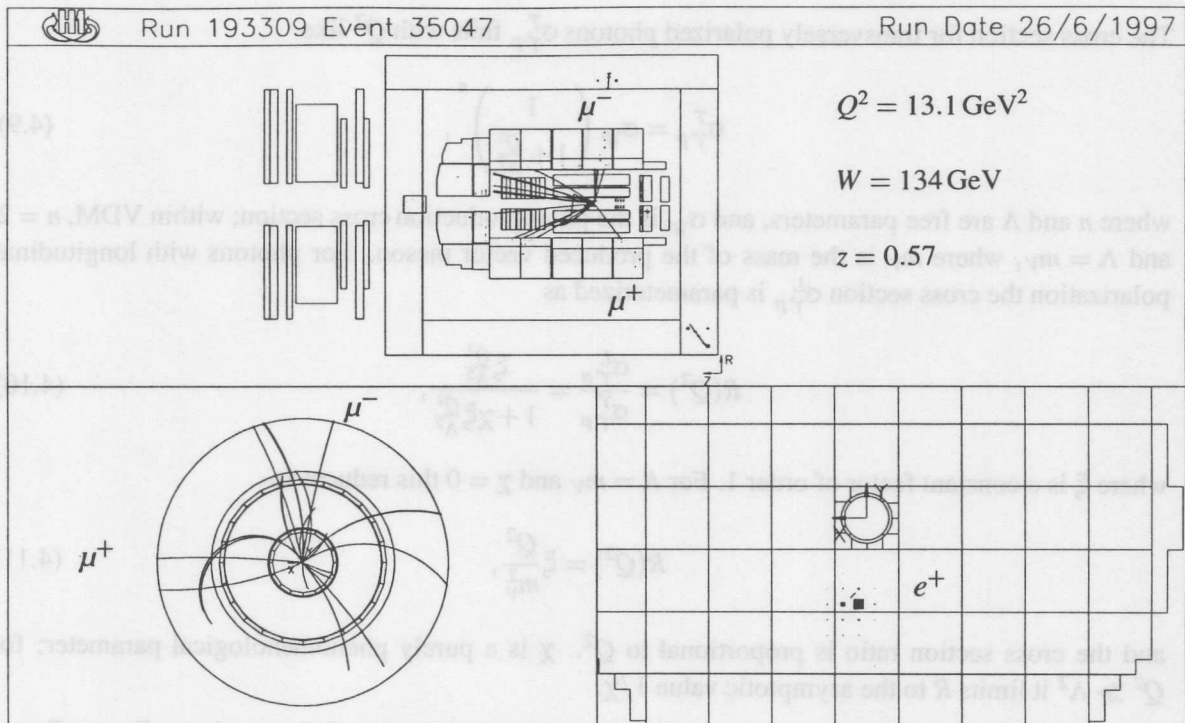
Figure 4.9: *A candidate event for inelastic J/ψ production in the decay channel $J/\psi \to \mu^+\mu^-$. The invariant mass of the $\mu^+\mu^-$ pair is 3.13 GeV, the muons have momenta of 2.50 GeV (μ^+) and 2.01 GeV (μ^-) respectively. The scattered electron's energy is $E_e = 21.6$ GeV.*

4.6 Monte Carlo Generators and Data Sets

Four Monte Carlo generators have been used: DIFFVM for the simulation of elastic and proton dissociative J/ψ and $\psi(2S)$ production, HITVM, simulating high $|t|$ J/ψ production with proton dissociation, EPJPSI for J/ψ production within the Colour Singlet Model, and LPAIR, which simulates QED lepton pair production, for studies of non-resonant background to Charmonium production. In the following sections the underlying physics will be outlined and the data sets used will be summarized.

4.6.1 DIFFVM

DIFFVM [150] is a Monte Carlo generator originally written to simulate diffractive vector meson production in ep scattering at HERA based on Regge theory, the Vector Meson Dominance Model VDM (see section 3.2.1), and helicity conservation in the s-channel. The elastic production $ep \to eVp$ of a vector meson V and the process $ep \to eVX$ where the proton diffractively dissociates can be simulated. Many parameters can be adjusted freely, therefore DIFFVM can be viewed as a largely model independent tool describing diffractive vector meson production which uses the basic ideas and terminology of Regge theory.

The emission of the photon from the incoming electron is treated within the equivalent photon approximation. Emission of additional photons from the initial or final state electron is not implemented. The transition to the virtual vector meson is modelled according to VDM as follows.

The cross section for transversely polarized photons $\sigma^T_{\gamma^* p}$ falls with Q^2 like

$$\sigma^T_{\gamma^* p} = \sigma_{\gamma p} \left(\frac{1}{1 + \frac{Q^2}{\Lambda^2}} \right)^n , \tag{4.9}$$

where n and Λ are free parameters, and $\sigma_{\gamma p}$ is the photoproduction cross section; within VDM, $n = 2$ and $\Lambda = m_V$, where m_V is the mass of the produced vector meson. For photons with longitudinal polarization the cross section $\sigma^L_{\gamma^* p}$ is parameterized as

$$R(Q^2) = \frac{\sigma^L_{\gamma^* p}}{\sigma^T_{\gamma^* p}} = \frac{\xi \frac{Q^2}{\Lambda^2}}{1 + \chi \xi \frac{Q^2}{\Lambda^2}}, \tag{4.10}$$

where ξ is a constant factor of order 1. For $\Lambda = m_V$ and $\chi = 0$ this reduces to

$$R(Q^2) = \xi \frac{Q^2}{m_V^2}, \tag{4.11}$$

and the cross section ratio is proportional to Q^2. χ is a purely phenomenological parameter; for $Q^2 \gg \Lambda^2$ it limits R to the asymptotic value $1/\chi$.

The dependence of the cross section on W and t is parameterized as follows. According to Regge theory,

$$\frac{d\sigma}{dt} = \frac{d\sigma}{dt}\bigg|_{t=0, W=W_0} \cdot e^{b|t|} \cdot \left(\frac{W}{W_0} \right)^{4\epsilon} \tag{4.12}$$

with

$$|b(W)| = |b(W_0)| + 2\alpha' \ln \left(\frac{W^2}{W_0^2} \right). \tag{4.13}$$

The slope parameter b at some specific value of $W = W_0$, the photoproduction cross section $\sigma_{\gamma p}$ at $W = W_0$, as well as ϵ, the intercept of the pomeron trajectory minus one, and its slope α', are adjustable parameters within DIFFVM. In Regge theory, the values $\epsilon \simeq 0.08$ and $\alpha' \simeq 0.25\,\mathrm{GeV}^{-2}$ determined from inclusive hadron-hadron scattering experiments are expected to be applicable also for elastic vector meson production.

In the case of vector meson production with proton dissociation, the cross section is proportional to $1/M_Y^{2(1+\delta)} \simeq 1/M_Y^2$, where M_Y is the mass of the dissociated proton system. For masses $M_Y < 1.9\,\mathrm{GeV}$, the system is treated as one of the nucleon resonances $N(1440)$, $N(1520)$, $N(1680)$ or $N(1710)$ which subsequently decay according to [30], while for larger masses a quark and a diquark are fragmented according to the Lund string fragmentation within the JETSET Monte Carlo program [138].

The steering parameters in use for the files used here are given in table 4.10.

4.6.2 HITVM

HITVM [152] is a Monte Carlo program simulating the reaction $ep \to eVX$ for high $|t|$ ($|t| \gg \Lambda^2_{QCD}$, i.e. $|t| \gtrsim 1\,\mathrm{GeV}^2$), where V is one of the vector mesons ρ, ω, ϕ, J/ψ or Υ, and X denotes the hadronic state originating from the dissociation of the proton. It is based on a calculation by J. R. Forshaw,

Produced vector meson	ε	n	Λ	ξ	χ	b [GeV^{-2}] (elastic)	b [GeV^{-2}] (p-diss.)	α'
J/ψ	0.225	3.0	m_ψ	1.0	0.0	4.8	1.6	0.0
$\psi(2S)$	0.225	2.5	$m_{\psi(2S)}$	1.0	0.0	4.0	2.0	0.0

Table 4.10: *Important steering parameters for DIFFVM. See the text for further explanations.*

M. Ryskin and others [153] where the exchanged pomeron is calculated as a gluon ladder in the BFKL formalism [154]. The high cross section — compared to the predictions of diffractive models — expected by [153] is considered to be one of the distinct signatures for the significance of BFKL resummations.

The differential cross section for transversely polarized photons in terms of t and the fraction of the proton momentum carried by the struck parton x_g is written in leading order as [153]

$$\frac{d^2\sigma^T(\gamma p \to VX)}{dt\,dx_g} = \left(G(x_g,t) + \frac{16}{81}\sum_f (q(x_g,t) + \bar{q}(x_g,t)) \right) \frac{\pi(\alpha_s^{LO})^4}{t^4} \mid \mathcal{F} \mid^2, \qquad (4.14)$$

where G, q and $\bar{q}$ represent the gluon, quark and antiquark densities respectively, and $\mathcal{F}$ is the product of the two-gluon scattering amplitude and the form factor associated with the γV vertex. The cross section for longitudinal photons is assumed to follow $R := \sigma^L/\sigma^T = \frac{Q^2}{m_V^2}$. The only free parameter in this model is the value of the QCD coupling constant, α_s^{LO}. Its value should be of the order of the value of α_s at the scale of the mass of the vector meson, m_V, or of $\sqrt{|t|}$ if this is larger. Note that the current results of the calculation are in leading order perturbation theory, while the parameter α_s^{LO} used in the model can only be identified with the strong coupling constant at a certain scale once next-to-leading order calculations become available.

For the hadronization of the proton remnant HITVM is interfaced to the JETSET Monte Carlo program [138].

The HITVM data sets used have been generated with the value of α_s^{LO} found to be in accordance with J/ψ photoproduction at large $|t|$ ($|t| > 1\,\mathrm{GeV}^2$) measured by H1 [155], $\alpha_s^{LO} = 0.207$; note that the magnitude of the cross section is extremely sensitive to the input value of α_s^{LO} such that the cross section can change by a factor of 20 when changing the value of α_s^{LO} from 0.2 to 0.3. The parton distributions used are GRV(HO) [112].

4.6.3 EPJPSI

The EPJPSI generator [156] has been written to simulate J/ψ meson production in a variety of processes in ep, μp, γp, pp and $p\bar{p}$ collisions. It is used here to generate events according to the Colour Singlet Model (see section 3.3.2) in leading order including relativistic corrections to the $c\bar{c}$ bound state [157]. The hadronization is done with the LUND string fragmentation in JETSET [138].

The matrix element used in EPJPSI is for photoproduction of J/ψ mesons, i.e. $\gamma p \to J/\psi X$. Virtual photons with *longitudinal* polarization are not taken into account. The cross section for $ep \to eJ/\psi X$ is obtained with the equivalent photon approximation [158]–[161]

$$\frac{d^2\sigma_{ep}(x,Q^2)}{dy\,dQ^2} = \Gamma_T \cdot \sigma_{\gamma p}, \qquad (4.15)$$

where the flux Γ_T of transversely polarized photons is given by

$$\Gamma_T = \frac{\alpha}{2\pi y Q^2} \cdot \left(1 + (1-y)^2 - 2m_e^2 \frac{y^2}{Q^2} \right).$$ (4.16)

The Q^2 dependence of the cross section has also been exactly calculated within the Colour Singlet Model [163, 164], but the result is not implemented in EPJPSI.

The files used here have been generated with the MRSA' parton distributions [162] as implememted in PDFLIB [165]. Only direct virtual photoproduction is simulated.

4.6.4   LPAIR

The LPAIR generator [166] simulates electromagnetic lepton pair production (e^+e^-, $\mu^+\mu^-$ or $\tau^+\tau^-$) via two photon exchange in the t channel. In the case of exclusive electron and muon pair production, this process is the dominant background contribution to the two lepton invariant mass spectrum in the J/ψ mass region. Furthermore the cross section is steeply falling with $|t|$ and therefore potentially affects the measured $|t|$ distribution for J/ψ production.

4.6.5   Summary of Monte Carlo Data Sets

A list of all Monte Carlo files used in this thesis is given in table 4.11. Files marked as "DIS" are generated with a lower Q^2 cut of 1 GeV^2 (HITVM: 1.5 GeV^2). All files are from different generator runs, i.e. those produced with the 1995 and 1996 detector simulation. Table 4.11 also includes estimates of the integrated luminosity the files correspond to, as calculated by the generators. The numbers given for DIFFVM are based on H1 measurements using the 1994 data [65]. It should be noted that in the case of EPJPSI a k-factor of around two on the leading order colour singlet prediction is expected, which is not included in the numbers given in table 4.11.

Generator	Process	Events	Simulation	$\int \mathcal{L}dt$
DIFFVM 1.0	DIS elastic $J/\psi \to \mu^+\mu^-$	10000	1995	135
	DIS elastic $J/\psi \to e^+e^-$	10000		135
	DIS p-diss. $J/\psi \to \mu^+\mu^-$	10000		135
	DIS p-diss. $J/\psi \to e^+e^-$	10000		135
	DIS elastic $J/\psi \to \mu^+\mu^-$	10000	1996	135
	DIS elastic $J/\psi \to e^+e^-$	10000		135
	DIS p-diss. $J/\psi \to \mu^+\mu^-$	10000		135
	DIS p-diss. $J/\psi \to e^+e^-$	10000		135
	all Q^2 elastic $\psi(2S) \to \mu^+\mu^-X$	20000	1995	175
	all Q^2 elastic $\psi(2S) \to e^+e^-X$	20000		175
	all Q^2 p-diss. $\psi(2S) \to \mu^+\mu^-X$	20000		175
	all Q^2 p-diss. $\psi(2S) \to e^+e^-X$	20000		175
HITVM 1.0	DIS p-diss. $J/\psi \to \mu^+\mu^-$	1000	1996	52
	DIS p-diss. $J/\psi \to e^+e^-$	1000		52
EPJPSI 3.3	all Q^2 $J/\psi \to e^+e^-$	10000	1995	15
	all Q^2 $J/\psi \to \mu^+\mu^-$	20000		29
	all Q^2 $J/\psi \to \mu^+\mu^-$	20000	1996	29
	DIS $J/\psi \to e^+e^-$ and $\to \mu^+\mu^-$	12000	1996	119
LPAIR 2.0	elastic $\mu^+\mu^-$	38400	1995	20
	inelastic $\mu^+\mu^-$	13600		20

Table 4.11: *Summary of Monte Carlo data sets. The $\psi(2S)$ files include direct decays and also those via J/ψ.*

Generator	Process	Events	Condition	$\int \mathcal{L}$
	DIS elastic $J/\psi \to \mu^+\mu^-$	10000		135
	DIS elastic $J/\psi \to e^+e^-$	10000	1995	135
	DIS p-diss. $J/\psi \to \mu^+\mu^-$	10000		135
	DIS p-diss. $J/\psi \to e^+e^-$	10000		135
DIPSI M	DIS elastic $J/\psi \to \mu^+\mu^-$	10000		135
1.0	DIS elastic $J/\psi \to e^+e^-$	10000	1996	135
	DIS p-diss. $J/\psi \to \mu^+\mu^-$	10000		135
	DIS p-diss. $J/\psi \to e^+e^-$	10000		135
	all Q^2 elastic $\psi(2S) \to \mu^+\mu^-X$	20000		175
	all Q^2 elastic $\psi(2S) \to e^+e^-X$	20000	1995	175
	all Q^2 p-diss. $\psi(2S) \to \mu^+\mu^-X$	20000		175
	all Q^2 p-diss. $\psi(2S) \to e^+e^-X$	20000		175
DIFFVM	DIS p-diss $J/\psi \to \mu^+\mu^-$	1000	1996	32
1.1	DIS p-diss. $J/\psi \to e^+e^-$	1000		32
	all Q^2 $J/\psi \to e^+e^-$	10000	1995	15
EPJPSI	all Q^2 $J/\psi \to \mu^+\mu^-$	20000		29
3.5	all Q^2 $J/\psi \to \mu^+\mu^-$	20000	1996	29
	DIS $J/\psi \to e^+e^-$ and $\to \mu^+\mu^-$	12000	1996	119
LPAIR	elastic $\mu^+\mu^-$	38400	1995	30
2.0	inelastic $\mu^+\mu^-$	13500		30

Table 4.11: Summary of Monte Carlo data sets. The $\psi(2S)$ files include direct decays and also those via J/ψ.

Chapter 5

Diffractive J/ψ Production

In this chapter, results on the diffractive production of J/ψ mesons in deep inelastic scattering will be derived and discussed. In the first section the procedure to correct the data for acceptance and efficiency losses as well as the separation of the elastic and the proton dissociation contribution will be developed. Extensive comparisons between the Monte Carlo simulation and the data are presented.

Results on cross sections as a function of W and Q^2 are derived next. They are interpreted within the pQCD based models of Ryskin, Frankfurt and others. The $|t|$ distributions are extracted and slope parameters determined. Finally, a first study of the helicity structure of exclusive J/ψ production is presented. The chapter closes with a discussion of the results.

5.1 Acceptance and Efficiency Determination for Diffractive J/ψ Production

In order to derive differential and total cross sections, the data have to be corrected for acceptance losses and detector deficiencies. The details of the necessary corrections will be discussed in this section.

5.1.1 Outline of the Correction Procedure

The procedure in order to derive cross sections as a function of Q^2 and W is as follows. First, a region of high acceptance in the W-Q^2-plane is selected, in order to be as independent as possible of the Monte Carlo model used for correction. Then, inefficiencies introduced by the deficiencies of the detector, i.e. trigger, track and vertex finding efficiency, lepton identification efficiency etc. are derived as far as possible from the data, and the Monte Carlo simulation is corrected accordingly. The corrected Monte Carlo is compared to the data.

Finally, the data are binned in Q^2 and W, and the elastic and proton dissociative events are extracted by means of a simple unfolding: let N_{tag} be the number of events which are tagged by the forward detectors (see section 4.5.1), and N_{ntag} the corresponding number without a tag, then the number of genuine elastic and proton dissociative events, N_{el} and N_{pd}, can be derived from

$$
\begin{aligned}
N_{ntag} &= \varepsilon_{ntag}^{el} \cdot N_{el} + \varepsilon_{ntag}^{pd} \cdot N_{pd}; \\
N_{tag} &= \varepsilon_{tag}^{el} \cdot N_{el} + \varepsilon_{tag}^{pd} \cdot N_{pd},
\end{aligned}
\tag{5.1}
$$

87

where ε_{tag}^{el}, ε_{tag}^{pd} and ε_{ntag}^{el}, ε_{ntag}^{pd} include the efficiencies for tagging and non-tagging of elastic and proton dissociative events as computed from the corrected Monte Carlo, as well as the acceptance and analysis efficiency.

5.1.2   Kinematical Acceptance

The restriction on the polar angle of the decay leptons ($20° < \theta_l < 160°$) and the fiducial cuts on the scattered electron ($R_{cog} > 8.1$ cm and $\theta_e \gtrsim 155°$, see section 4.3) have to be complemented by cuts on W and Q^2 in order to derive well-defined cross sections. W is correlated to the polar angle of the decay leptons, while the acceptance in Q^2 is determined by the scattering angle of the DIS electron. As has been shown in chapter 3, the energy of the scattered electron does not limit the kinematical acceptance (see figure 3.4). The correlation between the acceptance in W and in Q^2 can be seen in figure 5.1, both for elastic and proton dissociation events using the DIFFVM Monte Carlo. As naively expected, no difference between the two plots is visible. However, there is an indication that the acceptance plateau in both cases tends to be at higher W for higher Q^2. Because of this it is crucial that the Monte Carlo simulation describes both the W and the Q^2 dependence observed in the data very well.

The kinematic region used for this analysis is shown in figure 5.2. Here, the same cross section is assumed for the elastic and proton dissociation process, and the Monte Carlo samples have been mixed accordingly. The cut in Q^2 is motivated by the requirement of an almost flat acceptance, since the event rate falls steeply with Q^2:

$$2 < Q^2 < 80 \, \text{GeV}^2. \tag{5.2}$$

The acceptance is everywhere above 60 %. In W, the acceptance should be above 40 %, in order to avoid regions of phase space with large acceptance corrections; therefore the cut

$$40 < W < 160 \, \text{GeV} \tag{5.3}$$

has been chosen.

5.1.3   Trigger Efficiency

The efficiency of the selected trigger mix for J/ψ events has been determined almost completely from data. From the description of the trigger selection (section 4.4) it is obvious that the efficiency consists of three contributions, namely the SpaCal, the track trigger condition `ray-t0`, and further vetoes against non-ep background:

$$\varepsilon_{trig} = \varepsilon_{spacal} \cdot \varepsilon_{track} \cdot \varepsilon_v. \tag{5.4}$$

Using events which have been triggered by SpaCal independent triggers, ε_{spacal} can be determined. For this purpose, a dedicated data sample consisting of two-prong events has been selected, which fulfil this criterion and furthermore the selection outlined in section 4.5.1 with somewhat weaker cuts with respect to lepton identification. The efficiency of the selected trigger mix in relation to the SpaCal independent triggers is shown in figure 5.3. Small losses are observed especially for small Q^2, although these are not significant. For this study, 239 events from the data taking period 1996 and 245 events from 1997 were available.
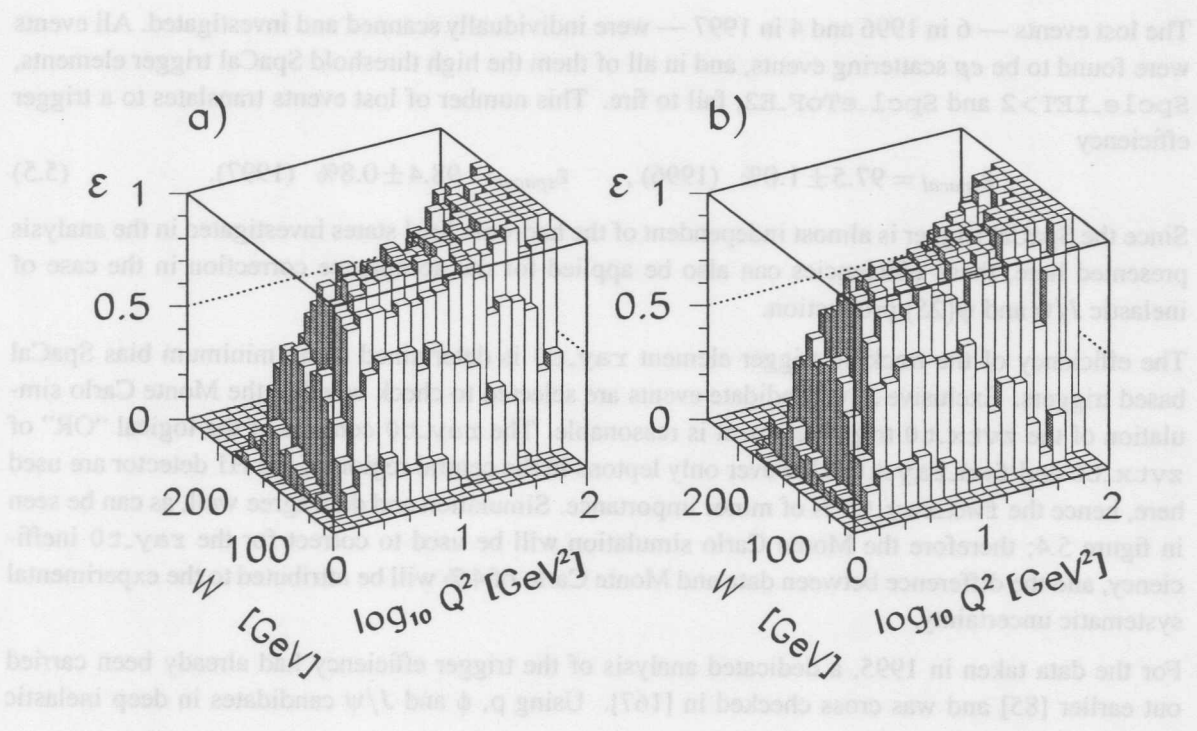
Figure 5.1: *Acceptance due to the fiducial cuts on the decay leptons and the scattered electron as a function of W and Q^2 for a) elastic and b) proton dissociation events.*
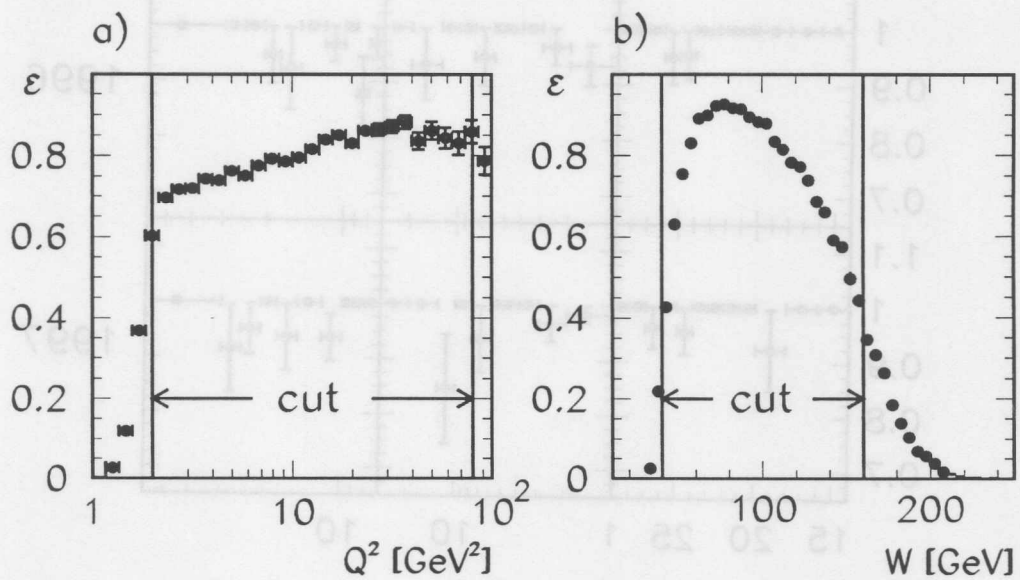
Figure 5.2: *Kinematic acceptance for diffractive (elastic and proton dissociation) J/ψ production as a function of a) Q^2 and b) W. In b) the cut marked in a) has already been applied and vice versa.*

The lost events — 6 in 1996 and 4 in 1997 — were individually scanned and investigated. All events were found to be *ep* scattering events, and in all of them the high threshold SpaCal trigger elements, `Spcle_IET>2` and `Spcl_eToF_E2`, fail to fire. This number of lost events translates to a trigger efficiency

$$\varepsilon_{spacal} = 97.5 \pm 1.0\% \ (1996), \qquad \varepsilon_{spacal} = 98.4 \pm 0.8\% \ (1997). \tag{5.5}$$

Since the SpaCal trigger is almost independent of the hadronic final states investigated in the analysis presented here, these efficiencies can also be applied for the acceptance correction in the case of inelastic J/ψ and $\psi(2S)$ production.

The efficiency of the tracking trigger element `ray_t0` is determined using minimum bias SpaCal based triggers. Exclusive J/ψ candidate events are selected to check whether the Monte Carlo simulation of the `zvtx_t0` trigger element is reasonable. The `ray_t0` consists of the logical "OR" of `zvtx_t0` and `fwd_ray_t0`. However only leptons in the central region of the H1 detector are used here, hence the `fwd_ray_t0` is of minor importance. Simulation and data agree well, as can be seen in figure 5.4; therefore the Monte Carlo simulation will be used to correct for the `ray_t0` inefficiency, and the difference between data and Monte Carlo of 4 % will be attributed to the experimental systematic uncertainty.

For the data taken in 1995, a dedicated analysis of the trigger efficiency had already been carried out earlier [85] and was cross checked in [167]. Using ρ, ϕ and J/ψ candidates in deep inelastic
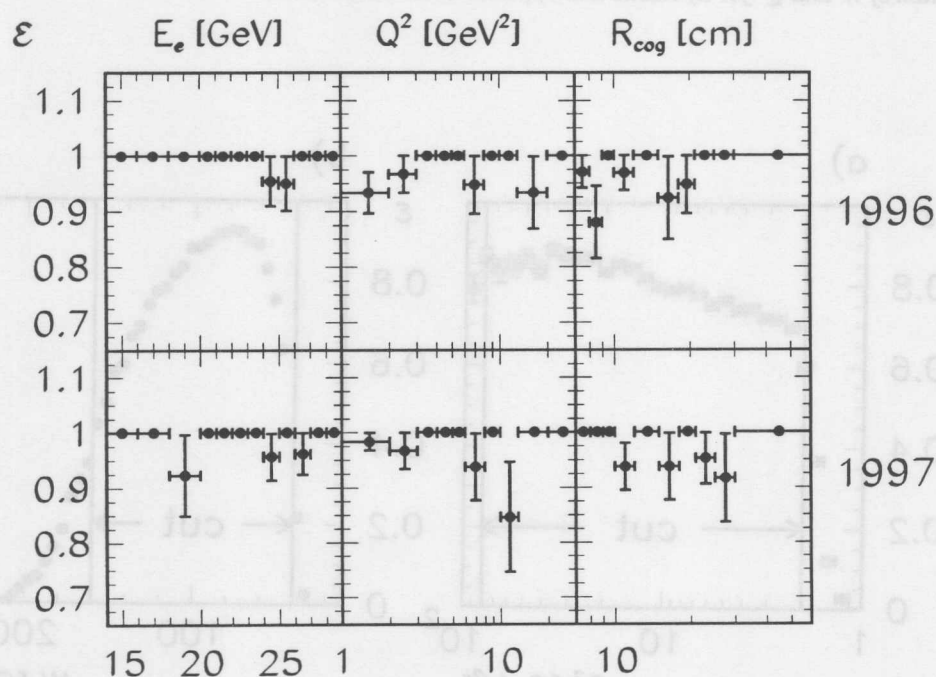
Figure 5.3: *SpaCal trigger efficiency determined from SpaCal-independent triggers as described in the text. The efficiency is given as a function of electron energy E_e for $Q^2 > 3\,\text{GeV}^2$, as a function of Q^2 for $E_e > 10\,\text{GeV}$, and as a function of the radial distance R_{cog} of the cluster's centre of gravity to the nominal beam position for $Q^2 > 2\,\text{GeV}^2$ and $E_e > 10\,\text{GeV}$, for the data taking periods 1996 and 1997.*

scattering, the SpaCal trigger efficiency including timing vetoes was determined to be $96 \pm 4\%$. For a fraction of the data corresponding to $1.1\,\mathrm{pb}^{-1}$, or about 5% of all data, the triggers used included the track condition dcrφ_Ta. The Monte Carlo simulation is used to correct for the inefficiency introduced; the dcrφ_Ta efficiency for diffractive and inelastic Monte Carlo data sets as a function of the number of central tracks fitted to the primary event vertex with $p_t > 0.1\,\mathrm{GeV}$ and $\sigma_{p_t}/p_t < 0.5$ is shown in figure 5.5. The good agreement between data and simulation has already been shown before, see for example [167]. The error deduced there on the single track efficiency (3%) is also
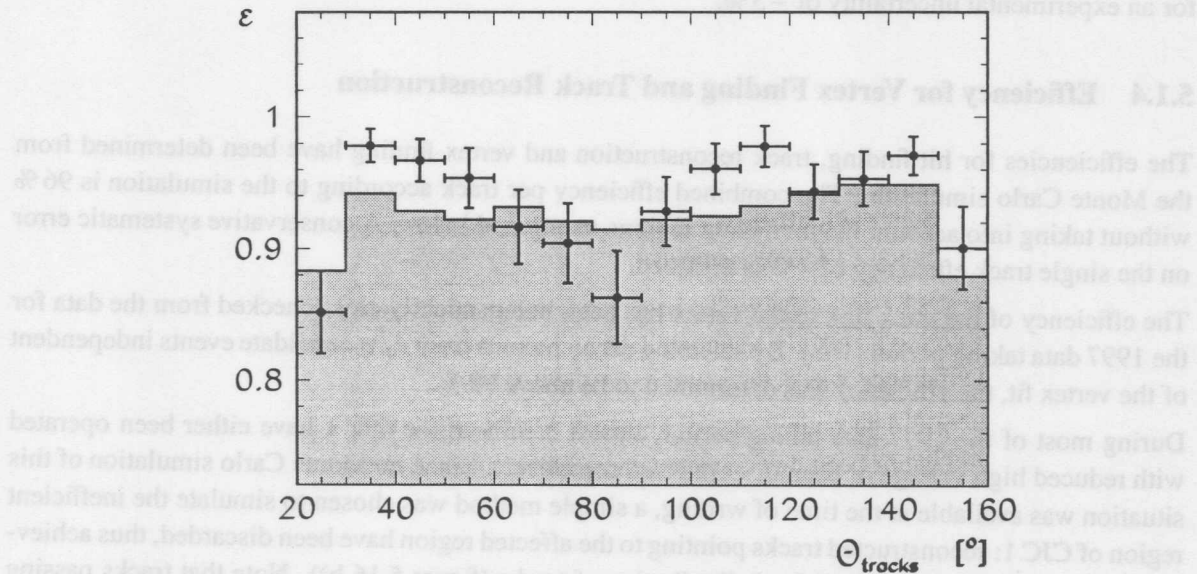
Figure 5.4: zvtx_t0 *trigger efficiency as a function of the polar angle θ of leptons from exclusive J/ψ candidate events, determined from SpaCal minimum-bias and kinematic-peak triggers. The dots are for 1995 to 1997 data, the histogram is determined using the DIFFVM Monte Carlo generator.*
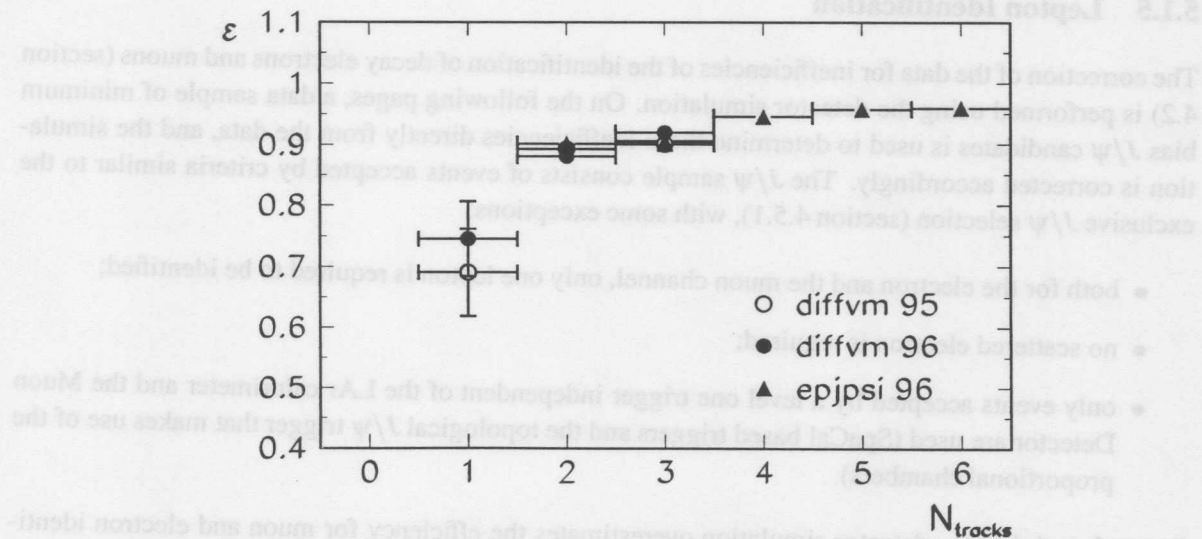
Figure 5.5: *Efficiency of the* dcrφ_Ta *trigger as a function of the number of good central tracks as defined in the text, for different Monte Carlo data sets.*

used here.

Finally, all triggers used include veto conditions against non-ep interactions. These are usually set up to be more than 99 % efficient for genuine deep inelastic scattering events. Furthermore, the combination of different subtriggers with different veto conditions as used in this analysis reduces the probability of rejecting events accidentally. In studies using partly independent triggers, no losses have been found. Since, however, the independent data samples are only of the order of 100 events, quantitative statements are difficult to derive; therefore an efficiency of $\varepsilon_v = 100$ % is used, allowing for an experimental uncertainty of -3 %.

5.1.4   Efficiency for Vertex Finding and Track Reconstruction

The efficiencies for hit finding, track reconstruction and vertex finding have been determined from the Monte Carlo simulation. The combined efficiency per track according to the simulation is 96 % without taking into account the inefficient regions mentioned below. A conservative systematic error on the single track efficiency of 4 % is assumed.

The efficiency of the track link to the vertex has been independently cross checked from the data for the 1997 data taking period [168]. By selecting decay leptons from J/ψ candidate events independent of the vertex fit, the efficiency was determined to be above 99 %.

During most of the 1997 data taking period, almost 3 cells of the CJC 1 have either been operated with reduced high voltage or been disconnected completely. Since no Monte Carlo simulation of this situation was available at the time of writing, a simple method was chosen to simulate the inefficient region of CJC 1: reconstructed tracks pointing to the affected region have been discarded, thus achieving a reasonable description of the ϕ distribution of tracks (figure 5.16 b)). Note that tracks passing through the inefficient cells could not be recovered for the analysis, because the event classification on L5 already requires hits in CJC 1 for lepton tracks.

5.1.5   Lepton Identification

The correction of the data for inefficiencies of the identification of decay electrons and muons (section 4.2) is performed using the detector simulation. On the following pages, a data sample of minimum bias J/ψ candidates is used to determine these inefficiencies directly from the data, and the simulation is corrected accordingly. The J/ψ sample consists of events accepted by criteria similar to the exclusive J/ψ selection (section 4.5.1), with some exceptions:

- both for the electron and the muon channel, only one lepton is required to be identified;

- no scattered electron is required;

- only events accepted by a level one trigger independent of the LAr calorimeter and the Muon Detector are used (SpaCal based triggers and the topological J/ψ trigger that makes use of the proportional chambers).

It was found that the detector simulation overestimates the efficiency for muon and electron identification in the LAr calorimeter, while the Muon Detector is described sufficiently well. This will be detailed in the following. Furthermore, no significant differences with respect to the identification performance were found between the three data taking periods used.
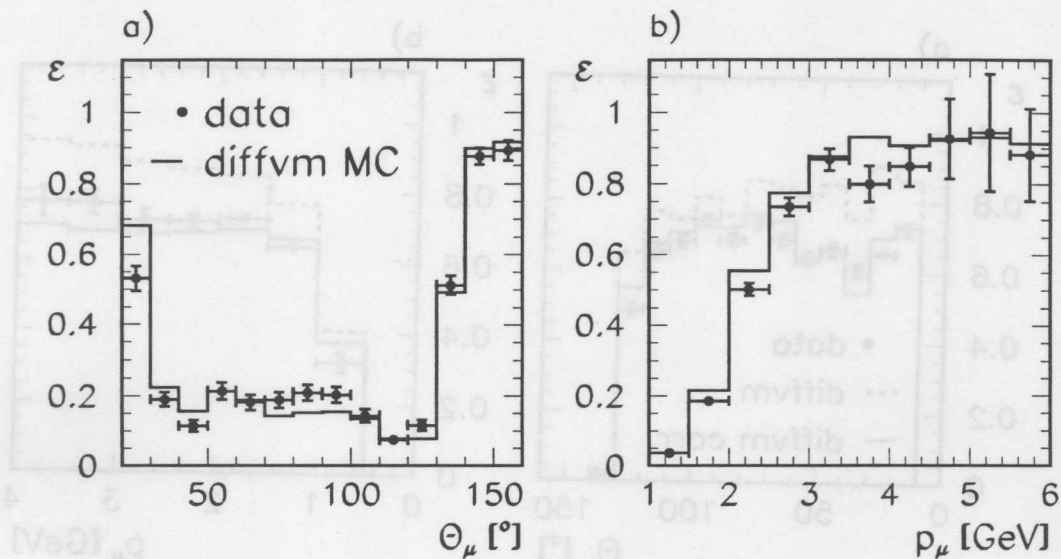
Figure 5.6: *Efficiency for the identification of J/ψ decay muons in the Muon Detector as a function of a) the muon polar angle θ_μ and b) its momentum p_μ.*

Muon Identification

The identification efficiency for muons in the Muon Detector as a function of the muon's polar angle θ_μ and its momentum p_μ is shown in figure 5.6. It includes effects of geometrical acceptance in the Muon Detector, limited chamber and reconstruction efficiency — e.g. muon track segments that cross subdetector boundaries are not linked to each other —, and also inefficiencies in the linking of central tracks to muon tracks.

The efficiency as a function of θ_μ is well described by the simulation. In the central region it is low due to the large amount of material in front of the Muon Detector (LAr calorimeter and magnet coil) and the relatively small momenta of the muons, while it rises strongly for $\theta_\mu \gtrsim 130°$ due to much less material that has to be traversed by the muons. For small polar angles $\theta_\mu \lesssim 30°$ the efficiency increases, since here the momenta of J/ψ decay muons are larger. As a function of p_μ data and Monte Carlo simulation generally agree sufficiently well.

The results for the muon identification efficiency in the LAr calorimeter are summarized in figure 5.7. Shown is the efficiency as a function of the muon polar angle θ_μ and its momentum p_μ for finding a muon of quality $Q_\mu \geq 2$. Note that the drop at large θ_μ is due to the limited geometric acceptance of the hadronic section of the LAr calorimeter; this is however the region where the efficiency of the Muon Detector is high.

Obvious discrepancies, most pronounced in the forward region, can be seen in both figures. In order to correct for this, the efficiency in the simulation was corrected by a θ_μ dependent factor that was determined from a 2nd order polynomial fitted to the ratio of data over Monte Carlo simulation. After this correction, good agreement both as a function of θ_μ and p_μ is observed (figure 5.7).
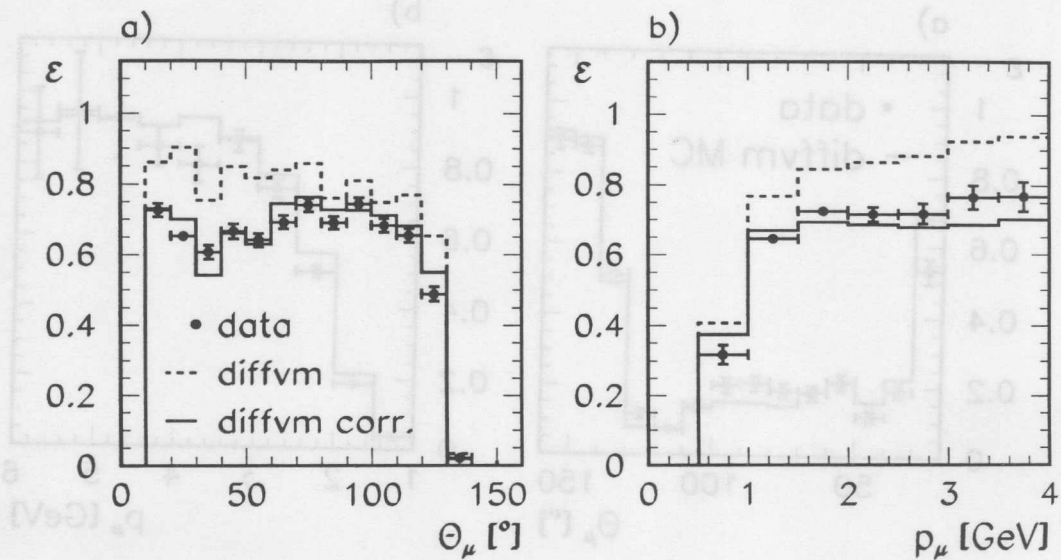
Figure 5.7: *Efficiency for the identification of J/ψ decay muons in the LAr calorimeter ($Q_\mu \geq 2$) as a function of a) the muon polar angle θ_μ and b) its momentum p_μ. Shown are results obtained from the data (points), from the DIFFVM Monte Carlo simulation (dashed histogram), and from the simulation after correcting the efficiency as a function of θ_μ (full histogram).*

Electron Identification

For the electron identification in the LAr calorimeter, the efficiency for finding electrons with quality $Q_e = 3$ is given in figure 5.8 as a function of the electron's polar angle θ_e and its transverse momentum p_{te}. A small mismatch between data and simulation is visible, which is corrected using the same method as for muon identification in the LAr calorimeter, i.e. by applying a θ_e dependent correction factor. After applying this correction, again good agreement as a function of p_{te} and θ_e is observed.

Concluding Remarks on the Lepton Identification

The corrections required to match data and detector simulation are of the same order as derived in previous analyses of, for example, J/ψ photoproduction [146], however no θ dependent correction was applied in the analysis of [146], mainly due to the limited statistics available for efficiency determination.

It turned out that the effect of the Monte Carlo tuning is surprisingly small in the final cross sections; as an example, in the seven bins in W and Q^2 in which cross sections for elastic J/ψ production will be calculated (section 5.2.1), the effect is always below 2.5 %. The reasons are on the one hand that in this specific case only one muon is required to be identified, and on the other hand, even more important, that the typical momentum of the decay leptons is high enough (figure 4.6f)) — on average 2.4 GeV — in order to be rather independent of the muon identification in the LAr calorimeter, which needs the largest correction.

From the remaining differences between data and Monte Carlo simulation the systematic error of the lepton identification is estimated to be 5 % per lepton.
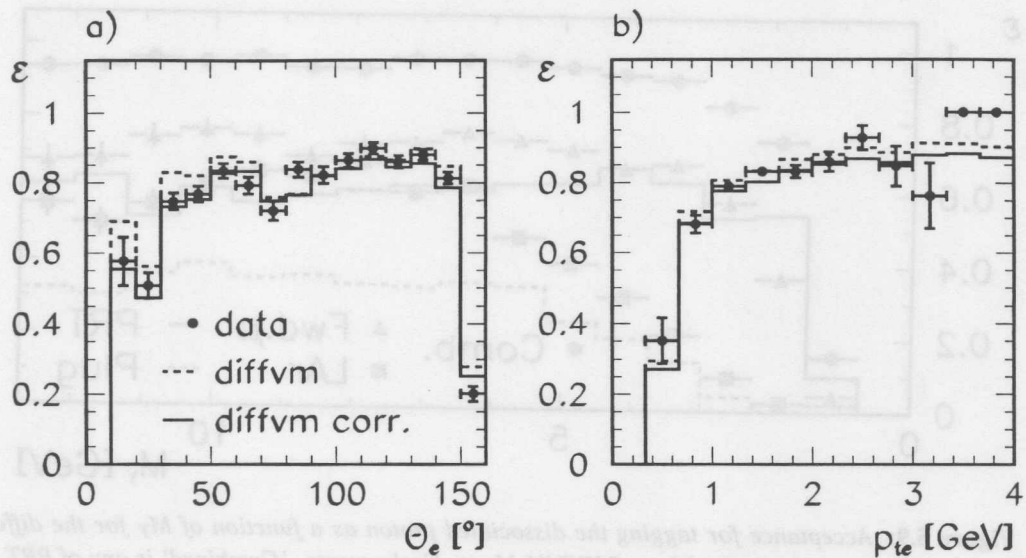
Figure 5.8: *Efficiency for the identification of J/ψ decay electrons in the LAr calorimeter ($Q_e = 3$) as a function of a) the electron polar angle θ_e and b) its transverse momentum p_{te}. Shown are results obtained from the data (points), from the DIFFVM Monte Carlo simulation (dashed histogram), and from the simulation after correcting the efficiency as a function of θ_e (full histogram).*

5.1.6 Separation of Elastic and Proton Dissociative Events

The separation of elastic and proton dissociative events relies on the so-called forward detectors, namely the Proton Remnant Tagger (PRT), the Forward Muon Detector (FMD), and the inner forward LAr calorimeter. The Plug calorimeter is not used in the present analysis. The proton remnant in proton dissociative events can scatter in the beampipe walls or in the collimators (mainly "C4", which is situated close to the Forward Tracking Detector), with the products being detected in one of the forward detectors. The different thresholds as a function of the mass of the dissociated proton M_Y for the different detectors is shown in figure 5.9. For $M_Y \gtrsim 3\,\text{GeV}$, a plateau of more than 90 % is reached for the tagging efficiency of proton dissociation events.

There is a certain probability that also the outgoing proton in elastic J/ψ production scatters and produces signals in the forward detectors; it is expected that this probability rises as a function of $|t|$, corresponding to a rise in the transverse momentum of the outgoing proton. Using DIFFVM elastic and proton dissociation Monte Carlo files, the tagging probability as a function of the kinematical variables Q^2, W and $|t|$ is shown in figure 5.10. For proton dissociation events it is almost flat in all variables, while for elastic J/ψ production a strong rise of the tagging probability at high $|t|$ is observed. This rise is almost completely due to the response of the PRT.

For a fraction of the data the response of the Proton Remnant Tagger and the Forward Muon Detector is, due to different reasons, not reliable. Affected are 8 % of the total luminosity both for PRT and FMD. For these data the information from PRT and FMD has been set to zero. In the Monte Carlo simulation, the information is also set to zero in a corresponding fraction of Monte Carlo events, chosen randomly.

The response of the forward detectors in data and Monte Carlo simulation is compared in figure 5.11.
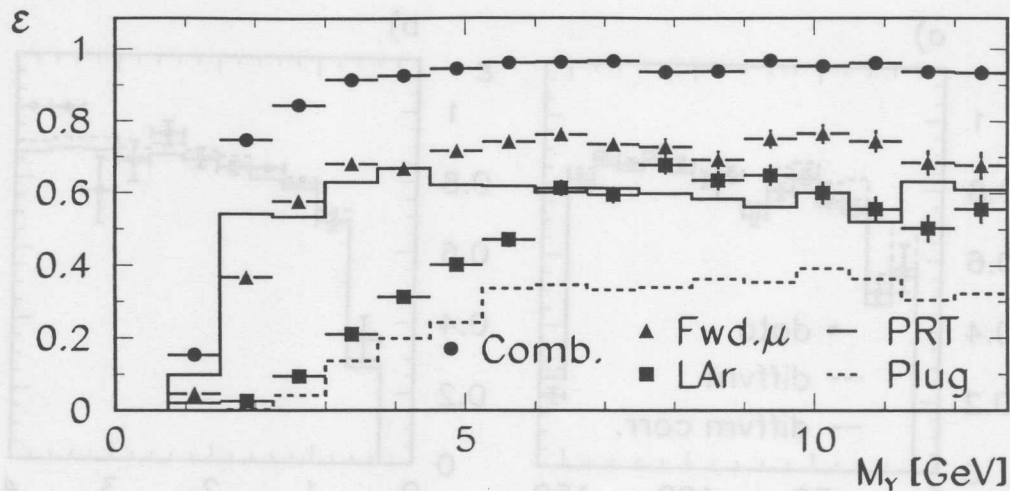
Figure 5.9: *Acceptance for tagging the dissociated proton as a function of M_Y for the different forward detectors, determined from DIFFVM Monte Carlo events. 'Combined' is any of PRT, LAr calorimeter and Forward Muon Detector.*
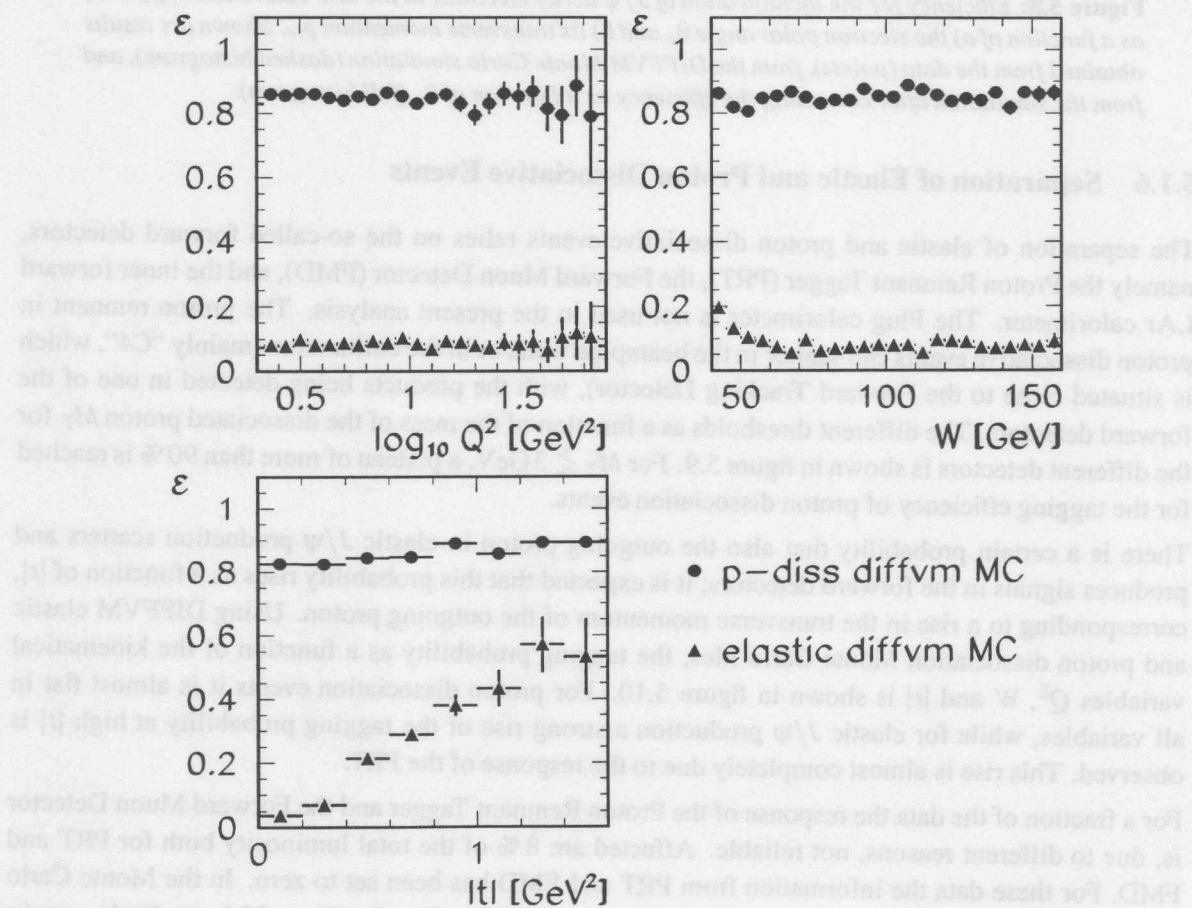
Figure 5.10: *Acceptance of the forward tag for elastic and proton dissociation events as a function of Q^2, W and $|t|$.*
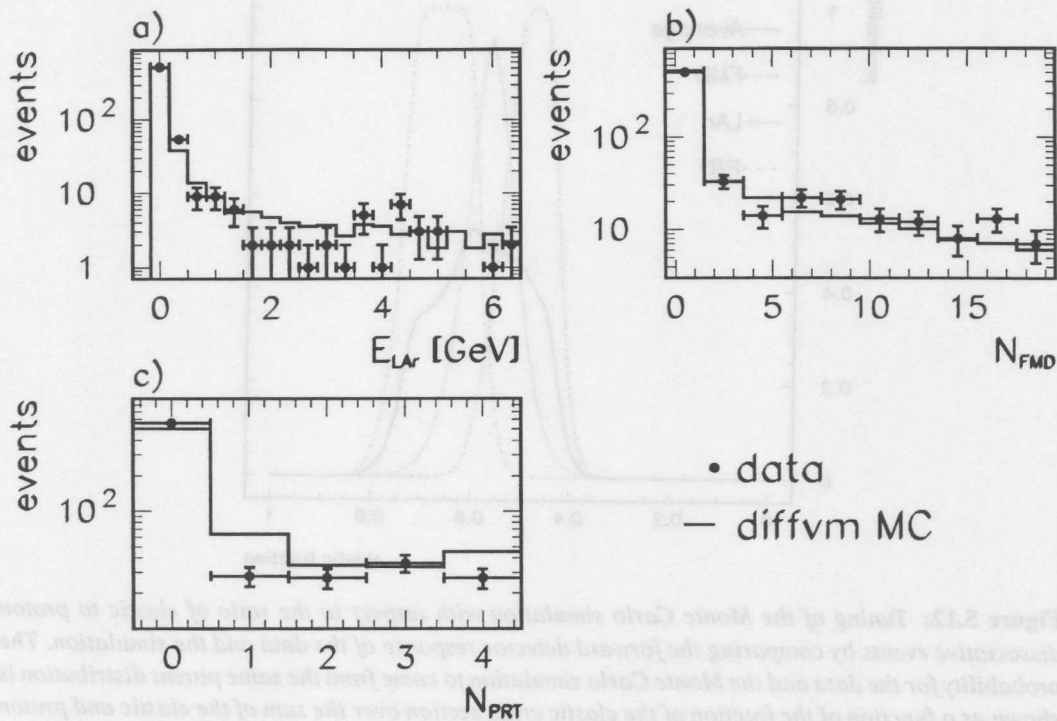
Figure 5.11: *Comparison of the response of the forward detectors for data and DIFFVM Monte Carlo. a) Energy in the LAr calorimeter for θ < 10°, b) number of hit pairs in the pre-toroid layers of the Forward Muon Detector, c) number of hits in the Proton Remnant Tagger.*

Events from the exclusive J/ψ selection (section 4.5.1) in a mass window of 250 MeV around the nominal J/ψ mass are selected, and for the simulation a mixture of elastic and proton dissociation DIFFVM Monte Carlo files assuming equal cross sections is used. No correction for non-resonant background is applied. The first bin of all histograms shown corresponds to the selection criteria for the forward untagged sample. Two things are to be noted in figure 5.11. Firstly the distributions agree for each subdetector separately between data and Monte Carlo, and secondly there is good overall agreement between PRT, LAr and FMD using one and the same mixture of elastic and proton dissociation Monte Carlo events.

The systematic error on the cross sections due to the separation of elastic and proton dissociation events is taken to be 10 %, inspired by previous investigations on J/ψ photoproduction [65, 146] and ρ meson production in deep inelastic scattering [78]. Some cross checks have been made in order to ensure its applicability to the current measurement:

- Variation of the M_Y dependence of the cross section in the proton dissociation Monte Carlo; variation of the M_Y dependence of the cross section (see section 4.6.1) between $1/M_Y^{2.1.08}$ and $1/M_Y^{2.9.1.08}$ decreases the elastic cross section by 5 %, the proton dissociation cross section by 3 %.

- Variation of the forward detectors used for tagging; the cross sections have been alternatively evaluated using only the LAr calorimeter and the Forward Muon System to tag proton dissociation events. Changes are of the order of 5 %.
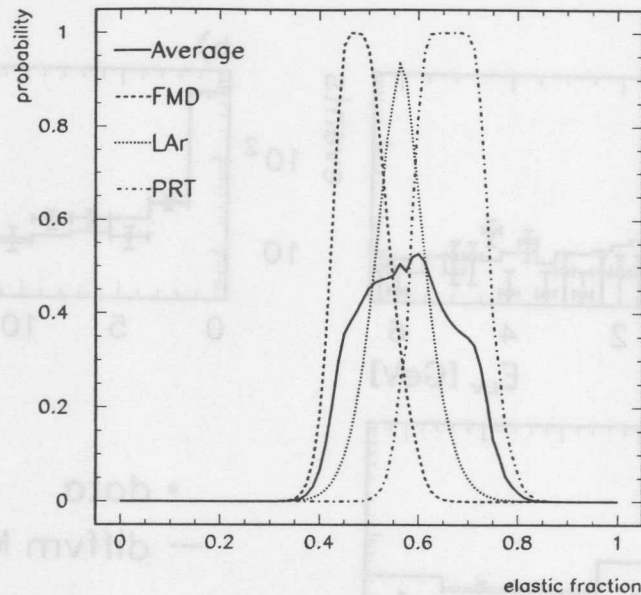
Figure 5.12: *Tuning of the Monte Carlo simulation with respect to the ratio of elastic to proton dissociative events by comparing the forward detector response of the data and the simulation. The probability for the data and the Monte Carlo simulation to come from the same parent distribution is shown as a function of the fraction of the elastic cross section over the sum of the elastic and proton dissociation cross sections. The curves are for each forward detector alone and the average of all three.*

- For the analysis of 1994 data [78], the acceptance of the forward detectors had been varied by 50 %; also here the effect on the elastic cross section was well within the 10 % systematic error quoted.

A word of caution has to be made on the interpretation of the proton dissociation cross sections. The cross section calculation is based on the assumption of a diffractive production mechanism. Significant non diffractive contributions, leading e.g. to a much flatter M_Y dependence of the cross section, can have large effects on the results; using for example an M_Y dependence $\sim 1/M_Y$ — which is experimentally excluded for proton diffractive dissociation [59, 60] — can easily increase the cross section results by 50 % in some kinematic regions. Note however that no such model dependencies have been found for elastic J/ψ production.

Finally, a complementary method to cross check the response of the different forward detectors and to determine the ratio of cross sections for elastic processes and proton diffractive dissociation is presented. Instead of unfolding the different contributions as described in section 5.1.1, one can vary the ratio of elastic and proton dissociative cross sections in the Monte Carlo simulation, and compare the resulting spectra in the forward detectors with the one observed in the data to find the ratio that gives the best description of the data. The result of applying such a method is shown in figure 5.12.

For figure 5.12, events in a mass window of 250 MeV around the nominal J/ψ mass are selected, and the full data sample of forward tagged and forward untagged events is used. The distributions of E_{LAr}, N_{PRT} and N_{FMD} are then statistically compared with the Monte Carlo simulation, applying a Kolmogorov test [169] to obtain a probability for the compatibility of data and Monte Carlo simulation; this procedure is repeated for different values of the ratio of the elastic to the proton dissociative

cross section in the simulation. The result for the "optimal" description of the data is within 10 % reproduced by each single forward detector. It is also in excellent agreement with the ratio of elastic to proton dissociative cross sections that will be derived with the unfolding method described in section 5.1.1.

5.1.7 Comparison to the Monte Carlo Simulation

The forward untagged and the forward tagged data samples have both been divided in 7 bins in W and Q^2, with a binning such that clear J/ψ signals are observed everywhere. The distribution of the J/ψ candidates in the data as a function of the kinematic variables x and Q^2 can be seen in the kinematic plane shown in figure 5.13. The observed mass spectra in each bin are shown in figure 5.14 for the forward untagged sample and in figure 5.15 for the forward tagged sample; also the kinematic boundaries in W and Q^2 are given there.

Before calculating cross sections, some comparisons between data and Monte Carlo simulation will
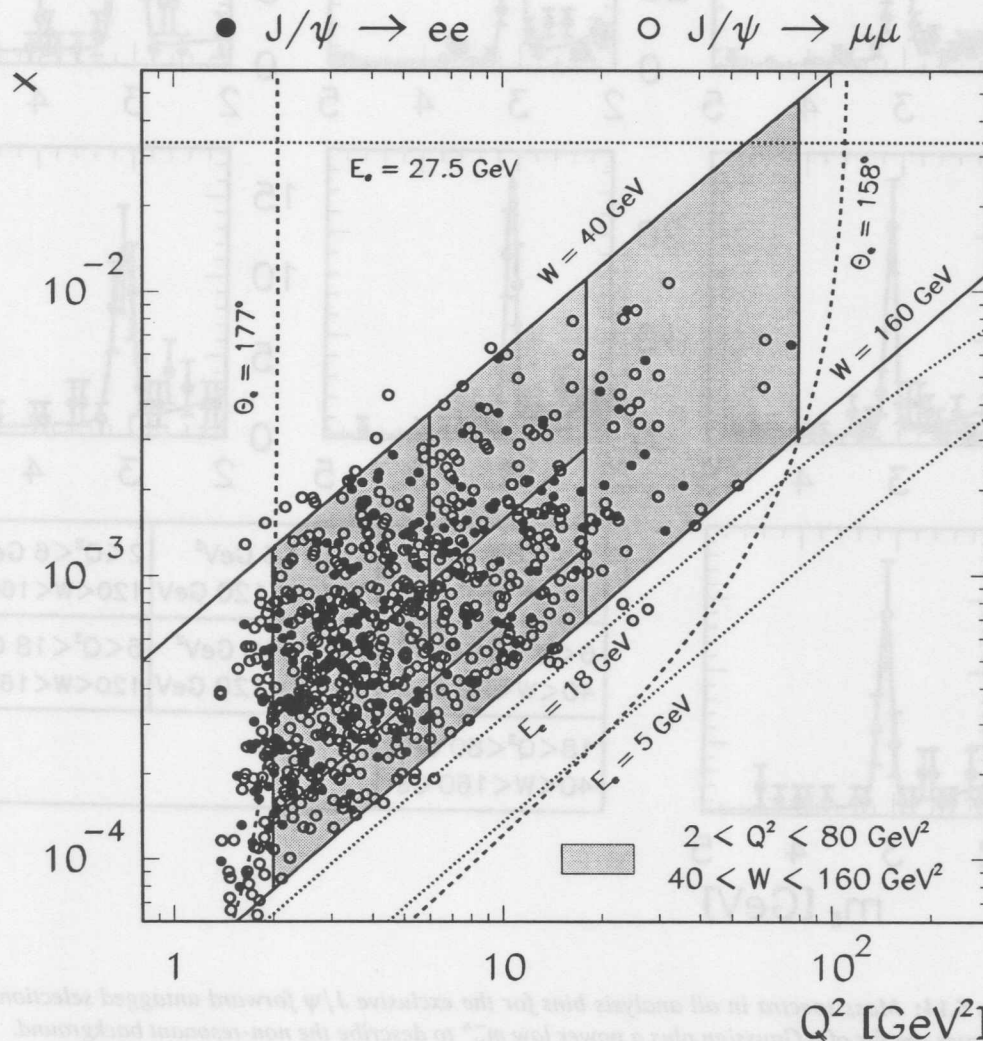
Figure 5.13: *J/ψ candidate events in the kinematic plane of x and Q^2. All cuts except those on W and Q^2 have been applied. The binning of the data is indicated by full lines.*
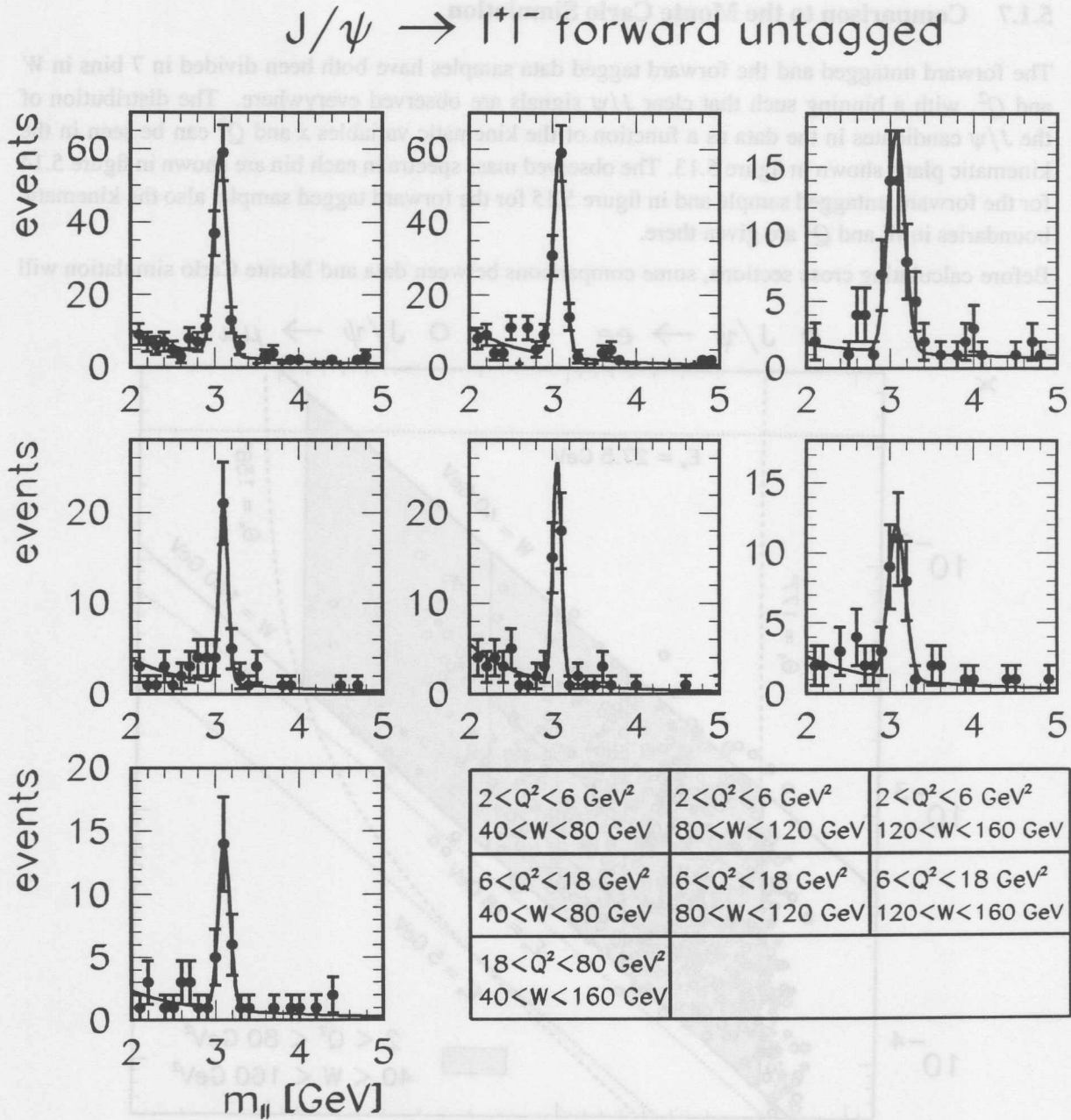
Figure 5.14: *Mass spectra in all analysis bins for the exclusive J/ψ forward untagged selection. The curves are fits of a Gaussian plus a power law m_{ll}^{-n} to describe the non-resonant background.*
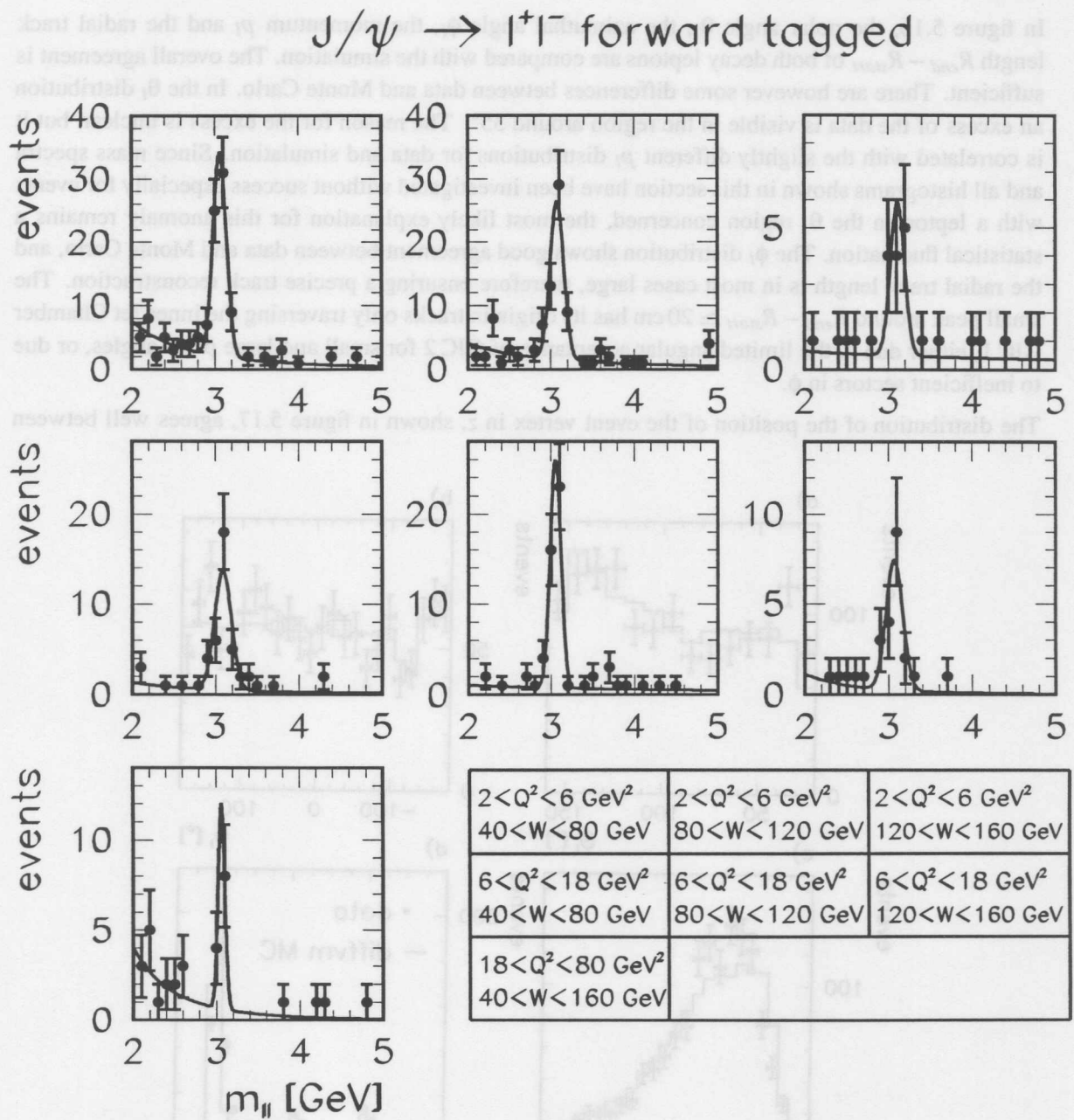
Figure 5.15: *Mass spectra in all analysis bins for the exclusive J/ψ forward tagged selection. The curves are fits of a Gaussian plus a power law m_{ll}^{-n}.*

be shown, including properties of the J/ψ decay leptons, kinematic variables, and key distributions
for the scattered electron. For these figures events in a mass window of 250 MeV around the nominal
J/ψ mass are selected, and elastic and proton dissociation DIFFVM Monte Carlo files are mixed
assuming equal cross sections for both processes. Again, no correction for non-resonant background
under the J/ψ signal is done.

In figure 5.16, the polar angle θ_l, the azimuthal angle ϕ_l, the momentum p_l and the radial track
length $R_{end} - R_{start}$ of both decay leptons are compared with the simulation. The overall agreement is
sufficient. There are however some differences between data and Monte Carlo. In the θ_l distribution
an excess of the data is visible in the region around 35°. The reason for the excess is unclear, but it
is correlated with the slightly different p_l distributions for data and simulation. Since mass spectra
and all histograms shown in this section have been investigated without success especially for events
with a lepton in the θ_l region concerned, the most likely explanation for this anomaly remains a
statistical fluctuation. The ϕ_l distribution shows good agreement between data and Monte Carlo, and
the radial track length is in most cases large, therefore ensuring a precise track reconstruction. The
small peak around $R_{end} - R_{start} \simeq 20$ cm has its origin in tracks only traversing the inner Jet Chamber
CJC 1, either due to the limited angular acceptance of CJC 2 for small and large polar angles, or due
to inefficient sectors in ϕ.

The distribution of the position of the event vertex in z, shown in figure 5.17, agrees well between
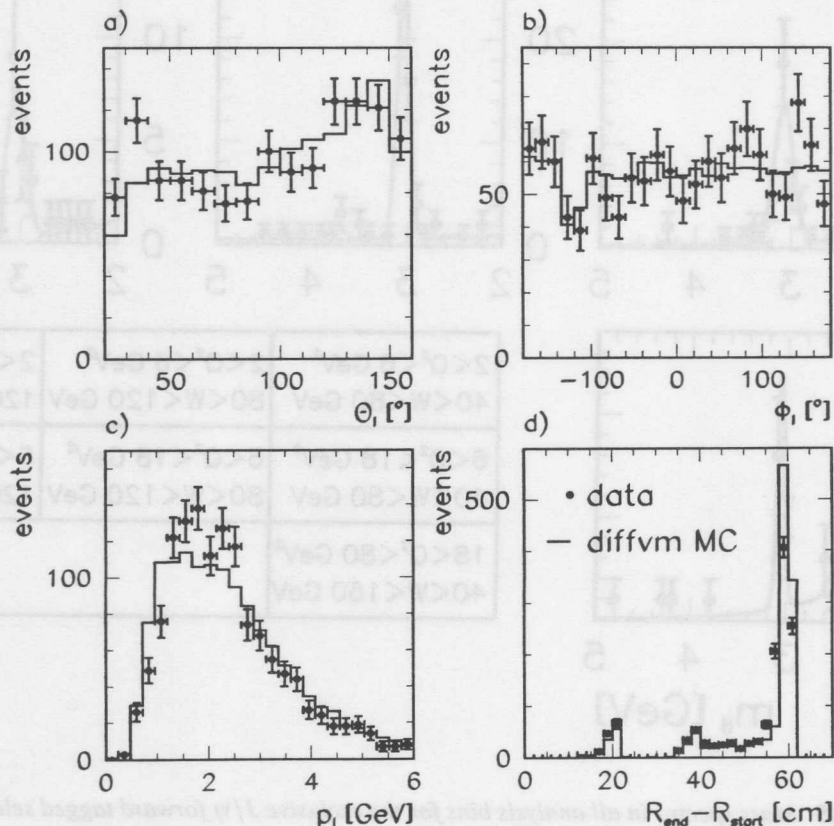
Figure 5.16: *Comparison of data and Monte Carlo simulation for exclusive J/ψ candidates; a)
polar angle θ_l, b) azimuth ϕ_l, c) momentum p_l and d) radial track length $R_{end} - R_{start}$ of the decay
leptons. The Monte Carlo histograms are normalized to the data.*

data and Monte Carlo; the peak position is only slightly shifted in the simulation with respect to the data, and both distributions have a width of 10.9 cm. The systematic uncertainty of the cross section measurements due to different vertex distributions in data and Monte Carlo simulation is estimated by varying the cut on the z-position of the event vertex by 2 cm in the simulation; the result for the cross section changes at most by 2 % in all analysis bins.

Kinematic variables of the selected events are displayed in figure 5.18. Q^2 and W measured with the double angle method agree well between data and Monte Carlo. For the high $|t|$ region, DIFFVM fails to reproduce the data; the impact of this on the total cross sections is small since most of the data are concentrated at small $|t|$, but care will have to be taken when measuring the $|t|$ dependence of the cross sections in this regime. The agreement of the $\sum(E - p_z)$ distributions is sufficient, given the fact that the only non negligible impact of the SpaCal energy scale on this analysis is through the cut on $\sum(E - p_z) > 45$ GeV. The width of the $\sum(E - p_z)$ distribution is well simulated, and the tail towards small values of $\sum(E - p_z)$ is due to initial state radiation which is not included in the Monte Carlo simulation.

Properties of the scattered electron are shown in figure 5.19. In general good agreement between data and simulation is observed.

5.1.8 Correction of the Data

The following procedure has been used to extract the number of signal events, and subsequently the "true" number of elastic and proton dissociation J/ψ events:

- All events in a region ± 250 MeV around the nominal J/ψ mass are counted as J/ψ candidates.

- The number of background events contributing to the J/ψ peak is determined by fitting a Gaussian to the signal plus a power law m_{ll}^{-n} for the background to the mass spectrum in each analysis bin separately, and integrating the exponential from $m_\psi - 250$ MeV to $m_\psi + 250$ MeV. This number is subtracted from the number of J/ψ candidates.

- The resulting event numbers N_{ntag} and N_{tag} are translated for each analysis bin separately into numbers of elastic and proton dissociation J/ψ events, N_{ela} and N_{pd}, using the elastic and proton dissociation DIFFVM Monte Carlo data sets and the method described in section 5.1.1, equation 5.1. The total acceptance for a bin $W_1 < W < W_2$ and $Q_1^2 < Q^2 < Q_2^2$ is calculated from

$$\varepsilon_{ntag}^{el} = \frac{N_{rec}(W_1 < W_{DA} < W_2, Q_1^2 < Q_{DA}^2 < Q_2^2)}{N_{gen}(W_1 < W_{gen} < W_2, Q_1^2 < Q_{gen}^2 < Q_2^2)} \tag{5.6}$$

and correspondingly for the other acceptances needed; W_{gen} and Q_{gen}^2 denote W and Q^2 as generated by the Monte Carlo, while W_{DA} and Q_{DA}^2 are the reconstructed quantities using the double angle method. In the denominator all events generated in the given limits are counted (N_{gen}), whereas only those that pass all analysis cuts enter the numerator (N_{rec}). As has been shown in section 3.1.4, the resolution in W and Q^2 is more than one order of magnitude better than the bin size chosen here; the bin-by-bin acceptance correction is therefore appropriate.

The total acceptances thus obtained are given in table 5.1. They include the acceptance due to angular cuts on the J/ψ decay leptons and fiducial cuts on the scattered electron as well as the trigger, reconstruction and selection efficiency. The W and Q^2 dependence of the given
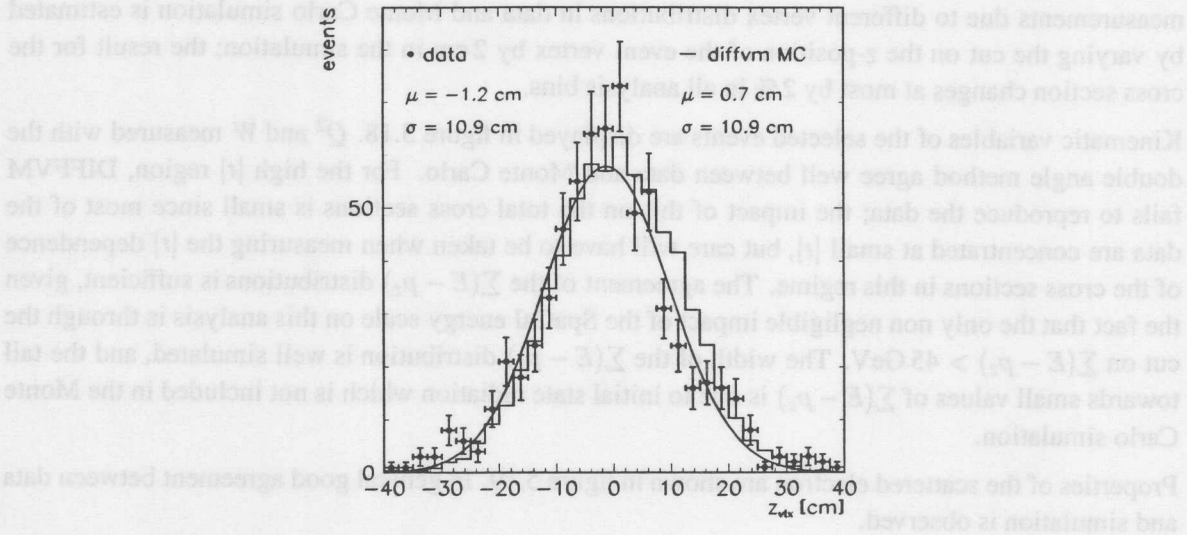
Figure 5.17: *Comparison of the distributions of the event vertex z position z_{vtx} in data and Monte Carlo. The full line is a fit of a Gaussian to the data.*
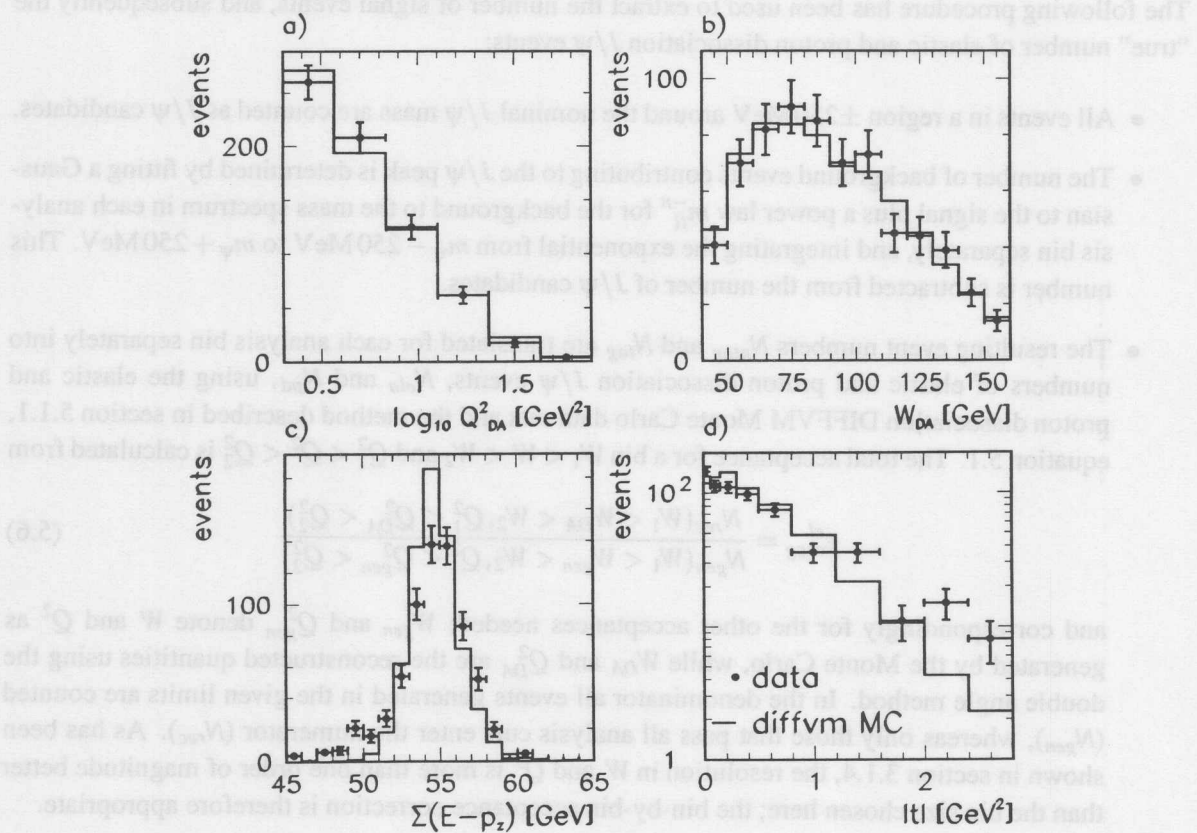
Figure 5.18: *Comparison of data and Monte Carlo simulation for exclusive J/ψ candidates; a) Q^2_{DA}, b) W_{DA}, c) $\Sigma(E - p_z)$ and d) $|t|$. The Monte Carlo histograms are normalized to the data.*
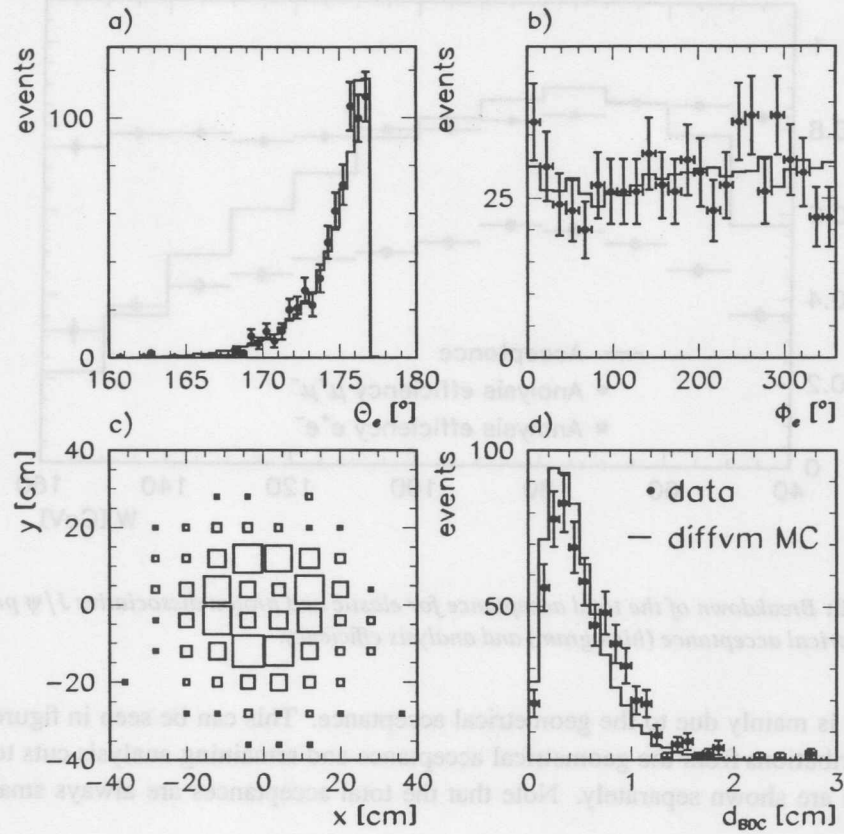
Figure 5.19: *Comparison of data and Monte Carlo simulation for exclusive J/ψ candidates with respect to the scattered electron; a) polar angle θ_e of the scattered electron, b) azimuthal angle ϕ_e, c) xy-coordinates of the scattered electron in the SpaCal (only data), d) distance d_{BDC} to the closest BDC track.*

Q^2 interval	W interval	$\varepsilon_{ntag}^{el}[\%]$	$\varepsilon_{tag}^{el}[\%]$	$\varepsilon_{ntag}^{pd}[\%]$	$\varepsilon_{tag}^{pd}[\%]$
$2 < Q^2 < 6\,\text{GeV}^2$	$40 < W < 80\,\text{GeV}$	42.6 ± 0.8	3.8 ± 0.3	8.9 ± 0.5	34.0 ± 0.8
	$80 < W < 120\,\text{GeV}$	47.3 ± 0.9	4.3 ± 0.4	7.2 ± 0.4	31.4 ± 0.8
	$120 < W < 160\,\text{GeV}$	22.9 ± 0.9	1.6 ± 0.3	3.4 ± 0.3	15.2 ± 0.7
$6 < Q^2 < 18\,\text{GeV}^2$	$40 < W < 80\,\text{GeV}$	42.8 ± 1.2	5.1 ± 0.6	9.7 ± 0.9	38.3 ± 1.4
	$80 < W < 120\,\text{GeV}$	54.8 ± 1.5	4.3 ± 0.5	9.7 ± 0.8	39.9 ± 1.4
	$120 < W < 160\,\text{GeV}$	33.6 ± 1.0	2.8 ± 0.5	6.0 ± 0.7	23.8 ± 1.4
$18 < Q^2 < 80\,\text{GeV}^2$	$40 < W < 160\,\text{GeV}$	48.6 ± 1.4	4.2 ± 0.7	8.6 ± 1.2	40.1 ± 2.0

Table 5.1: *Total acceptance for elastic and proton dissociative J/ψ production. The given errors are from Monte Carlo statistics.*
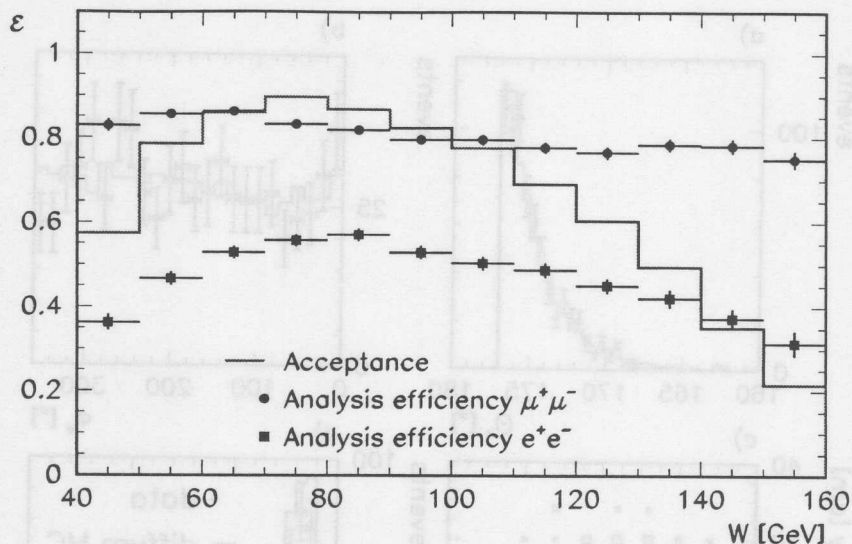
Figure 5.20: *Breakdown of the total acceptance for elastic and proton dissociative J/ψ production into geometrical acceptance (histogram) and analysis efficiency.*

numbers is mainly due to the geometrical acceptance. This can be seen in figure 5.20, where the contributions from the geometrical acceptance and remaining analysis cuts to the total acceptance are shown separately. Note that the total acceptances are always smallest for high W.

Tables comprising the acceptance in the electron and muon decay channels separately are given in the appendix.

The systematic error introduced by the method used for the determination of the number of signal events was estimated to be 4 % by changing the functional form of the background shape from a power law to an exponential.

5.2   Results on Elastic and Proton Dissociative J/ψ Production

In this section cross sections for elastic and proton dissociative J/ψ production will be derived and discussed in the light of available models. The first part includes an evaluation of the Q^2 and W dependencies, followed by an analysis of the $|t|$ spectra. Finally the helicity structure of exclusive J/ψ production will be investigated.

5.2.1   Elastic and Proton Dissociative Cross Section as Function of W and Q^2

This section is organized as follows: first the calculation of the integrated cross section for ep scattering is presented, and remaining backgrounds in the event samples are discussed. These ep cross sections, both for elastic and proton dissociation J/ψ production, are then converted into virtual photon proton cross sections at fixed values of W_0 and Q_0^2. A breakdown of systematic errors follows, before finally the W and Q^2 dependence of the $\gamma^* p$ cross sections is discussed.

Calculation of ep Cross Sections

The bin-integrated cross section for elastic and proton dissociation J/ψ production, σ_{ep}^{el} and σ_{ep}^{pd}, can be calculated from

$$\sigma_{ep}^{el} = \frac{N_{el} \cdot (1 - f_{\psi(2S)}) \cdot (1 + f_{noise})}{(1 + \delta_{RC}) \cdot BR \cdot \int L dt} \quad \text{and}$$

$$\sigma_{ep}^{pd} = \frac{N_{pd} \cdot (1 - f_{\psi(2S)}) \cdot (1 - f_{noise})}{(1 + \delta_{RC}) \cdot BR \cdot \int L dt},$$

(5.7)

where N_{el} and N_{pd} are the "true" numbers of elastic and proton dissociation events in each bin after acceptance and efficiency correction, obtained from the measured numbers as described in section 5.1.1, $f_{\psi(2S)}$ is the contamination from decays of the $\psi(2S)$ meson, $(1 + f_{noise})$ and $(1 - f_{noise})$ are factors taking into account noise in the Forward Muon Detector. δ_{RC} is the correction to the Born cross section necessary due to initial state radiation (section 3.1.6), and $\int L dt$ is the integrated luminosity as given in section 4.1.2. Finally, BR is the branching fraction for the J/ψ meson to decay into $\mu^+\mu^-$ or e^+e^- [30]:

$$BR = (12.03 \pm 0.38)\,\%$$

(5.8)

with almost equal contributions from the $\mu^+\mu^-$ and the e^+e^- decay channel.

Background from $\psi(2S)$ Production

$\psi(2S)$ mesons decay predominantly via channels which include a J/ψ meson: $BR(\psi(2S) \to \psi + \text{anything}) = (57 \pm 4)\,\%$ [30]; therefore $\psi(2S)$ production can be a major source of background to direct J/ψ production. The ratio of cross sections for $\psi(2S)$ and J/ψ production has been measured by H1 in the photoproduction regime in a comparable range of W to this analysis to be $(15.0 \pm 3.5)\,\%$ [170]. In the forthcoming chapter 6, this ratio will be determined for higher values of Q^2; this measurement is used to subtract the $\psi(2S)$ contribution to the J/ψ sample.

The only decay channels which contribute significantly are

$$
\begin{aligned}
\psi(2S) &\longrightarrow J/\psi\,\pi^0\pi^0, \\
\psi(2S) &\longrightarrow J/\psi\,\eta \quad \text{and} \\
\psi(2S) &\longrightarrow J/\psi\,\pi^0
\end{aligned}
$$

(5.9)

with a total branching fraction of $(20.4 \pm 3.0)\,\%$ [30], including only the neutral decay modes of the η meson. Other decay modes of the $\psi(2S)$, especially the most prominent one $\psi(2S) \to J/\psi\,\pi^+\pi^-$, are neglected since usually at least one of the charged pions is reconstructed in the jet chambers, and the event does not enter the J/ψ data sample.

The background from $\psi(2S)$ decays thus estimated varies in the Q^2 range used here between $f_{\psi(2S)} = (4.2 \pm 1.2)\,\%$ for low Q^2 and $(11.5 \pm 8.0)\,\%$ for high Q^2. It is subtracted from all cross sections for elastic and proton dissociative J/ψ production.

Noise in the Forward Detectors

In previous diffractive analyses using data taken in 1994 (for example [78]) a correction was applied in order to take into account spurious hits observed in the drift chambers of the forward muon system,

	Fraction [%]		
	1995	1996	1997
Proton Remnant Tagger	0.1 ± 0.0	0.1 ± 0.0	0.2 ± 0.1
Forward Muon Detector	5.7 ± 1.2	4.8 ± 0.9	7.2 ± 1.1

Table 5.2: *Fraction of events with noise in the forward detectors, leading to the classification as "forward tagged". The numbers are determined from randomly triggered events. Note that for each year only a short period of data taking was investigated, thus fluctuations within one year are not taken into account.*

which are not present in the Monte Carlo simulation. From the obervations in section 5.1.6 there is an indication that also in the data used here noise hits in the FMD are present, since the FMD is the forward detector which predicts the smallest amount of genuine elastic events. Therefore the elastic cross sections are increased by 2 %, while the proton dissociation cross sections are decreased by 2 %. The systematic errors due to noise in the forward detectors are already covered by the studies made in section 5.1.6.

A dedicated analysis has been performed to check the noise level in the FMD and PRT. Randomly triggered events taken during normal luminosity running are used to estimate the fraction of events accidentally classified as forward tagged. The results for the three data taking periods are given in table 5.2; noise in the PRT is generally negligible, while the noise level in the FMD is slightly higher than the correction of 2 % mentioned above that is actually applied. Note that due to random coincidences of noise and *true* hits the necessary correction of the cross sections is smaller than the measured noise level. Since about 40 % of all events are in the forward tagged sample, a noise level of 6 % corresponds to a cross section correction of about 3 %. Since the difference of this value to the 2 % correction actually applied is well within the systematic error due to the separation between elastic and proton dissociation events, no further correction is applied.

Calculation of $\gamma^* p$ Cross Sections

In the Weizsäcker-Williams-Approximation [158]–[161] the Born cross section $\frac{d^2\sigma_{ep}}{dy\,dQ^2}$ factorizes into the equivalent flux of transversely polarized virtual photons Γ_T times the total photon proton cross section $\sigma_{\gamma^* p} := \sigma_{\gamma^* p}^T + \sigma_{\gamma^* p}^L$ (see section 3.1.1):

$$\frac{d^2\sigma_{ep}(y, Q^2)}{dy\,dQ^2} = \Gamma_L \cdot \sigma_{\gamma^* p}^L + \Gamma_T \cdot \sigma_{\gamma^* p}^T \tag{5.10}$$

$$= \Gamma_T \cdot \sigma_{\gamma^* p}^T \cdot (1 + \varepsilon R) \tag{5.11}$$

$$= \Gamma_T \cdot \sigma_{\gamma^* p} \cdot \frac{1 + \varepsilon R}{1 + R} \tag{5.12}$$

$$\simeq \Gamma_T \cdot \sigma_{\gamma^* p}, \tag{5.13}$$

where $\sigma_{\gamma^* p}^T$ and $\sigma_{\gamma^* p}^L$ are the transverse and longitudinal photon proton cross sections, $R := \sigma_{\gamma^* p}^L / \sigma_{\gamma^* p}^T$, Γ_L is the flux of longitudinal photons, and the polarization parameter $\varepsilon := \Gamma_L/\Gamma_T$ denotes the ratio of

the longitudinal to the transverse photon flux:

$$\varepsilon := \frac{\Gamma_L}{\Gamma_T} = \frac{1-y}{1-y+y^2/2}.$$ (5.14)

In the kinematic region of this analysis ε varies between 0.95 and 1 with an average of 0.99. Γ_T is given by

$$\Gamma_T = \frac{\alpha}{2\pi y Q^2} \cdot \left(1 + (1-y)^2 - 2m_e^2 \frac{y^2}{Q^2}\right),$$ (5.15)

where α is the electromagnetic coupling and m_e the electron mass. Note that this is an improved form of the Weizsäcker-Williams-Approximation where terms of the order of m_e^2/Q^2 are included [161]. Integrating over y and Q^2 one obtains

$$\sigma_{ep} = \int_{y_{min}}^{y_{max}} dy \int_{Q_{min}^2}^{Q_{max}^2} dQ^2\, \Gamma_T(y,Q^2)\, \sigma_{\gamma^* p}(y,Q^2) \quad \text{with}$$ (5.16)

$$Q_{min}^2 = m_e^2 \cdot \frac{y^2}{1-y}.$$ (5.17)

Defining

$$\mathcal{F} = \int_{y_{min}}^{y_{max}} dy \int_{Q_{min}^2}^{Q_{max}^2} dQ^2\, \Gamma_T(y,Q^2),$$ (5.18)

a point (y_0, Q_0^2) — or equivalently (W_0, Q_0^2) — can be found for which

$$\sigma_{ep} = \mathcal{F} \cdot \sigma_{\gamma^* p}(W_0, Q_0^2),$$ (5.19)

holds. Equation 5.19 is used to convert the cross section for electron proton scattering integrated over a specific analysis bin into a cross section for virtual photon proton scattering at a point (W_0, Q_0^2). The *bin centre* (W_0, Q_0^2) is determined by requiring

$$\mathcal{F} \stackrel{!}{=} \int_{y_{min}}^{y_{max}} dy \int_{Q_{min}^2}^{Q_{max}^2} dQ^2\, \Gamma_T(y,Q^2) \left(\frac{W}{W_0}\right)^{4\varepsilon} \left(\frac{m_\psi^2 + Q_0^2}{m_\psi^2 + Q^2}\right)^n$$ (5.20)

assuming

$$\sigma_{\gamma^* p}(W, Q^2) \sim \frac{W^{4\varepsilon}}{(m_\psi^2 + Q^2)^n},$$ (5.21)

i.e. the plain integrated photon flux is required to be equal to the one weighted with the expected Q^2 and W dependence of the photon proton cross section. Due to the choice of ε and n an additional systematic error is introduced; it can be estimated by varying ε and n within reasonable values. For the results given below, $\varepsilon = 0.25$ and $n = 2$ have been chosen, and the change in W_0 and Q_0^2 under variation of ε between 0.1 and 0.4, and n between 1.5 and 2.5, have been translated into an error on the cross section normalization; it is generally smaller then 2 %, with the exception of the highest Q^2 bin, where the uncertainty reaches $^{+6\%}_{-3\%}$ due to the very large range in W covered by this bin.

Source		Amount [%]	see section
trigger efficiency	(*)	5	5.1.3
lepton identification		6	5.1.5
track and vertex efficiency		5	5.1.4
z-vertex distribution		2	5.1.7
e^+ angular resolution		5	5.2.1
radiative corrections		3	3.1.6
non-resonant background shape		4	5.1.8
separation elastic–p-dissociation		10	5.1.6
$\psi(2S)$ background	(*)	4	5.2.1
bin centre determination	(*)	2	5.2.1
J/ψ branching ratio		3.2	5.2.1
luminosity	(*)	2.8	4.1.2
Total systematic error	(*)	17	

Table 5.3: *Summary of systematic uncertainties for elastic and proton dissociative J/ψ production. For lines marked with (*), the error varies with W and Q^2, or with the data taking period; in these cases averages are given.*

Summary of Systematic uncertainties

All known experimental systematic uncertainties are summarized in table 5.3, together with a reference to the section where they are discussed. Adding all contributions in quadrature, the total systematic error of the cross section measurement amounts to typically 15 %. Note that the uncertainty arising from the limited statistics of the Monte Carlo data sets is absorbed into the statistical error; its size is about 1 % for small Q^2 and rises to 4 % in the high Q^2 bin.

Except for two relatively small contributions, namely the error on the J/ψ branching ratio and the luminosity, all errors not only affect the absolute normalization, but are potentially dependent on Q^2 and W.

The SpaCal energy scale uncertainty does not contribute significantly to the total systematic uncertainty, since the measured electron energy is only used for the calculation of $\sum(E - p_z)$; a shift in $\sum(E - p_z)$ of 2 GeV affects only the amount of the radiative corrections by less than 1 % of the cross section. The error due to the limited angular resolution for the scattered electron has been estimated by varying its angle up and down by 2 mrad in the case that no BDC track is associated to the electron, and by 0.5 mrad otherwise, and taking the change in the cross section as systematic error.

In table 5.4 numbers of observed events and ep and $\gamma^* p$ cross sections both for the elastic and proton dissociation case are summarized. The electron and muon decay channels as well as the three data taking periods have been combined here; the separate contributions are detailed in the appendix.

		$2 < Q^2 < 6\,\mathrm{GeV^2}$		
		$40 < W < 80\,\mathrm{GeV}$	$80 < W < 120\,\mathrm{GeV}$	$120 < W < 160\,\mathrm{GeV}$
N_{ntag}		109.3 ± 11.5	100.4 ± 10.9	42.1 ± 7.0
N_{tag}		62.1 ± 8.6	50.5 ± 7.8	10.6 ± 3.7
N_{el}		223.6 ± 28.5	192.1 ± 24.1	176.1 ± 32.2
σ_{ep}^{el}	$[pb]$	$88.0 \pm 11.2 \pm 14.1$	$75.6 \pm 9.5 \pm 12.1$	$69.3 \pm 12.7 \pm 11.1$
$\mathcal{F}$		0.003408	0.001858	0.001187
$\sigma_{\gamma^* p}^{el}$	$[nb]$	$25.8 \pm 3.3 \pm 4.1$	$40.7 \pm 5.1 \pm 6.5$	$58.4 \pm 10.7 \pm 9.3$
W_0	$[\mathrm{GeV}]$	57.5	98.4	138.6
Q_0^2	$[\mathrm{GeV^2}]$	3.5	3.5	3.5
N_{pd}		170.2 ± 25.6	147.2 ± 25.2	65.5 ± 24.3
σ_{ep}^{pd}	$[pb]$	$64.4 \pm 9.7 \pm 10.3$	$55.7 \pm 9.5 \pm 8.9$	$27.2 \pm 10.0 \pm 4.4$
$\sigma_{\gamma^* p}^{pd}$	$[nb]$	$18.9 \pm 2.8 \pm 3.0$	$30.0 \pm 5.1 \pm 4.8$	$22.9 \pm 8.3 \pm 3.6$
		$6 < Q^2 < 18\,\mathrm{GeV^2}$		
		$40 < W < 80\,\mathrm{GeV}$	$80 < W < 120\,\mathrm{GeV}$	$120 < W < 160\,\mathrm{GeV}$
N_{ntag}		29.7 ± 5.6	32.3 ± 6.1	26.8 ± 5.8
N_{tag}		32.5 ± 6.1	40.4 ± 6.7	17.8 ± 4.7
N_{el}		52.4 ± 14.1	41.5 ± 11.9	68.3 ± 18.4
σ_{ep}^{el}	$[pb]$	$20.6 \pm 5.5 \pm 3.7$	$16.4 \pm 4.7 \pm 3.0$	$26.8 \pm 7.2 \pm 4.8$
$\mathcal{F}$		0.003398	0.001859	0.001188
$\sigma_{\gamma^* p}^{el}$	$[nb]$	$6.05 \pm 1.62 \pm 1.09$	$8.80 \pm 2.50 \pm 1.65$	$22.5 \pm 6.1 \pm 4.0$
W_0	$[\mathrm{GeV}]$	57.5	98.4	138.6
Q_0^2	$[\mathrm{GeV^2}]$	10.1	10.1	10.1
N_{pd}		80.2 ± 16.1	98.9 ± 17.2	73.1 ± 20.0
σ_{ep}^{pd}	$[pb]$	$30.2 \pm 6.0 \pm 5.4$	$37.2 \pm 6.5 \pm 6.7$	$27.5 \pm 7.6 \pm 4.9$
$\sigma_{\gamma^* p}^{pd}$	$[nb]$	$8.88 \pm 1.79 \pm 1.60$	$20.0 \pm 3.5 \pm 3.6$	$23.2 \pm 6.3 \pm 4.2$
		$18 < Q^2 < 80\,\mathrm{GeV^2},\ 40 < W < 160\,\mathrm{GeV}$		
N_{ntag}		22.7 ± 5.2		
N_{tag}		8.9 ± 4.0		
N_{el}		43.0 ± 11.2		
σ_{ep}^{el}	$[pb]$	$16.0 \pm 4.1 \pm 3.2$		
$\mathcal{F}$		0.008675		
$\sigma_{\gamma^* p}^{el}$	$[nb]$	$1.84 \pm 0.48 \pm 0.37$		
W_0	$[\mathrm{GeV}]$	84.4		
Q_0^2	$[\mathrm{GeV^2}]$	33.6		
N_{pd}		20.4 ± 10.1		
σ_{ep}^{pd}	$[pb]$	$8.0 \pm 4.0 \pm 1.6$		
$\sigma_{\gamma^* p}^{pd}$	$[nb]$	$0.92 \pm 0.46 \pm 0.19$		

Table 5.4: *Summary of elastic and proton dissociation cross sections.*

Cross Section as a Function of W

The cross sections measured for elastic J/ψ production are displayed as a function of W in figure 5.21, together with other measurements performed at HERA [78, 66, 85, 86] both in photoproduction and at high Q^2.

Fits of the form $\sim W^\delta$ have been performed to the data separately for $Q^2 = 0$, 3.5 and 10.1 GeV^2, with the results also shown in figure 5.21. The values obtained for δ are

$$\begin{aligned}
\delta &= 0.99 \pm 0.15 \quad &\text{for} \quad Q^2 = 0\,\text{GeV}^2, \\
\delta &= 0.82 \pm 0.38 \quad &\text{for} \quad Q^2 = 3.5\,\text{GeV}^2 \text{ and} \\
\delta &= 1.42 \pm 0.55 \quad &\text{for} \quad Q^2 = 10.1\,\text{GeV}^2,
\end{aligned} \qquad (5.22)$$

where full systematic errors have been included in the fits. The cross section rises strongly with W, with some indication for an even stronger rise at high Q^2 than in photoproduction. For all Q^2, the rise is stronger than expected in "soft" Pomeron models (section 3.2.1), $\sim W^{0.22-0.32}$.

A comparison with results from fixed target experiments is done in figure 5.22. Data on elastic J/ψ production at Q^2 values comparable to this measurement are sparse. The only measurements avail-
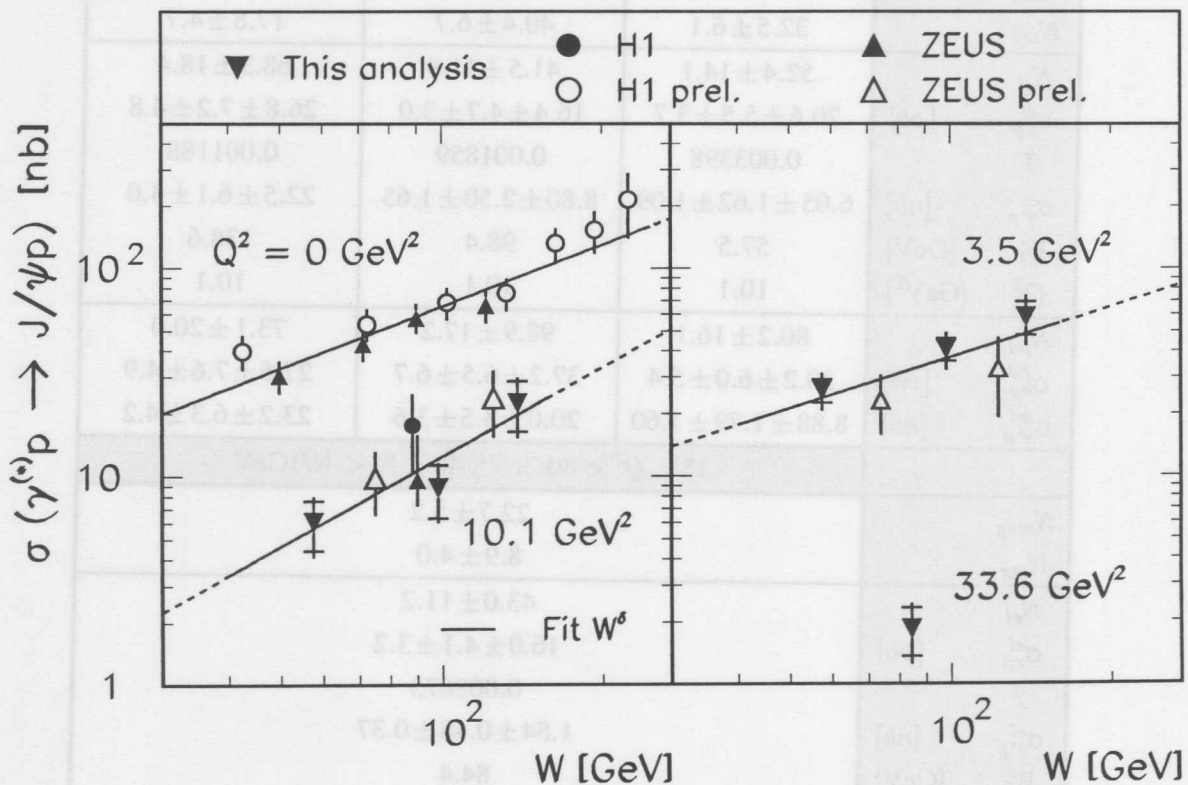
Figure 5.21: *Cross sections measured at HERA [78, 66, 85, 86] for* **elastic** *J/ψ production as a function of W in different domains of Q^2, on the left for photoproduction and $Q^2 = 10.1\,GeV^2$, on the right for $Q^2 = 3.5\,GeV^2$ and $Q^2 = 33.6\,GeV^2$. The inner error bars are statistical, while the outer ones include statistical and systematic errors added in quadrature. The lines are fits to the data of the form $\sim W^\delta$, the W range of the measurements is indicated by the full lines.*

able, from the EMC collaboration [38], do not explicitly separate elastic and proton dissociation J/ψ production. A comparison between different fixed target experiments reveals that in photoproduction the EMC measurements would be too high compared to other fixed target experiments if they were interpreted as elastic cross sections. Despite this problem, extrapolating the fits through the HERA data back to fixed target energies as done in figure 5.22 gives good agreement between the extrapolation and the EMC results for $Q^2 = 3.5\,\mathrm{GeV}^2$; at $Q^2 = 10.1\,\mathrm{GeV}^2$, EMC results are too high compared to the extrapolation.

Within calculations that model elastic J/ψ production with the exchange of gluons (see section 3.2.2) the rise of the cross section with W is connected to the rise of the gluon density in the proton towards smaller x. Later in this section, the measured cross section will be interpreted as a measurement of the gluon density within the Ryskin approach (see section 5.2.2).

In figure 5.23, the cross sections measured at HERA and in fixed target experiments are compared
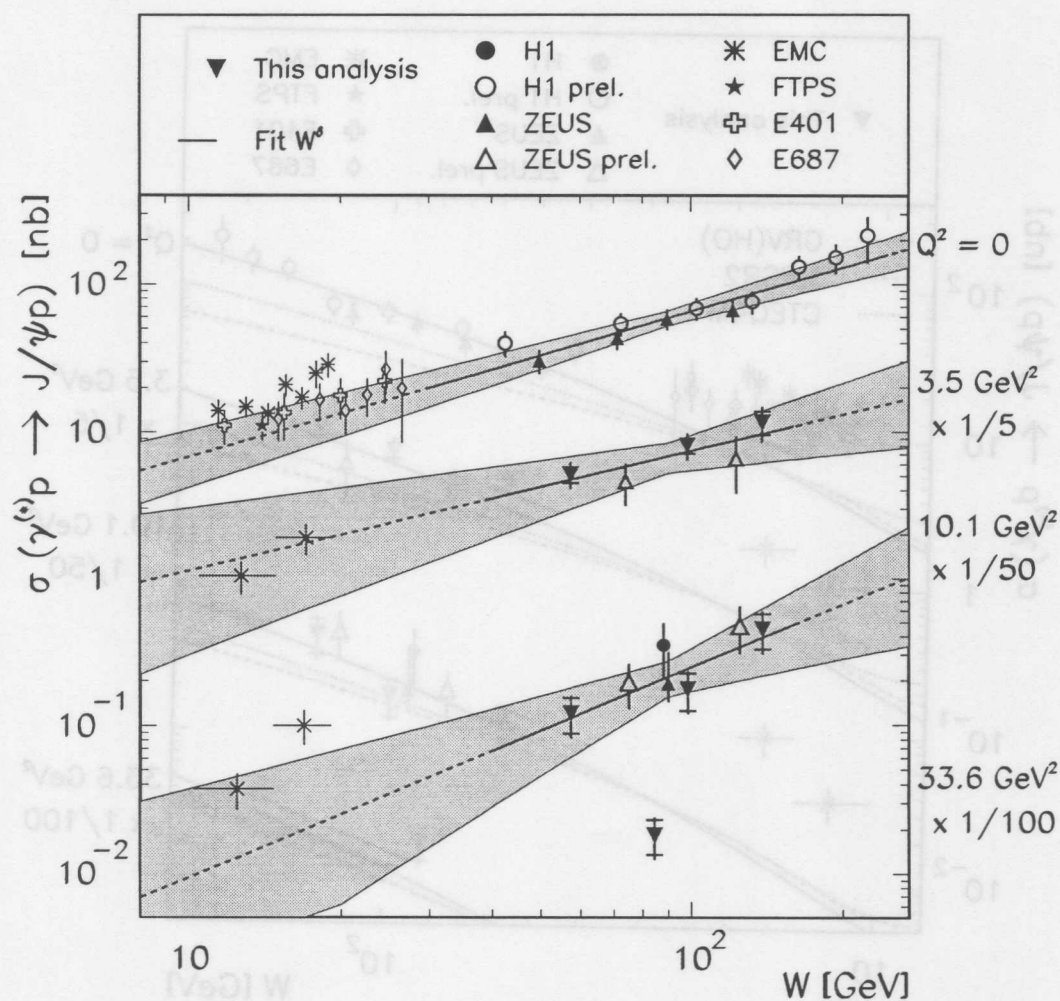
Figure 5.22: *Cross sections measured at HERA [78, 66, 85, 86] and in the fixed target experiments FTPS (E516) [171], E401 [172], E687 [173] and EMC [38] for* **elastic** *J/ψ production as a function of W in different domains of Q^2. Data at $Q^2 > 0\,\mathrm{GeV}^2$ have been scaled as indicated on the plot. The lines are fits to the HERA data of the form $\sim W^\delta$ (equation 5.22), with the errors from the fit indicated as bands.*

to calculations of Frankfurt, Koepf and Strikman [68] (see section 3.2.2) for different parton distributions. For the theoretical predictions, the charm quark mass has been set to $m = 1.5\,\text{GeV}$ and a logarithmic potential for the $c\bar{c}$ was used. The HERA data are rather well described both in shape and normalization, while the model is not able to describe low energy fixed target results. It should be noted that also other models predict a strong rise of the cross section with W, most notably the colour dipole approach employing the generalized BFKL equation by Nemchik, Nikolaev, Zakharov and others [46]–[49]; thus such an inclusive quantity as the total cross section is not well suited to distinguish different models for elastic J/ψ production.

As described in section 3.1.1, the total photon proton cross section is directly related to the structure function F_2:

$$\sigma_{\gamma^* p} \simeq \frac{4\pi^2 \alpha}{Q^2} \cdot F_2. \tag{5.23}$$
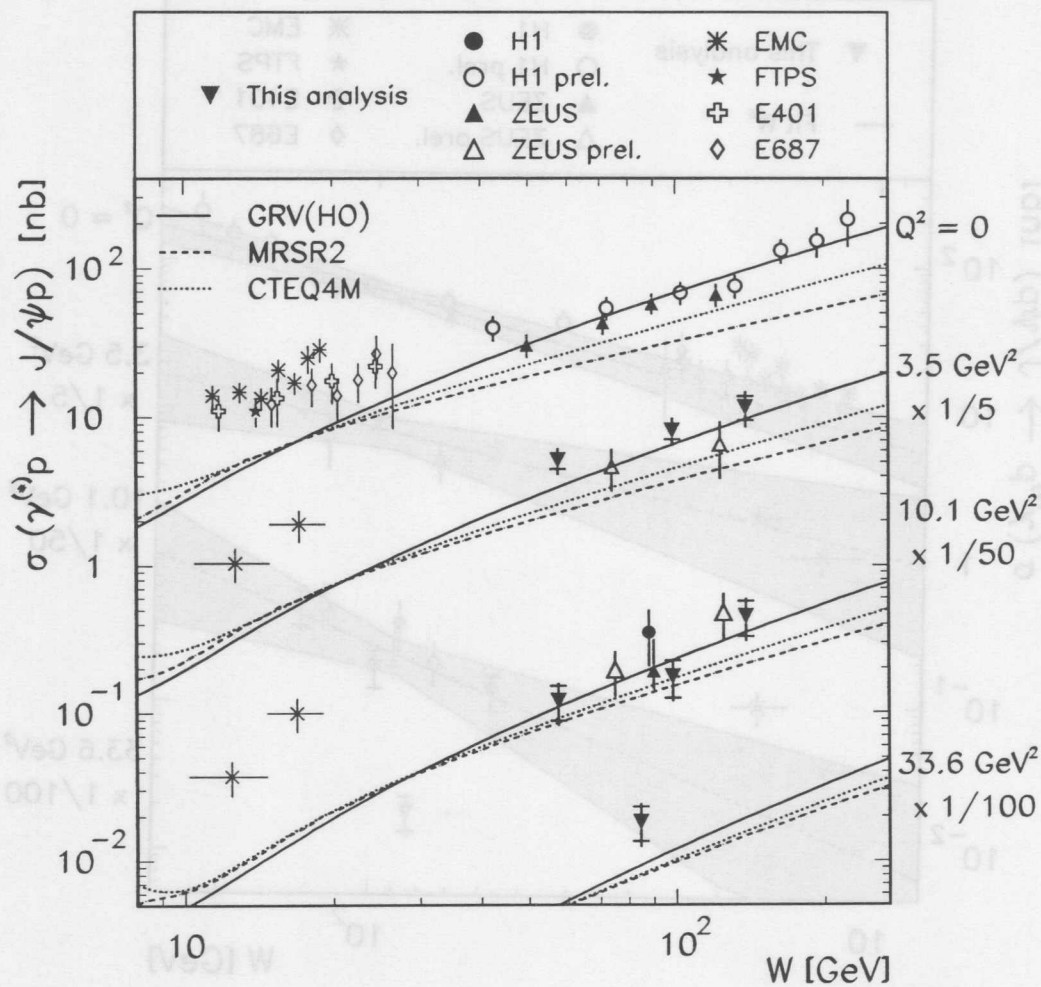
Figure 5.23: *Cross sections measured at HERA [78, 66, 85, 86] and in the fixed target experiments FTPS [171], E401 [172], E687 [173] and EMC [38] for* **elastic** *J/ψ production as a function of W in different domains of Q^2. Data at $Q^2 > 0\,\text{GeV}^2$ have been scaled by factors 5, 50, 100 as indicated. The lines are results of calculations from Frankfurt, Koepf and Strikman [68] for several recent parton distributions, GRV(HO) [112], MRSR2 [174] and CTEQ4M [108].*
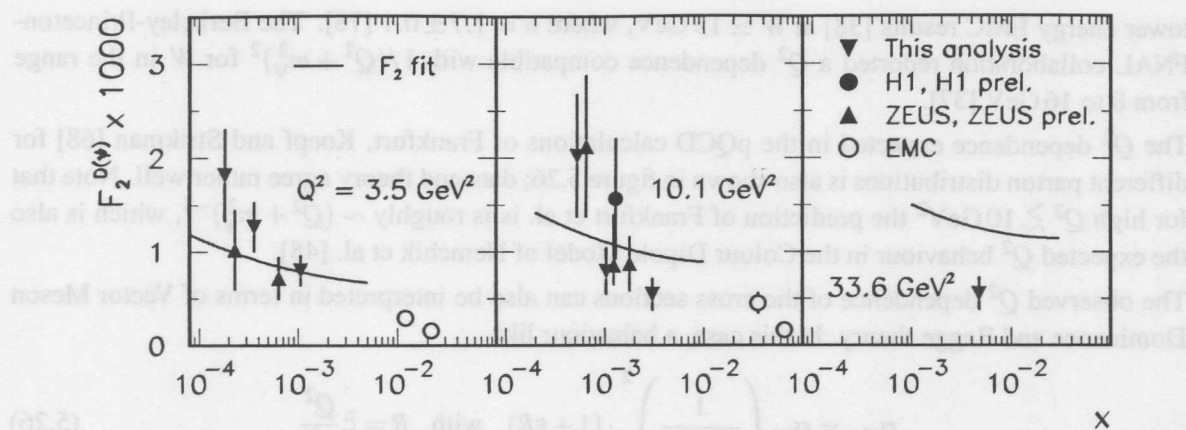
Figure 5.24: *Elastic J/ψ production cross sections expressed in terms of a structure function $F_2^{D(\psi)}$ as a function of x at three values of Q^2. Note the scale factor of 1000. A parameterization of the inclusive structure function F_2 (without this scale factor) is shown for comparison (equation 8, table 3 from [40]).*

Using an equivalent expression for J/ψ production

$$\sigma_{\gamma^* p}^{\psi} := \frac{4\pi^2 \alpha}{Q^2} \cdot F_2^{D(\psi)},$$ (5.24)

the J/ψ production cross section can equivalently be expressed in terms of a structure function $F_2^{D(\psi)}$, shown in figure 5.24 for elastic J/ψ production. As the inclusive F_2, $F_2^{D(\psi)}$ rises strongly towards smaller x. The ratio $F_2^{D(\psi)}/F_2$ is of the order of 10^{-3} for the kinematic range analyzed here.

The cross sections measured for J/ψ **production with proton dissociation** are displayed as a function of W in figure 5.25, together with the H1 measurement [65] in photoproduction and cross sections for elastic J/ψ production for comparison. Note that the given proton dissociation cross section are for $M_Y \lesssim 15\,\text{GeV}$ according to the Monte Carlo simulation implemented in the DIFFVM program.

As in the elastic case, the cross section rises strongly with W, with a slope that is compatible between photoproduction and $Q^2 > 0$. A simultaneous fit of the form $\sim W^\delta$ has been performed to the data on proton dissociation displayed in figure 5.25, with the results shown as full lines. Including full systematic errors, the value obtained for δ is

$$\delta = 1.05 \pm 0.20,$$ (5.25)

which is comparable to the elastic J/ψ results.

Cross Section as a Function of Q^2

The cross sections measured for elastic J/ψ production at $W_0 = 90\,\text{GeV}$ are displayed as a function of $Q^2 + m_\psi^2$ in figure 5.26, together with other measurements performed at HERA [78, 65, 66, 86] both in photoproduction and at high Q^2. The HERA data can be well parameterized with a function $\sim (Q^2 + m_\psi^2)^{-n}$, a fit through all data shown[1] yields $n = 2.24 \pm 0.19$. This can be compared to the

---

[1] H1 1995 preliminary results have not been used for the fit since the data taken in 1995 are included in the results derived here.

lower energy EMC results [38] at $W \simeq 15\,\mathrm{GeV}$, where $n = 1.7 \pm 0.1$ [78]. The Berkeley-Princeton-FNAL collaboration reported a Q^2 dependence compatible with $1/(Q^2 + m_\psi^2)^2$ for W in the range from 8 to 16 GeV [37].

The Q^2 dependence expected in the pQCD calculations of Frankfurt, Koepf and Strikman [68] for different parton distributions is also shown in figure 5.26; data and theory agree rather well. Note that for high $Q^2 \gtrsim 10\,\mathrm{GeV}^2$ the prediction of Frankfurt et al. is is roughly $\sim (Q^2 + m_\psi^2)^{-3}$, which is also the expected Q^2 behaviour in the Colour Dipole Model of Nemchik et al. [48].

The observed Q^2 dependence of the cross sections can also be interpreted in terms of Vector Meson Dominance and Regge theory. In this case, a behaviour like

$$\sigma_{\gamma^* p} = \sigma_{\gamma p} \left(\frac{1}{1 + \frac{Q^2}{m_\psi^2}} \right)^2 \cdot (1 + \varepsilon R) \quad \text{with} \quad R = \xi \frac{Q^2}{m_\psi^2} \tag{5.26}$$

is expected (see section 4.6.1), where ε is known and close to 1, and ξ positive and of the order 1; for $\xi = 1$, $\sigma_{\gamma^* p} \sim 1/(Q^2 + m_\psi^2)$ (see figure 5.26). A fit of equation 5.26 to all data shown yields
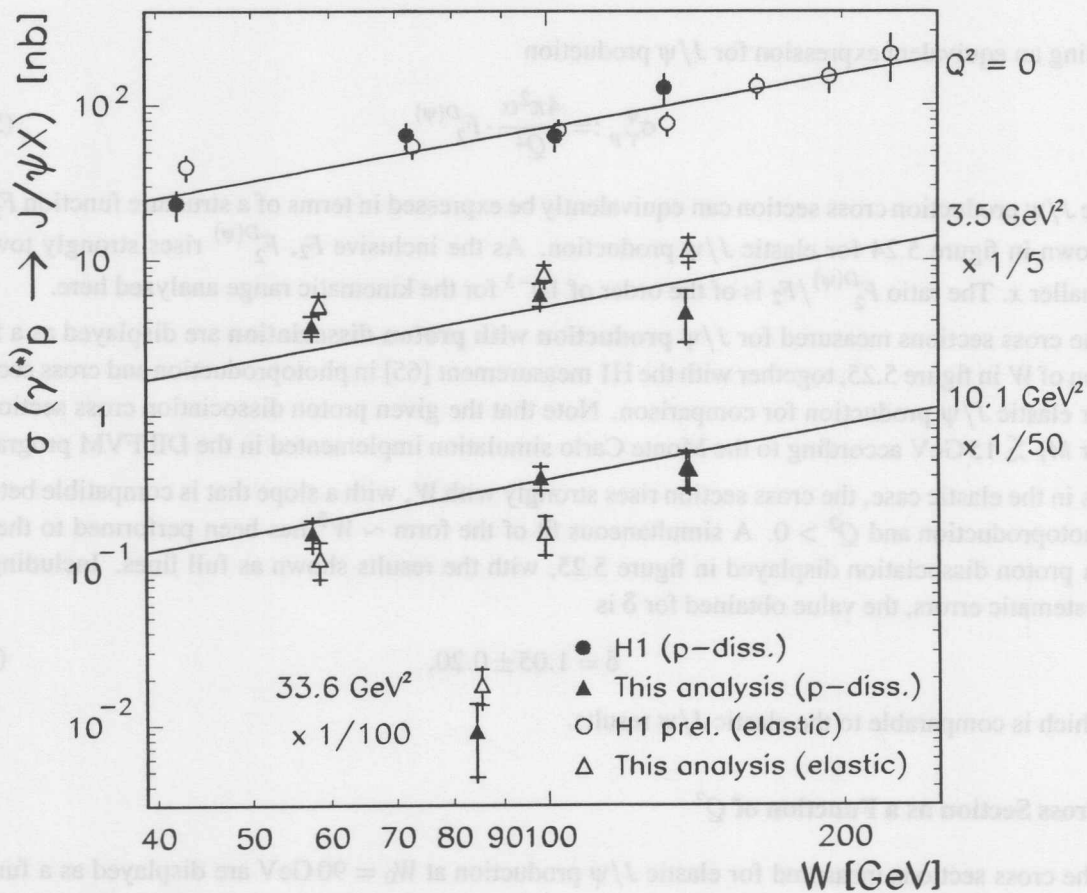
Figure 5.25: *Cross sections for J/ψ production with **proton dissociation** as a function of W in different domains of Q^2. The lines are the result of a simultaneous fit to the photoproduction data [65] and the results of the present analysis of the form $\sim W^\delta$. For comparison, the results for elastic J/ψ production — from [85] for $Q^2 = 0$ and this analysis for $Q^2 > 0$ — are shown as open symbols, at slightly shifted values of W to increase readability.*

$\xi = -0.09 \pm 0.07$, i.e. the cross section for longitudinally polarized photons is constrained to be very small; this is in contradiction to the decay angular distributions that will be extracted in section 5.2.5, and therefore indicates that VDM and Regge theory are not able to provide a consistent description of elastic J/ψ production. Measurements of $R = \sigma^L/\sigma^T$ for different vector mesons indicate a value of $\xi \simeq 0.3$ (see figure 5.37).

The cross section for proton dissociative J/ψ production is found to have a similar Q^2 dependence as for elastic production. Again, a fit $\sim (Q^2 + m_\psi^2)^{-n}$ to the data including H1 photoproduction results [65] has been performed; the result, as shown in figure 5.27, is $n = 2.6 \pm 0.3$, compatible with the above result for elastic J/ψ production.

5.2.2 The Gluon Density in the Proton

In the pQCD calculations of Ryskin et al. (see section 3.2.2) the elastic J/ψ virtual photoproduction cross section is directly related to the gluon density in the proton $xg(x)$. The leading order result for $xg(x)$ is

$$[xg(x, Q_{eff}^2)]^2 = \frac{48\alpha}{\Gamma_{ee} m_\psi^3 \pi^3} \cdot b^{el} \cdot \sigma_{\gamma p} \cdot \frac{Q_{eff}^8}{\alpha_s^2(Q_{eff}^2)} \cdot \left(1 + \frac{Q^2}{m_\psi^2}\right)^{-1} \tag{5.27}$$
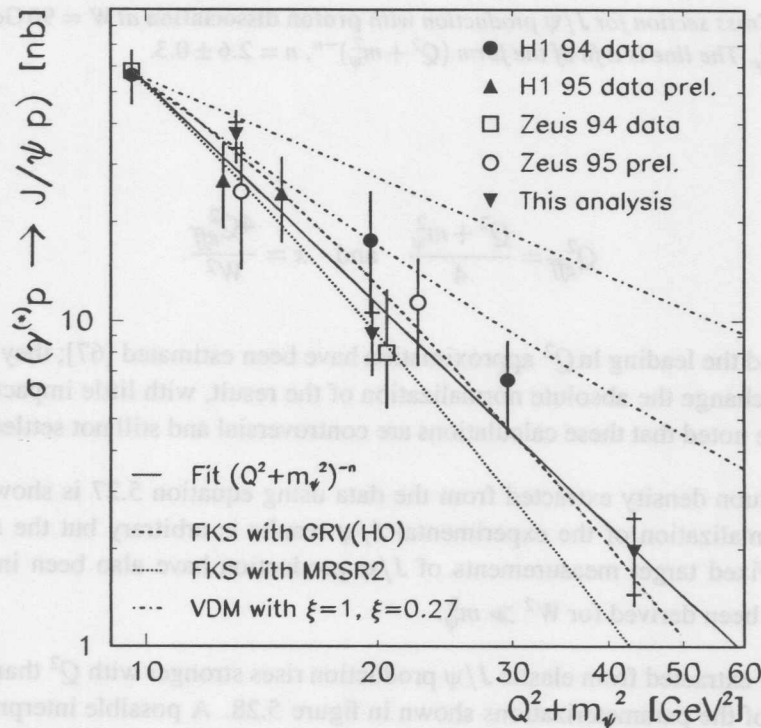
Figure 5.26: *Cross section for* **elastic** *J/ψ production at $W = 90$ GeV as a function of $Q^2 + m_\psi^2$. The full line is a fit of the form $(Q^2 + m_\psi^2)^{-n}$, $n = 2.24 \pm 0.19$. The dashed and dotted lines are predictions within the model of Frankfurt, Koepf and Strikman [68] for different parameterizations of the gluon density in the proton, GRV(HO) [112] and MRSR2 [174]. The dash-dotted lines are VDM predictions, the upper one with $\xi = 1$, $\sim 1/(Q^2 + m_\psi^2)$, the lower one with $\xi = 0.27$.*
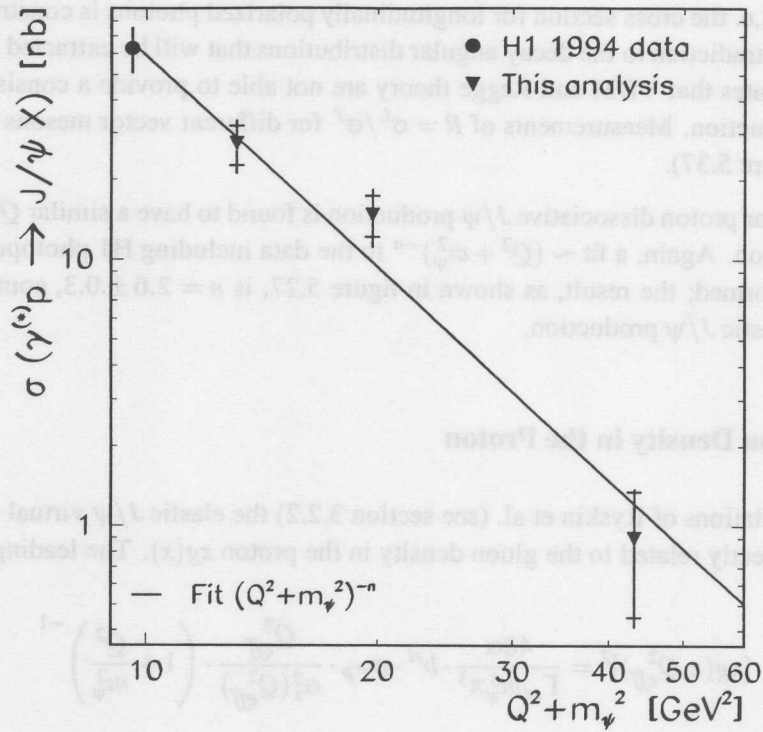
Figure 5.27: *Cross section for J/ψ production with* **proton dissociation** *at W = 90 GeV as a function of $Q^2 + m_\psi^2$. The line is a fit of the form $(Q^2 + m_\psi^2)^{-n}$, $n = 2.6 \pm 0.3$.*

with

$$Q_{eff}^2 = \frac{Q^2 + m_\psi^2}{4} \quad \text{and} \quad x = \frac{4Q_{eff}^2}{W^2}. \tag{5.28}$$

Corrections beyond the leading $\ln Q^2$ approximation have been estimated [67]; they have been found to predominantly change the absolute normalization of the result, with little impact on the shape. It should however be noted that these calculations are controversial and still not settled (see e.g. [68]).

Nevertheless, a gluon density extracted from the data using equation 5.27 is shown in figure 5.28. Note that the normalization of the experimental J/ψ results is arbitrary but the same for all four values of Q_{eff}^2. Fixed target measurements of J/ψ production have also been included, although equation 5.27 has been derived for $W^2 \gg m_\psi^2$.

The gluon density extracted from elastic J/ψ production rises stronger with Q^2 than predicted by the evolution of any of the parameterizations shown in figure 5.28. A possible interpretation is that the Q^2 dependence of the cross section used by Ryskin, $\sim (Q^2 + m_\psi^2)^{-3}$, is too steep compared to the data at least for small Q^2 (see figure 5.26). It is noted here that Frankfurt, Koepf and Strikman come as a result of their calculation to the conclusion [61, 68] that the Q^2 spectrum of elastic J/ψ production is harder than $\sim (Q^2 + m_\psi^2)^{-3}$, and that the effective scale Q_{eff}^2 at which the gluon density is probed is significantly larger than the value $Q_{eff}^2 = \frac{Q^2 + m_\psi^2}{4}$ proposed by Ryskin.
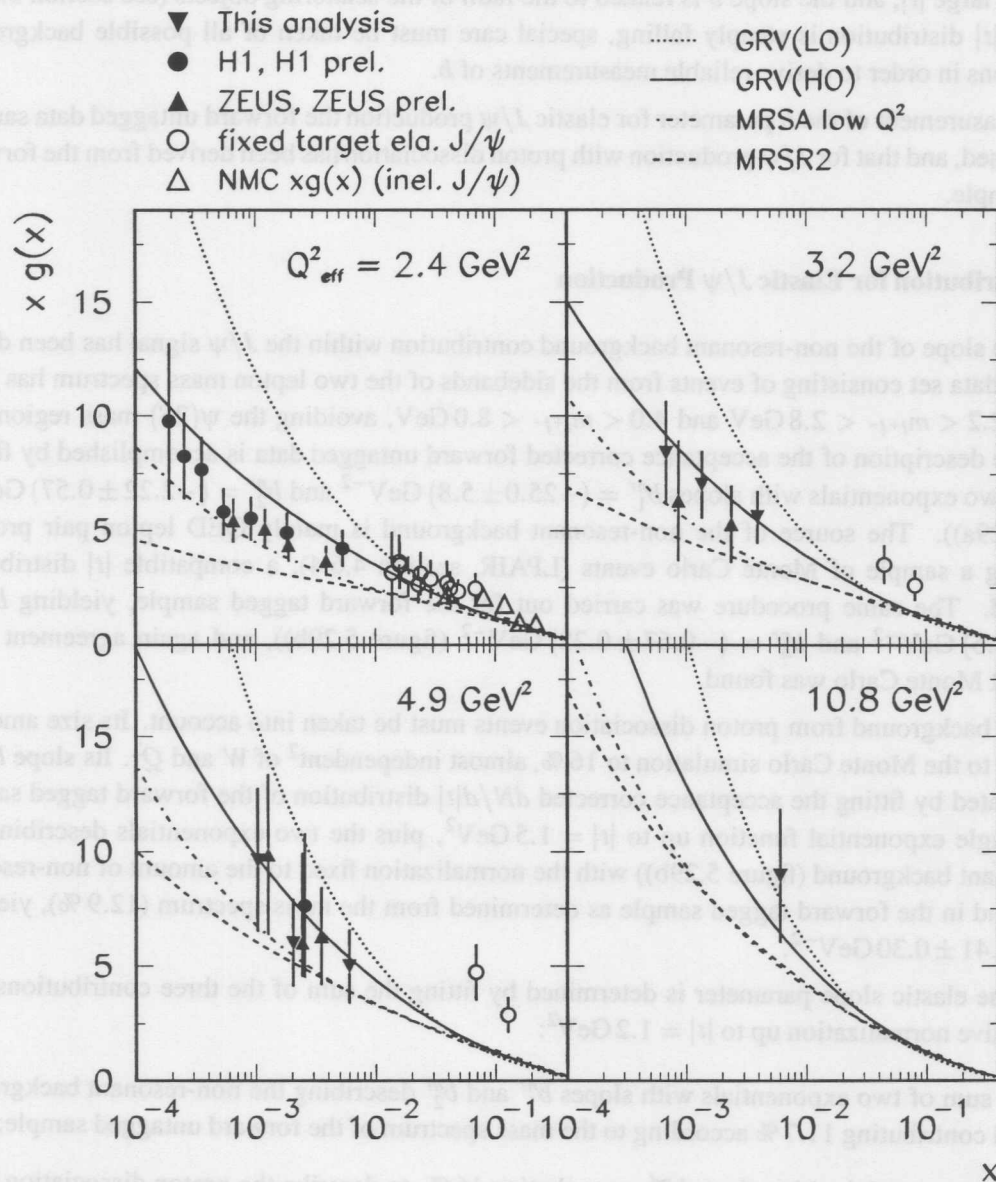
Figure 5.28: *The gluon density in the proton within the Ryskin model. HERA and fixed target data are compared to different parameterizations of the gluon density, from top to bottom: GRV(LO) (dotted line), GRV(HO) [112] (full line), MRSA low Q^2 [175] (dash-dotted) and MRSR2 [174] (dashed). For comparison, the gluon density at $Q^2 = 1.5 \, GeV^2$ and higher x extracted by the NMC collaboration from inelastic J/ψ production [176] is also included. The normalization of the HERA data with respect to the model is arbitrary but fixed for all Q^2_{eff}.*

5.2.3   The t Distribution for Elastic and Proton Dissociative J/ψ Production

For diffractive scattering, the differential cross section $d\sigma/d|t|$ is expected to fall exponentially $\sim e^{b|t|}$ for not too large $|t|$, and the slope b is related to the radii of the scattering objects (see section 3.2.1). Since the $|t|$ distribution is steeply falling, special care must be taken of all possible background contributions in order to derive reliable measurements of b.

For the measurement of the b parameter for elastic J/ψ production the forward untagged data sample has been used, and that for J/ψ production with proton dissociation has been derived from the forward tagged sample.

The t Distribution for Elastic J/ψ Production

Firstly, the slope of the non-resonant background contribution within the J/ψ signal has been determined. A data set consisting of events from the sidebands of the two lepton mass spectrum has been selected ($2.2 < m_{l^+l^-} < 2.8\,\mathrm{GeV}$ and $4.0 < m_{l^+l^-} < 8.0\,\mathrm{GeV}$, avoiding the $\psi(2S)$ mass region). A reasonable description of the acceptance corrected forward untagged data is accomplished by fitting a sum of two exponentials with slopes $b_1^{nr} = (-25.0 \pm 5.8)\,\mathrm{GeV}^{-2}$ and $b_2^{nr} = (-2.22 \pm 0.57)\,\mathrm{GeV}^{-2}$ (figure 5.29a)). The source of the non-resonant background is mainly QED lepton pair production; using a sample of Monte Carlo events (LPAIR, section 4.6.4), a compatible $|t|$ distribution was found. The same procedure was carried out for the forward tagged sample, yielding $b_3^{nr} = (-7.6 \pm 2.6)\,\mathrm{GeV}^{-2}$ and $b_4^{nr} = (-0.67 \pm 0.28)\,\mathrm{GeV}^{-2}$ (figure 5.29b)), and again agreement with the LPAIR Monte Carlo was found.

Secondly, background from proton dissociation events must be taken into account. Its size amounts according to the Monte Carlo simulation to 16 %, almost independent[2] of W and Q^2. Its slope b^{pd} is approximated by fitting the acceptance corrected $dN/d|t|$ distribution of the forward tagged sample with a single exponential function up to $|t| = 1.5\,\mathrm{GeV}^2$, plus the two exponentials describing the non-resonant background (figure 5.29b)) with the normalization fixed to the amount of non-resonant background in the forward tagged sample as determined from the mass spectrum (12.9 %), yielding $b^{pd} = -1.41 \pm 0.30\,\mathrm{GeV}^{-2}$.

Finally, the elastic slope parameter is determined by fitting the sum of the three contributions with fixed relative normalization up to $|t| = 1.2\,\mathrm{GeV}^2$:

- the sum of two exponentials with slopes b_1^{nr} and b_2^{nr} describing the non-resonant background, and contributing 11.7 % according to the mass spectrum of the forward untagged sample;

- one exponential with a slope b^{pd}, contributing 16 %, to describe the proton dissociation background;

- one exponential with a slope b^{el} that describes elastic J/ψ production.

The result of the fit is shown in figure 5.30, the slope parameter thus determined is

$$b^{el} = -3.9^{+0.3}_{-0.4}\,(\mathrm{stat})^{+0.3}_{-0.4}\,(\mathrm{syst})\,\mathrm{GeV}^{-2} \tag{5.29}$$

at a mean W of $96\,\mathrm{GeV}$ and a mean Q^2 of $8\,\mathrm{GeV}^2$. The systematic error quoted here was estimated by varying the fit range by one bin in each direction, changing the amount of non-resonant and proton

---

[2]It increases slightly towards lower W (up to 22 %) and higher Q^2 (up to 18 %).
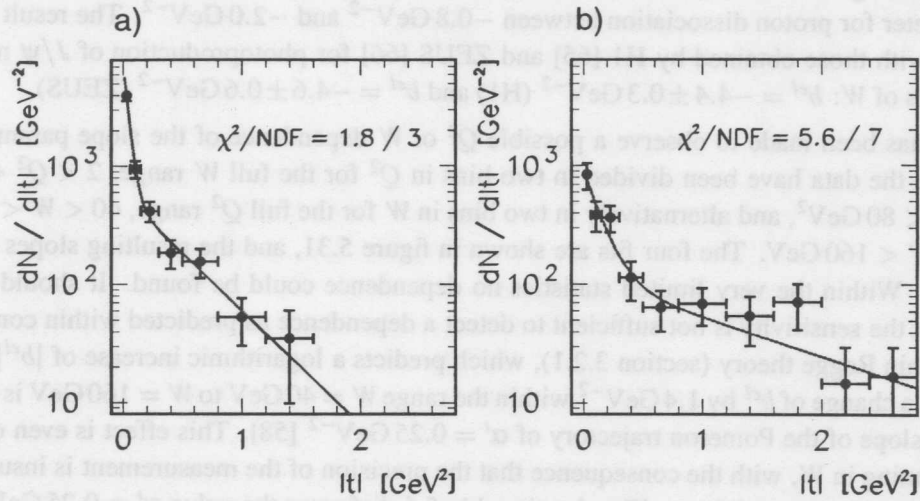
Figure 5.29: *Distribution of dN/d|t| for sidebands of the J/ψ mass spectrum; a) forward untagged sample, b) forward tagged sample. The lines are results of fits of the form $a \cdot e^{b_1|t|} + b \cdot e^{b_2|t|}$.*
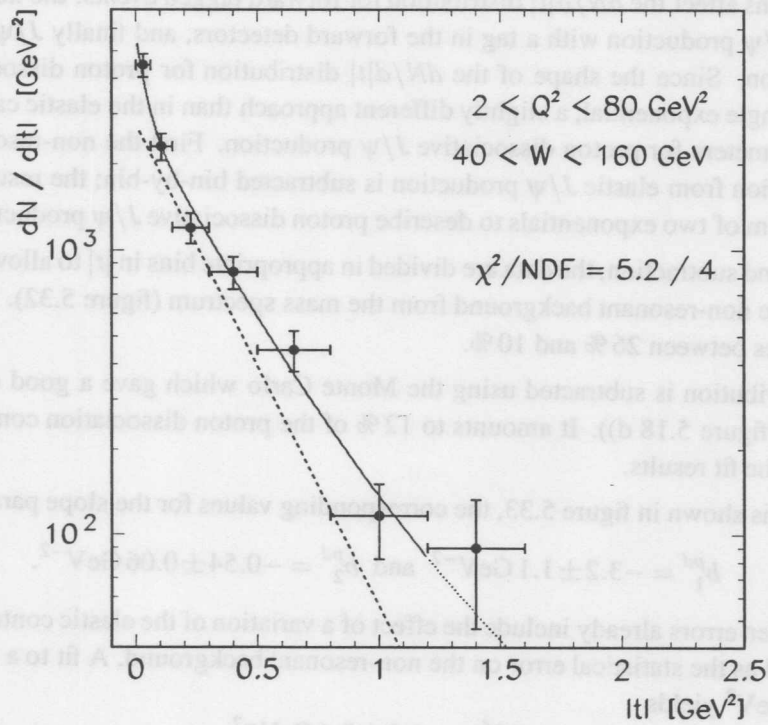
Figure 5.30: *Distribution of dN/d|t| for forward untagged events. The full line is the fit to the data, consisting of a sum of four exponentials with fixed relative normalizations as described in the text. The dashed line is the contribution from elastic J/ψ production.*

dissociation background between 5 % and 16 %, and 5 % and 28 % respectively, and changing the slope parameter for proton dissociation between $-0.8\,\mathrm{GeV}^{-2}$ and $-2.0\,\mathrm{GeV}^{-2}$. The result for b^{el} is compatible with those obtained by H1 [65] and ZEUS [66] for photoproduction of J/ψ mesons at similar values of W: $b^{el} = -4.4 \pm 0.3\,\mathrm{GeV}^{-2}$ (H1) and $b^{el} = -4.6 \pm 0.6\,\mathrm{GeV}^{-2}$ (ZEUS).

An attempt has been made to observe a possible Q^2 or W dependence of the slope parameter. For this purpose, the data have been divided in two bins in Q^2 for the full W range, $2 < Q^2 < 8\,\mathrm{GeV}^2$ and $8 < Q^2 < 80\,\mathrm{GeV}^2$, and alternatively in two bins in W for the full Q^2 range, $40 < W < 100\,\mathrm{GeV}$ and $100 < W < 160\,\mathrm{GeV}$. The four fits are shown in figure 5.31, and the resulting slopes are given in table 5.5. Within the very limited statistics no dependence could be found. It should be noted however that the sensitivity is not sufficient to detect a dependence as predicted within conventional models: within Regge theory (section 3.2.1), which predicts a logarithmic increase of $|b^{el}|$ with W^2 (*shrinkage*), a change of b^{el} by $1.4\,\mathrm{GeV}^{-2}$ within the range $W = 40\,\mathrm{GeV}$ to $W = 160\,\mathrm{GeV}$ is expected, assuming a slope of the Pomeron trajectory of $\alpha' = 0.25\,\mathrm{GeV}^{-2}$ [58]. This effect is even diluted by the large binning in W, with the consequence that the precision of the measurement is insufficient to make any statement on shrinkage. The data in table 5.5 disfavour the value $\alpha' = 0.25\,\mathrm{GeV}^{-2}$ at the level of 1.5 standard deviations, including statistical errors only. Models based on perturbative QCD predict smaller W dependences of b^{el}.

The t Distribution for J/ψ Production with Proton Dissociation

Three contributions affect the $dN/d|t|$ distribution for forward tagged events: the non-resonant background, elastic J/ψ production with a tag in the forward detectors, and finally J/ψ production with proton dissociation. Since the shape of the $dN/d|t|$ distribution for proton dissociation cannot be described by a single exponential, a slightly different approach than in the elastic case was chosen to derive slope parameters for proton dissociative J/ψ production. First the non-resonant background and the contribution from elastic J/ψ production is subtracted bin-by-bin; the resulting spectrum is then fitted to a sum of two exponentials to describe proton dissociative J/ψ production.

For the background subtraction, the data are divided in appropriate bins in $|t|$ to allow a reasonable determination of the non-resonant background from the mass spectrum (figure 5.32). The non-resonant background varies between 26 % and 10 %.

The elastic contribution is subtracted using the Monte Carlo which gave a good description of the small $|t|$ region (figure 5.18 d)). It amounts to 12 % of the proton dissociation contribution, and has little impact on the fit results.

The resulting fit is shown in figure 5.33, the corresponding values for the slope parameters are

$$b_1^{pd} = -3.2 \pm 1.1\,\mathrm{GeV}^{-2} \quad \text{and} \quad b_2^{pd} = -0.54 \pm 0.06\,\mathrm{GeV}^{-2}. \tag{5.30}$$

Note that the given errors already include the effect of a variation of the elastic contribution between 6 and 16 % as well as the statistical error on the non-resonant background. A fit to a single exponential up to $|t| = 1.2\,\mathrm{GeV}^2$ yields

$$b^{pd} = -1.9 \pm 0.4\,\mathrm{GeV}^{-2}, \tag{5.31}$$

compatible with the H1 result for J/ψ photoproduction [65] $b^{pd} = -1.7 \pm 0.3\,\mathrm{GeV}^{-2}$, and also with ρ production in DIS [82], where $b^{pd} = -2.1 \pm 0.7\,\mathrm{GeV}^{-2}$.

As in the elastic case, the data have been divided in two Q^2 and W domains in order to study a possible Q^2 or W dependence of the slope parameter. The results are given in table 5.6; there is an indication

$40 < W < 160\,\mathrm{GeV}$	
$2 < Q^2 < 8\,\mathrm{GeV}^2$	$8 < Q^2 < 80\,\mathrm{GeV}^2$
$b^{el} = -4.1 \pm 0.4\,\mathrm{GeV}^{-2}$	$b^{el} = -2.8 \pm 1.0\,\mathrm{GeV}^{-2}$
$2 < Q^2 < 80\,\mathrm{GeV}^2$	
$40 < W < 100\,\mathrm{GeV}$	$100 < W < 160\,\mathrm{GeV}$
$b^{el} = -4.1 \pm 0.5\,\mathrm{GeV}^{-2}$	$b^{el} = -3.7 \pm 0.5\,\mathrm{GeV}^{-2}$

Table 5.5: *Slope parameters for elastic J/ψ production $dN/d|t|$ distributions in different Q^2 and W domains. Errors are statistical only.*
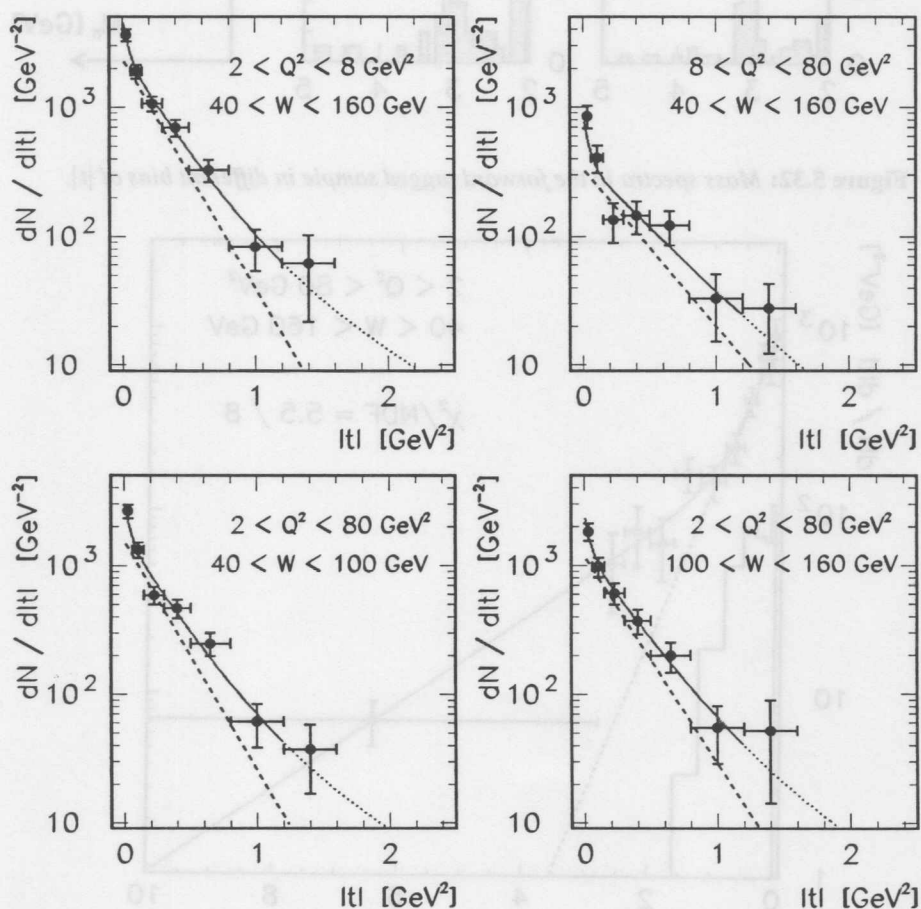
Figure 5.31: *Distribution of $dN/d|t|$ for forward untagged events in different domains of W and Q^2. The full lines are fits including all background contributions, the dashed lines are the contributions from elastic J/ψ production*
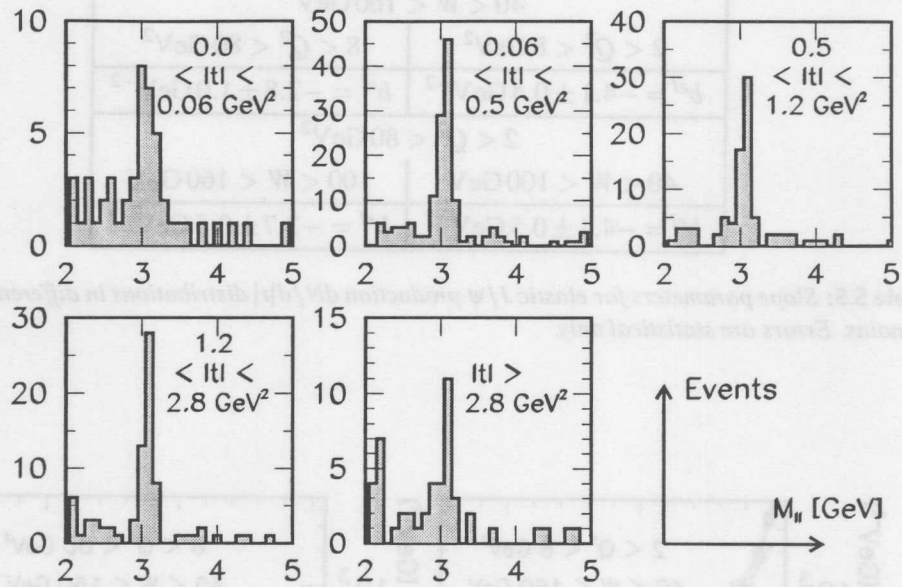
Figure 5.32: *Mass spectra in the forward tagged sample in different bins of $|t|$.*
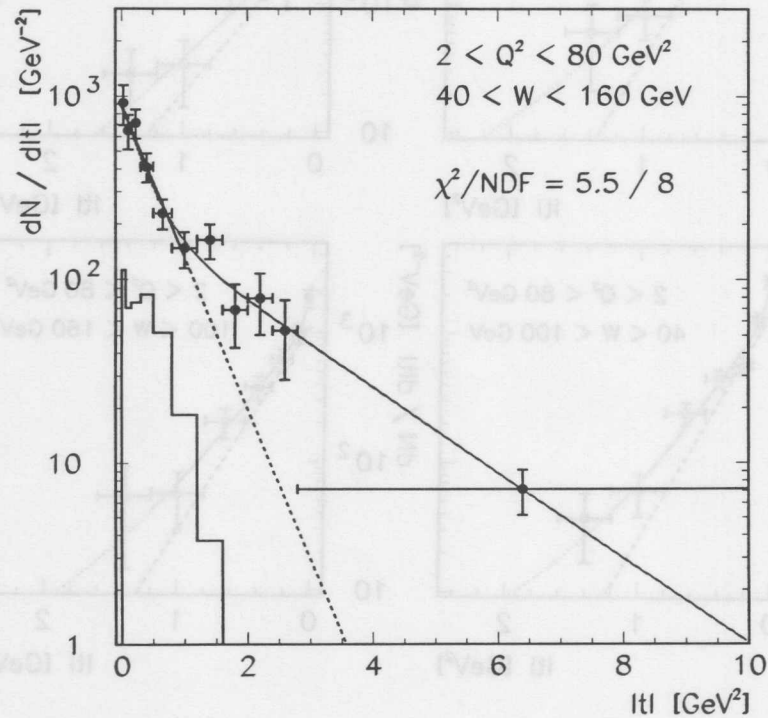
Figure 5.33: *Distribution of $dN/d|t|$ for the forward tagged event sample after subtraction of non-resonant and elastic J/ψ background. The full line is a fit of the form $a \cdot e^{b_1|t|} + b \cdot e^{b_2|t|}$ to the data in the full $|t|$ range, the dashed line is a fit with a single exponential up to $|t| = 1.2\,\mathrm{GeV}^2$. The histogram indicates the subtracted elastic J/ψ contribution.*

40 < W < 160 GeV	
$2 < Q^2 < 8\,\mathrm{GeV}^2$	$8 < Q^2 < 80\,\mathrm{GeV}^2$
$b_1^{pd} = -2.7 \pm 2.1\,\mathrm{GeV}^{-2}$	$b_1^{pd} = -4.1 \pm 1.7\,\mathrm{GeV}^{-2}$
$b_2^{pd} = -0.56 \pm 0.19\,\mathrm{GeV}^{-2}$	$b_2^{pd} = -0.44 \pm 0.13\,\mathrm{GeV}^{-2}$
$2 < Q^2 < 80\,\mathrm{GeV}^2$	
40 < W < 100 GeV	100 < W < 160 GeV
$b_1^{pd} = -1.6 \pm 0.8\,\mathrm{GeV}^{-2}$	$b_1^{pd} = -4.7 \pm 1.5\,\mathrm{GeV}^{-2}$
$b_2^{pd} = -0.23 \pm 0.56\,\mathrm{GeV}^{-2}$	$b_2^{pd} = -0.61 \pm 0.12\,\mathrm{GeV}^{-2}$

Table 5.6: *Slope parameters for proton dissociative J/ψ production in different Q^2 and W domains. Errors are statistical only.*

for a rise of $|b_1^{pd}|$ with W, but the errors are too large to draw any conclusions. Within Regge theory, a rise of $|b^{pd}|$ with W according to

$$|b(W, M_Y)| = |b_0| + 2\alpha' \ln(W^2/M_Y^2) \tag{5.32}$$

with $\alpha' = 0.25\,\mathrm{GeV}^{-2}$ [58] is expected.

Comparison with a BFKL Prediction for high $|t|$

Calculations exist [153] that use the BFKL formalism in leading order to predict the cross section for vector meson production with proton dissociation at high $|t| \gtrsim 1\,\mathrm{GeV}^2$; the outcome of these calculations is implemented in the Monte Carlo generator HITVM (see section 4.6.2 for details). The prediction is highly sensitive on the input of the only free parameter within the model, α_s^{LO}. Using a Monte Carlo sample generated with a value $\alpha_s^{LO} = 0.207$ in accordance with H1 results on photoproduction of J/ψ at large $|t|$ [155], the raw $|t|$ distribution for forward tagged events as observed in the detector is compared with the absolute Monte Carlo prediction after full detector simulation.

The result is shown in figure 5.34. Note that the HITVM events have been generated only for $|t| > 1\,\mathrm{GeV}^2$, therefore comparisons should only be done for $|t| \gtrsim 1.3\,\mathrm{GeV}^2$, taking into account smearing effects. The agreement both in normalization and shape between data and Monte Carlo simulation is quite remarkable.

5.2.4   Test of a Factorization Hypothesis

In the framework of Regge theory, the amplitudes for elastic as well as for proton dissociate virtual photoproduction can be written as a product of two vertex functions, one for the photon-Pomeron and one for the proton-Pomeron vertex, assuming single Pomeron exchange. The cross section ratio depends only on t and M_Y:

$$\frac{d^2 \sigma_{\gamma^* p}^{pd}/dt\, dM_Y^2}{d\sigma_{\gamma^* p}^{el}/dt} = f(t, M_Y^2). \tag{5.33}$$

Integrating over M_Y, the ratio of the elastic to the proton dissociation cross section should — at fixed t — be the same in different diffractive processes.

A test of factorization can thus be performed by comparing measurements of

$$\frac{d\sigma^{pd}/dt\,(t=0)}{d\sigma^{el}/dt\,(t=0)} = \frac{b^{pd} \cdot \sigma^{pd}}{b^{el} \cdot \sigma^{el}}. \tag{5.34}$$

for different processes; data are available for the H1 measurements of ρ production in DIS [82] $(\gamma^* p \to \rho\, Y)$ and J/ψ photoproduction [65] $(\gamma p \to J/\psi\, Y)$, the ISR results [177] of $pp \to p\, Y$ at $\sqrt{s} = 53\,\text{GeV}$, the ZEUS measurements of ρ photoproduction [77], and finally the present analysis. They are summarized in table 5.7. The ratio 5.34 agrees for the different processes, except possibly in the case of J/ψ photoproduction, where it is higher but still compatible with the other results. Both results from J/ψ production tend to higher values.

5.2.5 Studies of the Helicity Structure

In deep inelastic scattering, the helicity structure of J/ψ production can be accessed via the three decay angles θ^*, φ and ϕ measured in the s-channel helicity frame (see section 3.1.5). θ^* denotes the polar angle of the direction of flight of the positively charged decay lepton, while φ is its azimuthal angle. The angle ϕ is defined between the electron scattering plane and the J/ψ production plane. The measurement of these angles provides a crucial test for helicity conservation in the s-channel (SCHC), and, in the case that SCHC is fulfilled, a means to extract R, the ratio of cross sections for J/ψ production by longitudinally and transversely polarized photons.

It should be noted that for detailed investigations of the helicity structure, data samples much larger than those available here are necessary. Therefore the analysis has to focus on the most important aspects. No separation between elastic and proton dissociative J/ψ production will be done, it was however verified that the distributions are compatible for the forward untagged and forward tagged data sets.

Angular Distributions I: $\cos\theta^*$

Due to the very well measured final state, both with respect to the decay leptons as well as the scattered electron, $\cos\theta^*$ can be reconstructed with high precision (see figure 5.35), and the extraction of $\cos\theta^*$ distributions is rather straightforward.

The number of signal events is determined for the full W range, $40 < W < 160\,\text{GeV}$, and in three Q^2 domains, $2 < Q^2 < 4\,\text{GeV}^2$, $4 < Q^2 < 10\,\text{GeV}^2$ and $10 < Q^2 < 80\,\text{GeV}^2$, and corrected for acceptance and efficiency losses using the same Monte Carlo simulation that has been shown in previous sections to give a good description of the data. Furthermore, the contribution from non-resonant background is subtracted with normalized $\cos\theta^*$ distributions obtained from the sidebands of the J/ψ signal; due to the small level of non-resonant background (12 %) this correction is small.

The resulting $\cos\theta^*$ distributions are shown in figure 5.36 a) to c), in d) the applied acceptance correction is given.

From figure 5.36, the spin density matrix element r_{00}^{04} can be extracted using the relation

$$\frac{dN}{d\cos\theta^*} \sim 1 + r_{00}^{04} + (1 - 3r_{00}^{04})\cos^2\theta^*. \tag{5.35}$$
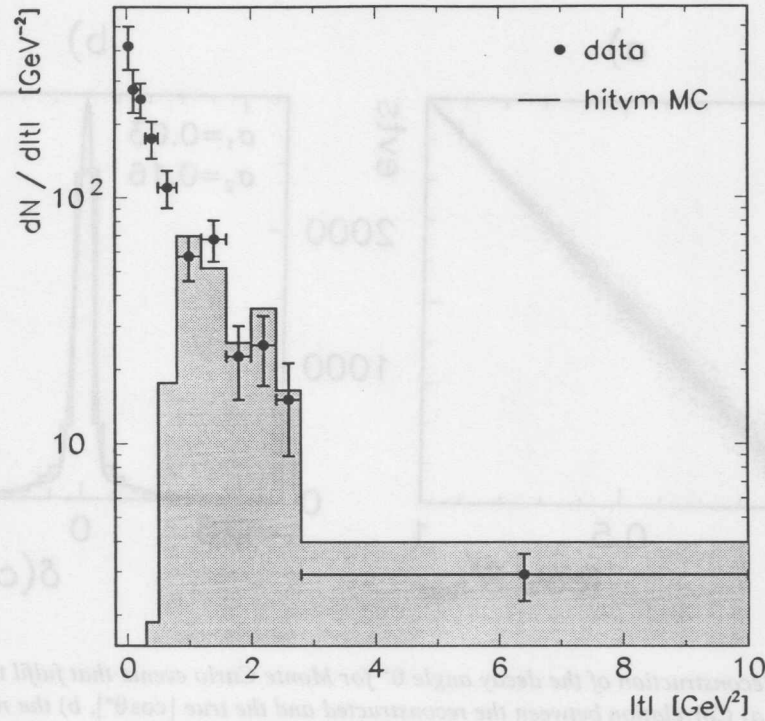
Figure 5.34: *Raw distribution of $dN/d|t|$ for the forward tagged event sample — uncorrected for detector effects — compared to the leading order BFKL Monte Carlo simulation described in the text.*

	ISR [177] $pp \rightarrow pY$	ZEUS [77] $\gamma p \rightarrow \rho Y$	H1 [82] $\gamma^* p \rightarrow \rho Y$	H1 [65] $\gamma p \rightarrow J/\psi Y$	This analysis $\gamma^* p \rightarrow J/\psi Y$
b^{el} [GeV^{-2}]	-13.1 ± 0.3	-10.9 ± 0.8	-7.0 ± 1.0	-4.4 ± 0.3	-4.8 ± 0.8
b^{pd} [GeV^{-2}]	-6.5 ± 1.0	-5.8 ± 0.6	-2.1 ± 0.7	-1.7 ± 0.3	-1.9 ± 0.4
σ^{pd}/σ^{el}	0.48 ± 0.03	0.50 ± 0.18	0.66 ± 0.17	1.0 ± 0.2	0.70 ± 0.16
$\dfrac{b^{pd} \cdot \sigma^{pd}}{b^{el} \cdot \sigma^{el}}$	0.24 ± 0.04	0.27 ± 0.10	0.20 ± 0.09	0.39 ± 0.11	0.34 ± 0.11

Table 5.7: *Comparison of different measurements of elastic and proton dissociation diffractive processes.*

Q^2 interval	χ^2/NDF	$\langle Q^2 \rangle$ [GeV^2]	r_{00}^{04}	R	α
$2 - 4\,\text{GeV}^2$	$0.6/3$	2.8	0.17 ± 0.20	$0.21^{+0.40}_{-0.23}$	$0.40^{+0.67}_{-0.50}$
$4 - 10\,\text{GeV}^2$	$0.4/3$	6.2	0.18 ± 0.21	$0.22^{+0.42}_{-0.24}$	$0.39^{+0.68}_{-0.51}$
$10 - 80\,\text{GeV}^2$	$1.4/3$	18.5	0.64 ± 0.26	$1.9^{+7.2}_{-1.1}$	$-0.56^{+0.44}_{-0.34}$

Table 5.8: *Results of fits to the decay angular distribution $\cos\theta^*$. The errors include statistical as well as systematic errors.*
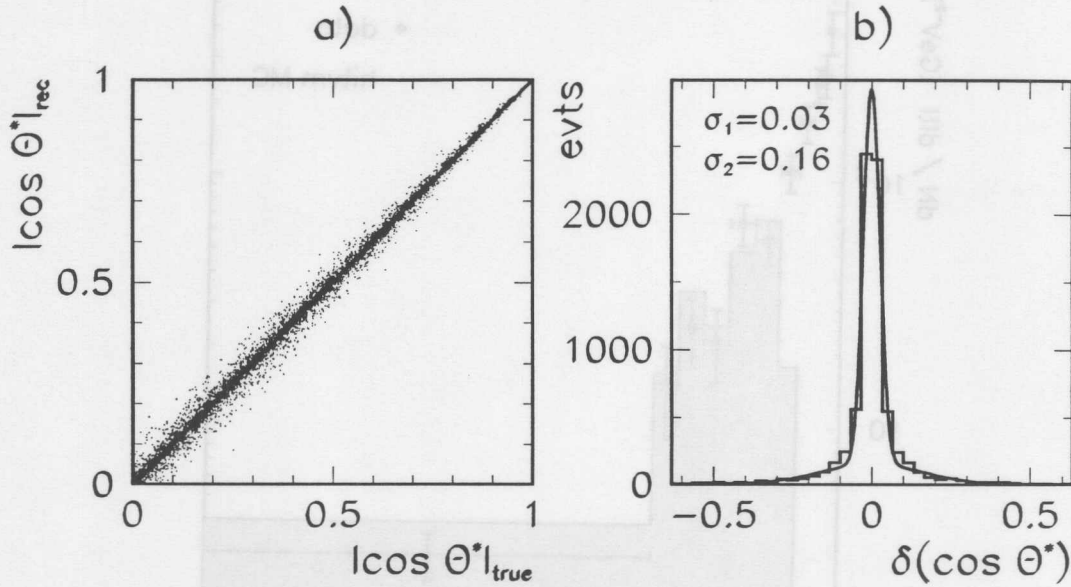
Figure 5.35: *Reconstruction of the decay angle θ^* for Monte Carlo events that fulfil the exclusive J/ψ selection. a) Correlation between the reconstructed and the true $|\cos\theta^*|$, b) the relative error $\delta(\cos\theta^*) = (\cos\theta^*_{true} - \cos\theta^*_{rec})/\cos\theta^*_{true}$. σ_1 and σ_2 are the widths of a fit of the sum of two Gaussians to the histogram.*

The results of fits of equation 5.35 to the data are shown as lines in figure 5.36, and numerical results are given in table 5.8. The shape of the $\cos\theta^*$ distribution changes as Q^2 is increased, and this change is parameterized by the increase of r_{00}^{04}.

r_{00}^{04} is a measure for the probability for the J/ψ meson to be longitudinally polarized, therefore it can be concluded that there is an indication that the fraction of longitudinally polarized J/ψ mesons increases with Q^2. In previous analyses [146, 66] of J/ψ photoproduction at H1 and ZEUS values of $r_{00}^{04} = -0.02 \pm 0.07$ and $r_{00}^{04} = -0.01 \pm 0.09$ have been found, compatible with the expectation that for $Q^2 \simeq 0$ all J/ψ mesons are transversely polarized; given that real photons have transverse polarization, these measurements confirm the SCHC hypothesis.

Assuming the validity of SCHC, r_{00}^{04} can be translated into $R := \sigma^L/\sigma^T$:

$$R = \frac{1}{\varepsilon} \frac{r_{00}^{04}}{1 - r_{00}^{04}}, \tag{5.36}$$

where ε is the polarization parameter. The numerical results for R are given in table 5.8. Within models based on pQCD, $R(Q^2)$ can be calculated and is approximately proportional to Q^2/m_V^2, while the Vector Meson Dominance Model gives no prediction but the phenomenological description:

$$R(Q^2) = \xi \frac{Q^2}{m_V^2}, \tag{5.37}$$

where ξ is an empirical parameter of order 1. Obviously, a measurement of ξ is beyond the scope of the available data, but a comparison of the measured values for R with those extracted for other

vector mesons, especially the ρ, may reveal whether the relation $R(Q^2) \sim Q^2/m_V^2$ is indeed universal for different vector mesons V.

A compilation of R measurements for vector meson production in deep inelastic scattering is shown in figure 5.37. Most precise measurements exist for ρ mesons, where many results also at lower centre of mass energies W are displayed, while for the J/ψ no other R measurement in deep inelastic scattering is known to date. J/ψ photoproduction at HERA was found to be compatible with $R = 0$ ($R = -0.01 \pm 0.09$ [66]). Within the large uncertainties of the present analysis, a universal behaviour of $R(Q^2)$ is consistent with the data.

Finally, the shape of the $\cos\theta^*$ distribution can conveniently be expressed using the polarization
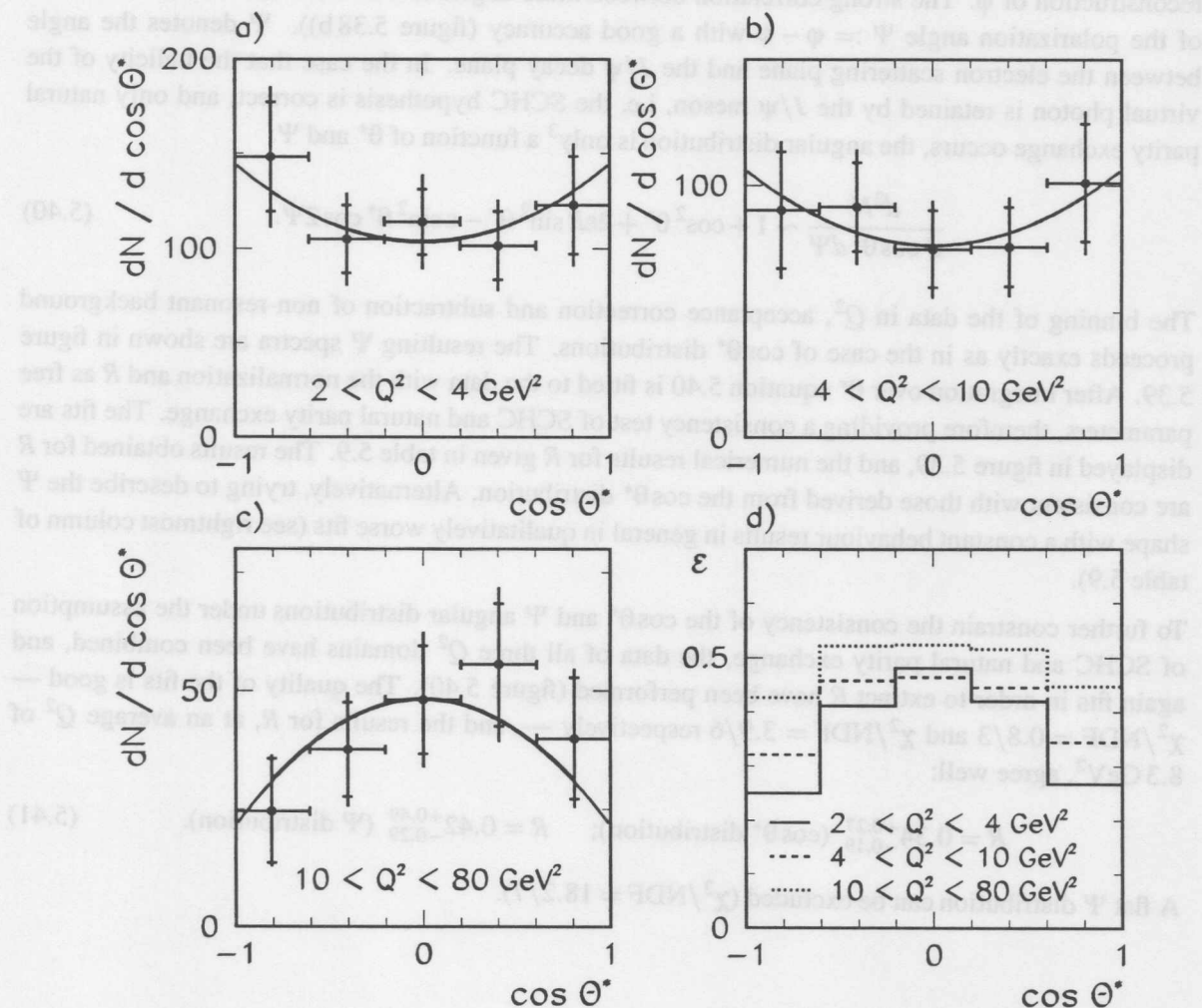
Figure 5.36: *Decay angular distribution* $\cos\theta^*$ *for exclusive J/ψ production for a) low b) medium and c) high Q^2. The inner error bars are statistical errors, the outer ones include statistical and systematic errors added in quadrature. The lines are fits to the data (see text). In d) the total acceptance in the three domains of Q^2 is shown.*

parameter α:

$$\frac{dN}{d\cos\theta^*} \sim 1 + \alpha\cos^2\theta^*,\tag{5.38}$$

where α is related to r_{00}^{04} by

$$\alpha = \frac{1 - 3r_{00}^{04}}{1 + r_{00}^{04}}.\tag{5.39}$$

Numerical results for α are also given in table 5.8.

Angular Distributions II: Ψ

Because of limited statistics and resolution, the analysis of φ and ϕ distributions is not possible. In the reconstruction of these angles significant smearing is observed, see e.g. figure 5.38 a) for the reconstruction of φ. The strong correlation between these angles allows however the reconstruction of the polarization angle $\Psi := \varphi - \phi$ with a good accuracy (figure 5.38 b)). Ψ denotes the angle between the electron scattering plane and the J/ψ decay plane. In the case that the helicity of the virtual photon is retained by the J/ψ meson, i.e. the SCHC hypothesis is correct, and only natural parity exchange occurs, the angular distribution is only[3] a function of θ^* and Ψ:

$$\frac{d^2N}{d\cos\theta^*\,d\Psi} \sim 1 + \cos^2\theta^* + 2\varepsilon R\sin^2\theta^* - \varepsilon\sin^2\theta^*\cos 2\Psi.\tag{5.40}$$

The binning of the data in Q^2, acceptance correction and subtraction of non-resonant background proceeds exactly as in the case of $\cos\theta^*$ distributions. The resulting Ψ spectra are shown in figure 5.39. After integration over θ^* equation 5.40 is fitted to the data with the normalization and R as free parameters, therefore providing a consistency test of SCHC and natural parity exchange. The fits are displayed in figure 5.39, and the numerical results for R given in table 5.9. The results obtained for R are consistent with those derived from the $\cos\theta^*$ distribution. Alternatively, trying to describe the Ψ shape with a constant behaviour results in general in qualitatively worse fits (see rightmost column of table 5.9).

To further constrain the consistency of the $\cos\theta^*$ and Ψ angular distributions under the assumption of SCHC and natural parity exchange, the data of all three Q^2 domains have been combined, and again fits in order to extract R have been performed (figure 5.40). The quality of the fits is good — $\chi^2/\mathrm{NDF} = 0.8/3$ and $\chi^2/\mathrm{NDF} = 3.9/6$ respectively —, and the results for R, at an average Q^2 of $8.3\,\mathrm{GeV}^2$, agree well:

$$R = 0.34^{+0.27}_{-0.19} \ (\cos\theta^* \ \text{distribution}); \quad R = 0.42^{+0.49}_{-0.29} \ (\Psi \ \text{distribution}).\tag{5.41}$$

A flat Ψ distribution can be excluded ($\chi^2/\mathrm{NDF} = 18.2/7$).

---

[3]A term parameterizing the phase difference between the amplitudes for J/ψ production by photons with longitudinal and transverse polarization has been left out since it vanishes in the one-dimensional distributions.
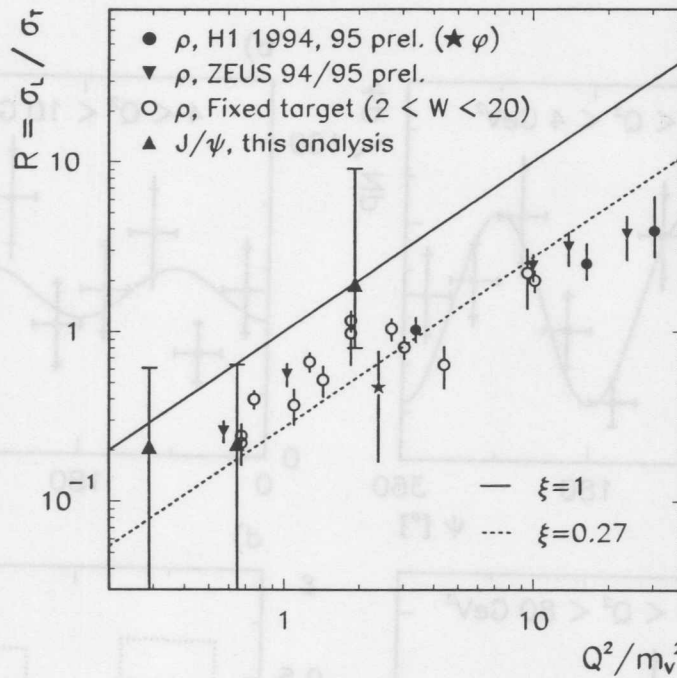
Figure 5.37: *Compilation of $R = \sigma^L/\sigma^T$ measurements as a function of Q^2/m_V^2 for exclusive vector meson production [178]. Some ρ results with large errors have been left out. The full line, $R = Q^2/m_V^2$, is drawn to guide the eye, $\xi = 0.27 \pm 0.01$ is a fit through all data shown.*
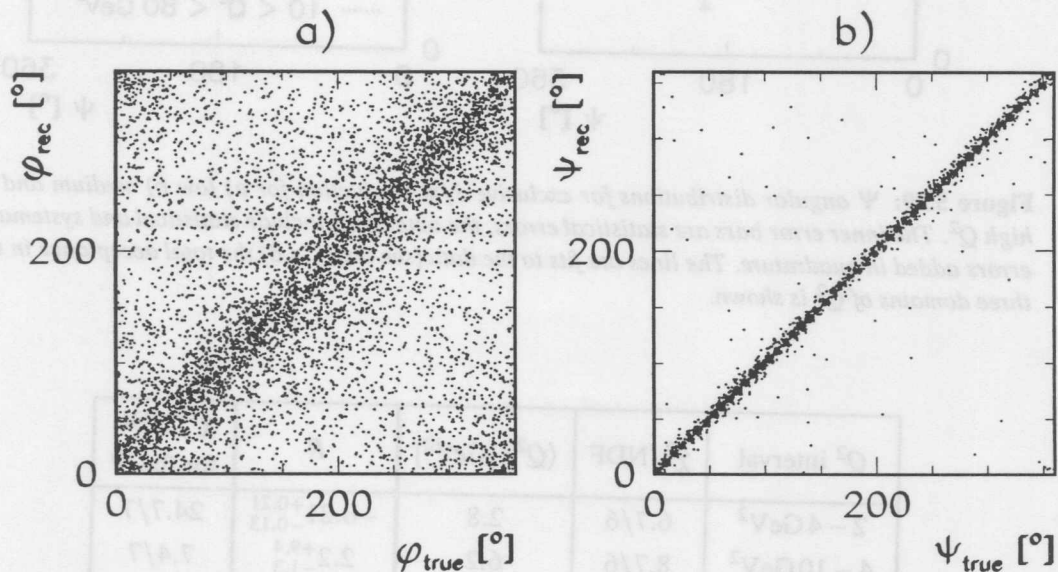
Figure 5.38: *Reconstruction of the angles a) φ and b) Ψ in the helicity frame. Using Monte Carlo events that fulfil the exclusive J/ψ selection, the correlation between the generated and reconstructed angles is shown.*
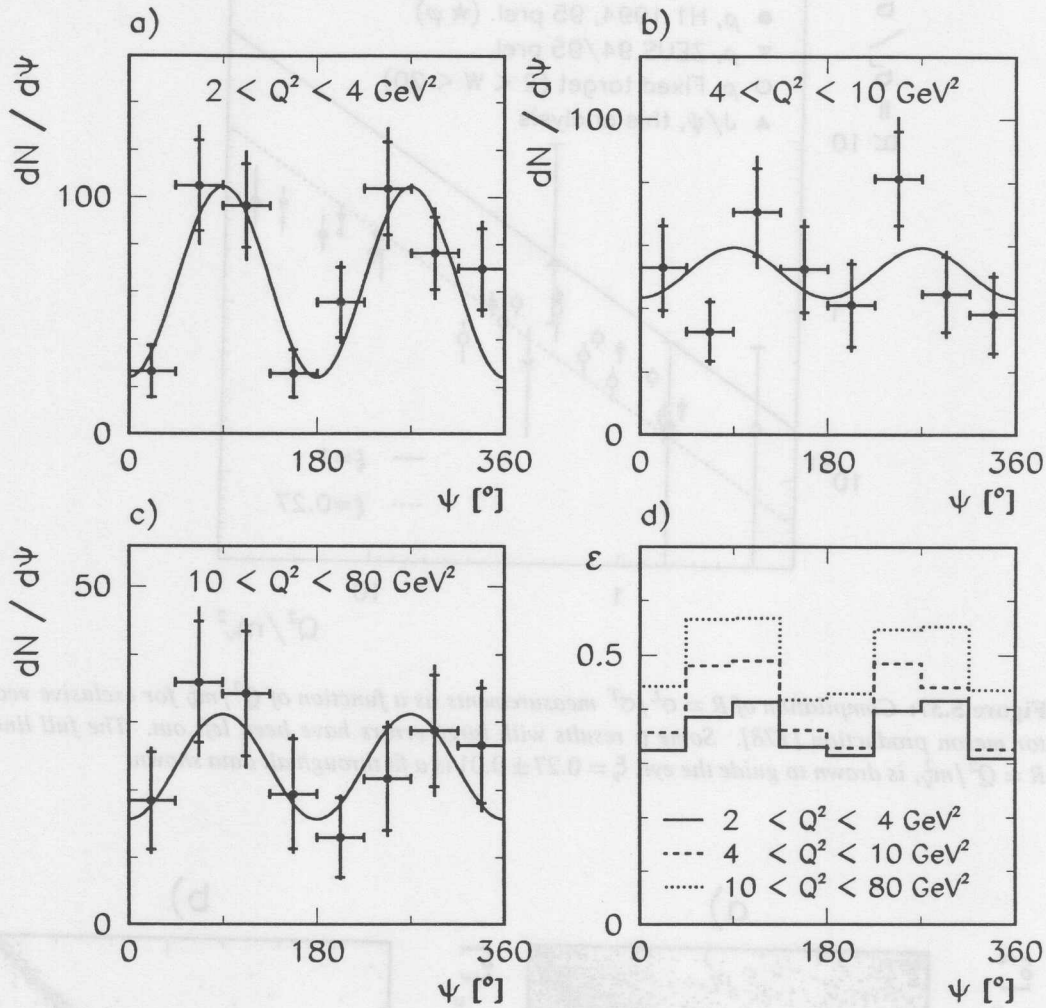
Figure 5.39: Ψ *angular distributions for exclusive J/ψ production for a) low b) medium and c) high Q^2. The inner error bars are statistical errors, the outer ones include statistical and systematic errors added in quadrature. The lines are fits to the data (see text). In d) the total acceptance in the three domains of Q^2 is shown.*

Q^2 interval	χ^2/NDF	$\langle Q^2 \rangle$ $[GeV^2]$	R	χ^2/NDF for flat Ψ
$2-4\,\mathrm{GeV}^2$	6.7/6	2.8	$-0.21^{+0.21}_{-0.13}$	24.7/7
$4-10\,\mathrm{GeV}^2$	8.7/6	6.2	$2.2^{+9.4}_{-1.3}$	7.4/7
$10-80\,\mathrm{GeV}^2$	2.8/6	18.5	$0.51^{+2.02}_{-0.55}$	5.8/7

Table 5.9: *Numerical results of fits to the Ψ distributions. Given errors include statistical as well as systematic errors.*
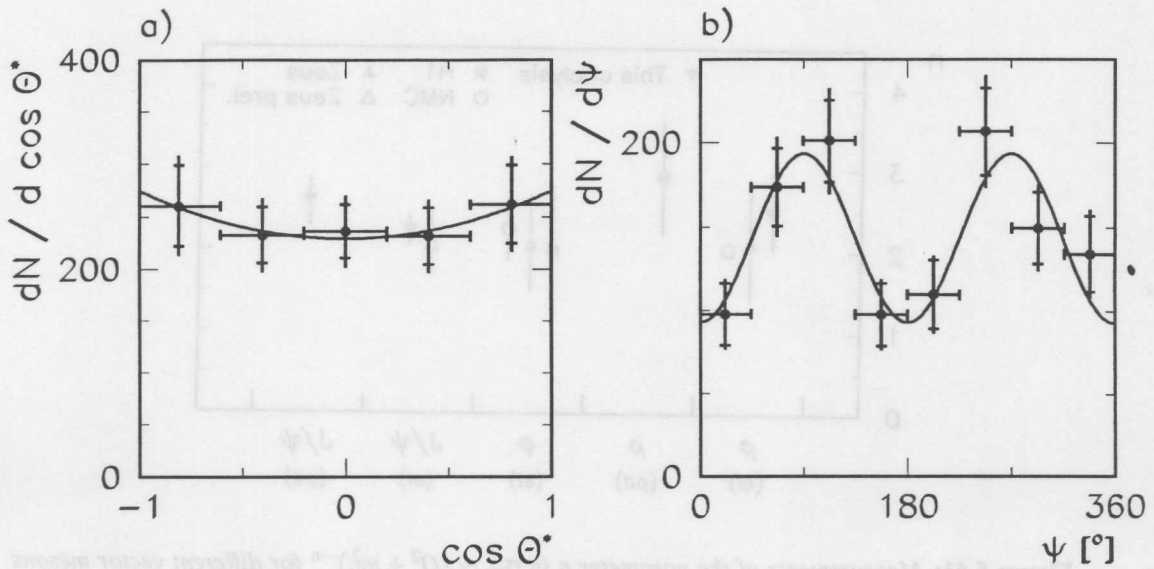
Figure 5.40: *a)* $\cos\Theta^*$ *and b)* Ψ *angular distributions over the full kinematic range* $40 < W < 160\,\mathrm{GeV}$ *and* $2 < Q^2 < 80\,\mathrm{GeV}^2$. *The lines are fits to the data with R as a free parameter, as described in the text.*

5.3   Summary and Discussion of Results

In previous sections, results on elastic and proton dissociative production of J/ψ mesons have been presented. Some concluding remarks will be made in this last section.

- One of the remarkable results of diffractive vector meson production at HERA is the **universal** Q^2 **dependence**; elastic and proton dissociative ρ and J/ψ production as well as elastic ϕ production cross sections are proportional to $1/(Q^2 + m_V^2)^n$ with $n \simeq 2.3$. This is still the case when including lower energy results from the NMC collaboration on elastic ρ and ϕ production. The experimental data are summarized in figure 5.41.

- The extraction of the **gluon density** in the proton using the elastic production of J/ψ mesons is very promising due to the high sensitivity of the cross section, $\sim [xg(x)]^2$, but currently lacks the theoretical certainty. A well-defined procedure of extracting $xg(x)$ including higher order corrections and an estimate of the theoretical uncertainties would be needed in order to be able to provide a competitive measurement of the gluon density.

- The precision of the data is not sufficient to decide whether **shrinkage** is present in elastic J/ψ production; a slope of the Pomeron trajectory of $\alpha' = 0.25\,\mathrm{GeV}^{-2}$ characteristic for the *soft Pomeron* picture is disfavoured by the data, but only at the level of 1.5 standard deviations.

- Diffractive J/ψ production at high $|t|$ provides one of the distinct features of the **BFKL formalism**. No other mechanism in perturbative QCD is known that leads to the large cross sections observed both in photoproduction and deep inelastic scattering. The compatibility of the results can be considered as a success of the BFKL formalism.
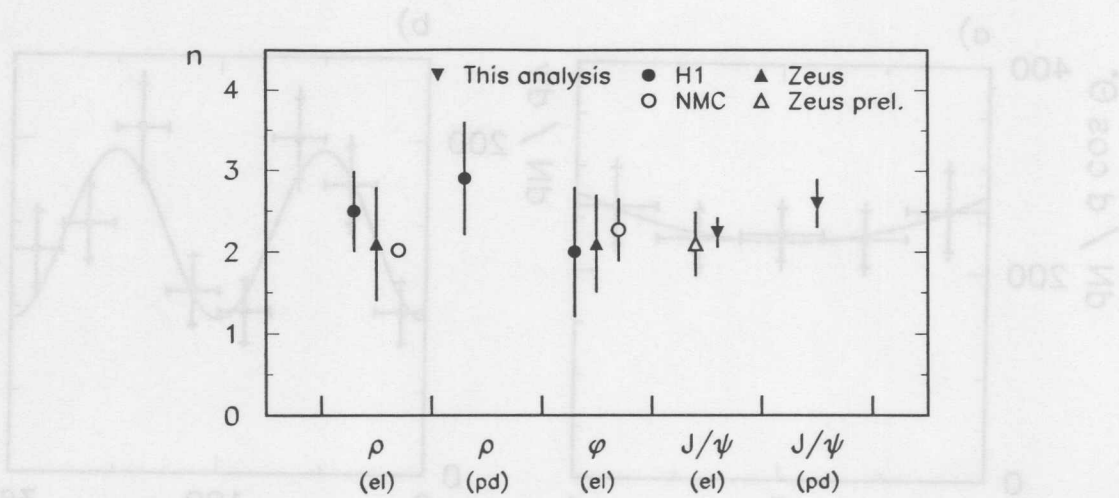
Figure 5.41: *Measurements of the parameter n in $\sigma_{\gamma p} \sim (Q^2 + m_V^2)^{-n}$ for different vector mesons measured at HERA by H1 [78, 82] and ZEUS [80, 84, 86], and by NMC [179].*

- By comparing results for different diffractive processes, a crude test of the **factorization of diffractive vertices** was presented. Within one experiment this test may be refined in future analyses by directly measuring the ratio σ^{pd}/σ^{el} for different vector mesons, exploiting the fact that most of the experimental systematic errors — e.g. due to the separation of elastic and proton dissociative events — cancel in the double ratio

$$\frac{\sigma_{V1}^{pd}/\sigma_{V1}^{el}}{\sigma_{V2}^{pd}/\sigma_{V2}^{el}} \tag{5.42}$$

for two vector mesons $V1$ and $V2$.

- Finally, first results on the **helicity structure** of exclusive J/ψ production have been discussed. No signs of a possible violation of the s-channel helicity conservation hypothesis have been found, but for precise measurements the available data samples are by far too small. In models based on two gluon exchange, SCHC is expected to be fulfilled.

  More precise measurements of $R = \sigma_L/\sigma_T$ than the one presented here would require a significant increase of the available luminosity.

Chapter 6

Diffractive Production of $\psi(2S)$

The objective of this chapter is first to establish the observation of $\psi(2S)$ mesons in deep inelastic scattering at HERA, and secondly to measure the ratio of cross sections for exclusive $\psi(2S)$ over J/ψ production. The measurement of this ratio profits from the cancellation of most systematic uncertainties.

$\psi(2S)$ mesons are identified via the decay channel $\psi(2S) \rightarrow J/\psi\pi^+\pi^-$, where the J/ψ again decays either in two electrons or two muons. The selection of the data has been described in section 4.5.2. After establishing the $\psi(2S)$ signal, the method to correct for detector effects will be described and some checks will be discussed; in the last section, the result are presented.

6.1   Observation of $\psi(2S)$ Meson Production

In order to maximize the available statistics, a slightly larger fraction of the data taken in 1997 is included here compared to the exclusive J/ψ analysis. The integrated luminosity used corresponds to $\int \mathcal{L}dt = 23.14 \pm 0.55\,\mathrm{pb}^{-1}$.

In analogy to section 5.1.2 a kinematical region in Q^2 and W is defined in which the analysis will be carried out. With respect to the exclusive J/ψ analysis the intervals are enlarged towards smaller Q^2 and larger W, since it is expected that the systematic error due to the acceptance correction cancels to a large extent in the ratio of the $\psi(2S)$ to J/ψ cross sections: except for the two pions which have typically low momenta, $\psi(2S)$ and J/ψ events are kinematically very similar. The cuts applied are

$$1 < Q^2 < 80\,\mathrm{GeV}^2 \quad \text{and} \tag{6.1}$$
$$40 < W < 180\,\mathrm{GeV}. \tag{6.2}$$

The reconstruction of kinematic variables is done — as in the exclusive J/ψ case — using the double angle method.

The mass spectra found are displayed in figure 6.1. Clear signals with little background are observed in the two-lepton mass spectrum (m_{ll}), in the four-track mass spectrum ($m_{ll\pi\pi}$) at the nominal $\psi(2S)$ mass of $m_{\psi(2S)} = 3.686\,\mathrm{GeV}$ [30], and in the mass difference $\Delta m = m_{ll\pi\pi} - m_{ll}$. The nominal value for Δm is 589 MeV. The width of the signals is completely due to the experimental resolution.

135
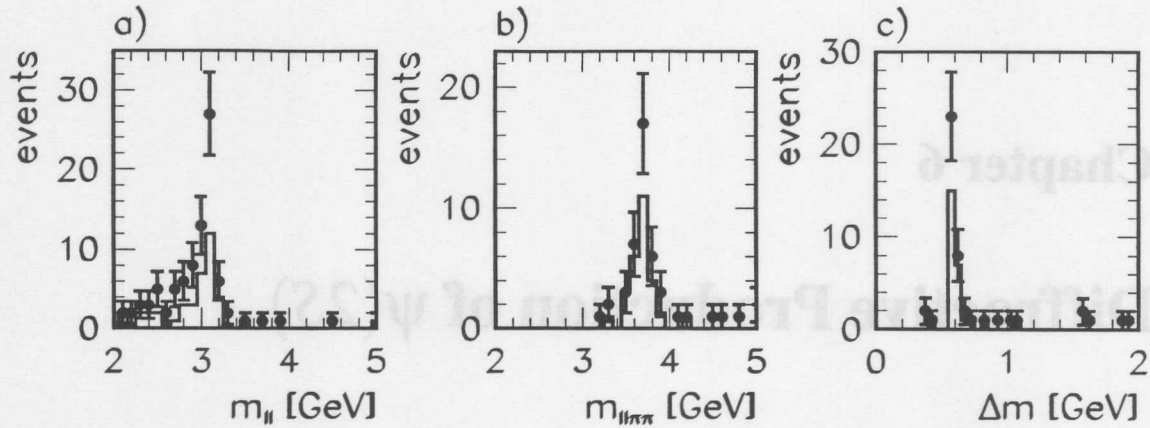
Figure 6.1: *Mass spectra showing* ψ(2S) *signals: a) two-lepton invariant mass* m_{ll}*, b) four-track invariant mass* $m_{ll\pi\pi}$ *for events fulfilling* $|m_{ll} - m_\psi| < 300$ MeV*, and c) the mass difference* $\Delta m = m_{ll\pi\pi} - m_{ll}$*. Full points denote all events in the loose selection, the histograms are the fraction also fulfilling the tight selection cuts (see section 4.5.2).*

6.2   Acceptance and Efficiency Determination for Exclusive ψ(2S) Production

The correction of the data proceeds as already presented for exclusive J/ψ production in chapter 5. The same trigger efficiencies for the scattered electron are used, and the correction of the muon and electron identification efficiency in the Monte Carlo simulation is done as described there. However, in view of the small statistics no separation of elastic and proton dissociative production mechanisms is attempted. Instead it is assumed that both processes have the same cross sections, and a Monte Carlo sample containing both processes is used for acceptance and efficiency determination. It has been checked that the ratio of the number of events with and without a forward tag is compatible for J/ψ and ψ(2S) candidate events.

It has already been shown in chapter 5 (section 5.1.7) that the simulation is able to describe the data for exclusive J/ψ production. In the following, properties of Monte Carlo and data events will be compared for ψ(2S) candidates.

The ψ(2S) signal region is defined by

$$|m_{ll} - m_\psi| \quad < \quad 300\,\text{MeV} \quad \text{and} \tag{6.3}$$
$$500\,\text{MeV} \quad < \quad \Delta m \quad < \quad 700\,\text{MeV}. \tag{6.4}$$

In the loose selection, 32 events pass these cuts. They are compared to the Monte Carlo simulation in figure 6.2. In general the agreement is good, but the statistics are too small to allow any definite conclusions. It is noted [180] that the two-pion mass spectrum — figure 6.2 c) — is not correctly implemented in the DIFFVM Monte Carlo program; the distribution of the ψ(2S) decay particles is generated according to phase space, while data from previous experiments [181, 182] show a different mass spectrum for the two pion system. The measured mass spectrum is more biased towards higher $m_{\pi\pi}$, as is also observed in figure 6.2 c). No correction is applied in order to correct for this effect.
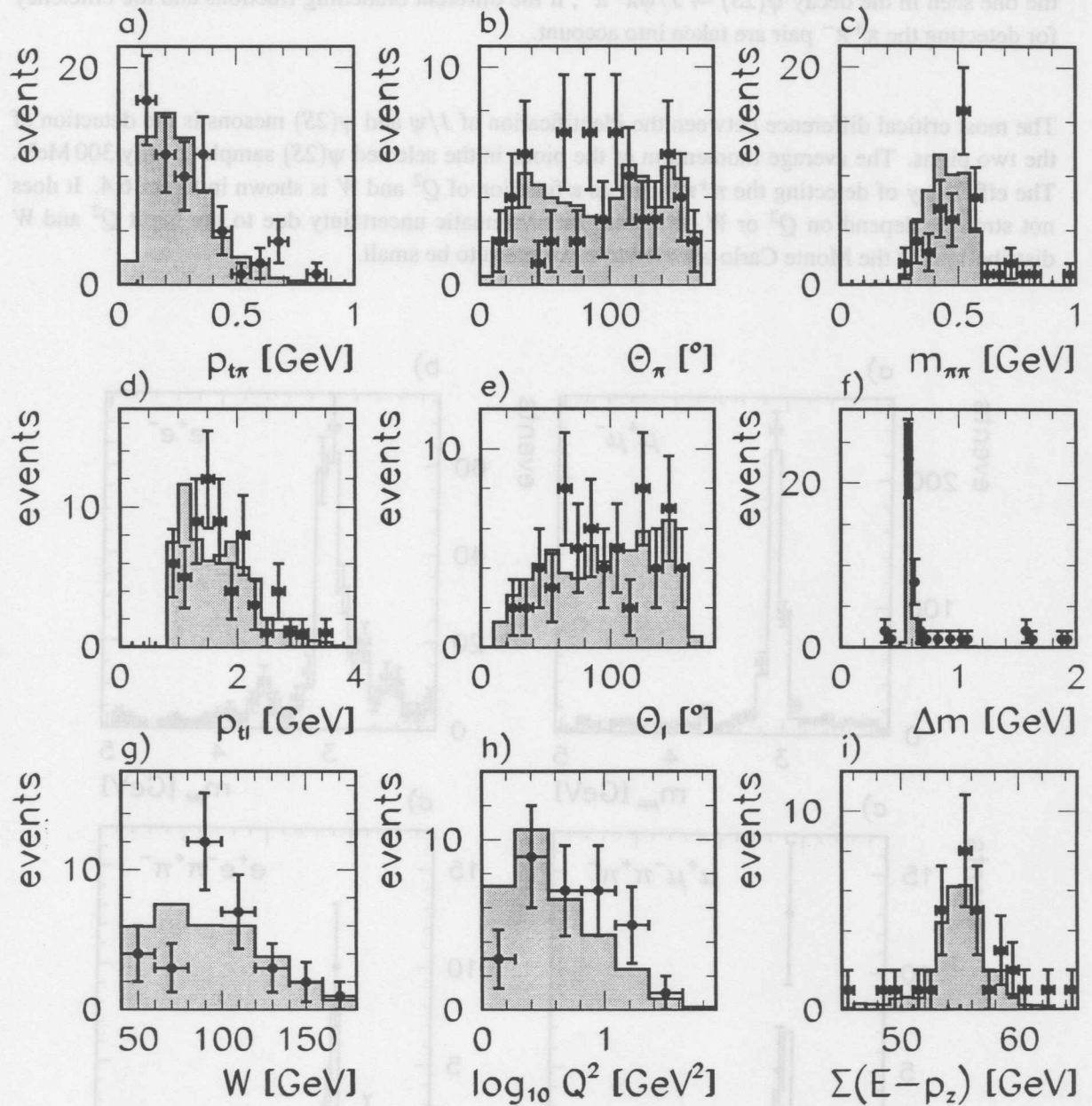
Figure 6.2: *Comparison between data and Monte Carlo simulation for some key distributions of the ψ(2S) signal events (loose selection). For figure f), the cut on Δm was not applied.*

The $\psi(2S)$ mass spectra for the electron and the muon decay channel separately are shown in figure 6.3, together with the mass spectra of the J/ψ selection later used for determination of the cross section ratio. In the latter plots there is an indication for a $\psi(2S)$ signal through the direct decay $\psi(2S) \to l^+l^-$. This signal is not used for cross section determination, but its size is compatible with the one seen in the decay $\psi(2S) \to J/\psi\pi^+\pi^-$, if the different branching fractions and the efficiency for detecting the $\pi^+\pi^-$ pair are taken into account.

The most critical difference between the identification of J/ψ and $\psi(2S)$ mesons is the detection of the two pions. The average momentum of the pions in the selected $\psi(2S)$ sample is only 300 MeV. The efficiency of detecting the $\pi^+\pi^-$ pair as a function of Q^2 and W is shown in figure 6.4. It does not strongly depend on Q^2 or W, therefore the systematic uncertainty due to the input Q^2 and W distributions of the Monte Carlo simulation is expected to be small.
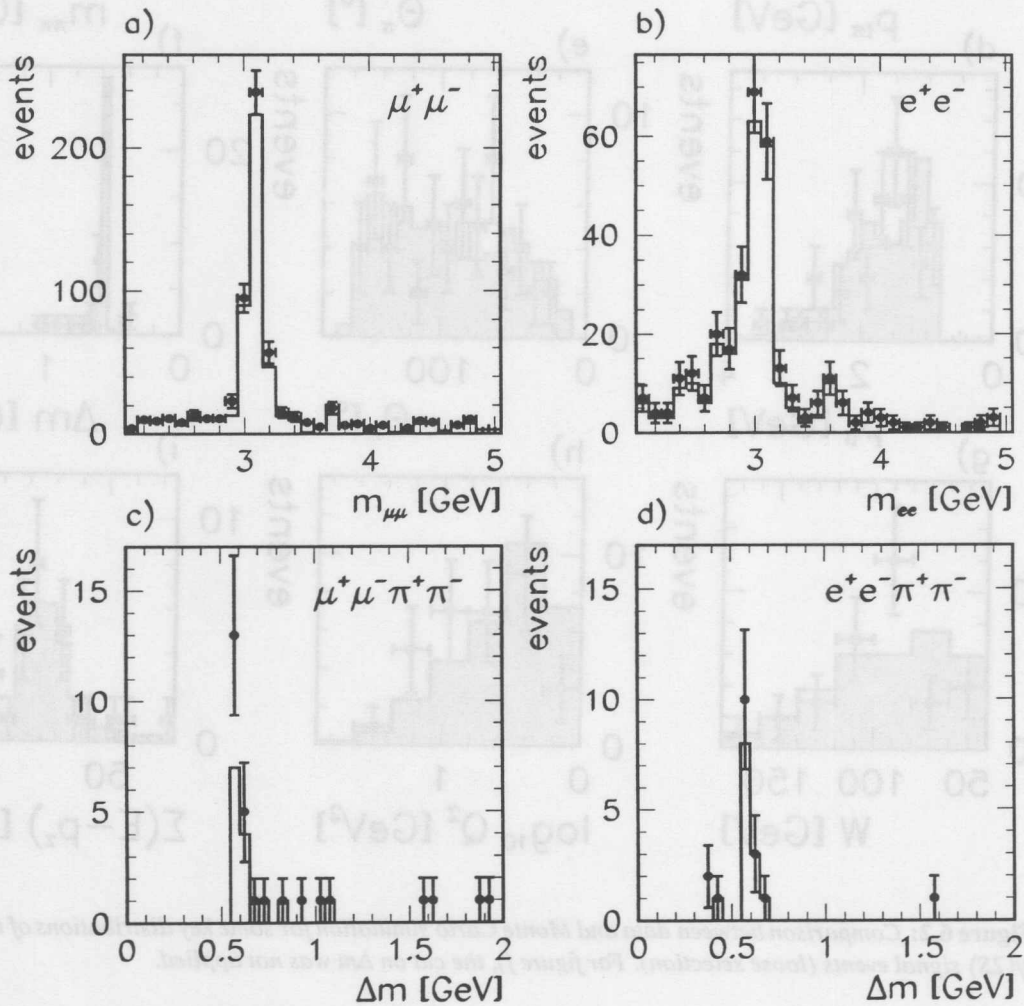
Figure 6.3: J/ψ (a), b)) and $\psi(2S)$ (c), d)) signals in the electron and muon decay channels. The points are for all events in the loose selection, the histograms show events that fulfil the tight selection.
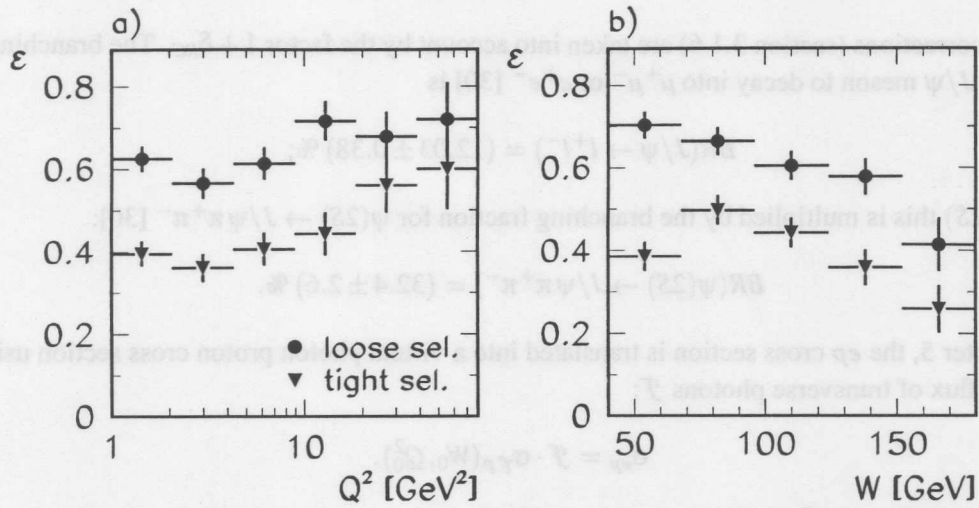
Figure 6.4: *Efficiency of detecting the $\pi^+\pi^-$ pair in $\psi(2S)$ decays as a function of a) Q^2 and b) W, determined from DIFFVM Monte Carlo events.*

6.3 Results on Exclusive ψ(2S) Production

To extract virtual photoproduction cross sections as a function of Q^2, the following procedure is adopted. The data are divided into three bins in Q^2, namely

$$1 \; < \; Q^2 \; < \; 5\,\text{GeV}^2, \tag{6.5}$$
$$5 \; < \; Q^2 \; < \; 12\,\text{GeV}^2 \quad \text{and} \tag{6.6}$$
$$12 \; < \; Q^2 \; < \; 80\,\text{GeV}^2. \tag{6.7}$$

The mass spectra obtained for the three analysis bins are shown in figure 6.5 both for the J/ψ and the $\psi(2S)$ selection.

In each bin, the number of J/ψ signal events is determined as described in the exclusive J/ψ chapter, section 5.1.8. The number of $\psi(2S)$ signal events is determined by counting events in the mass interval $500\,\text{MeV} < \Delta m < 700\,\text{MeV}$; from the sidebands of the Δm distribution, the background from other processes is estimated to be 8 %, and subtracted from the numbers obtained.

The total acceptance for each bin $Q_1^2 < Q^2 < Q_2^2$ is calculated from

$$\varepsilon = \frac{N(40 < W_{DA} < 180\,\text{GeV}, Q_1^2 < Q_{DA}^2 < Q_2^2)}{N(40 < W_{gen} < 180\,\text{GeV}, Q_1^2 < Q_{gen}^2 < Q_2^2)} \tag{6.8}$$

using the J/ψ and $\psi(2S)$ DIFFVM Monte Carlo, respectively. Here W_{gen} and Q_{gen}^2 denote W and Q^2 as generated by the Monte Carlo, while W_{DA} and Q_{DA}^2 are the reconstructed quantities using the double angle method. In the denominator all events generated in the given limits are counted, whereas only those that pass all analysis cuts enter the numerator.

The number of signal events N_{ev} is translated into an ep cross section using the relation

$$\sigma_{ep} = \frac{N_{ev}}{(1 + \delta_{RC}) \cdot \varepsilon \cdot BR \cdot \int L dt}. \tag{6.9}$$

Radiative corrections (section 3.1.6) are taken into account by the factor $1 + \delta_{RC}$. The branching ratio BR for the J/ψ meson to decay into $\mu^+\mu^-$ or e^+e^- [30] is

$$BR(J/\psi \to l^+l^-) = (12.03 \pm 0.38)\,\%; \tag{6.10}$$

for the $\psi(2S)$ this is multiplied by the branching fraction for $\psi(2S) \to J/\psi\pi^+\pi^-$ [30]:

$$BR(\psi(2S) \to J/\psi\pi^+\pi^-) = (32.4 \pm 2.6)\,\%. \tag{6.11}$$

As in chapter 5, the ep cross section is translated into a virtual photon proton cross section using the integrated flux of transverse photons $\mathcal{F}$:

$$\sigma_{ep} = \mathcal{F} \cdot \sigma_{\gamma^* p}(W_0, Q_0^2). \tag{6.12}$$

The values for W_0 and Q_0^2 are determined as described there (section 5.2.1).

The number of signal events, cross sections and the ratio of $\psi(2S)$ to J/ψ production thus derived are summarized in table 6.1. No systematic errors are given for the J/ψ and $\psi(2S)$ results separately. Note however that the cross sections obtained here for exclusive J/ψ production are within errors compatible with the sum of the elastic and proton dissociation cross sections derived in section 5.2.1.
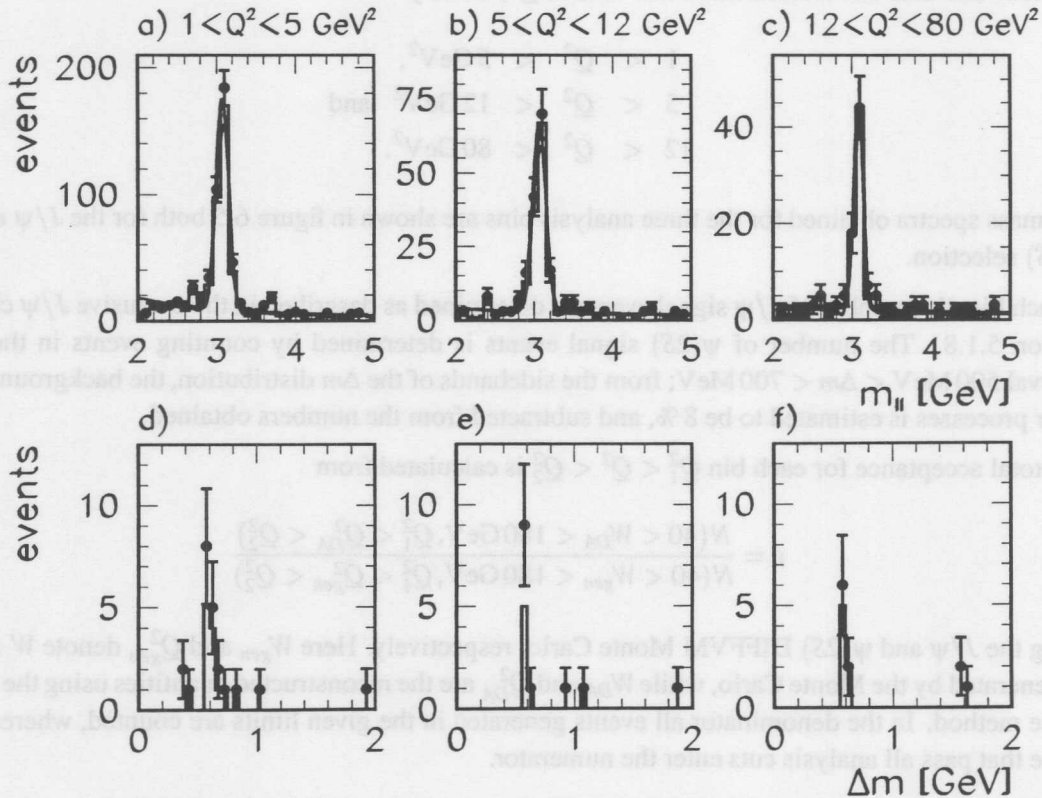
Figure 6.5: J/ψ (a), b), c)) and $\psi(2S)$ (d), e), f)) signals in bins of Q^2. Again, points are for all events in the loose selection, while the histograms contain events that fulfil the tight selection.

The systematic error on the ratio using the tight selection is estimated to be approximately of the same size (15 %) as determined for $\psi(2S)$ photoproduction by H1 [170], since the selection cuts used for the two pions are almost identical. No systematic error can be given for the ratio obtained using the loose selection, because in this case pions are selected with very small p_t and θ, where the efficiency of the tracking devices is not fully understood.

The ratio $\sigma_{\gamma^*p}^{\psi(2S)}/\sigma_{\gamma^*p}^{\psi}$ as a function of Q^2 is shown in figure 6.6 a) together with the H1 photoproduction measurement [170]

$$\sigma_{\gamma p}^{\psi(2S)}/\sigma_{\gamma p}^{\psi} = 0.150 \pm 0.027(\text{stat.}) \pm 0.022(\text{syst.}). \tag{6.13}$$

At small Q^2 good agreement between the H1 result from [170] and the analysis presented here is observed, and also with a preliminary ZEUS measurement in photoproduction [187]:

$$\sigma_{\gamma p}^{\psi(2S)}/\sigma_{\gamma p}^{\psi} = 0.16 \pm 0.02(\text{stat.}) \pm 0.04(\text{syst.}). \tag{6.14}$$

For higher Q^2 there is an indication of a rise of the ratio, which becomes more obvious when the statistics of the two high Q^2 bins are combined (6.6 b)); the result including statistical and systematic errors at $Q^2 = 15.4 \, \text{GeV}^2$ (tight selection) is

$$\sigma_{\gamma^*p}^{\psi(2S)}/\sigma_{\gamma^*p}^{\psi} = 0.55 \pm 0.20, \tag{6.15}$$

which is 2σ above the central value measured in photoproduction. The rise is consistent with that predicted by Nemchik et al. [48] in the framework of the Colour Dipole Model.

A significant increase in statistics by exploiting other decay channels ($\psi(2S) \to l^+l^-$) and an increase of luminosity is desirable.
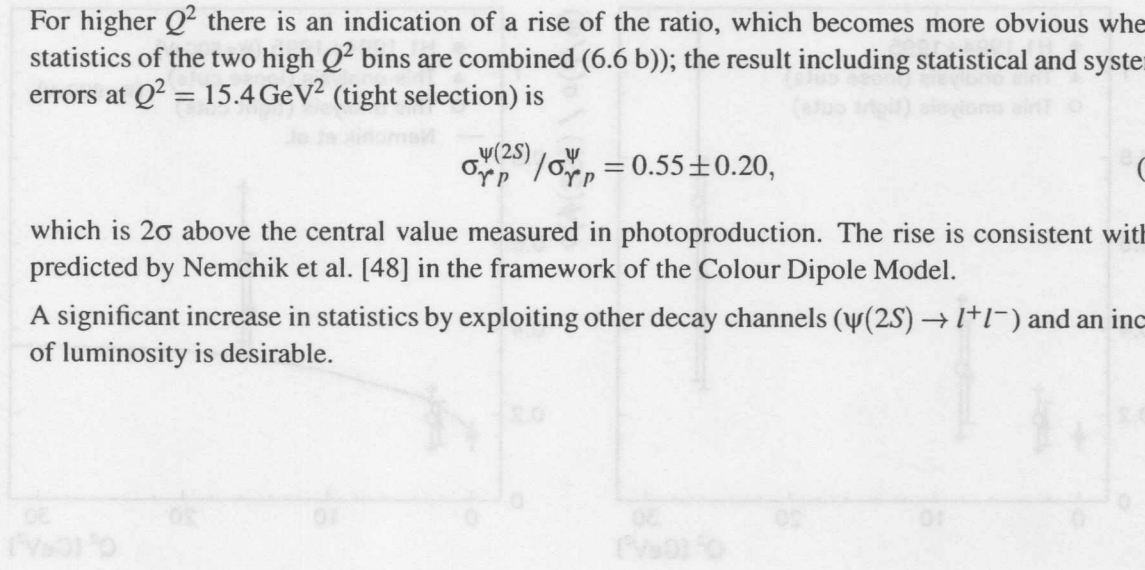
Figure 6.6: *Ratio of cross sections for exclusive $\psi(2S)$ over J/ψ production as a function of Q^2. Note that the results obtained using the tight selection are displayed slightly shifted in Q^2 to increase readability. Errors for the loose selection are statistical only. a) Three bins in Q^2; b) two bins in Q^2. In b), the prediction of Nemchik et al. [48] is shown in addition.*

	loose selection		tight selection	
	J/ψ	$\psi(2S)$	J/ψ	$\psi(2S)$
	$1 < Q^2 < 5\,\text{GeV}^2$ $40 < W < 180\,\text{GeV}$			
N_{ev}	336 ± 20	13.8 ± 3.7	306 ± 19	9.2 ± 3.0
σ_{ep} [pb]	679 ± 45	119 ± 34	663 ± 46	127 ± 46
$\mathcal{F}$	0.01009			
W_0 [GeV]	89.8			
Q_0^2 [GeV^2]	2.3			
$\sigma_{\gamma p}$ [nb]	67.3 ± 4.5	11.8 ± 3.4	65.7 ± 5.0	12.6 ± 4.5
$\sigma_{\gamma p}^{\psi(2S)}/\sigma_{\gamma p}^{\psi}$	0.18 ± 0.05		$0.19 \pm 0.07 \pm 0.03$	
	$5 < Q^2 < 12\,\text{GeV}^2$ $40 < W < 180\,\text{GeV}$			
N_{ev}	134 ± 13	9.2 ± 3.0	121 ± 12	5.5 ± 2.3
σ_{ep} [pb]	196 ± 22	60 ± 24	193 ± 22	60 ± 31
$\mathcal{F}$	0.00549			
W_0 [GeV]	89.8			
Q_0^2 [GeV^2]	7.7			
$\sigma_{\gamma p}$ [nb]	35.8 ± 3.9	10.9 ± 4.2	35.1 ± 4.0	10.9 ± 5.5
$\sigma_{\gamma p}^{\psi(2S)}/\sigma_{\gamma p}^{\psi}$	0.30 ± 0.12		$0.31 \pm 0.16 \pm 0.05$	
	$12 < Q^2 < 80\,\text{GeV}^2$ $40 < W < 180\,\text{GeV}$			
N_{ev}	68 ± 9	7.4 ± 2.7	66 ± 8	6.4 ± 2.5
σ_{ep} [pb]	77 ± 12	41 ± 20	80 ± 12	57 ± 33
$\mathcal{F}$	0.01182			
W_0 [GeV]	89.9			
Q_0^2 [GeV^2]	26.0			
$\sigma_{\gamma p}$ [nb]	6.5 ± 1.0	3.5 ± 1.7	6.8 ± 1.0	4.9 ± 2.8
$\sigma_{\gamma p}^{\psi(2S)}/\sigma_{\gamma p}^{\psi}$	0.53 ± 0.27		$0.70 \pm 0.42 \pm 0.06$	

Table 6.1: *Summary table of exclusive J/ψ and $\psi(2S)$ cross sections, both for the loose and the tight selection. All errors are statistical only, except for the ratio $\sigma_{\gamma p}^{\psi(2S)}/\sigma_{\gamma p}^{\psi}$ using the tight selection, where both statistical and systematic errors are given.*

Table 6.1: Summary table of exclusive J/ψ and $\psi(2S)$ cross sections, both for the loose and the tight selection. All errors are statistical only, except for the ratio $\sigma^{\psi(2S)}_{\gamma p}/\sigma^{J/\psi}_{\gamma p}$ using the tight selection, where both statistical and systematic errors are given.

Chapter 7

Inclusive J/ψ Production

In previous analyses of J/ψ production at HERA, the "diffractive" and "inelastic" regime have been separated by e.g. a cut in the elasticity variable z. Recent experimental and theoretical developments suggest however large non-diffractive contributions also in the high z regime from $c\bar{c}$ pairs produced in colour-octet states (see section 3.3.3). It is therefore desirable to undertake a model independent analysis of inclusive J/ψ production.

In this chapter, an attempt of such an analysis will be presented; the selection of the data sample was described in section 4.5.3. The chapter is structured as follows. In the first section, the method of acceptance and efficiency correction of the data is discussed. A Monte Carlo data set is constructed that gives a good description of the data, and that is used for acceptance and efficiency corrections. In the following section the resulting differential cross sections in z, Q^2, transverse momentum and rapidity of the J/ψ are presented for different cut scenarios and compared to expectations within the NRQCD formalism. The results are discussed in the final section.

7.1 Acceptance and Efficiency Determination for Inclusive J/ψ Production

The kinematic region used for the analysis is motivated as already discussed for diffractive J/ψ production in section 5.1.2. The limiting factor in Q^2 is the geometrical acceptance for the scattered electron, while the acceptance in W is restricted due to the cut $20° < \theta_l < 160°$ on the polar angle of the J/ψ decay leptons. In order to avoid large acceptance corrections, the analysis is limited to

$$2 < Q^2 < 80\,\text{GeV}^2 \quad \text{and} \tag{7.1}$$
$$40 < W < 180\,\text{GeV}, \tag{7.2}$$

which is identical to the diffractive J/ψ analysis of chapter 5 in Q^2, while the W region is slightly extended towards larger values ($160\,\text{GeV} \mapsto 180\,\text{GeV}$).

7.1.1 Mass Spectra and Background Subtraction

The fraction of non-resonant background in the J/ψ mass region is mainly a function of the elasticity z; therefore the following correction procedure is used:

- The data are divided into seven bins in z.

- In each bin, all events in a region $\pm 250\,\mathrm{MeV}$ around the nominal J/ψ mass are counted as J/ψ candidates.

- The number of background events contributing to the J/ψ peak in each z bin is determined by fitting a Gaussian to the signal plus a power law m_{ll}^{-n} for the background to the mass spectrum, and integrating the exponential from $m_\psi - 250\,\mathrm{MeV}$ to $m_\psi + 250\,\mathrm{MeV}$.

- Corresponding to its z value, each single event is assigned a non-resonant background fraction f_{nr} as determined in the corresponding z bin.

The mass spectra and fits are shown in figures 7.1 ($z < 0.65$) and 7.2 ($z > 0.65$) separately for the muon (left column) and electron (middle column) decay channels. Below $z = 0.35$ no significant J/ψ signal is observed.

The special selection for the $J/\psi \to \mu^+\mu^-$ channel ("$\mu^+\mu^-$ tight cuts", see section 4.5.3) was designed in order to further reduce the background in the low z regime, albeit with a reduced efficiency. As can be seen in the right column of figure 7.1, even in this sample no significant J/ψ signal is observed for very small z. It was thus decided not to use the tight selection for the cross section determination.

The systematic error introduced by the method used for the determination of the number of signal events was estimated to be between 10 % ($z < 0.5$) and 4 % ($z > 0.5$) by changing the functional form of the background shape from a power law to an exponential. In the cross section measurements, the electron channel will only be used for $z > 0.5$, while the full z range is included for the $\mu^+\mu^-$ channel.

7.1.2 Comparison of Data and Monte Carlo Simulation

The correction of the data for acceptance losses and detector effects is done with Monte Carlo simulations. Many of the results obtained for exclusive J/ψ production (chapter 5) concerning the quality of the detector simulation can be used here. The corrections for trigger inefficiencies (section 5.1.3) and of electron and muon identification (section 5.1.5) efficiencies are applied in the same manner. Also the systematic errors quoted there for trigger and lepton identification as well as for vertex finding and track reconstruction efficiency (section 5.1.4) are adopted.

In view of the absence of a Monte Carlo program that describes inclusive J/ψ production in the entire kinematical range, a Monte Carlo data set was constructed from available generators, namely:

- the EPJPSI program (section 4.6.3) based on the Colour Singlet Model. EPJPSI uses the matrix element for $\gamma g \to J/\psi + g$ including relativistic corrections. The equivalent photon approximation is applied to obtain ep cross sections also for $Q^2 > 0$;

- the DIFFVM program (section 4.6.1) for the description of J/ψ production at large z. For the ratio of elastic to proton dissociation cross sections in the DIFFVM simulation the result from chapter 5 is used.

Distributions of kinematical quantities of the two Monte Carlo programs in the kinematic region under study are shown in figure 7.3.

J/ψ → l⁺l⁻ inclusive
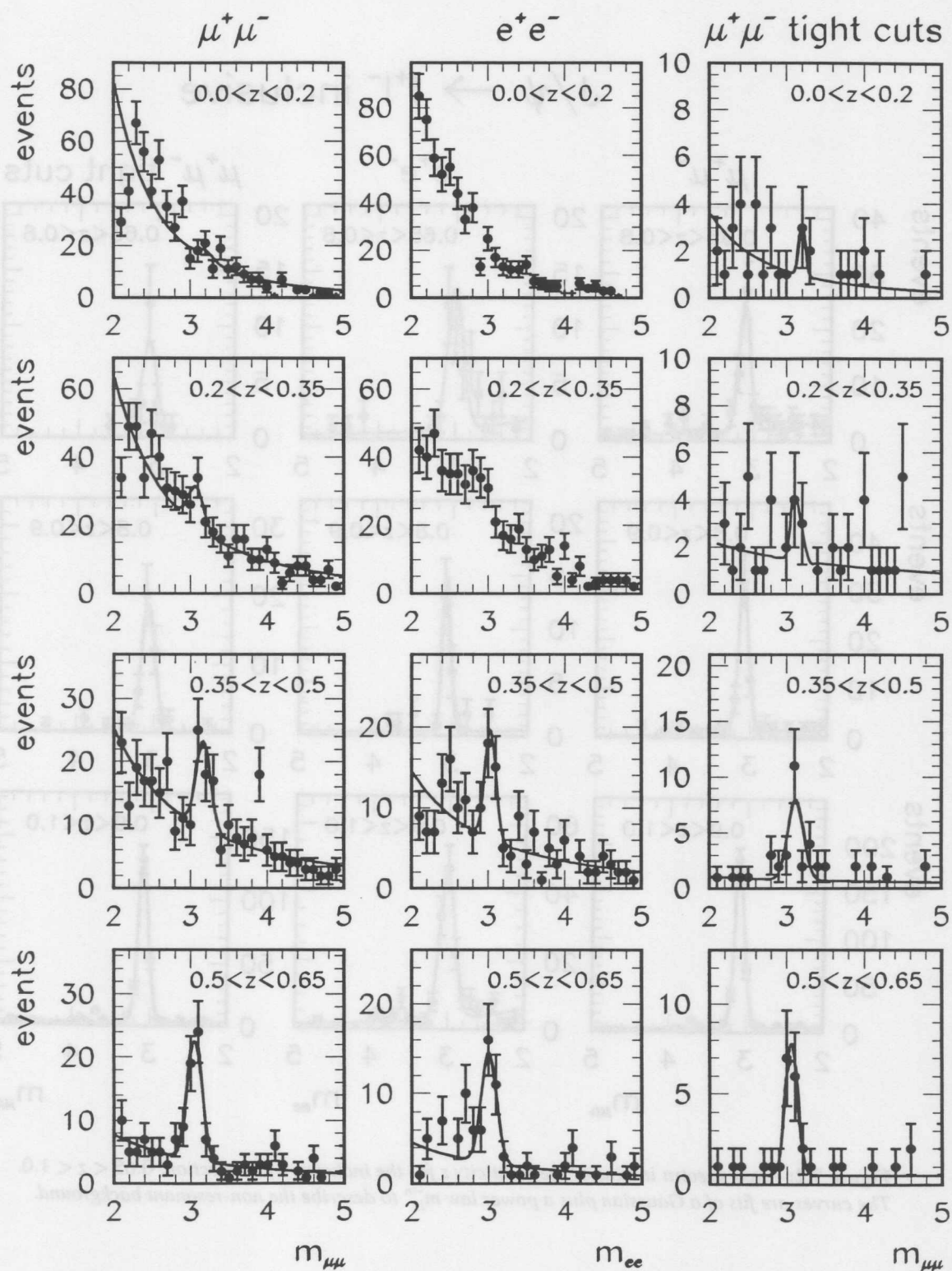
Figure 7.1: *Mass spectra in bins of the elasticity z for the inclusive J/ψ selection, 0.0 < z < 0.65. The curves are fits of a Gaussian plus a power law m_{ll}^{-n} to describe the non-resonant background.*
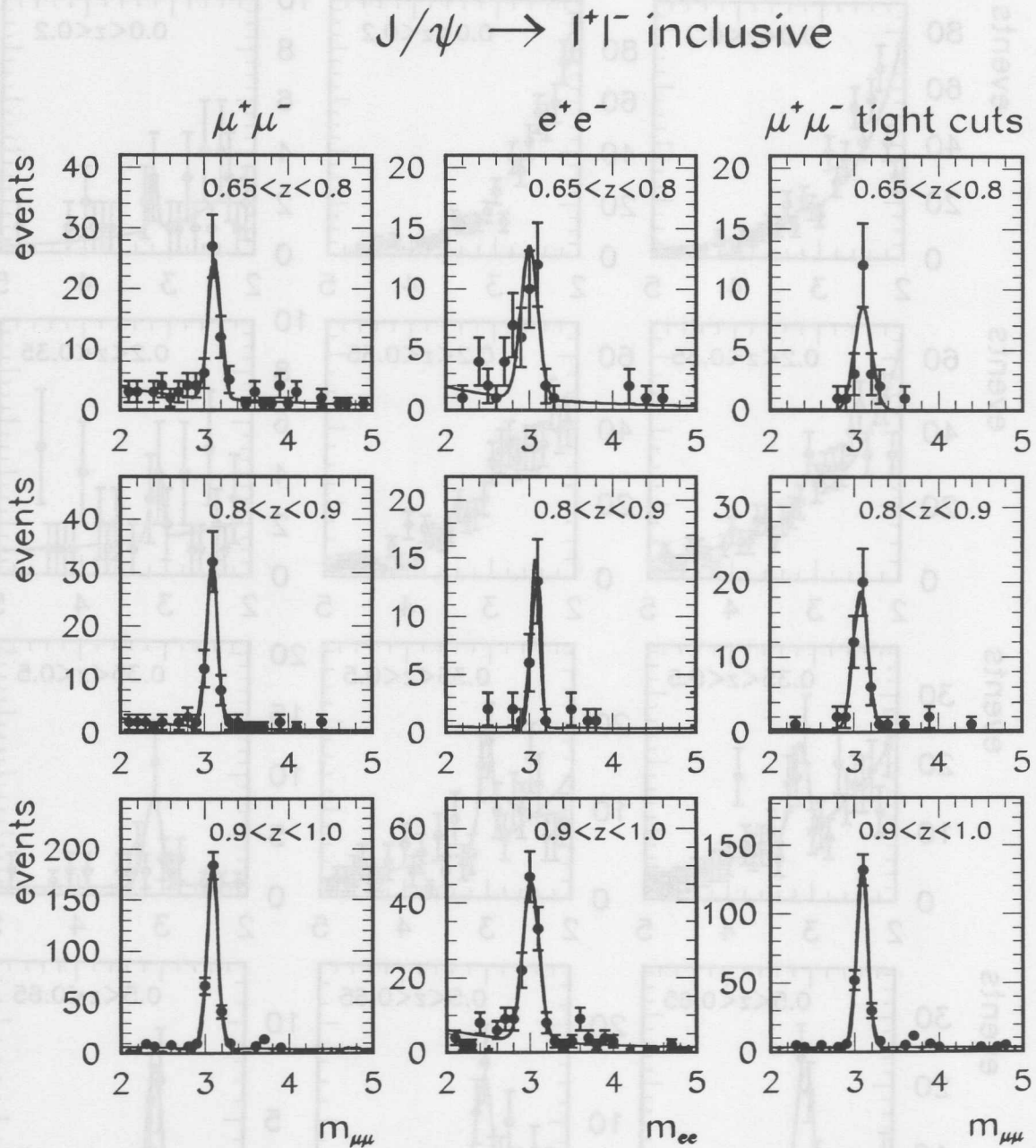
Figure 7.2: *Mass spectra in bins of the elasticity z for the inclusive J/ψ selection, $0.65 < z < 1.0$. The curves are fits of a Gaussian plus a power law m_{ll}^{-n} to describe the non-resonant background.*

The relative normalization of the two contributions to the Monte Carlo simulation was fixed using the background corrected z distribution: the EPJPSI fraction was chosen to match the overall normalization for $0.4 < z < 0.8$. The excess of the data over the EPJPSI Monte Carlo simulation at large z — $z > 0.95$ — was used to normalize the DIFFVM fraction.

The combined Monte Carlo data set is now compared to the data with respect to other observables. Note that all figures contain only statistical errors, and that the Monte Carlo data set is always normalized to the data. Non-resonant background is subtracted statistically as a funtion of z as described above.

Figure 7.4 shows quantities related to the scattered electron in the SpaCal. Small deviations in the peak region of the energy spectrum of the scattered electron and at large scattering angles θ_e can be traced back to the Q^2 distribution. The energy weighted cluster radius R_{cl} has been multiplied with a factor 1.1 in the simulation to achieve good agreement, as already described in section 4.3. The tail in the $\Sigma(E - p_z)$ distribution towards low values can be attributed to QED radiative events.

Kinematic variables important for J/ψ production are compared in figure 7.5. The distributions of W, $p_{t,\psi}^2$, η_ψ — the pseudorapidity of the J/ψ —, and y_Σ/y_e — the ratio of the measured y using the Σ and the electron method — are well reproduced by the Monte Carlo simulation. The Q^2 spectrum in the simulation slightly overshoots the data at small Q^2. The strong correlation between Q^2 and $p_{t,\psi}^2$ is shown in d). The z distribution is well described; a small excess can be seen at very low z, which could either be attributed to a resolved photon component that is not contained in the Monte Carlo
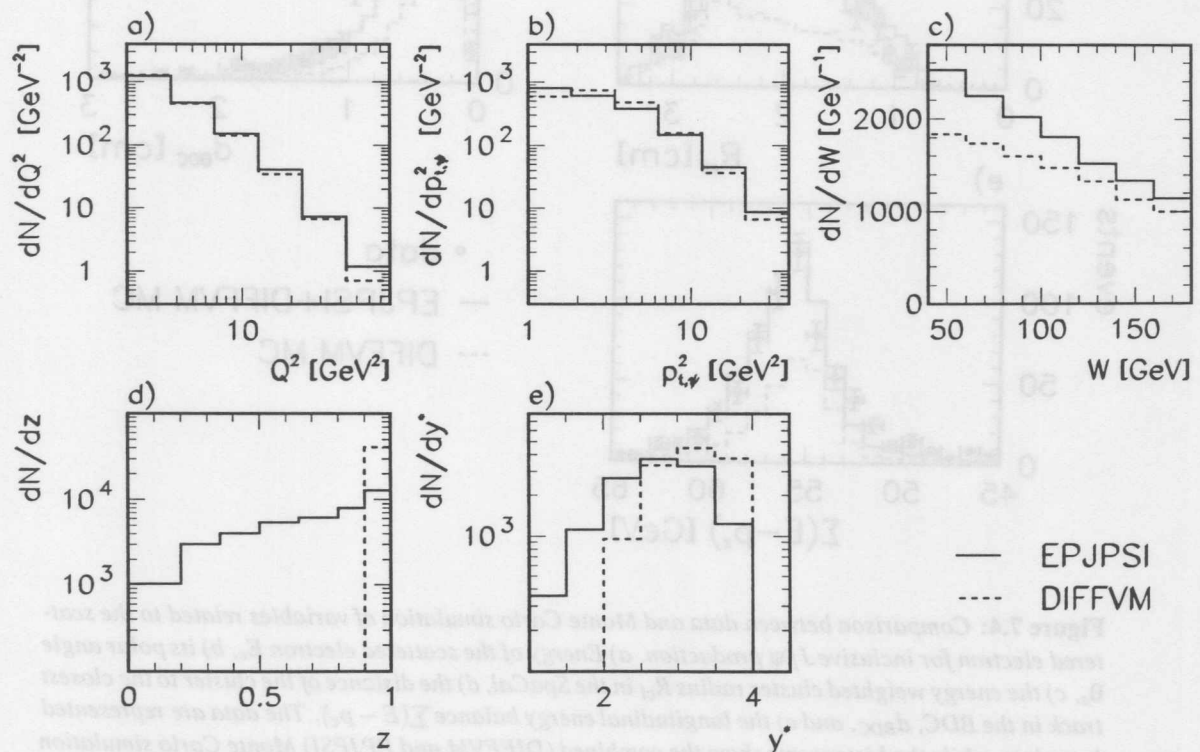
Figure 7.3: *Comparison of the two Monte Carlo programs DIFFVM and EPJPSI with respect to kinematical variables. The histograms are for $40 < W < 180\,\mathrm{GeV}$ and $2 < Q^2 < 80\,\mathrm{GeV}^2$, and are normalized to the same number of events. Detector effects are not included.*
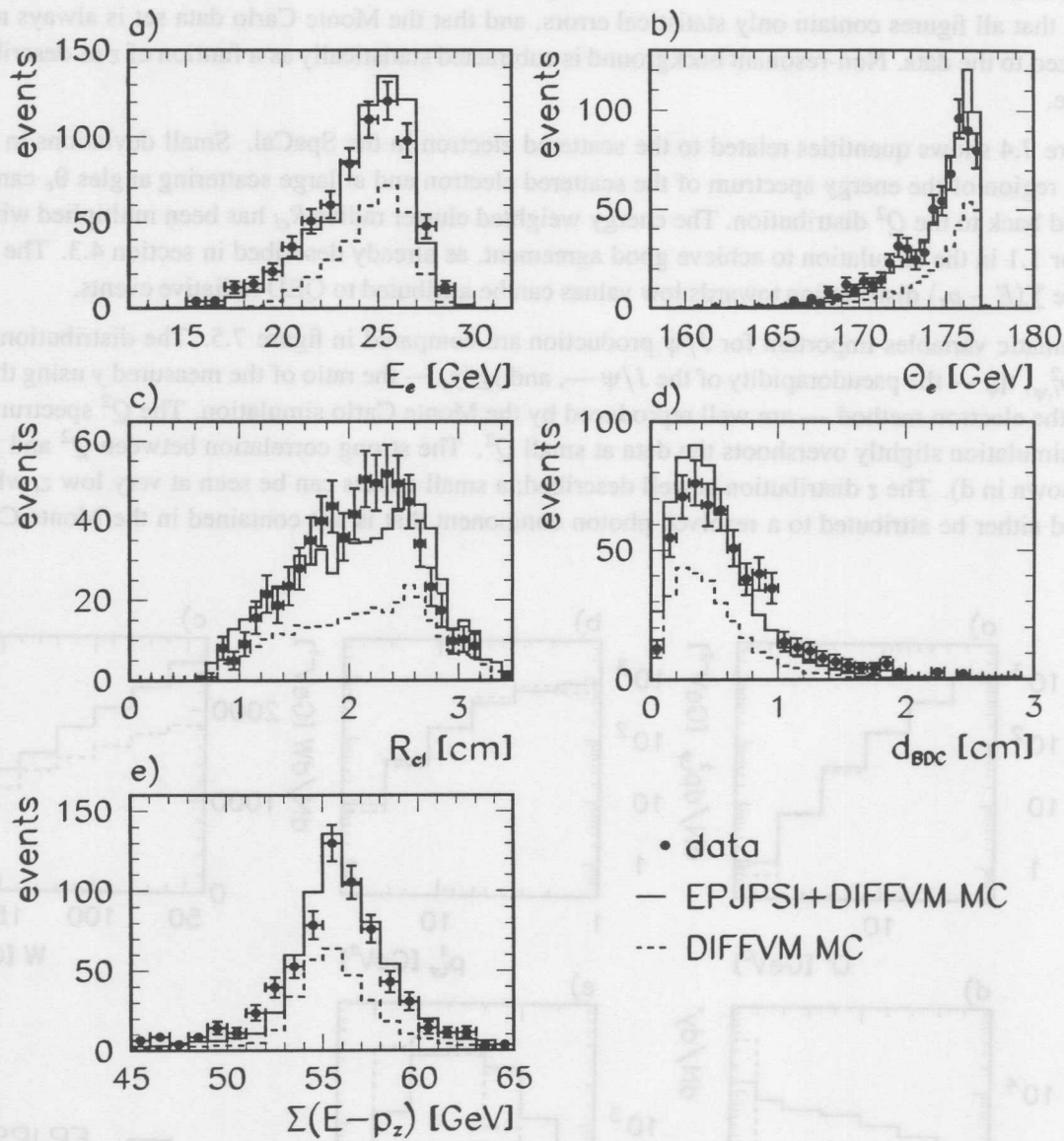
Figure 7.4: *Comparison between data and Monte Carlo simulation of variables related to the scattered electron for inclusive J/ψ production. a) Energy of the scattered electron E_e, b) its polar angle θ_e, c) the energy weighted cluster radius R_{cl} in the SpaCal, d) the distance of the cluster to the closest track in the BDC, d_{BDC}, and e) the longitudinal energy balance $\sum(E - p_z)$. The data are represented by points, while the histograms show the combined (DIFFVM and EPJPSI) Monte Carlo simulation (full lines) and the DIFFVM contribution separately (dashed).*

simulation used, or to J/ψ mesons from B meson decays[1]. The step at $z = 0.5$ is due to the fact that the electron decay channel is not used for $z < 0.5$.

The distribution of the polar angles and transverse momenta of the decay leptons are given in figure 7.6; again, good agreement between data and Monte Carlo simulation is observed.

The shapes of all distributions compared so far have been rather similar for the DIFFVM and the EPJPSI Monte Carlo program, the only exception being the inelasticity z. However, the agreement between data and Monte Carlo simulation in z is no surprise, because z was chosen to determine the composition of the Monte Carlo data set. Therefore some topological variables have been designed that should give more insight in how far the simulation is able to describe the data, and to make sure that the Monte Carlo data set can be used for the correction of the data. The following quantities are defined and compared to the Monte Carlo simulation in figure 7.7:

$E_\bullet$ is the summed energy in the LAr calorimeter in a cone with radius

$$R := \sqrt{(\Delta\eta)^2 + (\Delta\phi)^2} = 1 \qquad (7.3)$$

around the direction of flight of the J/ψ meson. Energy deposits attributed to the decay leptons are excluded from the sum.

$N_{tr\bullet}$ denotes the number of "good" tracks in a cone with radius $R = 1$ around the J/ψ direction, again excluding the decay leptons. "Good" tracks are defined by the condition $\sigma_{p_t}/p_t < 0.05$; both "forward" and "central" tracks are used, i.e. tracks reconstructed in the forward and central tracker.

E_{fwd} is the summed energy in the LAr calorimeter of deposits with polar angles $\theta_{cell} < 20°$, again excluding deposits originating from the J/ψ decay leptons.

$N_{tr,fwd}$ is the number of "good" tracks with polar angles $\theta_{tr} < 20°$; "good" tracks are defined as above.

η_{max} is the pseudorapidity of the most forward object in the detector, using "central" tracks with transverse momenta above 100 MeV, LAr clusters with energies above 400 MeV and SpaCal clusters above 200 MeV. The decay leptons are included.

The shapes of the DIFFVM and EPJPSI data sets differ significantly for all the above variables; nevertheless the data are remarkably well described by the combined Monte Carlo simulation, thus giving confidence that the simulation can be used for the extraction of fully inclusive cross sections for J/ψ production.

A slight discrepancy between data and simulation is observed in the η_{max} distribution (figure 7.7e)). A possible explanation could be the presence of contributions from $\psi(2S)$ production in the data — both elastic and inelastic —, where the $\psi(2S)$ decays into $J/\psi + X$, which are not contained in the simulation. The $\psi(2S)$ contamination can lead to larger track multiplicities and smearing in the η_{max} distribution due to the additional decay products X. However, a Monte Carlo data set of *diffractively*

---

[1]Using the recent H1 preliminary measurement of the inclusive visible $b\bar{b}$ photoproduction cross section [183], an estimate of the expected J/ψ yield from B meson decays is possible. The branching fraction for $b \rightarrow J/\psi +$ anything is 1.16 % [30]. The number of observed J/ψ events from B meson decays in the kinematic domain of the present analysis is expected to be of the order of 5 to 10.
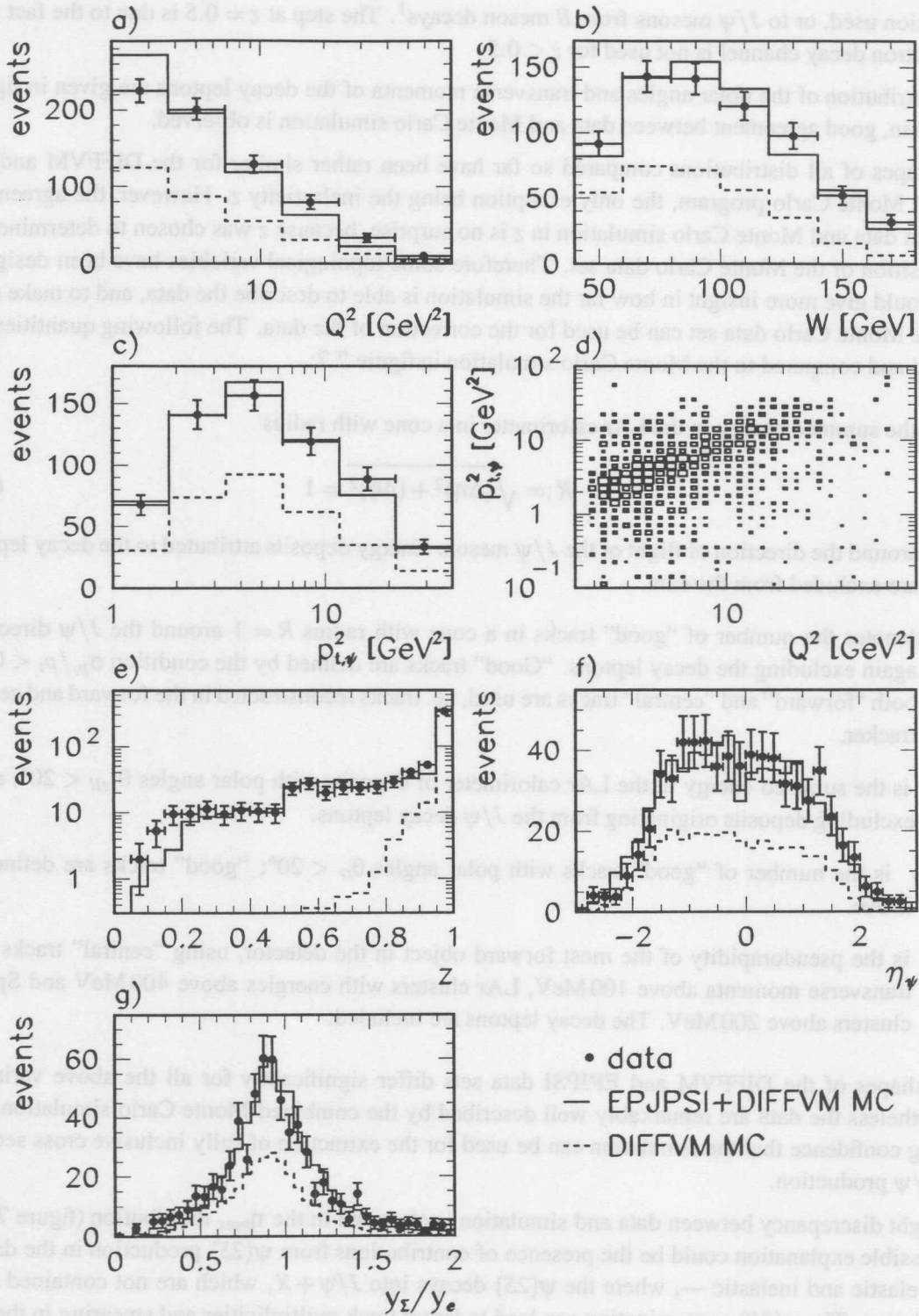
Figure 7.5: *Comparison between data and Monte Carlo simulation of kinematic variables for inclusive J/ψ production. a) Q^2, b) W, c) $p_{t,\psi}^2$, d) correlation between Q^2 and $p_{t,\psi}^2$ (data only), e) the inelasticity z, f) the pseudorapidity η_ψ of the J/ψ in the laboratory frame, and g) the ratio y_Σ/y_e of the measured y using the Σ and the electron method. The data are represented by points, while the histograms show the combined (DIFFVM and EPJPSI) Monte Carlo simulation (full lines) and the DIFFVM contribution separately.*
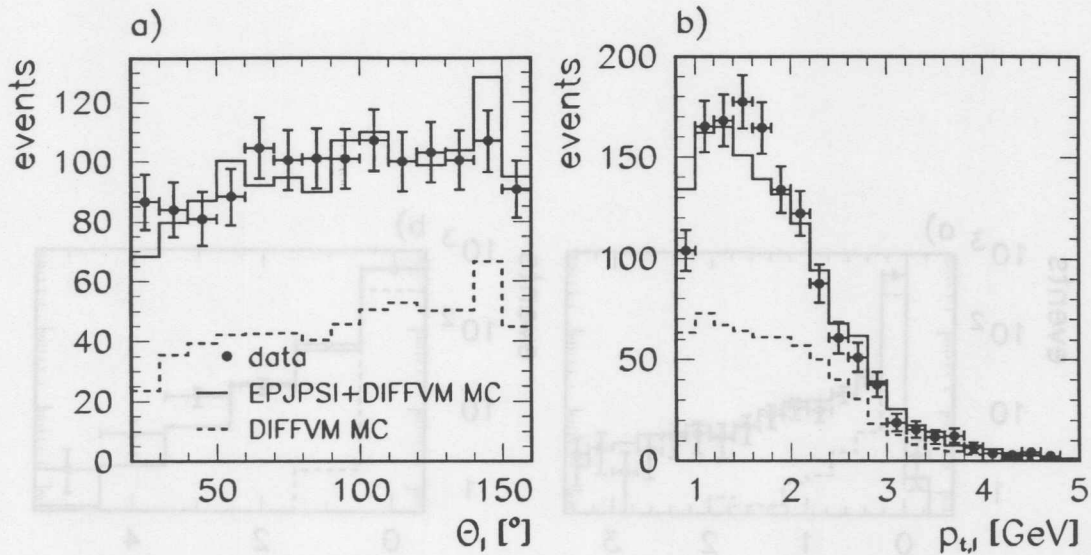
Figure 7.6: *Comparison between data and Monte Carlo simulation for inclusive J/ψ production; a) polar angle θ_l and b) transverse momentum p_{t,l} of decay leptons. The data are represented by points, while the histograms show the combined (DIFFVM and EPJPSI) Monte Carlo simulation (full lines) and the DIFFVM contribution separately.*

produced $\psi(2S)$ mesons — elastic and proton-dissociation DIFFVM —, was found not to reproduce the observed excess in the η_{max} distribution at $1.5 \lesssim \eta_{max} \lesssim 3.0$.

The rapidity distribution of the J/ψ candidates in the photon proton centre centre of mass frame, y^*, is shown in figure 7.8a), again compared to the Monte Carlo simulation. In figure 7.8b) the decay angular distribution $\cos\theta^*$ is compared with the simulation, where θ^* is the decay angle of the positive decay lepton in the helicity frame. Both figures show a good agreement between data and Monte Carlo simulation.

7.1.3 Systematic Uncertainties

Most of the systematic errors for the inclusive analysis can be taken from studies on diffractive J/ψ production (chapter 5), and will not be discussed further.

An additional systematic uncertainty is due to the uncertainty of the production mechanism for J/ψ mesons; to estimate its size all cross sections have been alternatively evaluated with a different Monte Carlo data set consisting only of events generated with the EPJPSI program. The Monte Carlo events have been reweighted as a function of z for $z > 0.8$ in order to match the z distribution observed in the data. The difference between the cross sections calculated with the EPJPSI and the combined EPJPSI+DIFFVM Monte Carlo data sets is taken as a symmetric systematic error around the central value obtained from the EPJPSI+DIFFVM Monte Carlo data sets. In most variables that have been shown in the previous section, the description of the data using EPJPSI alone is significantly worse than with the combined EPJPSI+DIFFVM Monte Carlo simulation.

The "model uncertainty" thus obtained varies between 0 and 30 %; it is large for large z ($20 - 30\,\%$) and small $p_{t,\psi}^2$ (21 %), and otherwise has typical values of $7 - 15\,\%$.

All systematic errors are summarized in table 7.1.
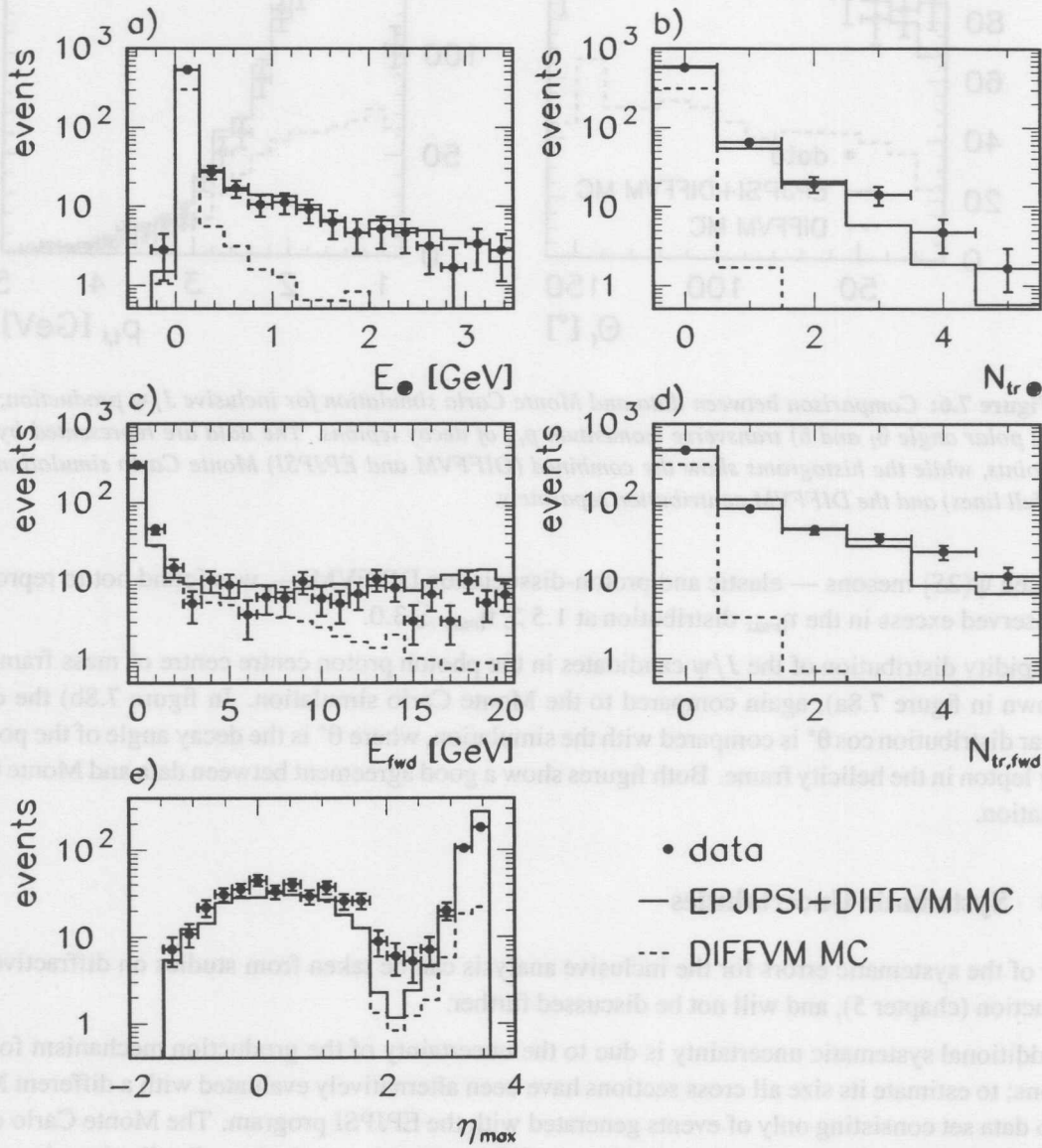
Figure 7.7: *Comparison between data and Monte Carlo simulation of topological variables for inclusive J/ψ production; a) energy and b) number of "good" tracks in a cone with radius $R = 1$ around the J/ψ direction of flight, c) energy deposited in the LAr calorimeter for $\theta < 20°$, d) number of "good" tracks with $\theta < 20°$, and e) η_{max} distribution measured with the LAr calorimeter. The data are represented by points, while the histograms show the combined (DIFFVM and EPJPSI) Monte Carlo simulation (full lines) and the DIFFVM contribution separately.*
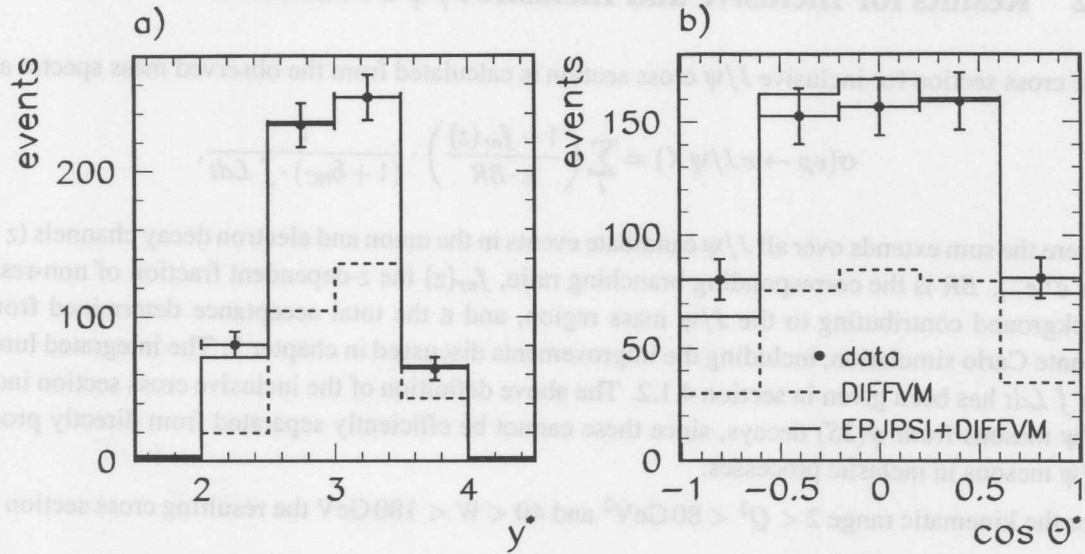
Figure 7.8: *Comparison between data and Monte Carlo simulation for inclusive J/ψ production; a) rapidity y^* of the J/ψ meson in the photon proton centre of mass frame and b) decay angle $\cos\theta^*$ of the positively charged decay lepton in the helicity frame. The data are represented by points, while the histograms show the combined (DIFFVM and EPJPSI) Monte Carlo simulation (full lines) and the DIFFVM fraction separately.*

Source	Amount [%]	see section
trigger efficiency	5	
lepton identification	6	
track and vertex efficiency	5	
z-vertex distribution	2	
e^+ angular resolution	5	
radiative corrections	3	
non-resonant background	$4-10$	7.1.1
J/ψ branching ratio	3.2	
luminosity	2.8	
model uncertainty	$0-30$	7.1.3
Total systematic error	$16-33$	

Table 7.1: *Summary of systematic uncertainties for inclusive J/ψ production. Where no reference section is given, the methods from the analysis of diffractive J/ψ production (chapter 5) are used.*

7.2   Results for Inclusive and Inelastic J/ψ Production

The cross section for inclusive J/ψ cross section is calculated from the observed mass spectra as

$$\sigma(ep \rightarrow eJ/\psi X) = \sum_i \left(\frac{1 - f_{nr}(z)}{\varepsilon \cdot BR} \right) \cdot \frac{1}{(1 + \delta_{RC}) \cdot \int \mathcal{L}dt}, \tag{7.4}$$

where the sum extends over all J/ψ candidate events in the muon and electron decay channels ($z > 0.5$ for e^+e^-). BR is the corresponding branching ratio, $f_{nr}(z)$ the z-dependent fraction of non-resonant background contributing to the J/ψ mass region, and ε the total acceptance determined from the Monte Carlo simulation, including the improvements discussed in chapter 5. The integrated luminosity $\int \mathcal{L}dt$ has been given in section 4.1.2. The above definition of the inclusive cross section includes J/ψ mesons from $\psi(2S)$ decays, since these cannot be efficiently separated from directly produced J/ψ mesons in inelastic processes.

For the kinematic range $2 < Q^2 < 80\,\text{GeV}^2$ and $40 < W < 180\,\text{GeV}$ the resulting cross section is

$$\sigma(ep \rightarrow eJ/\psi X) = 1.35 \pm 0.10(\text{stat.}) \pm 0.24(\text{syst.}) \pm 0.09(\text{model})\,\text{nb}. \tag{7.5}$$

The diffractive contribution to this cross section can be estimated by comparison with the cross section for elastic and proton dissociation J/ψ production — 0.31 ± 0.06 nb and 0.25 ± 0.05 nb — in a very similar Q^2 and W range, which was presented in chapter 5.

7.2.1   Inclusive Differential Cross Sections

In this and the following section, differential cross sections will be given as a function of Q^2, $p_{t,\psi}^2$, z and y^*, the rapidity of the J/ψ in the photon proton centre of mass frame. These variables have been chosen due to their potential sensitivity on the different production mechanisms. The results will be compared to three theoretical predictions: the results of calculations performed by Fleming and Mehen [129] in the NRQCD framework, namely the contributions from colour singlet and colour octet $c\bar{c}$ states, and also to the prediction of the EPJPSI Monte Carlo model.

Fleming and Mehen presented [129] predictions for the differential cross sections in Q^2, $p_{t,\psi}^2$ and y^*. The differential cross section $d\sigma/dz$ is not available due to theoretical uncertainties in its shape.

For the theory predictions shown here, the kinematical region has been adapted to the one used in the present analysis, i.e. $40 < W < 180\,\text{GeV}$ and $2 < Q^2 < 80\,\text{GeV}^2$. Note that Fleming and Mehen estimate their calculation to be reliable for $Q^2 > 4\,\text{GeV}^2$, while here initially a slighty larger region $Q^2 > 2\,\text{GeV}^2$ is considered. The parton density functions from GRV(LO) [112] have been used. The charm quark mass was set to $m_c = 1.55\,\text{GeV}$, and $\Lambda_{QCD} = 120\,\text{MeV}$ was chosen, corresponding to the strong coupling $\alpha_s(M_Z) = 0.118$ and consistent with the GRV parton distributions.

For the normalization of the theoretical predictions, the same NRQCD long distance matrix elements as in section 3.3.3, figure 3.26 are used:

$$\langle O_{(1)}^{J/\psi}(^3S_1) \rangle = 1.1\,\text{GeV}^3; \tag{7.6}$$

$$\langle O_{(8)}^{J/\psi}(^1S_0) \rangle = 0.01\,\text{GeV}^3; \tag{7.7}$$

$$\langle O_{(8)}^{J/\psi}(^3P_0) \rangle / m_c^2 = 0.005\,\text{GeV}^3. \tag{7.8}$$

As described there, the colour octet matrix elements have been determined from fits to J/ψ production cross sections at large $p_{t,\psi}$ measured by the CDF collaboration at the Tevatron; due to missing higher order corrections (see section 3.3.3) and since the measurements are only sensitive to a linear combination of the matrix elements, the given values should be considered as order-of-magnitude estimates (see table 3.2).

The EPJPSI Monte Carlo prediction that is given for comparison is based on the Monte Carlo files used for the acceptance correction, i.e. with the MRSA' parton distributions, and including relativistic corrections. The value of Λ_{QCD} is chosen according to the parton density function, in this case $\Lambda_{QCD} = 230\,\text{MeV}$. EPJPSI does not contain the full Q^2 evolution of the cross section and should in this sense not be understood as a prediction within the Colour Singlet Model (see section 4.6.3).

The fully inclusive differential cross sections are shown in figure 7.9. Neither of the theoretical predictions is able to describe both the normalization and the shape of the data in all details. The shape of the Q^2 dependence is well described by the EPJPSI prediction, but the noremalization is about a factor of two too small. The colour octet contributions are too steep, while the colour singlet prediction is too flat and about a factor of five below the data. A similar behaviour is observed for $d\sigma/dp_{t,\psi}^2$. The step in the colour octet prediction at $p_{t,\psi}^2 = 2\,\text{GeV}^2$ is due to the fact that in the leading order colour octet diagrams no additional hard gluon is present, as opposed to the colour singlet contribution.

At large z the diffractive contribution is clearly visible (figure 7.9c)), which is not expected to be described by the models. Note however that also colour octet contributions are expected at large z, and these are not shown in figure 7.9c). For intermediate z, $0.3 \lesssim z \lesssim 0.9$, the differential cross section in z is well described by the EPJPSI Monte Carlo model. Finally, the rapidity distribution of the J/ψ is shown in figure 7.9d). None of the models can adequately describe the observed distribution.

7.2.2 Inelastic Cross Sections

The inclusive cross sections presented in the last section include a significant contribution from diffractive — elastic and proton dissociative — J/ψ production, where the NRQCD factorization formalism is not applicable. Kinematically, these diffractive processes are very similar to J/ψ production via colour octet states (see section 3.3.3). A possibility to disentangle diffractive and colour octet processes has been proposed by Fleming and Mehen [129], and will be investigated in the following.

In the case of elastic J/ψ production, the proton remnant consists of a single proton, thus its invariant mass $M_Y = m_p$; for proton diffractive dissociation, the cross section falls steeply with M_Y, $d\sigma/dM_Y \sim 1/M_Y^2$. On the other hand, the soft gluon emitted by the $c\bar{c}$ pair combined with the proton remnant leads to masses of the order of vW, where v is the relative velocity of the c and the $\bar{c}$ in the J/ψ meson. Taking a typical value $v^2 = 0.3$ leads to the estimate $M_Y \gtrsim 20\,\text{GeV}$ for the analysis presented here.

In order to exploit experimentally these characteristic high values for M_Y, one can take advantage of the knowledge collected in analyses of diffractive processes, e.g. the one presented in chapter 5. Values of M_Y above a few GeV are easily tagged with the help of the LAr calorimeter. A cut $E_{fwd} > 5\,\text{GeV}$ is applied, where E_{fwd} is the summed energy in the LAr calorimeter of deposits with polar angles $\theta_{cell} < 20°$, excluding deposits originating from the J/ψ decay leptons. Using the DIFFVM Monte Carlo simulation of chapter 5, about 88 % of diffractively produced J/ψ mesons are thus rejected. The efficiency as a function of M_Y is shown in figure 7.10; it can be seen that low masses

$$ep \rightarrow e\,J/\psi\,X \quad (\text{inclusive})$$

- ● **data**
- ── $O_{(8)}(^1S_0) + O_{(8)}(^3P_0) + O_{(1)}(^3S_1)$
- ── — $O_{(1)}(^3S_1)$
- ········· **EPJPSI**
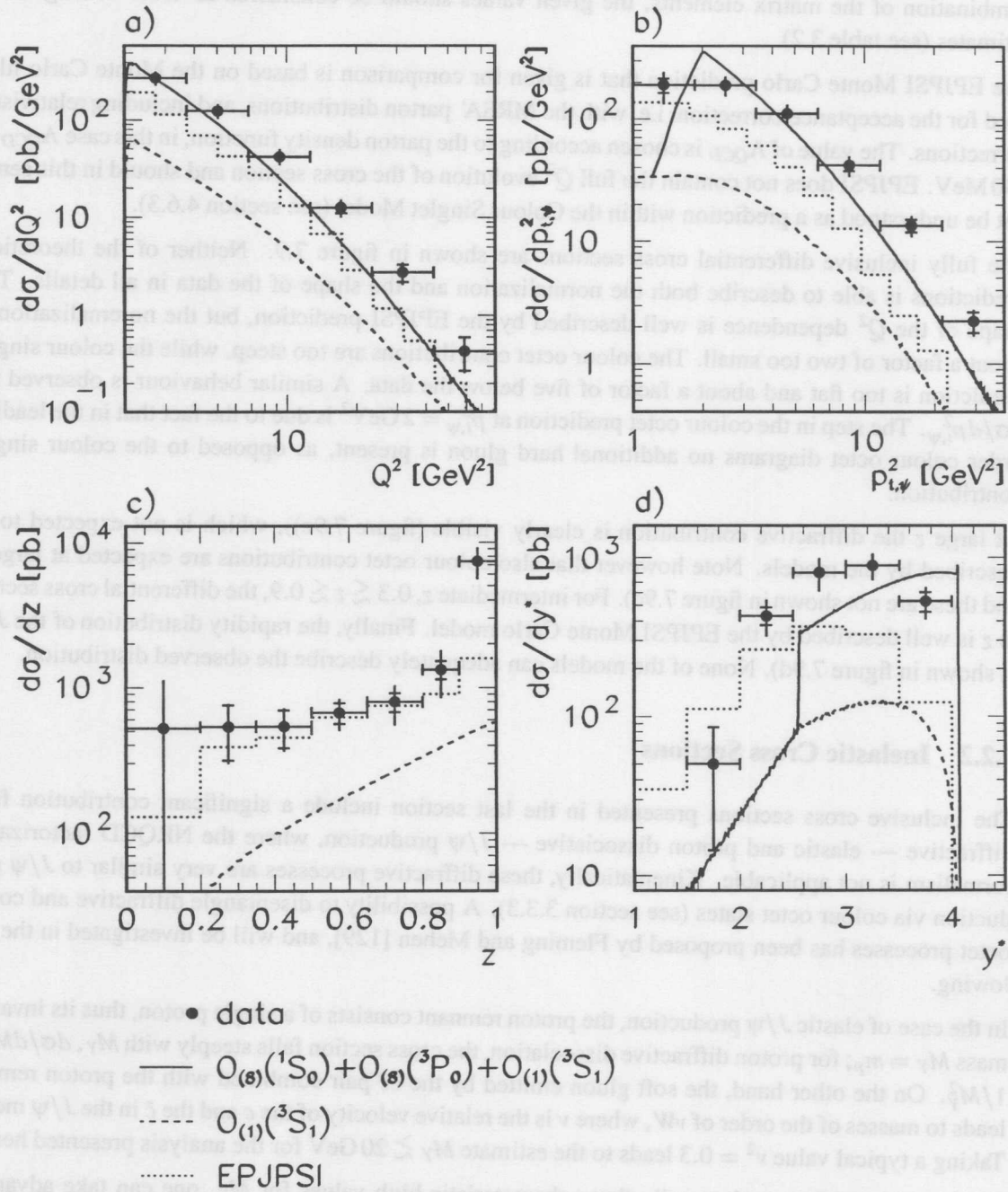
Figure 7.9: *Differential cross sections for the inclusive $ep \rightarrow e\,J/\psi\,X$ process; a) $d\sigma/dQ^2$, b) $d\sigma/dp_{t,\psi}^2$, c) $d\sigma/dz$ and d) $d\sigma/dy^*$. Inner error bars are statistical, outer error bars statistical and systematic errors added in quadrature. The curves are predictions [129] within the NRQCD factorization approach for the colour singlet contribution and the sum of singlet and octet contributions, with the colour octet matrix elements fixed to order-of-magnitude estimates by [129] based on the values extracted [109] from CDF measurements [100] (see text). Also shown is the prediction of the EPJPSI Monte Carlo simulation.*
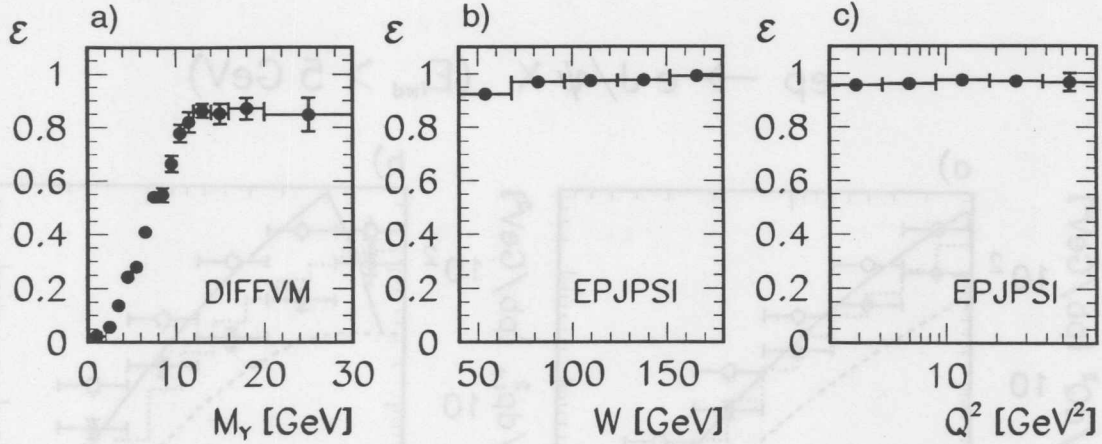
Figure 7.10: *a) Efficiency of a cut on the energy deposited in the forward LAr calorimeter — $E_{fwd} > 5$ GeV — as a function of the proton remnant mass M_Y for DIFFVM Monte Carlo events. b),c): Efficiency of the cut $E_{fwd} > 5$ GeV as a function of W and Q^2 for EPJPSI Monte Carlo events. For all plots, the same cuts as in the inclusive J/ψ selection are applied.*

are almost completely rejected. On the other hand, Monte Carlo events generated with the EPJPSI program are kept to a large extent.

In order to remain largely model independent, the cut $E_{fwd} > 5$ GeV is only applied to the data, but no correction for possible losses of events, e.g. based on the Monte Carlo simulation, is made. The reason is that the inefficiency introduced depends on the detailed simulation of the final state, which is however not available as long as the production mechanisms are not clarified. Based on the DIFFVM and EPJPSI Monte Carlo simulation at large z it is estimated that the losses are below 20 % for $M_Y > 15$ GeV.

For the same kinematic range as before, the cross section for $ep \rightarrow eJ/\psi X$ with $E_{fwd} > 5$ GeV, i.e. more than 5 GeV energy deposit in the polar angular region[2] $4° \lesssim \theta < 20°$, is determined to be

$$\sigma(ep \rightarrow eJ/\psi X) = 0.63 \pm 0.09(\text{stat.}) \pm 0.11(\text{syst.}) \pm 0.04(\text{model}) \text{ nb.} \tag{7.9}$$

Differential cross sections are shown, in analogy to the inclusive case, in figure 7.11. All distributions are well described by the EPJPSI Monte Carlo model, except possibly for large $p_{t,\psi}^2$. The peak at large z is significantly reduced by the cut on E_{fwd}. The calculations within the NRQCD approach fail to describe the data: the shape of the singlet contribution agrees with the data, but the normalization is about a factor of two low, while the octet contribution disagrees in the shapes. Trying to use the Q^2 or $p_{t,\psi}^2$ distributions for the determination of the NRQCD long distance matrix elements $\langle O_{(8)}^{J/\psi}(^1S_0) \rangle$ and $\langle O_{(8)}^{J/\psi}(^3P_0) \rangle$ would require one of the matrix elements to become negative. A negative value for $\langle O_{(8)}^{J/\psi}(^3P_0) \rangle$ was already obtained by Fleming [185] from fits to low Q^2 large z data on muoproduction of J/ψ measured by the EMC collaboration [38]. In [185] missing higher orders in the perturbative expansion in α_s were suggested as an explanation.

By further restricting the kinematic region in Q^2 and $p_{t,\psi}^2$ the reliability of the theoretical predictions in the NRQCD approach is enhanced. Therefore cross sections for $Q^2 > 3.7$ GeV^2 and $p_{t,\psi}^2 > 3.4$ GeV^2

---

[2]The lower limit for θ is given by the acceptance of the LAr calorimeter.
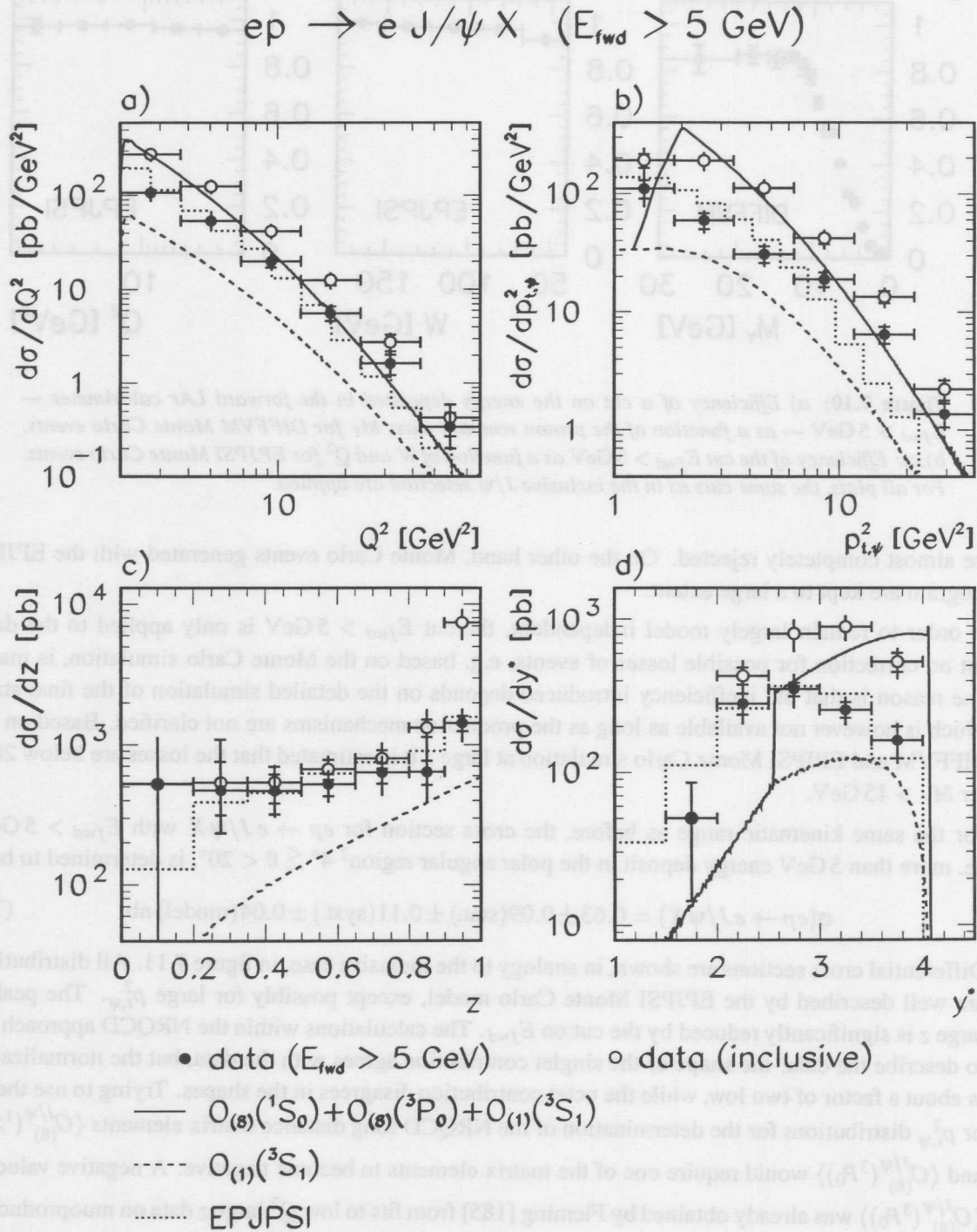
Figure 7.11: *Differential cross sections for* $ep \to e\,J/\psi\,X$ *with* $E_{fwd} > 5\,\text{GeV}$; *a)* $d\sigma/dQ^2$, *b)* $d\sigma/dp_{t,\psi}^2$, *c)* $d\sigma/dz$ *and d)* $d\sigma/dy^*$. *The curves are predictions [129] within the NRQCD factorization approach and the EPJPSI Monte Carlo model, identical to figure 7.9.*

have been calculated; they are shown in figure 7.12. In addition the cut $E_{fwd} > 5\,\text{GeV}$ has been applied here.

Conventionally, cross sections for J/ψ production in deep inelastic scattering have been presented for a limited region in z in order to reject diffractive events. In figure 7.13, differential cross sections are given for the limited region $z < 0.9$. Again, the EPJPSI Monte Carlo prediction agrees rather well with the data, except for large Q^2 and $p_{t,\psi}^2$. The NRQCD colour octet prediction is not expected to be applicable here since J/ψ mesons produced via colour octet $c\bar{c}$ states have predominantly large z.

In previous H1 analyses of inelastic J/ψ photoproduction [65, 145] hadronic activity in the detector — at least one track — besides the decay leptons was required additionally. The z distribution of the data used in the present analysis is shown in figure 7.14 for the inclusive case, and for the two conditions $E_{fwd} > 5\,\text{GeV}$ and $N_{tr} > 2$, where N_{tr} denotes the total number of "good" tracks in the tracking chambers including the decay leptons. Both cuts lead to a similar z distribution.

7.2.3 Comparison with Open Charm Production

The differential cross sections $d\sigma/dQ^2$ for J/ψ production can be compared to those for open charm production in a similar kinematic regime, as shown in figure 7.15. The preliminary H1 result for $ep \rightarrow e\,D^*X$ given in [184] covers a similar Q^2 range; y is restricted to $0.01 < y < 0.7$, corresponding to $30 \lesssim W \lesssim 250\,\text{GeV}$, a larger range than in the present J/ψ analysis. The D^* cross sections are visible cross sections for the D^* transverse momentum $p_t(D^*) > 1.5\,\text{GeV}$ and its pseudorapidity in the laboratory frame $|\eta(D^*)| < 1.5$.

The D^* cross section is observed to have a harder Q^2 dependence than the fully inclusive J/ψ cross section. However, the diffractive contribution to open charm production is much smaller than for bound states. Furthermore, as opposed to the D^*, no cut on the transverse momentum of the J/ψ is applied. Suppressing the diffractive J/ψ contribution and applying a cut $p_{t,\psi}^2 > 3.4\,\text{GeV}^2$ leads to a similar Q^2 dependence of the D^* and J/ψ cross sections (see figure 7.15).

$$ep \rightarrow e\,J/\psi\,X$$

$$(E_{fwd} > 5\,\text{GeV},\ Q^2 > 3.7\,\text{GeV}^2,\ p_{t,\psi}^2 > 3.4\,\text{GeV}^2)$$

- data ($E_{fwd} > 5$ GeV)
- ── $O_{(8)}(^1S_0) + O_{(8)}(^3P_0) + O_{(1)}(^3S_1)$
- ---- $O_{(1)}(^3S_1)$
- ········ EPJPSI
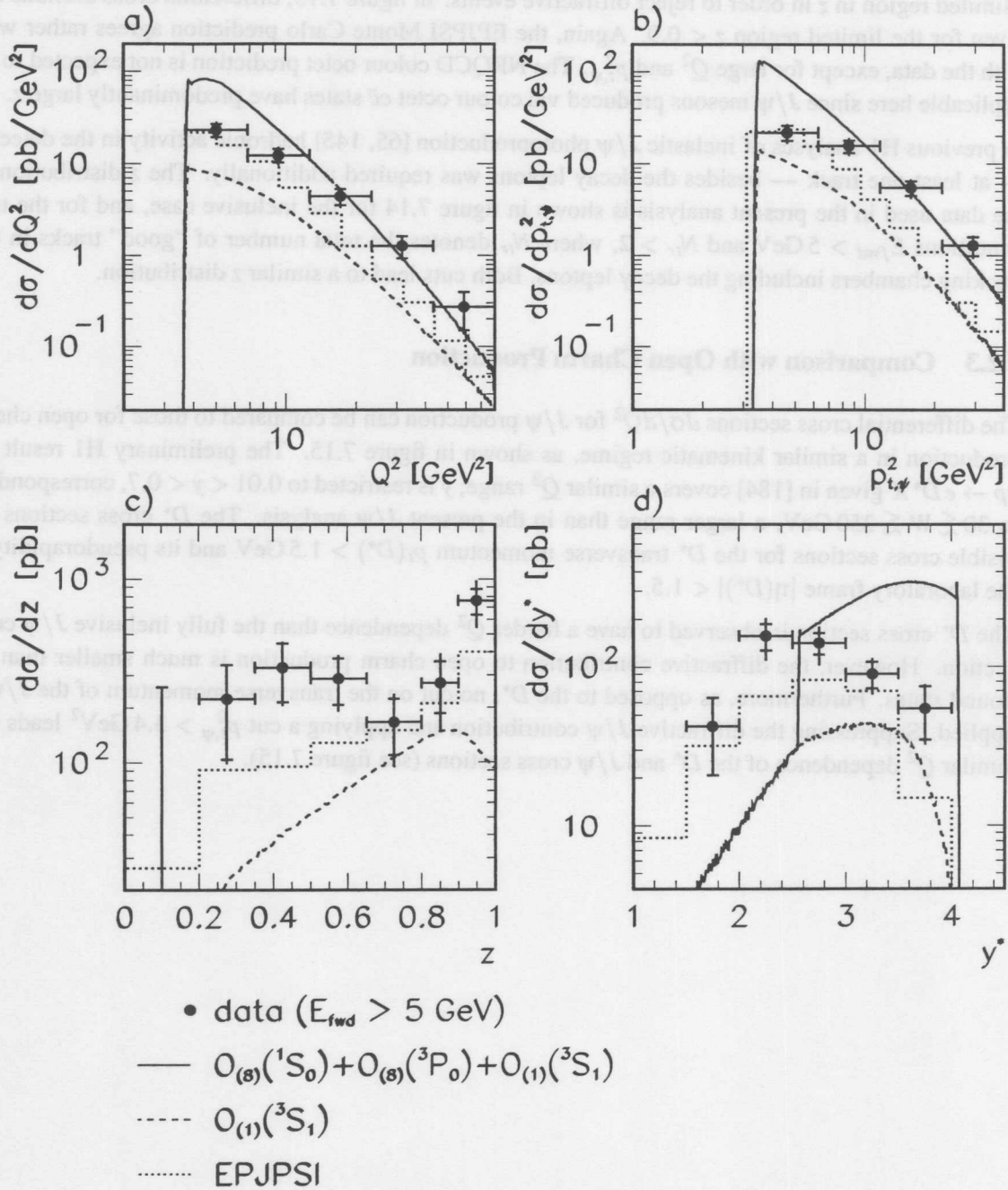
Figure 7.12: *Differential cross sections for ep → eJ/ψX with $E_{fwd} > 5$ GeV, $Q^2 > 3.7$ GeV^2 and $p_{t,\psi}^2 > 3.4$ GeV^2; a) dσ/dQ^2, b) dσ/dp$_{t,\psi}^2$, c) dσ/dz and d) dσ/dy*. The curves are predictions [129] within the NRQCD factorization approach and the EPJPSI Monte Carlo model, as explained in figure 7.9.*
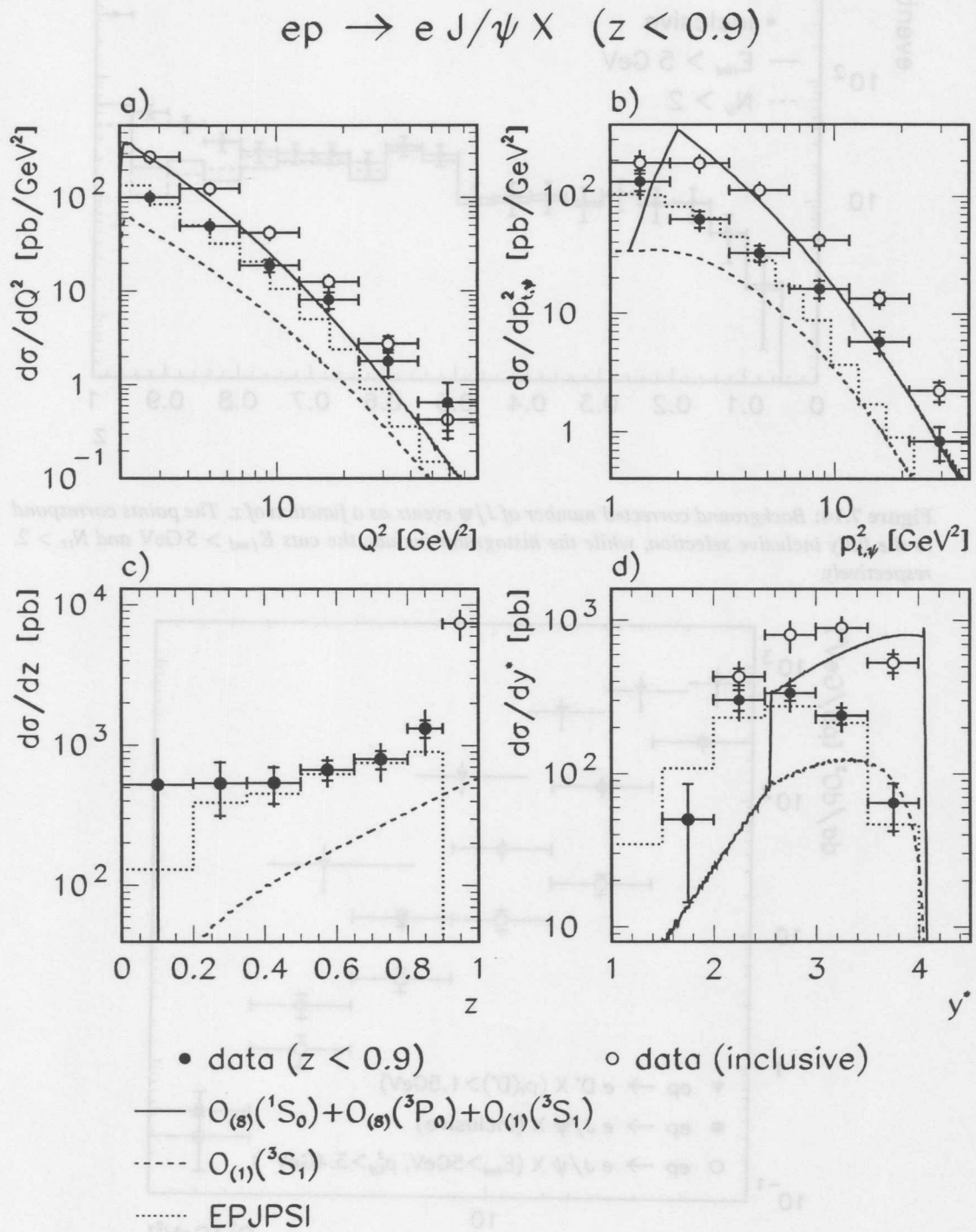
Figure 7.13: *Differential cross sections for ep → eJ/ψX with z < 0.9; a) dσ/dQ², b) dσ/dp²_{t,ψ}, c) dσ/dz and d) dσ/dy*. The curves are predictions [129] for the full z range within the NRQCD factorization approach, identical to figure 7.9, and the EPJPSI Monte Carlo model for z < 0.9.*
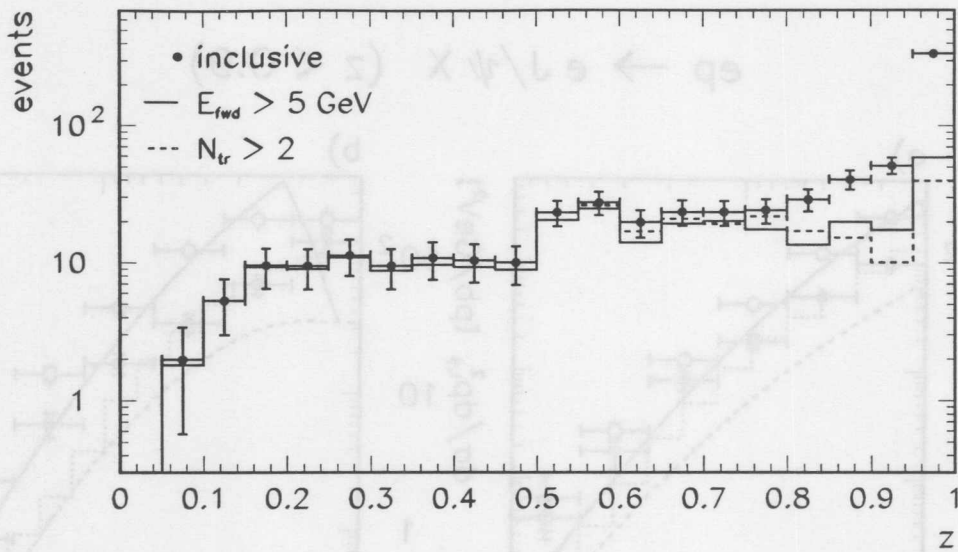
Figure 7.14: *Background corrected number of J/ψ events as a function of z. The points correspond to the fully inclusive selection, while the histograms include the cuts $E_{fwd} > 5\,\text{GeV}$ and $N_{tr} > 2$, respectively.*
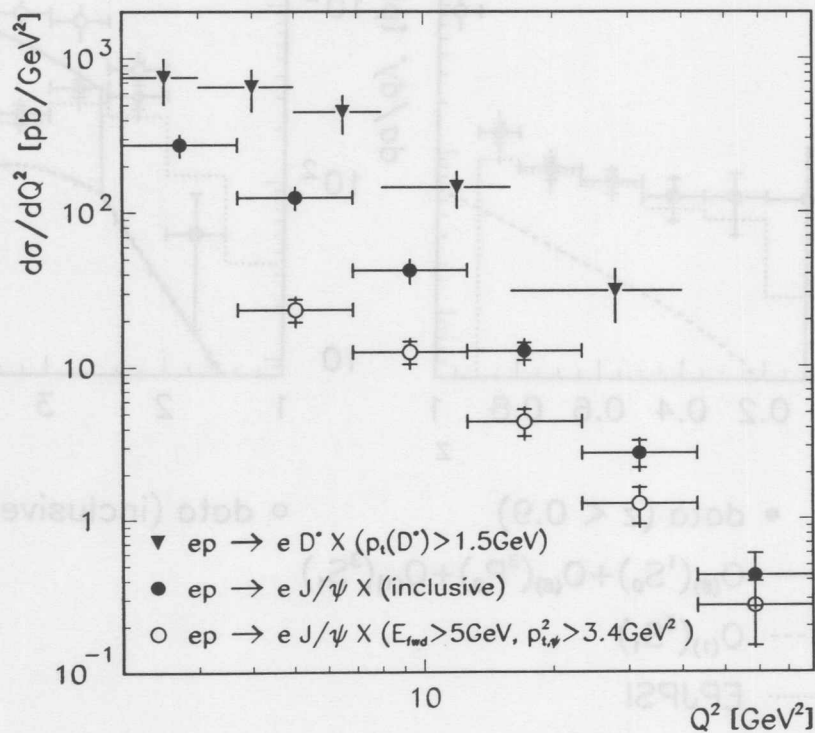
Figure 7.15: *Differential cross section $d\sigma/dQ^2$ for $ep \rightarrow eJ/\psi X$ in comparison to $ep \rightarrow eD^* X$ (H1 preliminary results from [184]). For J/ψ, the fully inclusive cross sections and those restricted to $p_{t,\psi}^2 > 3.4\,\text{GeV}^2$ and $E_{fwd} > 5\,\text{GeV}$ are given. D^* cross sections are for $p_t(D^*) > 1.5\,\text{GeV}$, $0.01 < y < 0.7$ and $|\eta(D^*)| < 1.5$.*

7.2.4 Decay Angular Distributions

The polarization of the produced J/ψ meson could provide another means to disentangle the relevant production mechanisms. In the NRQCD factorization approach, the polarization depends strongly on the ratio $R_{(8)}$ of the matrix elements $\langle O_{(8)}^{J/\psi}(^3P_0)\rangle$ and $\langle O_{(8)}^{J/\psi}(^1S_0)\rangle$:

$$R_{(8)} := \frac{\langle O_{(8)}^{J/\psi}(^3P_0)\rangle}{m_c^2\langle O_{(8)}^{J/\psi}(^1S_0)\rangle}. \tag{7.10}$$

Fleming and Mehen calculated [129] the expectation for the polarization parameter α as a function of $R_{(8)}$ and Q^2. α is measured from the decay angular distribution of the positive J/ψ decay lepton in the helicity frame (see section 3.1.5):

$$\frac{d\sigma}{d\cos\theta^*} \sim 1 + \alpha\cos^2\theta^*, \tag{7.11}$$

where θ^* is the angle of the positively charged decay lepton in this frame. The polarization parameter is related to the spin density matrix element r_{00}^{04} denoting the probability of the J/ψ meson to be longitudinally polarized, by the relation

$$\alpha = \frac{1 - 3r_{00}^{04}}{1 + r_{00}^{04}}. \tag{7.12}$$

If the intermediate $c\bar{c}$ pair is produced in an $^1S_0$ state, the J/ψ meson will be unpolarized, i.e. $\alpha = 0$ and $R_{(8)} = 0$. Positive values of $R_{(8)}$ lead to slightly longitudinally polarized J/ψ ($\alpha < 0$) with typical values for α between -0.2 and -0.5 in the kinematic regime under study here. On the other hand, transverse polarization ($\alpha > 0$) of the J/ψ is expected for $R_{(8)} < 0$, with α of the order of 0.2 to 0.5. A negative value for R was obtained by Fleming [185] from fits to muoproduction data of J/ψ at large z and low Q^2 measured by the EMC collaboration [38].

For the colour singlet contribution, a value of α of the order of 0.5 is predicted [186].

The results of the present analysis for the decay angular distribution and α are shown in figure 7.16. They are given for different cut scenarios, i.e. fully inclusive, separately for small z ($z < 0.9$) and large z ($z > 0.9$), and after applying a cut $E_{fwd} > 5\,\text{GeV}$. The results obtained for α are within errors compatible with each other, although the precision of the data does not yet allow any conclusions to be drawn. A positive value of α is favoured by approximately one standard deviation.

7.3 Discussion of Results

In the present chapter, a largely model independent analysis of inclusive J/ψ production has been presented. It has been shown that the data can be described by a composition of Monte Carlo data sets consisting of the DIFFVM program for diffractive J/ψ production and a second Monte Carlo program, EPJPSI, which is based on the Colour Singlet Model in leading order. The combined Monte Carlo simulation is used for the extraction of fully inclusive J/ψ production cross sections differentially in Q^2, $p_{t,\psi}^2$, the rapidity y^* and the elasticity z.

The theoretical predictions in the NRQCD approach are not expected to describe diffractive J/ψ production. Therefore, in order to suppress the diffractive contributions, cross sections have been given for two definitions of inelastic J/ψ production:

a)

$d\sigma/d\cos\Theta^*$ [pb]

inclusive

$z < 0.9$

b)

$d\sigma/d\cos\Theta^*$ [pb]

inclusive

$z > 0.9$

c)

$d\sigma/d\cos\Theta^*$ [pb]

inclusive

$E_{fwd} > 5$ GeV

$\cos\Theta^*$

d)

ε

—— all z

- - - $z < 0.9$

········ $z > 0.9$

$\cos\Theta^*$
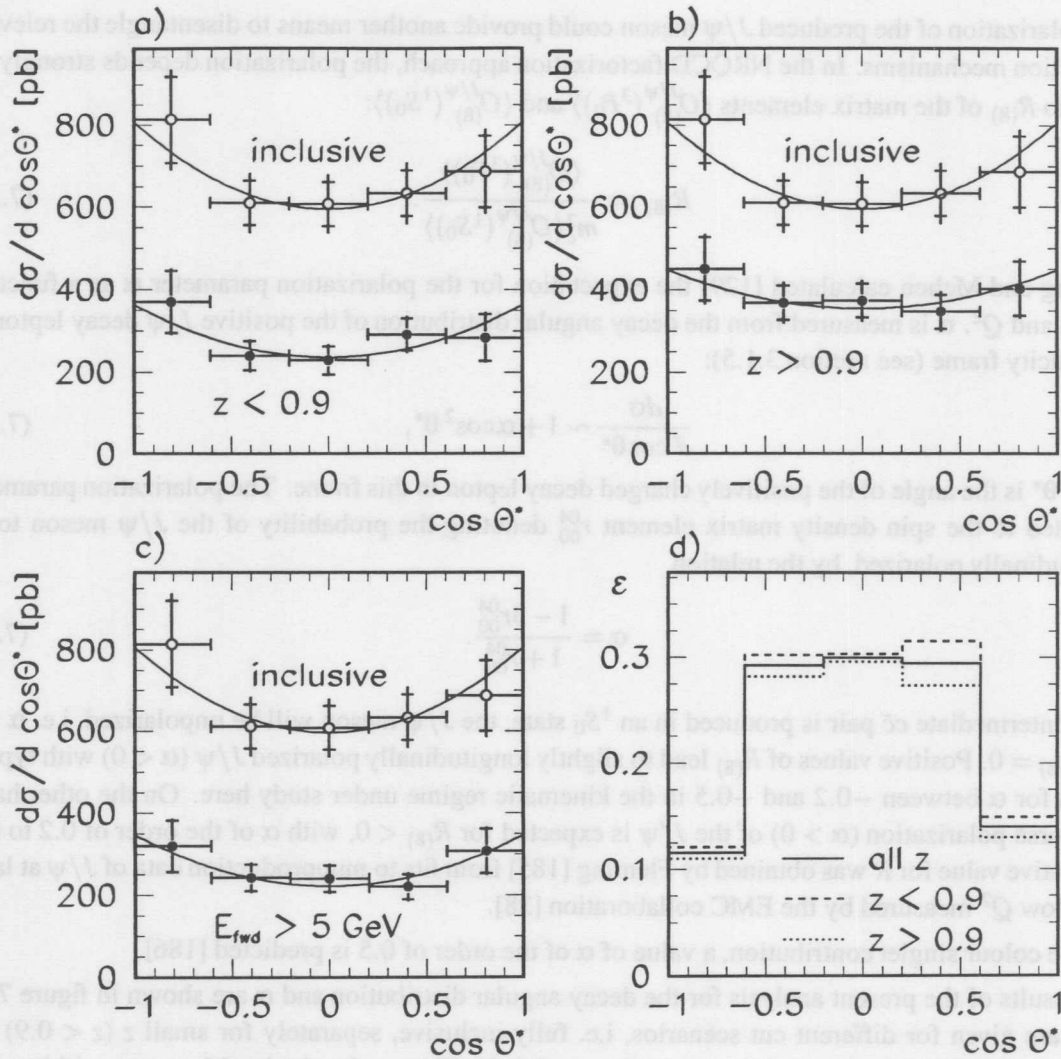
	α	χ^2/NDF
inclusive	$0.35^{+0.31}_{-0.27}$	0.7/3
$z < 0.9$	$0.54^{+0.49}_{-0.41}$	1.5/3
$z > 0.9$	$0.26^{+0.36}_{-0.30}$	0.5/3
$E_{fwd} > 5$ GeV	$0.57^{+0.49}_{-0.40}$	0.7/3

Figure 7.16: *Differential cross sections $d\sigma/d\cos\Theta^*$ for $ep \to e\,J/\psi\,X$; the fully inclusive cross section is shown in a), b), c) and in addition the cross section for a) $z < 0.9$, b) $z > 0.9$ and c) $E_{fwd} > 5$ GeV. The lines are fits to the form $\sim 1 + \alpha\cos^2\Theta^*$; the fit results are given in the table. In d) the total acceptance as a function of $\cos\Theta^*$ is shown.*

1. By requiring significant energy in the forward region of the LAr calorimeter, $E_{fwd} > 5\,\text{GeV}$, diffractive J/ψ production is efficiently reduced, while J/ψ mesons produced via colour octet mechanisms are kept to a large extent.

2. The cut $z < 0.9$ conventionally applied rejects diffractively produced J/ψ almost completely, but presumably also most of the J/ψ mesons produced via colour octet states.

The given cross sections are about a factor of two to four larger than expected from the leading order colour singlet calculation of Fleming and Mehen, indicating the necessity of including additional production mechanisms, i.e. via colour octet states, or higher order corrections. On the other hand, the shapes of the differential cross sections are in favour of the colour singlet compared to the colour octet contributions. Restricting the analysis to larger values of Q^2 and $p_{t,\psi}^2$, where the calculations are more reliable, does not change this conclusion.

The decay angular distribution $d\sigma/d\cos\theta^*$ is found to be compatible with the colour singlet prediction. With respect to possible colour octet contributions, the decay angular distributions are not sensitive, because the polarization depends strongly on the (unknown) ratio of two long distance colour octet matrix elements.

Since next-to-leading order corrections change the absolute normalization and the shape of the differential distributions — as found in the past for J/ψ photoproduction —, and the size of the colour octet matrix elements is only badly known from the Tevatron data, it is too early to draw definite conclusions with respect to the universality of the matrix elements and the validity of the NRQCD approach.

Chapter 8

Conclusions and Outlook

In this thesis, an analysis of exclusive J/ψ and $\psi(2S)$ as well as inclusive J/ψ production is presented, using the decay channels $J/\psi \rightarrow \mu^+\mu^-$, $J/\psi \rightarrow e^+e^-$ and $\psi(2S) \rightarrow J/\psi\pi^+\pi^-$, where the J/ψ again decays either in two electrons or two muons. The data have been collected with the H1 detector at the ep collider HERA and correspond to an integrated luminosity of about $21\,\mathrm{pb}^{-1}$.

For elastic and proton dissociative J/ψ production, virtual photoproduction cross sections are extracted as a function of W and Q^2 in the kinematic range in Q^2 between 2 and $80\,\mathrm{GeV}^2$ and W between 40 and $160\,\mathrm{GeV}$. The W dependence is found to be compatible to previous results obtained in quasi-real photoproduction at HERA; using a simple parameterization $\sim W^\delta$, $\delta \simeq 1$. Elastic J/ψ production can be well described by the model of Frankfurt et al. based on perturbative QCD. The Q^2 dependence can be parameterized as $(Q^2 + m_\psi^2)^{-n}$ with $n = 2.24 \pm 0.19$ and $n = 2.6 \pm 0.3$ for the elastic and proton dissociative case, respectively. This leads to the conclusion that all measurements of the Q^2 dependence of exclusive vector meson production at HERA carried out so far — ρ, ϕ and J/ψ, elastic and with proton diffractive dissociation — show a dependence of the cross section $\sim (Q^2 + m_V^2)^{-n}$ with $n \simeq 2.3$.

The slope parameter of $d\sigma/dt$ is determined for elastic J/ψ production at a mean W of $96\,\mathrm{GeV}$ and a mean Q^2 of $8\,\mathrm{GeV}^2$ as $b^{el} = -3.9^{+0.3}_{-0.4}\,(\mathrm{stat})^{+0.3}_{-0.4}\,(\mathrm{syst})\,\mathrm{GeV}^{-2}$, compatible with results obtained in photoproduction at HERA. The precision of the data is not sufficient to allow any conclusion as to whether the elastic peak "shrinks". The t distribution for proton dissociative J/ψ production is found to be significantly harder. At large $|t|$, the t distribution can be described with a calculation based on the BFKL formalism with an input parameter $\alpha_s^{LO} = 0.207$; this is a confirmation of H1 results obtained for J/ψ photoproduction.

A first study of the helicity structure of exclusive J/ψ production at HERA is presented. No sign of a possible violation of the s-channel helicity conservation hypothesis is found. With large uncertainties, a rise of $R = \sigma^L/\sigma^T$ with Q^2 is observed.

The first observation of $\psi(2S)$ production in deep inelastic scattering is reported. The ratio of cross sections for the exclusive production, $\sigma_{\gamma^* p}^{\psi(2S)}/\sigma_{\gamma^* p}^{\psi}$, is extracted as a function of Q^2; at small Q^2 the result agrees with the previous H1 result obtained in photoproduction, while an indication for a rise at higher Q^2 is observed, as predicted in several models.

An attempt of a largely model independent analysis of inclusive J/ψ production is presented. A composition of Monte Carlo simulations consisting of a program for diffractive J/ψ production and one based on the Colour Singlet Model in leading order is used for the correction of the data and the

169

extraction of differential cross sections as a function of Q^2, $p_{t,\psi}^2$, the rapidity y^*, the elasticity z and the decay angle θ^*. Differential cross sections in Q^2, $p_{t,\psi}^2$ and y^* are compared to the leading order colour singlet and colour octet calculations of Fleming and Mehen. It is found that the application of the colour octet matrix elements extracted using high p_t hadroproduction of J/ψ at the Tevatron to the HERA data leads to the correct order of magnitude of the predicted cross section. On the other hand, the shapes of the distributions are better described by the colour singlet prediction, which is however far too small in normalization. Since next-to-leading order corrections can be large and especially change the shape of the differential cross sections — as found in the past for J/ψ photoproduction —, and the size of the colour octet matrix elements is only badly known from the Tevatron data, it is too early to draw definite conclusions with respect to the universality of the long range matrix elements and the validity of the NRQCD approach. Inelastic J/ψ production remains a challenge for theoretical efforts.

The most obvious improvement to the analyses presented here would be a significant increase of the integrated luminosity, since most of the results are limited by statistics. On the other hand no order of magnitude improvement can be expected in this respect until the planned HERA luminosity upgrade [188] takes place, which will not happen before the year 2000. Even then, especially the triggering of Charmonium states will become more difficult than today and may limit the available statistics.

There are however many topics in Charmonium physics both from the experimental and theoretical point of view that can already be tackled today. Experimentally, the extension of the available phase space could prove to be extremely interesting. It has recently been shown by H1 [85] that the analysis of elastic J/ψ photoproduction up to the highest kinematically possible values of W — corresponding to smallest values of x — is feasible, if the decay electrons of the J/ψ are identified and measured in the backward calorimeter SpaCal. The extension of this analysis to the DIS regime and also towards inelastic J/ψ production should be possible. It should also not be forgotten that an increase of the beam energies would significantly increase the accessible kinematic range.

The transition region between photoproduction and DIS will be further exploited with the help of the "very low Q^2 calorimeter" VLQ with Q^2 acceptance in between the SpaCal and the electron taggers. The VLQ will be commissioned during the 1998 data taking.

Another future experimental topic will be the improvement of the lepton identification; especially the forward region, corresponding to small W or complementary small z, may only be analyzed once more efficient background rejection and lepton identification algorithms are available. Possible improvements could also come from the specific ionization dE/dx and the silicon vertex detectors.

The dominant systematic error on the elastic J/ψ production cross section has its origin in the uncertainty of the separation of elastic and proton dissociative events. This can be reduced drastically with the help of so-called *Roman Pots*, which are operated close to the beam in the proton beam direction and can detect the scattered proton in elastic events. Although their acceptance is small, future measurements could verify the absolute normalization of the cross sections. With the necessary hardware already installed and tested, this analysis could be possible with data from 1998 on.

Another possible measurement that overcomes this large experimental uncertainty would be the determination of cross section *ratios* for different vector mesons; the cancellation of uncertainties in such analyses has so far not been exploited.

A problem of current Charmonium analyses is the lack of a Monte Carlo generator that incorporates colour octet contributions; this will hopefully be available soon. It might also be interesting to what

extent the "Soft Colour Interactions" implemented in the LEPTO and AROMA Monte Carlo programs are able to describe inclusive Charmonium production.

All these improvements should lead to a better understanding of the production mechanisms involved in Charmonium production. It is however obvious that some of the most rigorous tests are only possible when combining results obtained in different processes, e.g. hadroproduction at the Tevatron and photo- and electroproduction at HERA.

Before the advent of HERA, inelastic J/ψ production was thought to be a "golden way" to extract the gluon density in the proton. From todays point of view, this turned out to be difficult as long as the production mechanisms are not fully understood. Also the proposed "new" way of extracting the gluon density using elastically produced J/ψ is not yet feasible, mainly due to a lack of certainty of the theoretical understanding.

Appendix A

Detailed Results for Diffractive J/ψ Production

All results for diffractive J/ψ production have already been discussed in chapter 5. For completeness, tables of cross sections in the chosen Q^2-W grid similar to table 5.4 are given here separately for the different data taking periods. Data taken in 1995 and 1996 are due to lack of statistics combined; it should be noted that results obtained for the elastic J/ψ cross section using the 1995 data alone [85] in a coarser binning have been shown to be compatible with the results derived here, see figure 5.26.

Finally, the total acceptance (as in table 5.1) and cross sections are given for the electron and muon decay channel separately.

173

	$2 < Q^2 < 6\,\mathrm{GeV}^2$		
	$40 < W < 80\,\mathrm{GeV}$	$80 < W < 120\,\mathrm{GeV}$	$120 < W < 160\,\mathrm{GeV}$
N_{ntag}	48.6 ± 7.6	46.2 ± 7.3	17.5 ± 4.6
N_{tag}	37.8 ± 6.6	26.7 ± 5.7	3.4 ± 2.2
N_{el}	93.1 ± 18.9	86.7 ± 16.2	74.4 ± 20.6
$\sigma^{el}_{\gamma^* p}$ $[nb]$	$23.6 \pm 4.8 \pm 3.8$	$40.2 \pm 7.5 \pm 6.5$	$54.1 \pm 14.9 \pm 8.6$
N_{pd}	105.5 ± 19.7	78.9 ± 20.3	20.3 ± 14.7
$\sigma^{pd}_{\gamma^* p}$ $[nb]$	$25.7 \pm 4.8 \pm 4.1$	$35.2 \pm 8.2 \pm 5.6$	$16.4 \pm 11.9 \pm 2.6$
	$6 < Q^2 < 18\,\mathrm{GeV}^2$		
	$40 < W < 80\,\mathrm{GeV}$	$80 < W < 120\,\mathrm{GeV}$	$120 < W < 160\,\mathrm{GeV}$
N_{ntag}	16.6 ± 5.1	15.6 ± 5.3	11.5 ± 3.8
N_{tag}	17.0 ± 4.4	20.3 ± 4.7	9.9 ± 2.7
N_{el}	30.1 ± 12.7	19.9 ± 10.1	27.4 ± 11.8
$\sigma^{el}_{\gamma^* p}$ $[nb]$	$7.53 \pm 3.17 \pm 1.36$	$9.12 \pm 4.62 \pm 1.64$	$19.7 \pm 8.5 \pm 3.6$
N_{pd}	41.8 ± 11.5	49.6 ± 12.0	40.9 ± 11.6
$\sigma^{pd}_{\gamma^* p}$ $[nb]$	$10.1 \pm 2.8 \pm 1.8$	$21.8 \pm 5.3 \pm 3.9$	$28.2 \pm 7.9 \pm 5.1$
	$18 < Q^2 < 80\,\mathrm{GeV}^2,\ 40 < W < 160\,\mathrm{GeV}$		
N_{ntag}	7.2 ± 3.1		
N_{tag}	4.9 ± 3.1		
N_{el}	12.5 ± 6.7		
$\sigma^{el}_{\gamma^* p}$ $[nb]$	$1.16 \pm 0.62 \pm 0.24$		
N_{pd}	11.7 ± 7.7		
$\sigma^{pd}_{\gamma^* p}$ $[nb]$	$1.03 \pm 0.68 \pm 0.21$		

Table A.1: *Summary of elastic and proton dissociation cross sections for data taken in* **1995** *and* **1996**.

	$2 < Q^2 < 6\,\mathrm{GeV}^2$		
	$40 < W < 80\,\mathrm{GeV}$	$80 < W < 120\,\mathrm{GeV}$	$120 < W < 160\,\mathrm{GeV}$
N_{ntag}	61.1 ± 8.9	54.8 ± 8.0	24.5 ± 5.4
N_{tag}	24.4 ± 5.7	23.9 ± 5.4	7.2 ± 2.8
N_{el}	138.2 ± 22.6	111.4 ± 18.7	105.9 ± 25.6
$\sigma^{el}_{\gamma p}$ [nb]	$29.2 \pm 4.8 \pm 4.7$	$43.1 \pm 7.2 \pm 6.9$	$64.2 \pm 15.6 \pm 10.4$
N_{pd}	66.7 ± 17.3	72.5 ± 18.3	52.7 ± 22.1
$\sigma^{pd}_{\gamma p}$ [nb]	$13.5 \pm 3.5 \pm 2.2$	$27.0 \pm 6.8 \pm 4.3$	$30.7 \pm 12.9 \pm 4.9$
	$6 < Q^2 < 18\,\mathrm{GeV}^2$		
	$40 < W < 80\,\mathrm{GeV}$	$80 < W < 120\,\mathrm{GeV}$	$120 < W < 160\,\mathrm{GeV}$
N_{ntag}	13.5 ± 3.8	16.5 ± 4.6	15.4 ± 4.3
N_{tag}	15.7 ± 4.4	19.9 ± 4.7	7.2 ± 2.8
N_{el}	24.3 ± 9.7	22.3 ± 9.3	42.1 ± 13.7
$\sigma^{el}_{\gamma p}$ [nb]	$5.08 \pm 2.04 \pm 0.91$	$8.51 \pm 3.55 \pm 1.53$	$25.2 \pm 8.2 \pm 4.5$
N_{pd}	39.6 ± 11.7	51.4 ± 12.9	30.2 ± 12.4
$\sigma^{pd}_{\gamma p}$ [nb]	$7.96 \pm 2.36 \pm 1.44$	$19.0 \pm 4.7 \pm 3.4$	$17.4 \pm 7.1 \pm 3.1$
	$18 < Q^2 < 80\,\mathrm{GeV}^2,\ 40 < W < 160\,\mathrm{GeV}$		
N_{ntag}	15.9 ± 4.2		
N_{tag}	4.1 ± 2.5		
N_{el}	32.4 ± 9.4		
$\sigma^{el}_{\gamma p}$ [nb]	$2.50 \pm 0.73 \pm 0.50$		
N_{pd}	9.4 ± 6.6		
$\sigma^{pd}_{\gamma p}$ [nb]	$0.70 \pm 0.49 \pm 0.14$		

Table A.2: *Summary of elastic and proton dissociation cross sections for data taken in* **1997**.

Q^2 interval	W interval	$\varepsilon^{el}_{ntag}[\%]$	$\varepsilon^{el}_{tag}[\%]$	$\varepsilon^{pd}_{ntag}[\%]$	$\varepsilon^{pd}_{tag}[\%]$
	$40 < W < 80\,\text{GeV}$	54.6 ± 1.4	5.4 ± 0.5	11.9 ± 0.8	41.5 ± 1.4
$2 < Q^2 < 6\,\text{GeV}^2$	$80 < W < 120\,\text{GeV}$	61.3 ± 1.7	5.8 ± 0.6	10.6 ± 0.8	36.8 ± 1.3
	$120 < W < 160\,\text{GeV}$	33.9 ± 1.5	2.6 ± 0.4	5.3 ± 0.6	23.7 ± 1.2
	$40 < W < 80\,\text{GeV}$	55.7 ± 2.3	3.6 ± 0.9	13.2 ± 1.4	51.9 ± 2.5
$6 < Q^2 < 18\,\text{GeV}^2$	$80 < W < 120\,\text{GeV}$	69.4 ± 2.6	5.6 ± 0.9	13.6 ± 1.4	47.9 ± 2.4
	$120 < W < 160\,\text{GeV}$	48.8 ± 3.0	4.4 ± 0.9	9.2 ± 1.2	31.9 ± 2.3
$18 < Q^2 < 80\,\text{GeV}^2$	$40 < W < 160\,\text{GeV}$	64.9 ± 3.4	5.4 ± 1.1	13.2 ± 1.9	76.3 ± 3.7

Table A.3: *Total acceptance for elastic and proton dissociative J/ψ production, decay $J/\psi \to \mu^+\mu^-$. Errors are from Monte Carlo statistics.*

	$2 < Q^2 < 6\,\text{GeV}^2$		
	$40 < W < 80\,\text{GeV}$	$80 < W < 120\,\text{GeV}$	$120 < W < 160\,\text{GeV}$
N_{ntag}	74.1 ± 9.7	74.2 ± 9.2	30.7 ± 5.9
N_{tag}	42.7 ± 7.1	43.2 ± 6.9	8.8 ± 3.4
N_{el}	116.5 ± 19.0	103.5 ± 16.1	86.0 ± 18.3
$\sigma^{el}_{\gamma^* p}$ $[nb]$	$27.2 \pm 4.5 \pm 4.4$	$44.4 \pm 6.9 \pm 7.1$	$57.7 \pm 12.3 \pm 9.2$
N_{pd}	98.2 ± 17.4	111.4 ± 19.2	38.8 ± 15.7
$\sigma^{pd}_{\gamma^* p}$ $[nb]$	$22.0 \pm 3.9 \pm 3.5$	$45.8 \pm 7.9 \pm 7.3$	$25.1 \pm 10.1 \pm 4.0$
	$6 < Q^2 < 18\,\text{GeV}^2$		
	$40 < W < 80\,\text{GeV}$	$80 < W < 120\,\text{GeV}$	$120 < W < 160\,\text{GeV}$
N_{ntag}	19.5 ± 4.6	26.9 ± 5.3	23.1 ± 5.2
N_{tag}	20.9 ± 4.8	25.4 ± 5.4	12.1 ± 3.6
N_{el}	26.3 ± 9.0	29.0 ± 8.3	41.4 ± 11.6
$\sigma^{el}_{\gamma^* p}$ $[nb]$	$5.96 \pm 2.04 \pm 1.07$	$12.3 \pm 3.5 \pm 2.2$	$27.4 \pm 7.7 \pm 4.9$
N_{pd}	38.9 ± 9.5	51.5 ± 11.5	36.3 ± 11.5
$\sigma^{pd}_{\gamma^* p}$ $[nb]$	$8.63 \pm 2.10 \pm 1.55$	$20.9 \pm 4.7 \pm 3.8$	$23.1 \pm 7.3 \pm 4.2$
	$18 < Q^2 < 80\,\text{GeV}^2,\ 40 < W < 160\,\text{GeV}$		
N_{ntag}	15.6 ± 4.3		
N_{tag}	7.5 ± 3.5		
N_{el}	21.6 ± 7.0		
$\sigma^{el}_{\gamma^* p}$ $[nb]$	$1.84 \pm 0.59 \pm 0.37$		
N_{pd}	13.7 ± 6.7		
$\sigma^{pd}_{\gamma^* p}$ $[nb]$	$1.13 \pm 0.54 \pm 0.22$		

Table A.4: *Summary of elastic and proton dissociation cross sections for data taken in 1995 to 1997, decay $J/\psi \to \mu^+\mu^-$.*

Q^2 interval	W interval	$\varepsilon_{ntag}^{el}[\%]$	$\varepsilon_{tag}^{el}[\%]$	$\varepsilon_{ntag}^{pd}[\%]$	$\varepsilon_{tag}^{pd}[\%]$
	$40 < W < 80\,\text{GeV}$	30.6 ± 1.1	2.3 ± 0.3	6.0 ± 0.6	26.6 ± 1.2
$2 < Q^2 < 6\,\text{GeV}^2$	$80 < W < 120\,\text{GeV}$	33.2 ± 1.4	2.7 ± 0.4	3.7 ± 0.5	25.9 ± 1.1
	$120 < W < 160\,\text{GeV}$	11.9 ± 1.0	0.5 ± 0.2	1.5 ± 0.3	6.6 ± 0.7
	$40 < W < 80\,\text{GeV}$	29.8 ± 1.8	2.9 ± 0.6	5.8 ± 1.0	25.3 ± 1.9
$6 < Q^2 < 18\,\text{GeV}^2$	$80 < W < 120\,\text{GeV}$	40.5 ± 2.2	3.1 ± 0.7	5.5 ± 1.0	31.2 ± 2.1
	$120 < W < 160\,\text{GeV}$	18.5 ± 1.9	1.2 ± 0.5	2.2 ± 0.7	14.6 ± 1.6
$18 < Q^2 < 80\,\text{GeV}^2$	$40 < W < 160\,\text{GeV}$	32.5 ± 2.6	3.0 ± 0.8	6.0 ± 1.3	27.6 ± 2.7

Table A.5: *Total acceptance for elastic and proton dissociative J/ψ production, decay $J/\psi \to e^+e^-$. Errors are from Monte Carlo statistics.*

	$2 < Q^2 < 6\,\text{GeV}^2$		
	$40 < W < 80\,\text{GeV}$	$80 < W < 120\,\text{GeV}$	$120 < W < 160\,\text{GeV}$
N_{ntag}	35.2 ± 6.8	26.4 ± 5.7	12.4 ± 4.1
N_{tag}	19.6 ± 5.2	7.4 ± 3.3	1.8 ± 1.4
N_{el}	102.3 ± 23.3	77.2 ± 17.6	102.1 ± 36.2
$\sigma_{\gamma^* p}^{el}$ [nb]	$23.8 \pm 5.4 \pm 3.8$	$33.1 \pm 7.5 \pm 5.3$	$68.4 \pm 24.2 \pm 10.9$
N_{pd}	72.3 ± 19.8	27.0 ± 12.8	29.7 ± 23.9
$\sigma_{\gamma^* p}^{pd}$ [nb]	$16.2 \pm 4.5 \pm 2.6$	$11.1 \pm 5.2 \pm 1.6$	$19.1 \pm 15.4 \pm 3.0$
	$6 < Q^2 < 18\,\text{GeV}^2$		
	$40 < W < 80\,\text{GeV}$	$80 < W < 120\,\text{GeV}$	$120 < W < 160\,\text{GeV}$
N_{ntag}	11.0 ± 3.7	5.5 ± 2.9	4.0 ± 2.3
N_{tag}	11.8 ± 3.6	15.0 ± 4.0	5.7 ± 2.5
N_{el}	28.6 ± 13.4	7.7 ± 8.4	16.8 ± 13.1
$\sigma_{\gamma^* p}^{el}$ [nb]	$6.61 \pm 3.09 \pm 1.19$	$3.12 \pm 3.40 \pm 0.56$	$11.7 \pm 9.1 \pm 2.1$
N_{pd}	46.0 ± 14.8	47.7 ± 13.2	38.1 ± 16.9
$\sigma_{\gamma^* p}^{pd}$ [nb]	$10.2 \pm 3.3 \pm 1.8$	$20.4 \pm 5.6 \pm 3.7$	$25.5 \pm 11.3 \pm 4.6$
	$18 < Q^2 < 80\,\text{GeV}^2,\ 40 < W < 160\,\text{GeV}$		
N_{ntag}	7.2 ± 3.1		
N_{tag}	1.7 ± 2.0		
N_{el}	21.6 ± 9.9		
$\sigma_{\gamma^* p}^{el}$ [nb]	$1.84 \pm 0.84 \pm 0.37$		
N_{pd}	5.7 ± 7.3		
$\sigma_{\gamma^* p}^{pd}$ [nb]	$0.47 \pm 0.60 \pm 0.10$		

Table A.6: *Summary of elastic and proton dissociation cross sections for data taken in 1995 to 1997, decay $J/\psi \to e^+e^-$.*

Appendix B

Diffractive J/ψ Production at Large $Q^2 \gtrsim 100\,\text{GeV}^2$

The analysis presented in chapter 5 was restricted to the region of $Q^2 < 80\,\text{GeV}^2$ for the following reasons: firstly the angular acceptance of the SpaCal calorimeter sets this limit, and secondly the cross section falls steeply with Q^2, $d\sigma_{ep}/dQ^2 \sim 1/Q^6$ to $1/Q^8$ at large Q^2.

Nevertheless, a simple search for J/ψ candidate events at large Q^2 was performed. The selection of events follow the exclusive J/ψ selection of section 4.5.1. The run selection was relaxed, resulting in a larger integrated luminosity of about $25\,\text{pb}^{-1}$. For the identification of the scattered electron in the LAr calorimeter the H1 software package H1KINE was used. The energy of the scattered electron had to exceed $12\,\text{GeV}$.

The mass spectrum of the selected events is shown in figure B.1. No J/ψ signal is found. A candidate event with an invariant mass of $m_{ll} = 3.60\,\text{GeV}$ is displayed in figure B.2.
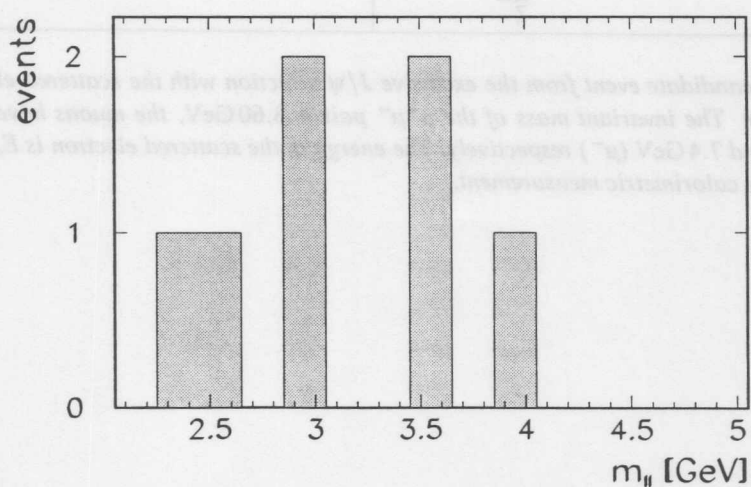
Figure B.1: *Mass spectrum of exclusive J/ψ candidate events with the scattered electron in the LAr calorimeter.*

179
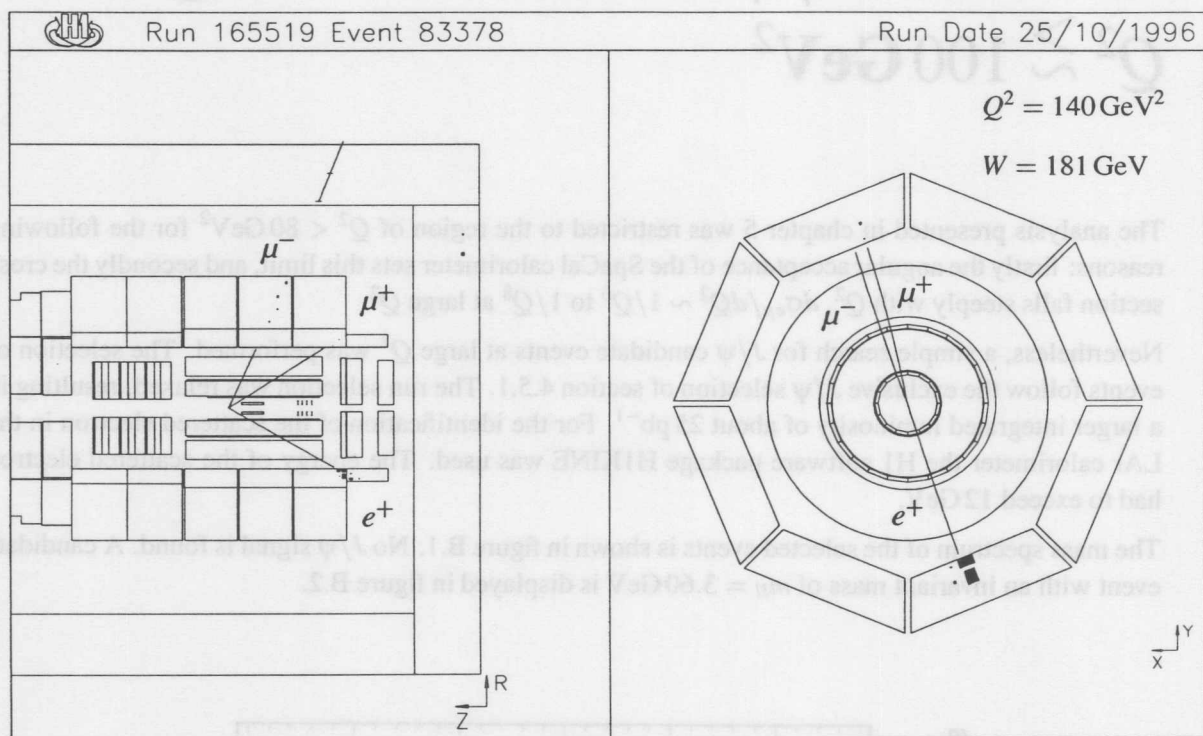
Figure B.2: *A candidate event from the exclusive J/ψ selection with the scattered electron in the LAr calorimeter. The invariant mass of the $\mu^+\mu^-$ pair is $3.60\,\mathrm{GeV}$, the muons have momenta of $5.2\,\mathrm{GeV}$ (μ^+) and $7.4\,\mathrm{GeV}$ (μ^-) respectively. The energy of the scattered electron is $E_e = 17.8\,\mathrm{GeV}$ according to the calorimetric measurement.*

List of Figures

List of Tables

Bibliography

[1] H1 Collaboration, I. Abt et al., Nucl. Instr. and Meth. **A386** (1997) 310 and Nucl. Instr. and Meth. **A386** (1997) 348.

[2] Judith Katzy, *Messung der Strukturfunktion F_2 bei kleinen Bjorken-x und kleinen Impulsüberträgen am H1-Experiment bei HERA*, Dissertation, Heidelberg (1997).

[3] H1 Calorimeter Group, B. Andrieu et al., Nucl. Instr. Meth. **A 336** (1993) 460.

[4] H1 Calorimeter Group, B. Andrieu et al., Nucl. Instr. Meth. **A 336** (1993) 499.

[5] H1 Calorimeter Group, B. Andrieu et al., Nucl. Instr. Meth. **A 344** (1994) 492.

[6] H1 Calorimeter Group, B. Andrieu et al., Nucl. Instr. Meth. **A 350** (1994) 57.

[7] M. Fleischer et al., *Performance and Upgrade of H1 Calorimeters: LAr Calorimeter, SpaCal and VLQ*, DESY Report **98-005** (1998).

[8] H1 SpaCal Group, R.D. Appuhn et al., Nucl. Instr. Meth. **A386** (1997) 397.

[9] Andreas Meyer, *Measurement of the Structure Function $F_2(x, Q^2)$ of the Proton at low Q^2 with the H1-Detector at HERA Using the New Detector Components Spacal and BDC*, Dissertation, Hamburg (1997).

[10] H1 Collaboration, S. Aid et al., *Luminosity Measurement in the H1 Experiment at HERA*, contributed paper pa17-026 to ICHEP 1996, Warsaw.

[11] H1 Collaboration, T. Ahmed et al., Z. Phys. **C66** (1995) 529.

[12] H. Bethe and W. Heitler, Proc. Roy. Soc. **A146** (1934) 83.

[13] C. Wissing, A. Beglarian, P. Biddulph and M. Fleischer, *The H1 ToF System in 1996 and 1997*, Internal H1 Note H1-01/98-533 (1998).

[14] S. Eichenberger, *A Fast Pipelined Trigger for the H1 Experiment at HERA Based on Multiwire Proportional Chamber Signals*, Dissertation, Zürich (1993).

[15] D. Handschuh, *Studien zum protoninduzierten Untergrund am H1 Detektor und Entwicklung von Filteralgorithmen zu dessen Unterdrückung*, Dissertation, DESY FH1T-93-03, Hamburg (1993).

[16] U.–P. Krüger, *Untersuchung der Erzeugung schwerer Quarks durch ihren Zerfall in Myonen im H1-Detektor bei HERA*, Dissertation, DESY F11/F22 94-02, Hamburg (1994).

[17] T.C. Nicholls, *A Measurement of the Diffractive Proton Structure Function at HERA*, Ph.D. Thesis, Birmingham (1997).

[18] V. Boudry et al., *The Inclusive Electron Trigger for SpaCal: Design and CERN-Test Results*, Internal H1-Note H1-03/95-430.

[19] H.-P. Beck, *Measurement of the Total Photoproduction Cross Section at the Electron Proton Collider HERA at $W_{\gamma p}$ of 200 GeV*, Dissertation, Zürich (1996).

[20] V. Blobel, *The BOS System — Dynamic Memory Management*, Universität Hamburg (1987).

[21] V. Blobel, P. Binko, S. Esenov, R. Gurin and Z. Szkutnik, *FPACK — F-Package for Input/Output*, H1 Internal Software Manual (1997).

[22] *GEANT — Detector Description and Simulation Tool*, CERN Program Library Long Writeup W5013.

[23] J.D. Bjorken, Phys. Rev. **179** (1969) 1547.

[24] C.G. Callan and D.J. Gross, Phys. Rev. Lett. **22** (1969) 156.

[25] L.N. Hand, Phys. Rev. **129** (1963) 1834.

[26] F.J. Gilman, Phys. Rev. **167** (1967) 1365.

[27] J.J. Aubert et al., Phys. Rev. Lett. **33** (1974) 1404.

[28] J.E. Augustin et al., Phys. Rev. Lett. **33** (1974) 1406.

[29] Y.S. Derbenev et al., Part. Accel. **8** (1978) 115.

[30] R. M. Barnett et al., Phys. Rev. **D54** (1996) 1.

[31] E. Leader and E. Predazzi, *An Introduction to Gauge Theories and Modern Particle Physics*, Cambridge University Press, Cambridge (1996).

[32] G. Zweig, *An SU*(3) *Model for Strong Interaction Symmetry and its Breaking*, CERN preprint CERN-TH-412;
J. Iizuka, Suppl. Progr. Theo. Phys. **37-38** (1966) 21.

[33] S. Bentvelsen, J. Engelen and P. Kooijman, *Reconstruction of* (*x*, Q^2) *and Extraction of Structure Functions in Neutral Current Scattering at HERA*, in: Proc. of the Workshop on Physics at HERA, ed. W. Buchmüller and G. Ingelman, Hamburg (1992), Vol. 1, p. 23;
K.C. Hoeger, *Measurement of x, y, Q^2 in Neutral Current Events*, ibid., p. 43.

[34] F. Jacqet and A. Blondel, *Proceedings of the Study of an ep Facility for Europe*, DESY, Hamburg, 2.-4. April 1979, DESY Report **79-048** (1979) 377.

[35] U. Bassler and G. Bernardi, Nucl. Instr. and Meth. A361 (1995) 197.

[36] K. Schilling and G. Wolf, Nucl. Phys. **B61** (1973) 381.

[37] BPF (Berkeley-Princeton-FNAL) Collaboration, A.R. Clark et al., Phys. Rev. Lett. **43** (1979) 187; Phys. Rev. Lett. **45** (1980) 2092.

[38] EMC Collaboration, J.J. Aubert et al., Nucl. Phys. **B213** (1983) 1.

[39] A. Arbuzov, D. Bardin, J. Bluemlein, L. Kalinovskaya and T. Riemann, *HECTOR 1.00 - A Program for the Calculation of QED, QCD and Electroweak Corrections to ep and l$^{\pm}$N Deep Inelastic Neutral and Charged Current Scattering*, DESY Report **95-185** (1995).

[40] H1 Collaboration, S. Aid et al., Nucl. Phys. **B470** (1996) 3.

[41] H1 Collaboration, C. Adloff et al., Nucl. Phys. **B497** (1997) 3.

[42] W. Buchmüller and A. Hebecker, Phys. Lett. **B355** (1995) 573.

[43] A. Edin, G. Ingelman and J. Rathsman, Phys. Rev. **D56** (1997) 7317.

[44] G. Ingelman, A. Edin and J. Rathsman, Comput. Phys. Commun. **101** (1997) 108.

[45] G. Ingelman J. Rathsman and G.A. Schuler, Comput. Phys. Commun. **101** (1997) 135.

[46] J. Nemchik and B. G. Zakharov, Z. Phys. **C64** (1994) 631.

[47] N.N. Nikolaev, B.G. Zakharov and V. R. Zoller, Phys. Lett. **B328** (1994) 486.

[48] B.Z. Kopeliovich, J. Nemchik, N.N. Nikolaev and B.G. Zakharov, Phys. Lett. **B309** (1993) 179; J. Nemchik, N.N. Nikolaev, E. Predazzi and B.G. Zakharov, *The Diffraction Cone for Exclusive Vector Meson Production in Deep Inelastic Scattering*, preprint, hep-ph/9712469 (1997).

[49] J. Nemchik, N.N. Nikolaev, E. Predazzi and B.G. Zakharov, Phys. Lett. **B374** (1996) 199.

[50] A. Donnachie and P.V. Landshoff, Phys. Lett. **B296** (1992) 227.

[51] T. Regge, Nuovo Cim. **14** No. 5 (1959) 951.

[52] J. J. Sakurai, Annals Phys. **11** (1960) 1.

[53] P.D.B. Collins, *An Introduction to Regge Theory and High Energy Physics*, Cambridge University Press, Cambridge (1977).

[54] J.J. Sakurai, Phys. Rev. Lett. **22** (1969) 981; J.J. Sakurai and D. Schildknecht, Phys. Lett. **B40** (1972) 121.

[55] T. H. Bauer, R. D. Spital, D. R. Yennie and F. M. Pipkin, Rev. Mod. Phys. **50** (1978) 261, and references therein; Erratum ibid. **51** (1979) 407.

[56] J. Hüfner and B.Z. Kopeliovich, *J/ψN and ψ(2S)N Cross Sections from Photoproduction Data: Failure of Vector Dominance*, preprint, hep-ph/9712297 (1997).

[57] M.G. Ryskin, Z. Phys. **C57** (1993) 89.

[58] A. Donnachie and P.V. Landshoff, Nucl. Phys. **B231** (1984) 189.

[59] K. Goulianos, Phys. Rep. **101** (1983) 169.

[60] E710 Collaboration, N. Amos et al., Phys. Lett. **B301** (1993) 313.

[61] L. Frankfurt, W. Koepf and M. Strikman, Phys. Rev. **D54** (1996) 3194.

[62] F.E. Low, Phys. Rev. **D12** (1975) 163;
S. Nussinov, Phys. Rev. Lett. **34** (1975) 1268.

[63] H1 Collaboration, C. Adloff et al., Z. Phys. **C76** (1997) 613 .

[64] ZEUS Collaboration, J. Breitweg et al., Phys. Lett. **B407** (1997) 432;
ZEUS Collaboration, M. Derrick et al., Z. Phys. **C72** (1996) 399.

[65] H1 Collaboration, S. Aid et al., Nucl. Phys. **B472** (1996) 3.

[66] ZEUS Collaboration, J. Breitweg et al., Z. Phys. **C75** (1997) 215.

[67] M.G. Ryskin, R.G. Roberts, A.D. Martin and E.M. Levin, Z. Phys. **C76** (1997) 231.

[68] L. Frankfurt, W. Koepf and M. Strikman, Phys. Rev. **D57** (1998) 512.

[69] M. Arneodo, L. Lamberti and M.G. Ryskin, Comput. Phys. Commun. **100** (1997) 195.

[70] S.J. Brodsky, L. Frankfurt, J.F. Gunion, A.H. Mueller and M. Strikman, Phys. Rev. **D50** (1994) 3134.

[71] L. West (for the H1 and ZEUS Collaborations), *Diffractive Heavy Flavour Production at HERA*, talk given on the LAFEX International School on High-Energy Physics (LISHEP 98), Rio de Janeiro (1998).

[72] P. Merkel, private communication (1998).

[73] G.A. Schuler and T. Sjöstrand, Nucl. Phys. **B407** (1993) 539.

[74] ZEUS Collaboration, M. Derrick et al., Z. Phys **C63** (1994) 391.

[75] H1 Collaboration, S. Aid et al., Z. Phys. **C69** (1995) 27.

[76] H1 Collaboration, S. Aid et al., Nucl. Phys. **B463** (1996) 3.

[77] ZEUS Collaboration, J. Breitweg et al., Eur. Phys. J. **C2** (1998) 247

[78] H1 Collaboration, S. Aid et al., Nucl. Phys. **B468** (1996) 3.

[79] ZEUS Collaboration, M. Derrick et al., Zeit. Phys. **C69** (1995) 39.

[80] ZEUS Collaboration, M. Derrick et al., Phys. Lett. **B356** (1995) 601.

[81] ZEUS Collaboration, M. Derrick et al., Zeit. Phys. **C73** (1996) 73.

[82] H1 Collaboration, C. Adloff et al., Z. Phys. **C75** (1997) 607.

[83] ZEUS Collaboration, M. Derrick et al., Phys. Lett. **B377** (1996) 259.

[84] ZEUS Collaboration, M. Derrick et al., Phys. Lett. **B380** (1996) 220.

[85] H1 Collaboration, C. Adloff et al., *Elastic Production of J/ψ Mesons in Photoproduction and at High Q^2 at HERA*, contributed paper 242 to HEP 1997, Jerusalem.

[86] ZEUS Collaboration, J. Breitweg et al., *Exclusive Vector Meson production in Deep Inelastic Scattering at HERA*, contributed paper 639 to HEP 1997, Jerusalem.

[87] A. Levy, *Evidence for No Shrinkage in Elastic Photoproduction of J/ψ*, Tel Aviv University preprint TAUP 2468-97, hep-ph/9712519 (1997).

[88] E. Braaten, S. Fleming and T. C. Yuan, *Production of Heavy Quarkonium in High-Energy Colliders*, Ann. Rev. Nucl. Part. Sci. **46** (1996) 197.

[89] G.A. Schuler, *Quarkonium Production and Decays*, CERN preprint CERN-TH.7170/94 (1994), submitted to Phys. Rep.

[90] H. Fritzsch, Phys. Lett. **B67** (1977) 217.

[91] F. Halzen, Phys. Lett. **B69** (1977) 105.

[92] M. Glück, J. Owens and E. Reya , Phys. Rev. **D17** (1978) 2324.

[93] J.F. Amundson, O.J.P. Eboli, E.M. Gregores and F. Halzen, Phys. Lett. **B390** (1997) 323; Phys. Lett. **B372** (1996) 127;
O.J.P. Eboli, E.M. Gregores and F. Halzen, *(No) Colour in QCD: Charmonium, Charm and Rapidity Gaps*, preprint, hep-ph/9611258 (1996);
O.J.P. Eboli, E.M. Gregores and F. Halzen, *Inelastic Photoproduction at HERA: a Second Charmonium Crisis?*, University of Wisconsin-Madison preprint MADPH-98-1045, hep-ph/9802421 (1998).

[94] C.-H. Chang, Nucl. Phys. **B172** (1980) 425.

[95] E.L. Berger and D. Jones, Phys. Rev. **D 23** (1981) 1521.

[96] R. Baier and R. Rückl, Phys. Lett. **B102** (1981) 364; Nucl. Phys. **B201** (1982) 1; Z. Phys. **C19** (1983) 251.

[97] M. Krämer, Nucl. Phys. **B459** (1996) 3.

[98] CDF Collaboration, F. Abe et al., Phys. Rev. Lett. **69** (1992) 3704.

[99] M.W. Bailey (for the CDF Collaboration), *Charmonium and Bottomonium Production in pp̄ collisions at CDF*, Contributed to 1996 Annual Divisional Meeting (DPF 96) of the Division of Particles and Fields of the American Physical Society, Minneapolis (1996), FERMILAB-CONF-96-235-E.

[100] A. Sansoni (for the CDF Collaboration), Nucl. Phys. **A610** (1996) 373.

[101] CDF Collaboration, F. Abe et al., Phys. Rev. Lett. **79** (1997) 572.

[102] D0 Collaboration, S. Abachi et al., Phys. Lett. **B370** (1996) 239.

[103] UA1 Collaboration, C. Albajar et al., Phys. Lett. **B256** (1991) 112.

[104] D. M. Kaplan, Int. J. Mod. Phys. **A12** (1997) 3827.

[105] E705 Collaboration, L. Antoniazzi et al., Phys. Rev **D46** (1992) 4828; Phys. Rev Lett. **70** (1993) 383; Phys. Rev **D49** (1994) 543.

[106] E771 Collaboration, T. Alexopoulos et al., Phys. Lett. **B374** (1996) 271.

[107] E672-E706 Collaboration, V. Koreshev et al., Phys. Rev. Lett. **77** (1996) 4294.

[108] H. L. Lai et al., Phys. Rev. **D55** (1997) 1280.

[109] M. Beneke and M. Krämer, Phys. Rev. **D55** (1997) 5269.

[110] H1 Collaboration, S. Aid et al., *Diffractive and Non-diffractive Photoproduction of J/ψ at HERA*, contributed paper pa02-085 to ICHEP 1996, Warsaw.

[111] ZEUS Collaboration, J. Breitweg et al., Z. Phys. **C76** (1997) 599.

[112] M. Glück, E. Reya and A. Vogt, Z. Phys. **C67** (1995) 433.

[113] M. Cacciari and M. Krämer, Phys. Rev. Lett. **76** (1996) 4128.

[114] H. Jung, G.A. Schuler and J. Terron, Int. J. Mod. Phys. **A 7** (1992) 7955

[115] G.T. Bodwin, E. Braaten and G.P. Lepage, Phys. Rev. **D46** (1992) 1914.

[116] G.T. Bodwin, E. Braaten and G.P. Lepage, Phys. Rev. **D51** (1995) 1125, Erratum ibid. **D55** (1997) 5853.

[117] E. Braaten and Y. Chen, Phys. Rev. **D54** (1996) 3216.

[118] E. Braaten and S. Fleming, Phys. Rev. Lett. **74** (1995) 3327.

[119] W.E. Caswell and G.P. Lepage, Phys. Lett. **B167** (1986) 437.

[120] G.T. Bodwin, D.K. Sinclair and S. Kim, Phys. Rev. Lett. **77** (1996) 2376.

[121] S. Fleming and I. Maksymyk, Phys. Rev. **D54** (1996) 3608;
M. Beneke and I.Z. Rothstein, Phys. Rev. **D54** (1996) 2005;
S. Gupta and K. Sridhar, Phys. Rev. **D54** (1996) 5545 and Phys. Rev. **D55** (1997) 2650.

[122] E. Braaten and Y. Chen, Phys. Rev. Lett. **76** (1996) 730;
K. Cheung, W. Keung and T. C. Yuan, Phys. Rev. Lett. **76** (1996) 877;
P. Cho, Phys. Lett. **368** (1996) 171.

[123] G. Japaridze and A. Tkabladze, *Color Octet Contribution to J/ψ Production at a Photon Linear Collider*, DESY Report **98-032** (1998).

[124] Y. Chen and E. Braaten, *An Explanation for the ρ − π Puzzle of J/ψ and ψ(2S) Decays*, Ohio State University preprint OHSTPY-TH-98-001, hep-ph/9801226 (1998).

[125] M. Krämer, Int. J. Mod. Phys. **A12** (1997) 3985.

[126] J. Amundson, S. Fleming and I. Maksymyk, Phys. Rev. **D56** (1997) 5844.

[127] S. Fleming, Int. J. Mod. Phys. **A12** (1997) 3995.

[128] M. Beneke, M. Krämer and M. Vänttinen, Phys. Rev. **D57** (1997) 4258

[129] S. Fleming and T. Mehen, Phys. Rev. **D57** (1998) 1846.

[130] B. A. Kniehl and G. Kramer, Phys. Rev. **D56** (1997) 5820.

[131] T. Mehen, Phys. Rev. **D55** (1997) 4338.

[132] M. Cacciari, M. Greco and M. Krämer, Phys. Rev. **D55** (1997) 7126.

[133] S. Fleming and T. Mehen, *Photoproduction of h_c*, California Institute of Technology preprint CALT-68-2154, hep-ph/9801328 (1998).

[134] OPAL Collaboration, G. Alexander et al., Phys. Lett. **B384** (1996) 343.

[135] L3 Collaboration, M. Acciarri et al., Phys. Lett. **B407** (1997) 351.

[136] P. Cho and A.K. Leibovich, Phys. Rev. **D53** (1996) 6203.

[137] B. Cano-Coloma and M.A. Sanchis-Lozano, Nucl. Phys. **B508** (1997) 753 and Phys. Lett. **B406** (1997) 232.

[138] T. Sjöstrand, Comput. Phys. Commun. **82** (1994) 74.

[139] A. D. Martin, R. G. Roberts and W. J. Stirling, Phys. Rev. **D47** (1993) 867.

[140] B.A. Kniehl and G. Kramer, *Tevatron-HERA Colour Octet Charmonium Anomaly Versus Higher Order QCD Effects*, DESY Report **98-023** (1998).

[141] R. Barbieri, R. Gatto, R. Kögerler and Z. Kunzst, Phys. Lett. **57B** (1975) 455; Nucl. Phys. **B105** (1976) 125.

[142] Andreas Meyer, private communication (1996).

[143] S. Levonian, H1 internal communication (1997).

[144] B. Naroska, S. Schiek and G. Schmidt, *Lepton Identification in the H1 Detector at Low Momenta*, Internal H1 Note H1-05/97-518 (1997).

[145] S. Schiek, *Untersuchung der inelastischen Photoproduktion von J/ψ-Mesonen im H1-Detektor bei HERA*, Dissertation, Hamburg (1997).

[146] G. Schmidt, *Untersuchung der diffraktiven Photoproduktion von J/ψ-Mesonen im H1-Detektor bei HERA*, Dissertation, Hamburg (1997).

[147] K. Pfeiffer and M. Dirkmann, *Improved Position-Reconstruction in the SpaCal's Inner Region*, Internal H1 Note H1-01/97-512 (1997).

[148] F. Gaede, *Exklusive Produktion von ϕ-Mesonen in ep-Streuung am H1-Experiment bei HERA*, Dissertation, Kiel (1998).

[149] T Jansen, *Untersuchung diffraktiver J/ψ Erzeugung bei HERA*, Dissertation, Hamburg (1995).

[150] B. List, *Diffraktive J/ψ-Produktion in Elektron-Proton-Stössen am Speicherring HERA*, Diploma Thesis, Techn. Univ. Berlin, unpublished (1993).

[151] S. Levonian, H1 Collaboration Week Feb. 1998 and H1 Meeting March 1998, H1 internal communication (1998).

[152] L. West, to be published.

[153] J. R. Forshaw and M. Ryskin, Z. Phys. **C68** (1995) 137;
J. Bartels, J. R. Forshaw, H. Lotter and M. Wüsthoff, Phys. Lett. **B375** (1996) 301.

[154] V.S. Fadin, E.A. Kuraev and L.N. Lipatov, Sov. Phys. JETP **45** (1977) 199;
I.I. Balitsky and L.N. Lipatov, Sov. J. Nucl. Phys. **28** (1978) 822;
L.N. Lipatov, Sov. Phys. JETP **63** (1986) 904.

[155] H1 Collaboration, C. Adloff et al., *Production of J/ψ Mesons with Large |t| at HERA*, contributed paper 274 to HEP 1997, Jerusalem.

[156] H. Jung, *The Monte Carlo Generator EPJPSI for J/ψ-Mesons in High Energy Electron Proton Collisions*, in: Proc. of the Workshop on Physics at HERA, ed. W. Buchmüller and G. Ingelman, Hamburg (1992), Vol. 3, p. 1488.

[157] H. Jung, D. Krücker, C. Greub and D. Wyler, Z. Phys. **C60** (1993) 721.

[158] E. Fermi, Z. Phys. **29** (1924) 315.

[159] C.F. von Weizsäcker, Z. Phys. **88** (1934) 612.

[160] E.J. Williams, Phys. Rev. **45** (1934) 729.

[161] V.M. Budnev, I.F. Ginzburg, G.V. Meledin and V.G. Serbo, Phys. Rep. **15** (1975) 181.

[162] A. D. Martin, R. G. Roberts and W. J. Stirling, Phys. Lett. **354B** (1995) 155.

[163] H. Merabet, J.-F. Mathiot and R. Mendez-Galain, Z. Phys. **C62** (1994) 639; H. Merabet, J.-F. Mathiot, Z. Phys. **C75** (1997) 495.

[164] J.G. Körner, J. Cleymans, M. Kuroda and G.J. Gounaris, Phys. Lett. **114B** (1982) 195.

[165] H. Plothow-Besch, *PDFLIB: Nucleon, Pion and Photon Parton Density Functions and α_s Calculations*, User's Manual, Version 7.09, CERN Program Library Long Writeup W5051, 1997;
H. Plothow-Besch, Int. J. Mod. Phys. **A10** (1995) 2901.

[166] S. P. Baranov, O. Dünger, H. Shooshtari and J. A. M. Vermaseren, *LPAIR: A Generator for Lepton Pair Production*, in: Physics at HERA, Proceedings of the Workshop, Vol.3, 1478, Hamburg (1991);
O. Dünger, *Untersuchung der Myonpaar-Erzeugung durch Photon-Photon-Kollision am ep-Speicherring HERA*, Dissertation, DESY F11/F22-94-01, Hamburg (1994).

[167] B. List, *Tiefunelastische ep-Streuung bei HERA unter Nachweis eines vorwärts gestreuten Protons*, Dissertation, Hamburg (1997).

[168] S. Mohrdieck, private communication (1998).

[169] *HBOOK — Reference Manual*, Version 4.22, CERN Program Library Long Writeup Y250.

[170] H1 Collaboration, S. Adloff et al., *Photo-production of $\psi(2S)$ Mesons at HERA*, submitted to Phys. Lett. B.

[171] E516 Collaboration, B.H. Denby et al., Phys. Rev. Lett. **52** (1984) 795.

[172] E401 Collaboration, M. Binkley et al., Phys. Rev. Lett. **48** (1982) 73.

[173] E687 Collaboration, P.L. Frabetti et al., Phys. Lett. **B316** (1993) 197.

[174] A. D. Martin, R. G. Roberts and W. J. Stirling, Phys. Lett. **B387** (1996) 419.

[175] A. D. Martin, R. G. Roberts and W. J. Stirling, Phys. Rev. **D51** (1995) 4756.

[176] NMC Collaboration, D. Allasia et al., Phys. Lett. **B258** (1991) 493.

[177] CHLM Collaboration, J. C. M. Armitage et al., Nucl. Phys. **B194** (1982) 365; N. Amos et al., Phys. Lett. **B120** (1983) 460.

[178] H1 Collaboration, S. Aid et al., *Elastic Electroproduction of ρ and ϕ Mesons at Intermediate Q^2 at HERA*, contributed paper 381 to HEP 1997, Jerusalem; E665 Collaboration, M.R. Adams et al., FERMILAB-PUB-97-103-E, submitted to Z.Phys. C; T. Monteiro (for the ZEUS Collaboration), in: Proceedings of the 5th International Workshop on Deep Inelastic Scattering and QCD, Chicago 1997; [78] and references therein.

[179] NMC Collaboration, M. Arneodo et al., Nucl. Phys. **B429** (1994) 503.

[180] V.L. Hudgson, *Measurement of the Cross Section for the Quasi-elastic Photoproduction of $\psi(2S)$ at HERA*, Ph.D. Thesis, Birmingham (1997).

[181] T.N. Pham et al., Phys. Lett. **B61** (1976) 183.

[182] Mark III Collaboration, D. Coffman et al., Phys. Rev. Lett. **68** (1992) 282.

[183] U. Langenegger (for the H1 and ZEUS Collaborations), *Heavy Flavour Physics at HERA*, talk given on the 6th International Workshop on Deep-Inelastic Scattering and QCD (DIS 98), Brussels (1998).

[184] H1 Collaboration, C. Adloff et al., *Determination of the Gluon Density in the Proton from Deep Inelastic ep Charm Production using NLO QCD*, contributed paper 275 to HEP 1997, Jerusalem.

[185] S. Fleming, Int. J. Mod. Phys. **A12** (1997) 3995.

[186] S. Fleming, private communication (1997).

[187] T. Doyle (for the ZEUS Collaboration), *Highlights and Open Questions from ZEUS*, talk given on the 6th International Workshop on Deep-Inelastic Scattering and QCD (DIS 98), Brussels (1998).

[188] H1 Collaboration, *ep Physics Beyond 1999*, Internal H1 Note H1-10/97-531 (1997).

Danksagung

Drei Jahre sind eine viel zu lange Zeit, als daß es möglich wäre, die Beiträge anderer zu dieser Arbeit angemessen zu würdigen; bleibt nur die Möglichkeit, eine subjektive Auswahl zu treffen.

Die erste Stelle gebührt naturgemäß denjenigen, die die größte Arbeit mit diesem Werk haben: Frau Beate Naroska, die mich mit ihrer Kritik an allen Aspekten meiner Arbeit immer wieder angespornt hat, und Herrn Klanner für die Übernahme des zweiten Gutachtens.

Ein großer Beitrag zum Gelingen einer Promotion liegt in der Arbeitsgruppe. Vielen Dank an alle Mitglieder der *Myon- und FPS-Gruppe*. Außerdem sollten einige Ko-Doktoranden erwähnt werden: die SLAC-Genossen Frank und Frank, Büro-Genosse Tim, und selbstverständlich alle Susis.

Sehr hilfreich beim Ausmerzen inhaltlicher und sprachlicher Fehler waren Petra, Katja, Frank, Chris und Paul (... Lehner, Hilton und Sutton).

Daß ich den Glauben an die Hochenergiephysik und einen naiven Enthusiasmus nicht verloren habe, ist einigen "senior physicists" von H1 zu verdanken, namentlich insbesondere Pierre Marage und John Dainton.

Am wichtigsten schließlich waren wohl all diejenigen, für die Physik fremd und langweilig ist, und die mich (hoffentlich) vor dem Status der Weltfremdheit bewahrt haben. Aber deren Namen hier zu erwähnen ist überflüssig.

ICH HABE FERTIG.